

Catalyst design for photocatalytic steam reforming of
methane around room temperature

Katsuya Shimura

Department of Applied Chemistry
Graduate School of Engineering
Nagoya University

2010

Preface

Nowadays, it has generally become recognized that hydrogen as a clean energy carrier should be produced from not the irreproducible fossil fuels but renewable resources. Currently hydrogen is produced from natural gas with the steam reforming at high temperature, which consumes huge energy. Thus, development of alternative hydrogen production method is absolutely imperative to solve the environmental and energy issues. Photocatalytic hydrogen production from water and renewable resources, such as ethanol, glycerol, sugars and methane is one of the attractive systems, since it can utilize the solar energy.

The photocatalytic steam reforming of methane is also an attractive reaction to convert solar energy into the chemical potential of the storable hydrogen by consuming only renewable resources, methane and water. The efficiency of this photocatalytic system is, however, still low and development of an efficient photocatalyst is required now. In the present thesis, the author focused on the designing heterogeneous photocatalysts for the steam reforming of methane around room temperature in order to obtain the basic strategy to design photocatalyst for this reaction. It is expected that the knowledge obtained in the present study will contribute to the development of other photocatalytic reactions, especially the hydrogen production from water.

The present thesis has been carried out during 2005-2011 at Department of Applied Chemistry, Graduate School of Engineering, Nagoya University under the supervision of Professor Hisao Yoshida.

The author would like to express his sincere appreciation for kind encouragement, suggestions, valuable discussions, and careful reviewing of the manuscript, given by Professor Hisao Yoshida. The author acknowledges Professor Atsushi Satsuma, Tsukasa Torimoto, Masao Tabuchi and Shushi Suzuki for valuable comments and reviewing this thesis. I would like to thank Professor Ryo Sasai and Hideaki Itoh for scientific guidance, suggestions and valuable discussions. I wish to thank Professor Tomoko Yoshida for the measurement of XAFS and TEM. I thank Professor Shunsuke Muto and Mr. Shinichi Komai for TEM measurements.

Hearty thanks are made to all members of the laboratories, especially Kazuhisa Hirao, Jun-ichi Nishimoto, Satoru Kato, Leny Yuliati, Kazuki Maeda, Hiroyo Miyanga, Hiromasa Kawai and Tomoki Teshima for their collaborations. Grateful thanks for the staff of the Photon Factory, Institute of Materials Structure Science, High Energy Accelerator Research Organization (KEK-PF) in Tsukuba for

making the beam time available for the XAFS measurements.

Finally, I would like to express special gratitude to my parents Masaru and Chikako, and my sister Mie for their support, understanding and continual encouragement.

Katsuya Shimura

Nagoya

January, 2011

Contents

Preface	i
Chapter 1 General Introduction	1
1.1. Hydrogen Production Methods from Biomass Derivatives other than Photocatalysis	2
1.2. The Thermodynamic and Electrochemical View	5
1.3. Photocatalytic Hydrogen Production of Water and Biomass	6
1.4. Photocatalytic hydrogen production from alcohols, aldehyde, and acid with water over TiO ₂	8
1.5. Photocatalytic hydrogen production from alcohols, aldehyde, and acid with water over CdS	16
1.6. Hydrogen production from alcohols over various photocatalysts	18
1.7. Photocatalytic hydrogen production from water and glycerol	20
1.8. Photocatalytic hydrogen production from saccharides and water	20
1.9. Photocatalytic hydrogen production from water and methane	22
1.10. Summary	23
1.11. Object and Outlines	23
Chapter 2 Photocatalytic Steam Reforming of Methane over Pt-loaded Titanium Oxide	29
Chapter 3 Photocatalytic Steam Reforming of Methane over Sodium Tantalate	53
Chapter 4 Photocatalytic Steam Reforming of Methane over Gallium Oxide	81
4.1. Photocatalytic Activation of Water and Methane over Modified Gallium Oxide for Hydrogen Production	82
4.2. Thermal Acceleration of Electron Migration in Gallium Oxide Photocatalysts	105
4.3. Doping Effect on Photocatalytic Activity of Gallium Oxide for Hydrogen Production from Water and Methane	121
Chapter 5 Photocatalytic Hydrogen Production from Water Vapor and Methane over Pt/CaTiO₃	141

5.1. Hydrogen Production from Water and Methane over Pt-loaded Calcium Titanate Photocatalyst	142
5.2. Preparation of Calcium Titanate Photocatalysts for Hydrogen Production	147
Chapter 6 Photocatalytic Steam Reforming of Methane over Potassium Titanate	159
Chapter 7 Summary	179
7.1. Summary of Each Chapter	180
7.2. General Conclusion	183
7.3. Perspective and Outlook	183
List of Publications	186

Chapter 1

General Introduction

1.1. Hydrogen production methods from biomass derivatives other than photocatalysis

The depletion of fossil fuel and the worldwide spread of environmental problems due to fossil fuels have induced the development of the alternative energy production. Since hydrogen is a storable and environmentally-benign fuel, and it can efficiently provide electricity by using fuel cells without any emission other than water, hydrogen is considered as the ideal energy source. However, we must consider the current state that about 95% of hydrogen consumed in the world is produced from petroleum and natural gas by steam reforming at high temperature.¹ The hydrogen produced in such ways cannot be regarded as the really environmentally-benign fuel.

Biomass derivatives such as ethanol, glycerol, sugars and methane are from biological substrates such as plants, starch, oil and fat, which are regarded as the renewable resources. If the biomass and derivatives are consumed to produce hydrogen with CO₂ formation, the produced CO₂ can be again converted into biomass through the plant photosynthesis (Figure 1). This means that the CO₂ produced from the biomass should not contribute to the global warming in principle, because it belongs to the carbon cycle (carbon neutral).

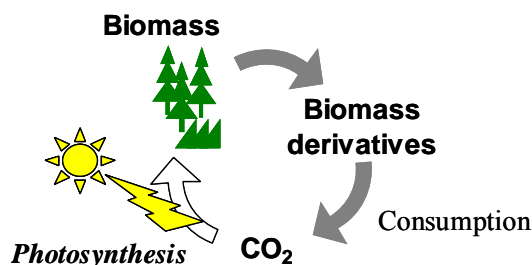


Figure 1. A carbon neutral cycle.

In this manuscript, after reviewing the possible hydrogen production methods other than photocatalysis briefly, we introduce the various attempts for photocatalytic hydrogen production from water and biomass derivatives such as ethanol, glycerol, saccharide and methane.

Currently, there are two possible methods for hydrogen production from biomass, i.e. thermal chemical process and biological process. Thermal chemical process is a method to decompose biomass thermally, such as high temperature gasification and supercritical water gasification, while the biological process is a method to decompose biomass by fermentation, such as methane fermentation. Since the methane is obtained as one of the main final products, the steam reforming of methane and successive water-gas shift reaction must be finally carried out to obtain the maximum yield of hydrogen from either method, which will be also mentioned.

1.1.1. Thermal chemical process^{2,3}

In the high temperature gasification, biomass can be thermally decomposed in the presence of oxidant such as H₂O and CO₂. The obtained gas products are H₂, CO, CO₂ and CH₄. They can be further converted into H₂ and CO₂ by steam reforming and water-gas shift reaction. The gasification of biomass is usually carried out at high temperature like 1273 K, because gasification at low temperature produces a large amount of intermediates such as tar and char. This method should not be suitable for the biomass containing a lot of water from the viewpoint of energy efficiency due to a large specific heat capacity of water.

The use of suitable catalyst can lower the reaction temperature. Although dolomite, which is natural mineral containing CaCO₃ and MgCO₃, was used as catalyst, the activity of dolomite was not high.^{4,5} On the other hand, Rh catalysts are reported to show the excellent activity for the gasification of raw biomass such as wood powder.^{6,7} Ni-based catalyst has been studied a lot, since Ni is much cheaper than precious metals. The current situation in the high temperature gasification was reviewed in references,^{8,9}

On the other hand, in the supercritical water gasification, biomass is decomposed to small molecules by the high solubility and reactivity of the supercritical water. This method is suitable for the decomposition of the biomass including water. Supercritical gasification is divided into two: one is carried out at high temperature more than 773 K and the other is done at low temperature less than 673 K. In the former condition, decomposition of biomass proceeds without the presence of catalyst, while, in the latter condition, the use of catalyst is necessary. For example, Ru catalyst was reported to show high activity.^{10,11} Ni catalyst has been extensively studied. Details of the supercritical water of biomass were reviewed in references.^{9, 12}

In the supercritical water, reactions shown in eq. 1–3 would proceed to yield hydrogen, carbon dioxide and methane. In eq. 1, cellulose is used as the model biomass. From the thermodynamic equilibrium, CO₂ and H₂ were dominantly obtained at high temperature, while CH₄ and CO₂ were main products at low temperature.



1.1.2. Biological process

Methane fermentation is a popular process for the conversion of biomass under an anaerobic condition. Figure 2 shows some routes of methane fermentation, which are roughly divided into three

steps. First, large organic compounds such as carbohydrates, proteins and fatty oils are decomposed to smaller molecules such as monosaccharide, amino acid and higher fatty acid by acid-producing bacterium and are further decomposed to lower fatty acid (i.e. propionic acid and butyric acid), lactic acid and ethanol. Then, these products are converted into hydrogen and acetic acid by the hydrogen-producing bacteria. Finally, they are transformed into methane and CO₂ by the methanogenic bacteria. The obtained methane can be converted into hydrogen by the conventional steam reforming and water-gas shift reactions. Details of the hydrogen production from biomass by fermentation were reviewed by several researchers.¹³⁻¹⁵ Since the fermentation proceeds at ambient temperature, the reaction rate is low. Furthermore, the treatment of fermentation residues is also a serious problem.

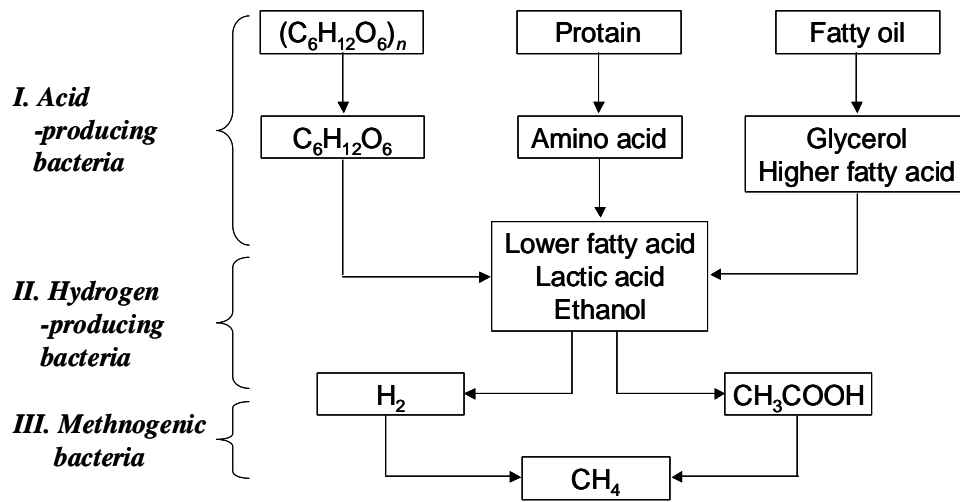


Figure 2. Some routes of the methane fermentation.

1.1.3. Steam reforming of methane

Steam reforming of methane (SRM) by using heterogeneous catalyst such as Ni or Ru catalysts has been industrially employed for hydrogen production from methane.¹⁶⁻¹⁸ The chemical equation of SRM is shown as equation 4. To obtain the maximum yield of hydrogen from methane, the produced CO is further reacted with H₂O by using both Fe-Cr and Cu-Zn catalysts as shown in equation 5, i.e., water-gas shift reaction.



SRM has the positive and large Gibbs free energy change so that high temperature typically more than 1073 K is required even in the presence of these catalysts. Steam reforming is also applied for the hydrogen production from other organic compounds such as hydrocarbon and alcohols.

Table 1 Change of Gibbs free energy at 298 K for the reaction of hydrogen production

Entry	Chemical equation	$\Delta G^0 / \text{kJ mol}^{-1}$
1	$\text{CH}_4 + 2 \text{H}_2\text{O}(\text{g}) \rightarrow \text{CO}_2 + 4 \text{H}_2$	114
2	$\text{C} + 2 \text{H}_2\text{O}(\text{g}) \rightarrow \text{CO}_2 + 2 \text{H}_2$	63
3	$\text{CH}_3\text{OH}(\text{g}) \rightarrow \text{HCHO}(\text{g}) + \text{H}_2$	59
4	$\text{CH}_3\text{OH}(\text{g}) + \text{H}_2\text{O}(\text{g}) \rightarrow \text{CO}_2 + 3 \text{H}_2$	-4
5	$\text{HCHO}(\text{g}) + \text{H}_2\text{O}(\text{g}) \rightarrow \text{HCOOH}(\text{g}) + \text{H}_2$	-20
6	$\text{CO}(\text{g}) + \text{H}_2\text{O}(\text{g}) \rightarrow \text{CO}_2 + \text{H}_2$	-29
7	$\text{HCOOH}(\text{g}) \rightarrow \text{CO}_2 + \text{H}_2$	-43
8	$\text{HCHO}(\text{g}) + \text{H}_2\text{O}(\text{g}) \rightarrow \text{CO}_2 + 2\text{H}_2$	-63
9	$1/2\text{C}_2\text{H}_6 + 2\text{H}_2\text{O}(\text{g}) \rightarrow \text{CO}_2 + 7/2\text{H}_2$	79
10	$\text{C}_2\text{H}_5\text{OH}(\text{g}) + 3\text{H}_2\text{O}(\text{g}) \rightarrow 2\text{CO}_2 + 6\text{H}_2$	65
11	$\text{C}_2\text{H}_5\text{OH}(\text{g}) \rightarrow \text{CH}_3\text{CHO}(\text{g}) + \text{H}_2$	36
12	$\text{CH}_3\text{CHO}(\text{g}) + 3\text{H}_2\text{O}(\text{g}) \rightarrow 2\text{CO}_2 + 5\text{H}_2$	30
13	$\text{CH}_3\text{CHO}(\text{g}) + \text{H}_2\text{O}(\text{g}) \rightarrow \text{CH}_3\text{COOH}(\text{g}) + \text{H}_2$	-13
14	$\text{CH}_3\text{COOH}(\text{g}) \rightarrow \text{CO}_2 + \text{CH}_4$	-71
15	$\text{CH}_3\text{CH}(\text{OH})\text{COOH}(\text{s}) + 3\text{H}_2\text{O}(\text{g}) \rightarrow 3\text{CO}_2 + 6\text{H}_2$	25
16	$\text{CH}_3\text{CH}(\text{OH})\text{CH}_3(\text{g}) \rightarrow \text{CH}_3\text{COCH}_3(\text{g}) + \text{H}_2$	21
17	$\text{C}_3\text{H}_8\text{O}_3(\text{l}) + 3\text{H}_2\text{O}(\text{g}) \rightarrow 3\text{CO}_2 + 7\text{H}_2$	-20
18	$\text{C}_6\text{H}_{12}\text{O}_6(\text{s}) + 6\text{H}_2\text{O}(\text{g}) \rightarrow 6\text{CO}_2 + 12\text{H}_2$	-85
19	$\text{H}_2\text{O}(\text{g}) \rightarrow \text{H}_2 + 1/2 \text{O}_2$	229
20	$\text{H}_2\text{O}(\text{l}) \rightarrow \text{H}_2 + 1/2 \text{O}_2$	237

1.2. The thermodynamic and electrochemical view

Table 1 shows the values of the change of Gibbs free energy at 298 K for the reactions of water vapour with some small organic compounds and water splitting.¹⁹ A reaction can proceed preferably when the change of Gibbs free energy is negative. On the other hand, reactions with positive values of the Gibbs free energy change are thermodynamically unfavorable ones. For example, the changes of Gibbs free energy for the steam reforming reactions of methane, carbon, ethane and ethanol (Table 1, entries 1, 2, 9 and 10) are largely positive values. This means that these reaction systems require energy supply and a part of the energy is stored as chemical potential in the products. This type of reaction can be called as an uphill reaction. On the other hand, in the steam reforming reactions of methanol, formaldehyde, CO, glycerol and glucose (Table 1, entries 4, 6, 8, 17 and 18), the changes of Gibbs free energy are negative values. This means that these systems must lose the chemical potential

energy. This type of reaction can be called as a downhill reaction. Here, it is noted that the changes of Gibbs free energy for the hydrogen production from water and organic compounds are obviously smaller than that for the water splitting (Table 1 entries 19 and 20). Thus, it is expected that these reactions can produce hydrogen more efficiently than the water splitting.

Table 2 shows the redox potential of some organic compounds.^{20, 21} The redox potentials of these compounds are smaller than that of water. This means that these organic compounds can be more easily oxidized than water by oxidant or the holes in the valence band of photoexcited semiconductor to release proton or hydrogen.

Table 2 Some electrochemical reactions with corresponding redox potential^a
(E_{redox}^0 vs. NHE at pH=0)

Entry	Reaction	E_{redox}^0 / V vs. NHE
1	$\text{CH}_3\text{CHO} + \text{H}_2\text{O} + 2\text{h}^+ \rightarrow \text{CH}_3\text{COOH} + 2\text{H}^+$	-0.12
2	$\text{CO} + \text{H}_2\text{O} + 2\text{h}^+ \rightarrow \text{CO}_2 + 2\text{H}^+$	-0.12
3	$\text{HCHO} + \text{H}_2\text{O} + 4\text{h}^+ \rightarrow \text{CO}_2 + 4\text{H}^+$	-0.07
4	$\text{C}_6\text{H}_{12}\text{O}_6 + 6\text{H}_2\text{O} + 24\text{h}^+ \rightarrow 6\text{CO}_2 + 24\text{H}^+$	-0.01
5	$\text{H}_2 + 2\text{h}^+ \rightarrow 2\text{H}^+$	0.00
6	$\text{CH}_3\text{OH} + \text{H}_2\text{O} + 6\text{h}^+ \rightarrow \text{CO}_2 + 6\text{H}^+$	0.03
7	$\text{C}_2\text{H}_5\text{OH} + 3\text{H}_2\text{O} + 12\text{h}^+ \rightarrow 2\text{CO}_2 + 12\text{H}^+$	0.08
8	$2\text{CH}_3\text{COOH} + 2\text{h}^+ \rightarrow \text{C}_2\text{H}_6 + 2\text{CO}_2 + 2\text{H}^+$	0.12
9	$\text{CH}_4 + \text{H}_2\text{O} + 8\text{h}^+ \rightarrow \text{CO}_2 + 8\text{H}^+$	0.17
10	$\text{C}_2\text{H}_5\text{OH} + 2\text{h}^+ \rightarrow \text{CH}_3\text{CHO} + 2\text{H}^+$	0.19
11	$\text{H}_2\text{O} + 2\text{h}^+ \rightarrow 1/2\text{O}_2 + 2\text{H}^+$	1.23

1.3. Photocatalytic hydrogen production of water and biomass

To realize sustainable society, hydrogen must be produced from renewable resources and renewable energy. Photocatalytic water splitting ($\text{H}_2\text{O} \rightarrow \text{H}_2 + 1/2\text{O}_2$) is one of the ideal methods, since hydrogen can be produced from water by using solar energy. From the discovery of Honda-Fujishima effect,²² water splitting with photoenergy and photocatalysts has been widely studied all over the world.^{23, 24} Various materials (for example, metal oxide, oxynitride and sulfide), cocatalyst (for example, NiO_x , RuO_2 and Rh-Cr) and modification (for example, doping metal ions) of photocatalysts had been examined. Nowadays, some photocatalytic systems driven in the visible light has been developed to utilize the main part of the solar spectrum.²⁵⁻²⁷ However, criteria for practical application have not been achieved yet.

Photocatalytic hydrogen production from water and biomass derivatives is also the attractive hydrogen production method. In this system, biomass derivatives and water can be converted to hydrogen and carbon dioxide by photoenergy and photocatalyst (Figure 3). The formed CO₂ can be transformed into sugars by photosynthesis, or after the growth of plant the biomass can be degraded into small organic compounds such as ethanol and methane by fermentation. On the other hand, the formed H₂ is used to yield electricity by using fuel cell, or to supply motive power by hydrogen-fueled engine.

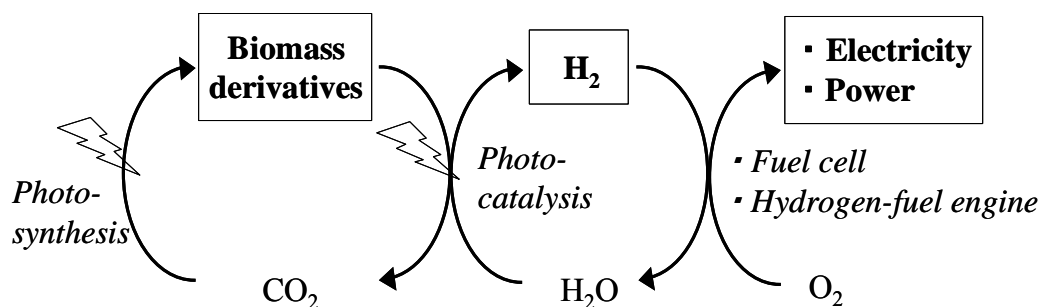
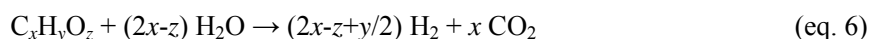


Figure 3. Carbon neutral cycle with photocatalysis.

In the early 1980's, Sakata and Kawai reported that hydrogen could be efficiently produced from water and many kinds of organic compounds, i.e. active carbon,²⁸ methanol,²⁹ ethanol,³⁰ saccharide,³¹ amino acid,³² polymer,³² raw biomass³² and fossil fuel³³ over TiO₂ loaded with Pt and/or RuO₂ cocatalyst. Sato and White examined the hydrogen production from water vapor and organic compounds such as CO,³⁴ C₂H₄³⁵ and C³⁶ over Pt/TiO₂. Harada et al. reported that hydrogen could be produced from water and lactic acid over Pt/TiO₂ and Pt/CdS.³⁷

After these early reports, the hydrogen production from water and methanol has been frequently applied as the test reaction to confirm the hydrogen production potential of the photocatalyst.^{23,24} However, there were few researches for the photocatalytic hydrogen production from water and other organic compounds.

In the present century, the photocatalytic hydrogen production from water and biomass derivatives has become an active research field. For example, Kondarides et al. examined the photocatalytic hydrogen production from aqueous solution containing not only organic compounds such as azo-dyes,³⁸ alcohols and organic acids,³⁹ but also biomass (glycerol and saccharide)⁴⁰ over Pt/TiO₂. They confirmed the stoichiometry of the products and clarified that hydrogen and carbon dioxide were produced at room temperature and atmospheric pressure as shown in the eq. 6 and Figure 4.



Various attempts have been carried out to enhance the efficiency of these photocatalytic

systems. Among the biomass derivatives, ethanol was most studied for the photocatalytic hydrogen production. In this chapter, we will overview the photocatalytic hydrogen production from ethanol, glycerol, saccharide and methane in the presence of water.

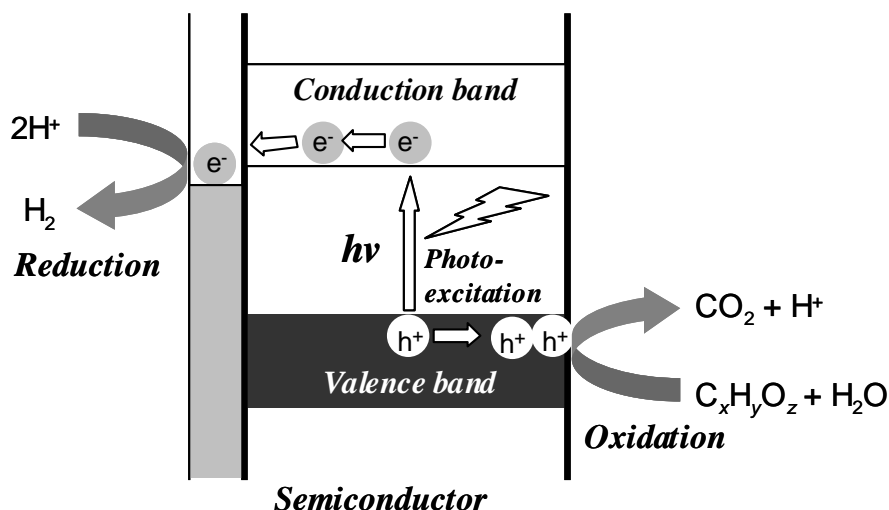


Figure 4. Photocatalytic steam reforming of biomass.

1.4. Photocatalytic hydrogen production from alcohols, aldehyde, and acid with water over TiO₂

Ethanol can be produced by fermentation of sugars and starch. Thus, it is regarded as one of the representative renewable resources. Various studies for photocatalytic hydrogen production from water and ethanol have elucidated the reaction mechanism, the effect of the reaction condition and many active photocatalysts and cocatalysts. Here, after reviewing the research using TiO₂, which is the most famous photocatalyst, the example for other semiconductor such as CdS will be also described.

1.4.1. Reaction mechanism

Sakata and Kawai examined the photocatalytic reaction of water and ethanol over metal-loaded TiO₂ in the solution without oxygen.³⁰ The obtained products were H₂, CH₃CHO, CH₃COOH, CH₄ and CO₂. At the early stage of irradiation, a lot of CH₃CHO was produced but CO₂ was not obtained. These showed that the reactions shown in equations 7–9 successively proceeded.



Assuming that reactions shown in equations 7–9 would be completed, a molar ratio of CH₄ to H₂ was expected to be 0.5. However, the result was that the ratio was ca. 0.1 even after the long reaction. Thus, they suggested that the complete oxidation of CH₃CHO shown in eq. 10 may proceed simultaneously.



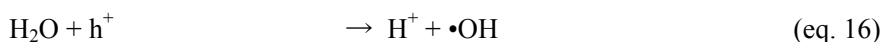
For the dehydration of ethanol (eq. 7), some mechanisms were proposed. The first is that ethanol is directly oxidized into acetaldehyde and two protons by photoexcited holes and the protons (H⁺) are reduced by photoexcited electrons as following equations 11 and 12.⁴¹



The second is that ethanol dissociatively adsorbed on the surface of TiO₂. Then, adsorbed •OCH₂CH₃ species on TiO₂ would be directly oxidized by photoformed holes, while proton would be reduce on metal cocatalyst by photoformed electrons as following equations 13–15,^{42, 43}



where, Ti(s) and O(s) show the surface Ti and O atoms on TiO₂. The third is following. It is clear that water is necessary for the complete oxidation of alcohol into CO₂. In addition, the reaction rate of the dehydration of alcohol was also accelerated by the existence of water.^{42, 44, 45} Thus, it is suggested that the active species originated from water would promote the activation of alcohols for example, as shown in equations 12, 16 and 17.



In addition, water would promote the desorption of products to enhance the reaction rate.

When the reaction was carried out in the aqueous alcohol solution containing HCl and H₂SO₄ or over the catalyst with a lot of acid sites, acetal was obtained as the major product in the solution.^{46, 47} This was because the acid-catalyzed reaction between ethanol and photoformed acetaldehyde could produce acetal as shown in eq. 18.



1.4.2 Reactivity of various alcohols

The photocatalytic hydrogen production rate from aqueous ethanol solution was compared with that from water and other organic chemicals such as alcohol, aldehyde and aliphatic acid. When the

hydrogen production rates from various neat alcohols were compared over Pt/TiO₂, the hydrogen production rate decreased as the following order: methanol \approx ethanol > 1-propanol \approx 2-propanol > 1-butanol.⁴³ The clear correlation between the hydrogen production rate and the polarity of alcohol was obtained. The same result was observed for the hydrogen production from aqueous C1-C4 alcohols over Pt/TiO₂.⁴⁸ Thus, the dissociative adsorption of alcohol over Pt/TiO₂ shown in eq. 13 would mainly govern the reaction rate. It is also obvious that with increasing carbon chain length and branches, the steric hindrance in the molecule enhanced to decrease the hydrogen production rate.

The photocatalytic hydrogen production rate from the aqueous solution of methanol was compared with those from the oxidation products (HCHO and HCOOH) over SrTiO₃ photocatalyst.⁴⁹ The hydrogen production rate decreased as following order; HCOOH (33.3 μ mol/h) > HCHO (8.1 μ mol/h) > CH₃OH (4.8 μ mol/h). This means that the rates for the consecutive reaction of the methanol oxidation are fast. In other words, the complete oxidation of methanol by water would be relatively easy to proceed. On the other hand, the oxidation products of ethanol showed a different reactivity from those of methanol. The hydrogen production rates from aqueous acetaldehyde and acetic acid over Pt/TiO₂ were 1/3 and 1/8 as large as that from aqueous ethanol, respectively.⁵⁰ This shows that the complete oxidation of ethanol into H₂ and CO₂ would be rather difficult. The complete oxidation of 2-propanol into CO₂ would be further more difficult. It was reported that almost the equivalent mole of hydrogen and acetone was photocatalytically produced over Pt/TiO₂^{42, 51} and CdS⁴⁴ even in the presence of water. These results show that the development of highly active photocatalyst would be required for the application of these alcohols other than methanol.

1.4.3. *Effect of reaction conditions*

The reaction conditions such as the concentration of alcohol, the solution pH and the reaction temperature are important factors to determine the hydrogen production rate.

It is obvious that the concentration of alcohols largely influences the hydrogen production rate. With increasing the concentration of alcohols, the hydrogen production rate first increased and then decreased in many cases.^{48, 52, 53} The increase can be understood by considering the chemical kinetics. On the other hand, the addition of excess amount of alcohol would disturb the adsorption of water to decrease the photocatalytic activity.

The solution pH also influences the hydrogen production rate from aqueous alcohol. In aqueous methanol with Pt/TiO₂, the hydrogen production rate increased with an increase of pH until 6, and then decreased with further increasing pH.⁴⁸ The optimum pH was around 6, and the point of zero

charge (PZC) of the TiO₂ is known to be pHPZC=5.8-6.0. At a pH lower than the pHPZC the TiO₂ surface is positively charged, whereas at a pH higher than the pHPZC the TiO₂ surface is negatively charged, as shown in equations 19 and 20.



Therefore, at acidic pHs (pH < 5), an electrostatic repulsion between the positively charged surface of TiO₂ and the proton (H⁺) would retard the adsorption of H⁺ to decrease the hydrogen production rate. At alkaline pHs (pH > 7), since an electrostatic repulsion between the negatively charged surface of TiO₂ and lone-pair electron of oxygen atom in alcohols would inhibit the adsorption of alcohol, the activity would decrease under the alkaline condition. When the photocatalyst has no charge, the species and molecules would more easily reach the photocatalyst surface and high photocatalytic activity could be obtained. The solution pH also influence various factors such as the agglomeration of the photocatalyst particles, the redox potential of water and organic compounds, the band bending of the semiconductor and so on. Thus, they may influence the hydrogen production rate. The same tendency for the pH of the solution was reported for the hydrogen production from aqueous ethanol over Au/TiO₂⁴¹ and the hydrogen production from aqueous 2-propanol over CdS-based photocatalyst.⁵⁴

Thermal acceleration of the photocatalytic reaction rate has been reported by many researchers so far, such as dehydration of various alcohols over metal-loaded TiO₂,^{42, 43, 55, 56} photocatalytic reaction of water and alcohol over metal-loaded TiO₂^{50, 53, 57} and SrTiO₃,⁵⁸ and the photocatalytic hydrogen production from water with active carbon, CO and glycerol over Pt/TiO₂.^{34, 36, 59} Thermal activation energies of these photocatalytic systems were varied with the kinds of reactions, semiconductor and cocatalysts, or the concentration of organic compounds. However, they were similarly less than 30 kJ/mol, which was very lower than the activation energy for the conventional catalytic reaction. Thus, thermal energy would influence only the mild activation steps such as the desorption of products^{53, 59} and the migration of the photoexcited carriers.^{55, 56}

1.4.4. Effect of cocatalyst on TiO₂

Loading metal cocatalyst is effective way to increase the activity of semiconductor photocatalyst. The work function of various metals and the reduction potential of metal ions were summarized in Table 3 for references.

When the hydrogen production rates from aqueous ethanol were compared for four metal (Pt, Rh, Pd and Ni)-loaded TiO₂ samples prepared by the photodeposition method, the activity decreased in

the following order; Pt/TiO₂ > Rh/TiO₂ > Pd/TiO₂ > Ni/TiO₂ > TiO₂.³⁰ Pt/TiO₂ showed the highest quantum yield (38% at 380 nm), which was more than 40 times higher than that for TiO₂ alone (0.9%). Pt was effective for the increase of the activity even when the metal-loading was carried out by the impregnation⁴³ and sonochemical methods.⁶¹ The high photocatalytic activity of the Pt-loaded sample was originated from the advancement of the electron-hole separation at the interface between the semiconductor and metal, and/or the catalytic activity of the Pt cocatalyst for the ethanol oxidation and the hydrogen evolution. It was also reported that loading of RuO₂ increased the photocatalytic activity of TiO₂ for hydrogen production from aqueous ethanol, although the activity of RuO₂/TiO₂ was smaller than those of Pt/TiO₂ and Pd/TiO₂.⁶² It was suggested that the RuO₂ would also work as hydrogen-evolution catalyst.

Table 3 Work function and redox potential of metal

	Work function ^a	Reaction	E_{redox}^0 at pH=0 / V vs. NHE ^b
Co	5.0	$Co^{2+} + 2e^- \rightarrow Co$	-0.287
Ni	5.15	$Ni^{2+} + 2e^- \rightarrow Ni$	-0.228
Cu	4.65	$Cu^{2+} + 2e^- \rightarrow Cu$	0.337
Ru	4.71	$Ru^{2+} + 2e^- \rightarrow Ru$	0.46
Rh	4.98	$Rh^{3+} + 3e^- \rightarrow Rh$	0.758
Ag	4.26	$Ag^+ + e^- \rightarrow Ag$	0.799
Pd	5.12	$Pd^{2+} + 2e^- \rightarrow Pd$	0.915
Ir	5.27	$Ir^{3+} + 3e^- \rightarrow Ir$	1.16
Pt	5.65	$Pt^{2+} + 2e^- \rightarrow Pt$	1.19
Au	5.1	$Au^{3+} + 3e^- \rightarrow Au$	1.50

^a Values reported in reference [60]. ^b Values reported in reference [19].

The photoatalytic hydrogen production rate from aqueous alcohol over the metal (Pt, Rh, Pd, Au, Ni, Cu, and Ag)-loaded TiO₂ photocatalysts exponentially increased with increasing the work function of metal cocatalyst.⁶³ Thus, it is suggested that the function of the metal nanoparticles would be to produce an electric field gradient, causing an efficient electron-hole separation.

Effect of loading methods was examined for Pt/TiO₂ and Au/TiO₂ photocatalysts.⁴¹ The catalysts were prepared by four methods, i.e. deposition-precipitation, impregnation, photodeposition and physical mixing. The activity of the Au-loaded samples was generally about 30% lower than that of the Pt-loaded samples. The activity for the hydrogen production from aqueous ethanol over the Au-loaded samples strongly depended on the preparation method, while Pt-loaded samples were less

sensitive. For both series of samples, the sample prepared by the photodeposition method showed higher activity than those prepared by other preparation methods did. The optimum loading amounts were 0.3-1 wt% for Pt-loaded sample and 1-2 wt% for Au-loaded sample. The exposed surface area of cocatalyst had only a small influence on the hydrogen production rate. Thus, the active sites for the reaction are proposed to be the metal surface close to the TiO₂ or the TiO₂ surface around the perimeter of the metal nanoparticles.

Pt/TiO₂ prepared by the sonochemical method showed higher activity for the hydrogen production from aqueous ethanol than that prepared by the conventional impregnation method did, since Pt particles formed by the sonochemical method was much smaller than those prepared by the impregnation method.⁶¹ The photocatalytic activity of TiO₂ loaded with Au-core/Pd-shell or Au-Pd random alloy in this method was higher than those of Pd/TiO₂ and Au/TiO₂.⁶⁴

Nonnoble metals were also examined as the cocatalyst of TiO₂, since the cost of these metals were much lower than those of noble metals. The hydrogen production rate from aqueous ethanol over CoO_x/TiO₂ prepared by an impregnation method was much higher than that over pure TiO₂ (0.13 μmol h⁻¹), although it decreased by a factor of 50% (16.1 → 8.0 μmol h⁻¹) during the long reaction (240 h).⁶⁵ The leaching of active CoO_x species on the surface of TiO₂ would be a main reason for the deactivation.

The hydrogen production from aqueous ethanol was examined for Cu, Ni or Ag-loaded TiO₂ samples prepared by the in-situ photodeposition method. Although no noticeable hydrogen was produced over the bare TiO₂, formation of hydrogen was observed over the metal-loaded TiO₂ samples. Cu-loaded sample showed much higher activity than Ni or Ag-loaded sample did.⁵³ It was estimated that the electric interaction between metal nanoparticles and TiO₂ surface would be an important factor to determine the activity. In other words, the high photocatalytic activity of the Cu-loaded sample would be originated from the adjustable junction or strong interaction between Cu nanoparticles and TiO₂ surface, which would promote the electron migration in the conduction band of TiO₂ into metal nanoparticles. The high photocatalytic activity of Cu-loaded TiO₂ was reported by other researchers.^{66, 67} CuO_x-embedded TiO₂ prepared by a water-in-oil microemulsion method showed the high quantum yield (27% at 365 nm) for the hydrogen production from aqueous ethanol.⁶⁷ Furthermore, no deactivation was observed during 30 h of reaction and the leaching of Cu species was hardly observed.

1.4.5. Particle size, morphology and polymorphs of TiO₂

The particle sizes of Pt and TiO₂ also influence on the hydrogen production rate from water and ethanol over Pt/TiO₂.⁶⁸ Loading very small amount of Pt (smaller than 0.01 monolayer on TiO₂) and

the use of TiO₂ with a particle size smaller than 0.4 μm remarkably increased the activity.

Pt/TiO₂ photocatalysts with different polymorphs were examined for the hydrogen production from 2-propanol. Anatase TiO₂ showed the high photocatalytic activity for this reaction, while rutile TiO₂ showed the negligible activity.⁵¹ The low activity of the rutile TiO₂ is attributed to the disadvantageous potential level for the reduction of proton to hydrogen as compared with anatase TiO₂. The flat band potential of rutile TiO₂ exists at almost the similar level to the reduction potential of proton, while that of anatase TiO₂ is shifted cathodically by ca. 0.2 eV (Figure 5). Thus, the energy of photoexcited electrons in the conduction band of rutile TiO₂ would be lower than that of those in anatase TiO₂. The activity of amorphous TiO₂ was also negligible, since it would contain many recombination sites of photoexcited electrons and holes.⁶⁹

Brookite TiO₂ prepared by a solvothermal method followed by hydrothermal treatment was as active as commercial TiO₂ (P-25) for the hydrogen production from 2-propanol.⁷⁰ Brookite nanorods prepared by the thermal hydrolysis of aqueous solution of titanium bis(ammonium lactate) dihydroxide in the presence of high concentration of urea exhibited higher activity in the hydrogen production rate from aqueous methanol than those over the anatase nanoparticles with a larger surface area and commercial TiO₂ (P-25).⁷¹ The high activity of the brookite sample is attributed to the high flat band potential of the brookite nanorods is more cathodically shifted by 0.14 V than that of the anatase nanoparticles.

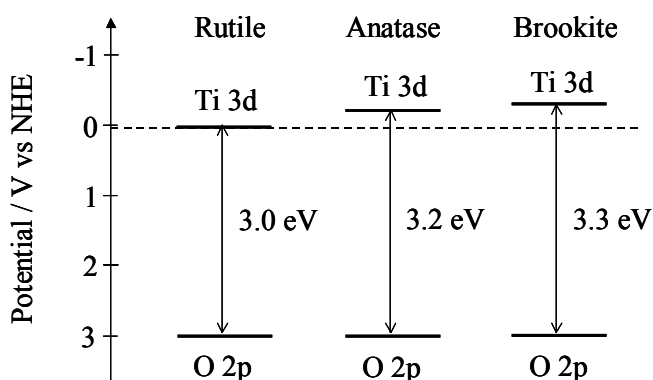


Figure 5. Band structure of TiO₂ with different polymorphs.

TiO₂(B), which is another polymorphs of TiO₂ was examined for the photocatalytic dehydration of ethanol.⁷²⁻⁷⁴ TiO₂(B) samples were prepared by a hydrothermal treatment of anatase TiO₂ powder in 10 M NaOH, followed by washing with acid and calcination at various temperatures. The hydrothermal treatment at 387 K gave TiO₂(B) nanotube, while that at 403 K gave TiO₂(B) nanofiber. With increasing the calcination temperature, TiO₂(B) transformed into anatase nanoparticles. The TiO₂(B) nanotube calcined at 673 K was composed of the mixture of TiO₂(B) nanotube and anatase nanoparticles, and showed the highest activity, which was 20% higher than that over P-25 TiO₂.

Pt/TiO₂ nanosheets with exposed (001) facets were prepared by a hydrothermal route in a Ti(OC₄H₉)₄-HF-H₂O mixed solution followed by the photodeposition of Pt nanoparticles.⁷⁵ The sample loaded with 2 wt% of Pt showed the highest activity (334 μmol/h), which was much higher than Pt/P-25

TiO₂ (223 μmol/h). A high photocatalytic activity would be originated from the synergistic effect of surface fluorination and exposed (001) facets.

The photocatalytic hydrogen production from aqueous alcohols over mesoporous TiO₂ was examined by various researchers.^{48, 50, 53, 76} For example, mesoporous TiO₂ synthesized by surfactant-assisted templating sol-gel method from laurylamine hydrochloride, tetraisopropyl orthotitanate and acetyl acetone, showed the high activity for the hydrogen production from aqueous methanol (331 μmol/h), which was much higher than those over commercial TiO₂ P-25 (31 μmol/h) and ST-01 (84 μmol/h).⁷⁶

Anpo et al. developed oxygen deficient TiO₂ film that confunction in visible light (Vis-TiO₂) by a radio frequency magnetron sputtering deposition method and examined the hydrogen production from aqueous alcohols in an H-type glass container.⁷⁷ Vis-TiO₂ has a unique anisotropic structure that the concentration of O²⁻ ions decreases from the top surface (O/Ti = 2.00) to the inside bulk (O/Ti = 1.93). The separate evolution of pure hydrogen could proceed under visible light irradiation.

1.4.6. Modification of TiO₂

Doping metal and nonmetal ions had been frequently applied to increase the photocatalytic activity of TiO₂ and other semiconductor photocatalysts. Doping of nonmetals (N, S, C etc.)⁷⁸⁻⁸⁰ or transition metals with partially filled d orbitals (Cr, Ni, Rh etc.)⁸¹⁻⁸³ can lower the bandgap of the semiconductor, since the doped ions can form the impurity levels in the forbidden band of the semiconductor. Since UV light is minor portion (only 5%) in the solar light, narrowing the bandgap of the semiconductor is necessary for the efficient utilization of solar energy. For example, Muramatsu et al. prepared TiO₂ thin film doped with sulfur (S) by atmosphere-controlled pulsed laser deposition and examined the hydrogen production from pure ethanol under the irradiation of both UV and visible light.⁸⁴ UV-vis and XPS studies demonstrated that the sulfur atoms would substitute for oxygen atoms of TiO₂ lattice to induce visible light sensitivity. Although sulfur-doping decreased the crystallization of TiO₂, the photocatalytic activity of S-doped TiO₂ was more than two times higher than that of bare TiO₂. Furthermore, nickel deposition by the chemical vapor reductive deposition method drastically increased the activity several times as much as Ni-free thin film.

On the other hand, doping metal ions such as alkali, alkaline earth and some lanthanide ions hardly influence the band structure of the semiconductor. However, doping these ions can sometimes increase the activity, since it would promote the migration of photoexcited carriers or give the positive effect on the particle size and the morphology of the photocatalyst.⁸⁵⁻⁸⁷ For example, Pt/TiO₂ doped

with 0.5 mol% of Gd showed the highest activity for the hydrogen production from aqueous methanol, which was ca. 1.4 times higher than that of none-doped Pt/TiO₂.⁸⁸

1.5. Photocatalytic hydrogen production from alcohols, aldehyde, and acid with water over CdS

CdS has a small band gap (ca. 2.4 eV) and high chemical potential of its conduction band (-0.9 V vs. NHE) as shown in Figure 6. Thus, it is one of the promising materials for the hydrogen production under the irradiation of visible light. However, the photocorrosion of the photocatalyst sometimes becomes the problems for sulfide photocatalysts including CdS.

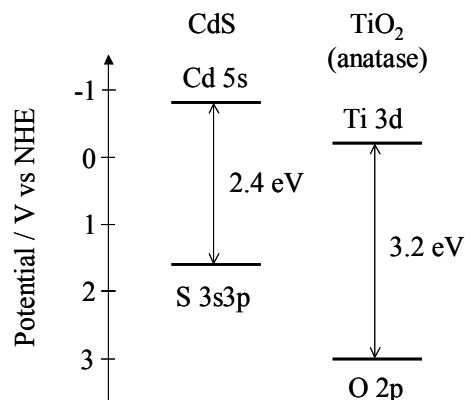


Figure 6. Band structure of CdS and TiO₂.

1.5.1. Catalyst preparation

Pt/CdS photocatalyst was prepared by the photodeposition of PtCl₆²⁻ and examined for the hydrogen production from aqueous solutions of various alcohols.⁴⁵ The activity of Pt/CdS was largely enhanced by the air-treatment at high temperature (ca. 773 K). The photoreduction product of PtCl₆²⁻ on CdS was PtS. This could be converted into metallic Pt through the thermal treatment and the metallic Pt would promote the migration of electrons to increase the photocatalytic activity.

RhO_x/CdS was examined for the hydrogen production from aqueous methanol.⁸⁹ Treatment at high temperature (773 K) and etching with acetic acid increased the photocatalytic activity. Calcination at 773 K oxidized RhCl₃ to Rh₂O₃ completely and improved the interaction between Rh₂O₃ and the surface of CdS. Although the calcination formed CdO, CdSO₄ and CdCl₂ on the surface of CdS, etching with acid would remove these species to make the surface clean. The strong interaction between Rh₂O₃ and CdS would promote the smooth charge transfer to increase the photocatalytic activity.

MoS₂/CdS photocatalyst showed the higher activity for the hydrogen production from water and lactic acid than Pt/CdS did.^{90,91} The excellent catalytic activity of MoS₂ for hydrogen evolution, together with an improvement of the junction between MoS₂ and CdS would be very important factors for the enhancement of the photocatalytic activity. It was also reported that loading of NiS on CdS largely increased the hydrogen production rate from aqueous lactic acid.⁹² NiS/CdS photocatalyst prepared by the hydrothermal method showed a high quantum efficiency of 51.3% at 420 nm.

Combination of CdS photocatalyst with zeolite would be effective for controlling the particle size of CdS.⁹³ It may also protect the CdS particles from the photocorrosion. Among the samples combined with zeolites, the order of the photocatalytic hydrogen production rate from aqueous ethanol under the visible light irradiation was zeolite-Y > SBA-15 > zeolite-L. Cavity size of zeolite influenced the particle size of CdS and the photocatalytic activity.

The CdS combined with KNbO₃ showed a higher activity than that combined with zeolite did.^{54, 94} Loading quantum sized CdS on KNbO₃ would promote the separation of photoexcited electrons and holes in CdS, since the electrons would be injected into the conduction band of KNbO₃ (Figure 7). Loading Ni/NiO on KNbO₃ further increased the activity. Quantum yield of this Ni/NiO/KNbO₃/CdS photocatalyst for the hydrogen production from aqueous 2-propanol was 8.8% ($\lambda > 400$ nm). A mixed-phase CdS matrix, which was composed of quantum-sized cubic-phase CdS and bulk-phase hexagonal CdS interlinked with platinum, also showed a high photocatalytic activity for the hydrogen production from 2-propanol.⁹⁵

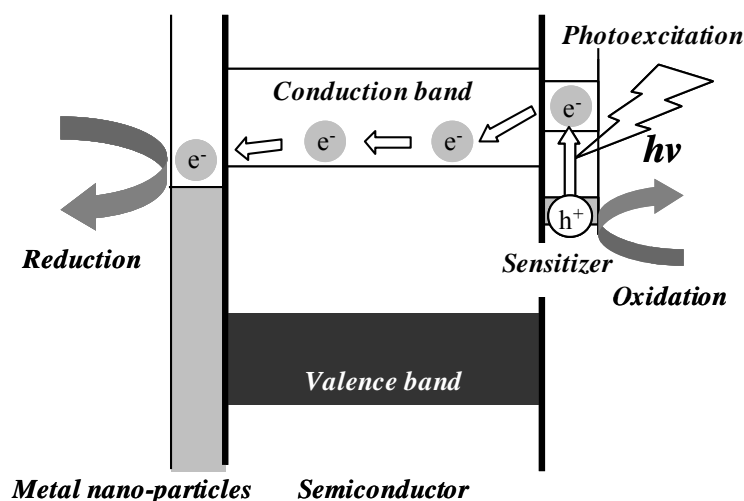


Figure 7. The mechanism of photosensitization with dye or quantum dot upon visible light irradiation.

1.5.2. Reactivity of various organic compounds

The chemistry of hydrogen production from aqueous alcohols over CdS and related photocatalysts were different from those over TiO₂ photocatalysts. The difference in the surface property and the band structure between TiO₂ and CdS (Figure 6) may cause the difference in the activities for the hydrogen production from water and various organic compounds. For example, the hydrogen production rate from aqueous alcohols solution over the Ni/NiO/KNbO₃/CdS photocatalyst decreased in the following order: 2-propanol > ethanol > methanol.⁵⁴ For the Pt/CdS, the order of the

photocatalytic activity was $\text{EtOH} > \text{MeOH} \approx \text{n-PrOH} \approx \text{1-BuOH} > \text{iso-BuOH} > \text{tert-BuOH}$.⁴⁵ For the MoS_2/CdS , the hydrogen production rate decreased in the following order; lactic acid \gg glycerol $>$ ethylene glycol $>$ ethanol $>$ methanol.⁹¹ Unlike the TiO_2 , hydrogen production rate from aqueous methanol was quite small over the CdS-based photocatalyst.

The valence band position of a $\text{CdS}_{1-x}\text{Se}_x$ solid solution was controlled by varying the ratio of sulfur to selenium and the photocatalytic activities for the hydrogen production from water and some organic compounds were examined.⁹⁶ The hydrogen production rate from aqueous solution of ethanol, methanol and Na_2SO_3 over the CdS and the solid solution samples monotonically decreased with increasing the ratio of Se, and CdSe (Bandgap was ca. 1.7 eV) produced no hydrogen. On the other hand, the hydrogen production rates from oxalic acid and formic acid over pure CdS and CdSe were high, while those over the solid solution of CdS and CdSe were very low. For the former group of the sacrificial reagents such as ethanol, the donor level of each reducing agent is relatively close to the valence band edge of the semiconductor, and it would strongly affect the reaction rate. On the other hand, for the latter group of the oxalic acid and formic acid, the donor level is negative enough to donate electrons to the valence band, and thus the other properties such as the carrier mobility would largely influence the reaction rate. In other words, the low activity of the solid solution would be due to having many trap sites reducing the mobility of the photoexcited carriers.

1.6. Hydrogen production from alcohols over various photocatalysts

The alkaline-earth titanates were well-researched for the hydrogen production from aqueous alcohols.^{44, 49, 58, 97, 98} The hydrogen production rate from aqueous 2-propanol over alkaline-earth titanates prepared by the solid-state reaction method decreased in the following order; SrTiO_3 (30 $\mu\text{mol/h}$) $>$ anatase- TiO_2 (15 $\mu\text{mol/h}$) $>$ CaTiO_3 (13 $\mu\text{mol/h}$) $>$ BaTiO_3 (6 $\mu\text{mol/h}$).⁴⁹ The hydrogen production rates from aqueous alcohols over Pt/SrTiO_3 decreased in the following order: methanol $>$ ethanol $>$ 2-propanol.⁵⁸ This order was the same as that of TiO_2 , since potentials of the valence band edge and the conduction band edge in SrTiO_3 are close to those in TiO_2 . Pt/CaTiO_3 ⁹⁷ and Pt/BaTiO_3 ⁹⁸ samples prepared by the polymerized complex (PC) method showed much higher activity for the hydrogen production from aqueous ethanol than those prepared by the solid-state reaction method, since samples prepared by the PC method were composed of homogeneous crystals and had relatively large surface area. Furthermore, the activity of CaTiO_3 was drastically improved by Zr-doping.

Nanorods of vanadium dioxide (VO_2) with body-centered-cubic (bcc) structure was synthesized, which exhibited a high quantum efficiency (38.7%) for the hydrogen production from

aqueous ethanol.⁹⁹

Some oxynitrides (TaON, Y₂Ta₂O₅N₂ and LaTaON₂) were examined for the hydrogen production from aqueous ethanol under the visible light irradiation.¹⁰⁰⁻¹⁰² In these cases, Ru-loaded samples showed much higher activity than Pt-loaded sample did. The high photocatalytic activity of the Ru-loaded sample would be attributed to the good contact with Ru and oxynitride. A remarkable improvement in hydrogen production rate was observed when both Pt and Ru were present. Co-loading of Ru and Pt would cause the facile electron migration from the conduction band of the semiconductor to metal particles.

The n-type Si powder modified with polypyrrole, Ag and Pt was prepared to prevent the corrosion of Si and was examined for the hydrogen production from aqueous ethanol.²¹ The coated Si was more stable than the bare Si in the aqueous solution, and showed much higher activity than the bare sample did. The quantum efficiency was at 2.1% at 550 nm.

The semiconductor photocatalysts for the hydrogen production from aqueous methanol were circumstantially described in references.^{23, 24}

The highly dispersed photocatalyst¹⁰³ was also active for the hydrogen production from aqueous alcohol. Mesoporous W-MCM-48 with three-dimensional pore system was examined for the hydrogen production from aqueous methanol.¹⁰⁴ Tungsten oxide species were highly dispersed in the MCM-48 matrix without destroying the ordered mesoporous structure. W-MCM-48 showed notable hydrogen evolution under UV-light irradiation, although bulk WO₃ was not active for this reaction.

Photocatalytic evolution of hydrogen from aqueous ethanol solution of polytungstate has been studied in the presence of colloidal metal catalysts.¹⁰⁵ Rustamov et al. demonstrated that UV-vis and ESR spectra of the irradiated polytungstate solution containing ethanol indicated the subsequent formation of one- and two-electron reduced decatungstates (i.e. [W₁₀O₃₂]⁵⁻ and [W₁₀O₃₂]⁶⁻, respectively). The addition of colloidal platinum increased the hydrogen production rate. The reaction mechanism was proposed involving the formation of two-electron reduced polytungstate and its subsequent reoxidation yielding hydrogen in the presence of colloidal platinum (Figure 8).

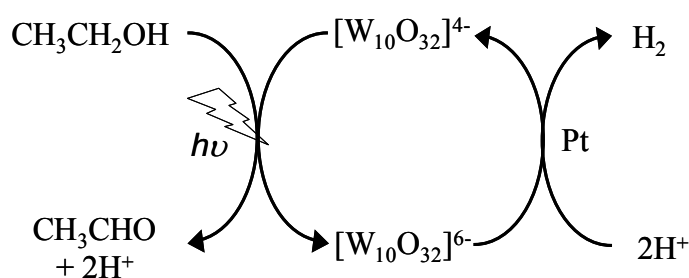


Figure 8. Photocatalytic hydrogen production from aqueous ethanol solution over Pt modified polytungstate catalyst.

1.7. Photocatalytic hydrogen production from water and glycerol

When producing biodiesel from fat oil, 10 wt% of glycerol (glycerin) per total biodiesel production is produced as a by-product. Since the world demand for glycerol is limited, development of the technology to convert glycerol into useful chemicals attracts much attention. To use glycerol as the renewable resource of hydrogen is one of the promising ways.

Kondarides et al. examined the hydrogen production from aqueous glycerol over Pt/TiO₂.⁵⁹ The reaction proceeded with the formation of intermediates such as methanol and acetic acid, and eventually resulted in the complete conversion of glycerol to H₂ and CO₂ (eq. 21).



TiO₂ loaded with 0.1-0.5 wt% of Pt showed the highest activity and further increase of Pt content decreased the activity. The hydrogen production rate was higher at neutral and basic solution than at acid solution.

Metals other than Pt were examined as the cocatalyst of TiO₂ for the hydrogen production from aqueous glycerol. The activity of Pd/TiO₂ was 1.7 times higher than that of Au/TiO₂ and was almost the same as that over Pt/TiO₂.¹⁰⁶ CuO_x/TiO₂ photocatalyst prepared by the water-in-oil microemulsion method also showed high activity for the hydrogen production from aqueous glycerol solution.⁶⁷ The quantum yield was 29% at 365 nm.

Development of the TiO₂ that can function in the visible light was also examined for the hydrogen production from aqueous glycerol. TiO₂ doped with B and N showed a higher activity under the irradiation of both UV and visible light than TiO₂ doped with either B or N, and bare TiO₂ did.¹⁰⁷ Several reasons were proposed for the increase of activity; N-doping would promote the incorporation of B into TiO₂ lattice, and codoping of B would reduce the recombination of photoexcited carriers. Pt/TiO₂ modified with heteropoly blue (HPB) showed the activity for the hydrogen production from aqueous glycerol under visible light.¹⁰⁸ The electrons formed by the excitation of HPB would migrate to TiO₂, which would enable the hydrogen production under visible light (Figure 7).

1.8. Photocatalytic hydrogen production from saccharides and water

Kawai and Sakata examined the photocatalytic hydrogen production from liquid water and carbohydrate, (C₆H₁₂O₆)_n, such as saccharose (*n*=2), starch (*n*≈100) and cellulose (*n*≈1000-5000).³¹ The RuO₂/TiO₂/Pt photocatalyst exhibited their activities. The evolved gases were mainly H₂ and CO₂, with small amount of CH₃OH and C₂H₅OH (less than 0.2% of the total amount). No CO, CH₄ and O₂ were

obtained. The atomic ratio of produced H₂ to CO₂ was 3:1 to 4:1 at the initial stage and then became 2:1 in the stoichiometric ratio. The same phenomenon was observed from the photocatalytic reaction of liquid water and glucose (*n*=1) over Pt/TiO₂.¹⁰⁹ The excess formation of hydrogen at the beginning of the reaction would be due to the dehydrogenation of carbohydrate to form >C=O, -CH=O or -COOH groups at the initial stage. The terminal hydroxyl group of glucose would be sequentially oxidized into carbon dioxide (eq. 22), and finally all carbons would be converted to carbon dioxides.



where, R shows C₅H₉O₅. Hydrogen production rate was the largest when saccharose was used as the carbohydrate. It decreased with increasing the molecular weight, since starch and cellulose were insoluble in water.

In the hydrogen production from aqueous glucose over metal-loaded TiO₂, the hydrogen production rate of metal (1 wt%)-loaded TiO₂ decreased in the following order: Pd/TiO₂ > Pt/TiO₂ > Au/TiO₂ ≈ Rh/TiO₂ > Ag/TiO₂ ≈ Ru/TiO₂.¹¹⁰ Anatase TiO₂ was more active than rutile TiO₂. The hydrogen production rate was strongly dependent on the solution pH. When pH increased from 1 to 13, the hydrogen production rate gradually increased with increasing pH and reached maximum at pH=11, followed by drastic decrease with further increasing the solution pH, where the pK_a of glucose (ca. 12.3) would influence the hydrogen production rate. At pH lower than the pK_a, the glucose in the solution is mainly in molecular form and would prefer to bond with undercoordinated surface Ti atoms through its oxygen atom of hydroxyl group. With increasing the solution pH, the dissociative adsorption of glucose would become possible and it would enhance the activity. However, at pH higher than the pK_a, glucose in the solution mainly exists as RCH₂-O⁻. Thus, the electrostatic repulsion between the negatively charged TiO₂ surface and RCH₂-O⁻ would inhibit the adsorption of glucose to decrease the hydrogen evolution rate. Therefore, the maximum activity would be obtained at the pH close to the pK_a.

Sulfides such as ZnInS₂ and CdS were also examined for the hydrogen production from aqueous glucose under visible light.^{111, 112} In the case of ZnIn₂S₄, the highest hydrogen production rate was obtained at pH=12.7.¹¹¹ which supports the above mechanism more clearly. The photocatalytic activity of ZnIn₂S₄ was increased by ZnS-coating. The ZnS on ZnInS₂ promoted the adsorption of glucose, which would be one possible reason for the increase of the photocatalytic activity.

Photocatalytic hydrogen production from aqueous glucose solution was examined for alkali tantalites.¹¹³ The order of the hydrogen production rate was NaTaO₃ >> KTaO₃ > LiTaO₃. NiO-loading increased the hydrogen production rate over NaTaO₃, which was more effective than Pt cocatalyst.

Conduction band edge of Fe₂O₃ does not satisfy the potential for the hydrogen production in usual. However, Mcfarland et al. found that Ti-doped Fe₂O₃ thin films modified by CoF₃ were active for

the hydrogen production from aqueous glucose.¹¹⁴ The modification of Fe_2O_3 surface with CoF_3 negatively shifted the flat-band potential of Fe_2O_3 (Figure 9). Thus, the hydrogen production without an extra bias was achieved. The incident photon to current efficiency (IPCE) was 3.7% at 400 nm.

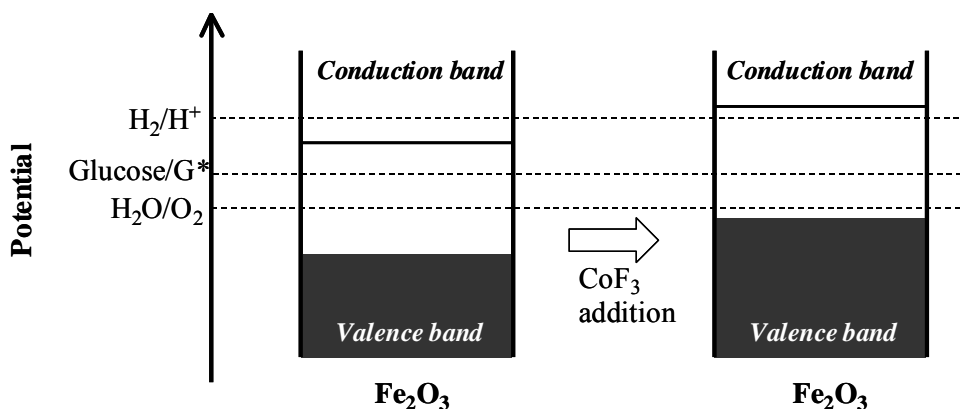


Figure 9. Schematic energy level diagram of Fe_2O_3 based photocatalyst before and after CoF_3 aqueous solution treatment.

1.9. Photocatalytic hydrogen production from water and methane

The technology to convert methane into hydrogen is very important because methane is often obtained as the ultimate product from biomass. However, the conversion of it usually requires much energy, i.e., high temperature, since methane is the most stable chemical compounds among hydrocarbons. It is reported that methane can be photocatalytically activated around room temperature or at a mild condition with or without the oxidant molecule such as O_2 and CO_2 .¹¹⁵ The photocatalytic reaction of water and methane was also reported by some researchers.

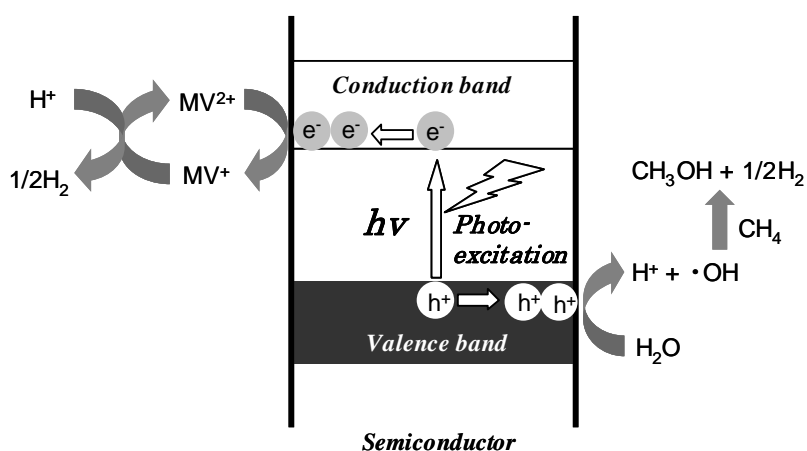


Figure 10. Proposed mechanism of photocatalytic conversion of methane into methanol over La/WO_3 .

Taylor examined the reaction of liquid water containing electron-transfer reagent (MV: methyl viologen) and methane with a metal oxide photocatalyst (La-doped WO₃ or TiO₂) upon photoirradiation at high pressure of 1.0 or 10.1 MPa.¹¹⁶ Hydrogen, methanol, ethane, oxygen, formic acid and carbon dioxide were produced. The mechanism for the formation of methanol was proposed as shown in Figure 10.

Gonal et al. examined the photocatalytic conversion of methane and liquid water to methanol by using a visible laser light (514 nm) and a WO₃ photocatalyst at room temperature.¹¹⁷ The products observed were methanol, O₂ and CO₂. They also examined that the reaction of methane and water over WO₃, TiO₂ (rutile) and NiO photocatalysts under the irradiation of a strong UV beam at 355 nm.¹¹⁸ The hydrogen and methanol were photocatalytically produced at room temperature.

Recently, we found that the photocatalytic steam reforming of methane (PSRM) shown in eq. 23 could proceed over Pt-loaded semiconductor photocatalysts around room temperature at atmosphere pressure.¹¹⁹



1.10. Summary

Photocatalytic hydrogen production from water and biomass derivatives is an attractive reaction, since it has a potential of converting solar energy into the chemical potential of the storable hydrogen with water and biomass as renewable resources. As reviewed, various attempts had been done to achieve the efficient hydrogen evolution, such as development of various semiconductors and cocatalyst, modification of photocatalyst, the morphology control of photocatalyst, optimization of reaction condition and so on. So far, several photocatalysts showing high quantum efficiency under the UV light irradiation have been developed (Table 4). However, efficiency of these photocatalytic reactions is still low and many problems to be solved remain for a practical application.

1.11. Object and Outlines

In this thesis, the author focused on the designing heterogeneous photocatalysts for the steam reforming of methane around room temperature in order to obtain the basic strategy to design photocatalyst for this reaction.

In the chapter 2, the reaction mechanism in the photocatalytic steam reforming of methane was examined by using Pt/TiO₂ photocatalyst. In the chapter 3, effects of doping metal ions and loading

cocatalysts on the activity of NaTaO₃ photocatalyst was examined. In the chapter 4.1, the structural factors influencing the activity of Ga₂O₃ photocatalyst was examined. In the chapter 4.2, the author examined the influence of the external thermal energy on the activity of Ga₂O₃ photocatalyst. In the chapter 4.3, the local structure of the dopants and the photocatalytic activity of the doped Ga₂O₃ were studied. In the chapter 5.1, effect of the coexistence of methane on the hydrogen production from water vapor was examined by using Pt/CaTiO₃ photocatalyst. In the chapter 5.2, the author prepared various CaTiO₃ samples and examined their photocatalytic activities. In the chapter 6, effect of Rh cocatalyst on the activity of K₂Ti₆O₁₃ photocatalyst was examined. The whole chapter would picture the fundamental knowledge to design catalysts for photocatalytic steam reforming of methane.

Table 4 Quantum yield for photocatalytic hydrogen production from water and organic compounds

Entry	Sacrificial reagent	Photocatalyst	Wavelength /nm	QY / %	Ref.
1	Ethanol	Pt/TiO ₂ (rutile)	380	38.0	30
2		Pt/CaTi _{0.973} Zr _{0.07} O ₃	365	13.3	97
3		Pt/BaTi ₄ O ₉	365	11.7	98
4		VO ₂	UV light	38.7	90
5		Pt(Ag)/Si/polypyrrole	550	2.1	21
6	Ethanol	Ru/TaON	420 < λ < 500	2.1	101
	Methanol			0.8	
7	Ethanol	CuO _x /TiO ₂ (anatase)	365	27	67
	Glycerol			29	
8	Ethanol	Pt/TiO ₂ (P-25)	365	50	40
	Glycerol			70	
	Glucose			63	
9	methanol	Pt/SrTiO ₃	UV light	1.9	58
10	2-propanol	Ni/NiO/KNbO ₃ /CdS	λ ≥ 400	8.8	94
11	Lactic acid	Pt/TiO ₂ (rutile)	360	71	37
		Pt/CdS	440	38	
12		MoS ₂ /CdS	420	7.3	91
13		NiS/CdS	λ ≥ 420	51.3	92
14	Saccharose	RuO ₂ /TiO ₂ /Pt	380	1.5	31

Reference

- 1) Balat, H.; Kirtay, E. *Int. J. Hydrogen Energy* **2010**, 35, 7416–7426.
- 2) Inaba, M.; Murata, K.; Saito M.; Takahara, I. *Energy and Fuels* **2006**, 20, 432–438.
- 3) Yamaguchi, A.; Hiyoshi, N.; Sato, O.; Bando, K.; Osada, M.; Shirai, M. *Catal. Today* **2009**, 146,

- 192–195.
- 4) Bridgwater, A. V. *Appl. Catal. A* **1994**, 116, 5–47.
 - 5) Sutton, D.; Kelleher, B.; Ross, J. R. H. *Fuel Process. Tech.* **2001**, 73, 155–173.
 - 6) Asadullah, M.; Tomishige, K.; Fujimoto, K. *Catal. Comm.* **2001**, 2, 63–68.
 - 7) Asadullah, M.; Miyazawa, T.; Ito, S.; Kunimori, K.; Tomishige, K. *Appl. Catal. A* **2003**, 246, 103–116.
 - 8) Yung, M. M.; Jablonski, W. S.; Magrini-Bair, K. A. *Energy and Fuel* **2009**, 23, 1874–1887.
 - 9) Tanksale, A.; Beltramini, J. N.; Lu, G. M. *Renewable and Sustainable Energy Reviews* **2010**, 14, 166–182.
 - 10) Park, K. C.; Tomiyama, H. *Chem. Comm.* **2003**, 694–695.
 - 11) Osada, M.; Sato, T.; Watanabe, M.; Adschiri, T.; Arai, K. *Energy and Fuels* **2004**, 18, 327–333.
 - 12) Guo, Y.; Wang, S. Z.; Xu, D. H.; Gong, Y. M.; Ma, H. H.; Tang, X. Y. *Renewable and Sustainable Energy Reviews* **2010**, 14, 334–343.
 - 13) Chong, M.; Sabaratnam, V.; Shirai, Y.; Hassan, M. A. *Int. J. Hydrogen Energy* **2009**, 34, 3277–3287.
 - 14) Lu, Y.; Lai, Q.; Zhang, C.; Zhao H.; Ma, K.; Zhao, X.; Chen, H.; Liu, D.; Xing, X. *Bioresource Technology* **2009**, 100, 2889–2895.
 - 15) Zhnag, Y. -H. P.; *Int. J. Hydrogen Energy* **2010**, 35, 10334–10342.
 - 16) Rostrup-Nielsen, J. R. *Catal. Today* **1993**, 18, 305–324.
 - 17) Peña, M. A.; Gómez, J. P.; Fierr, J. L. G. *Appl. Catal. A* **1996**, 144, 7–57.
 - 18) Armor, J. N.; *Appl. Catal. A* **1999**, 176, 159–176.
 - 19) The Chemical Society of Japan Kagakubinran Kisoheh, 3rd Ed. Maruzen, Tokyo **1984**.
 - 20) Indrakanti, P. V.; Kubicki, J. D.; Schobert, H. H. *Energy Environ. Sci.* **2009**, 2, 745–758.
 - 21) Taniguchi, Y.; Yoneyama, H.; Tamura, H. *Chem. Lett.* **1983**, 269–272.
 - 22) Fujishima, A.; Honda, K. *Nature* **1972**, 238, 37–38.
 - 23) Kudo, A.; Miseki, Y. *Chem. Soc. Rev.* **2009**, 38, 253–278.
 - 24) Chen, X.; Shen, S.; Guo, L.; Mao, S. S. *Chem. Rev.* **2010**, 110, 6503–6570.
 - 25) Maeda, K.; Teramura, K.; Lu, D. L.; Takata, T.; Saito, N.; Inoue, Y.; Domen, K. *Nature* **2006**, 440, 295.
 - 26) Sasaki, Y.; Nemoto, H.; Saito, K.; Kudo, A. *J. Phys. Chem. C* **2009**, 113, 17536–17542.
 - 27) Maeda, K.; Higashi, M.; Abe, R.; Domen, K. *J. Am. Chem. Soc.* **2010**, 132, 5858–5868.
 - 28) Sakata, T.; Kawai, K. *Nature* **1979**, 282, 283–284.
 - 29) Kawai, T.; Sakata, T. *J. Chem. Soc. Chem. Comm.* **1980**, 15, 694–695.
 - 30) Kawai, T.; Sakata, T. *Chem Phys Lett.* **1981**, 80, 341–344.
 - 31) Kawai, T.; Sakata, T. *Nature* **1980**, 286, 474–476.
 - 32) Kawai, T.; Sakata, T. *Chem. Lett.* **1981**, 81–84.
 - 33) Hashimoto, K.; Kawai, T.; Sakata, T. *J. Phys. Chem.* **1984**, 88, 4083–4088.
 - 34) Sato, S.; White, J.M.; *J. Am. Chem. Soc.* **1980**, 102, 7206–7210.

- 35) Sato, S.; White, J.M. *Chem Phys Lett.* **1980**, 70, 131–134.
- 36) Sato, S.; White, J.M. *J.Phys. Chem.* **1981**, 85, 336–341.
- 37) Harada, H.; Sakata, T.; Ueda, T. *J. Am. Chem. Soc.* **1985**, 107, 1773–1774.
- 38) Patsoura, A.; Kondarides, D. I.; Verykious, X. E. *Appl. Catal. B* **2006**, 64, 171–179.
- 39) Patsoura, A.; Kondarides, D. I.; Verykious, X. E. *Catal. Today* **2007**, 124, 94–102.
- 40) Kondarides, D. I.; Daskalaki, V. M.; Patsoura, A.; Verykious, E. *Catal. Lett.* **2008**, 122, 26–32.
- 41) Bamwenda, G. R.; Tsubota, S.; Nakamura, T.; Haruta, M. *J. Photochem. Photobiol. A* **1995**, 89, 177–189.
- 42) Ait-Ichou, I.; Formenti, M.; Pommier, B.; Teichener, S. J. *J. Catal.* **1985**, 91, 293–307.
- 43) Yang, Y. Z.; Chang, C. -H.; Idriss, H. *Appl. Catal. B* **2006**, 67, 217–223.
- 44) Domen, K.; Naito, S.; Onishi, T.; Tamaru, K. *Chem. Lett.* **1982**, 555–558.
- 45) Jin, Z.; Lin, Q.; Zheng, X.; Xi, C.; Wang, C.; Zhang, H.; Feng, L.; Wang, H.; Chen, Z.; Jiang, Z. *J. Photochem. Photobiol. A* **1993**, 71, 85–96.
- 46) Ohtani, B.; Kakimoto, M.; Nishimoto, S.; Kagiya, T. *J. Photochem. Photobiol. A* **1993**, 70, 265–272.
- 47) Lee, C.-H.; Lee, C. -H.; Chao, J. -H.; Kuo, C. -Y.; Cheng, Y. -C.; Huang, W. -N.; Chang, H. -W.; Huang, Y. -M.; Shih, Y. -M. *Catal.Lett.* **2004**, 98, 61–66.
- 48) Sreethawong, T.; Puangpeth, T.; Chavadej, S.; Yoshikawa, S. *J. Powder Sources* **2007**, 165, 861–869.
- 49) Zielinska, B.; Borowiak-Palen, E.; Kalenczuk, R. *J. Int. J. Hydrogen energy* **2008**, 33, 1797–1802.
- 50) Sun, W.; Zhang, S.; Liu, Z.; Wang, C.; Mao, Z. *Int. J. Hydrogen energy* **2008**, 33, 1112–1117.
- 51) Nishimoto, S.; Ohtani, B.; Kajiwarra, H.; Kagiya, T. *J. Chem. Soc. Faraday Trans.* **1985**, 81, 61–68.
- 52) Chiarello, G. L.; Aguirre, M. H.; Selli, E. *J. Catal.* **2010**, 273, 182–190.
- 53) Korzhak, A. V.; Ermokhina, N. I.; Stroyuk, A. L.; Bukhtiyarov, V. K.; Raevskaya, A. E.; Litvin, V. I.; Bukhtiyarov, S. Y.; Ilyin, V. G.; Manorik, P. A. *J. Photochem. Photobiol. A* **2008**, 198, 126–134.
- 54) Choi, J.; Ryu, S. Y.; Balcerski, W.; Lee, T. K.; Hoffmann, M. R. *J. Mater. Chem.* **2008**, 18, 2371–2378.
- 55) Hussein, F. H.; Rudham, R. *J. Chem. Soc. Faraday Trans.* **1984**, 80, 2817–2825.
- 56) Hussein, F. H.; Rudham, R. *J. Chem. Soc. Faraday Trans.* **1987**, 83, 1631–1639.
- 57) Naito, S. *Can. J. Chem.* **1986**, 64, 1795–1799.
- 58) Puangpetch, T.; Sreethawong, T.; Yoshiawa, S.; Chavadej, S. *J. Mol. Catal. A* **2009**, 312, 97–106.
- 59) Daskalaki, V. M.; Kondarides, D. I. *Catal. Today* **2009**, 144, 75–80.
- 60) Michaelson, H. B. *J. Appl. Phys.* **1977**, 48, 4729–4733.
- 61) Mizukoshi, Y.; Makise, Y.; Shuto, T.; Hu, J.; Tominaga, A.; Shironita, S.; Tanabe, S. *Ultrason. Sonochem.* **2007**, 14, 387–392.
- 62) Sakata, T.; Hashimoto, K.; Kawai, T. *J. Phys. Chem.* **1984**, 88, 5214–5221.
- 63) Nosaka, Y.; Norimatsu, K.; Miyama, H. *Chem. Phys. Lett.* **1984**, 106, 128–130.

- 64) Mizukoshi, Y.; Sato, K.; Konno, T. J.; Masahashi, N. *Appl. Catal. B* **2010**, 94, 248–253.
- 65) Wu, Y.; Lu, G.; Li, S. *J. Photochem. Photobiol. A* **2006**, 181, 263–267.
- 66) Wu, N. -L.; Lee, M. -S. *Int. J. Hydrogen Energy* **2004**, 29, 1601–1605.
- 67) Gombac, V.; Sordelli, L.; Montini, T.; Delgado, J. J.; Adamski, A.; Adami, G.; Cargnello, M.; Bernal, S.; Fornasiero, P. *J. Phys. Chem. A* **2010**, 114, 3916–3925.
- 68) Sakata, T.; Kawai, T.; Hashimoto, K. *Chem. Phys. Lett.* **1982**, 88, 50–54.
- 69) Ohtani, B.; Ogawa, Y.; Nishimoto, S. *J. Phys. Chem. B* **1997**, 101, 3746–3752
- 70) Kominami, H.; Ishii, Y.; Kohno, M.; Konishi, S.; Kera, Y.; Ohtani, B. *Catal. Lett.* **2003**, 91, 41–47
- 71) Kandiel, T. A.; Feldhoff, A.; Robben, L.; Dillert, R.; Bahnemann, D. W. *Chem. Mater.* **2010**, 22, 2050–2060.
- 72) Kuo, H. -L.; Kuo, C. -Y.; Liu, C. -H.; Chao, J. -H.; Lin, C. -H. *Catal. Lett.* **2007**, 113, 7–12.
- 73) Lin, C. -H.; Chao, J. -H.; Liu, C. -H.; Chang, J. -C.; Wang, F. -C. *Langmuir* **2008**, 24, 9907–9915.
- 74) Wang, F. -C.; Lin, C. -H.; Liu, C. -W.; Chao, J. -H.; Lin, C. -H. *J. Phys. Chem. C* **2009**, 113, 13832–13840.
- 75) Yu, J.; Qi, L.; Jaroniec, M. *J. Phys. Chem. C* **2010**, 114, 13118–13125.
- 76) Sreethong, T.; Suzuki, Y.; Yoshikawa, S. *J. Solid State Chem.* **2005**, 178, 329–338.
- 77) Fukumoto, S.; Kitano, M.; Takeuchi, M.; Matsuoka, M.; Anpo, M. *Catal. Lett.* **2009**, 127, 39–43.
- 77) Asahi, R.; Morikawa, T.; Ohwaki, T.; Aoki, K.; Taga, Y. *Science* **2001**, 293, 269–271.
- 79) Ohno, T.; Mitsui, T.; Matsumura, M. *Chem. Lett.* **2003**, 32, 364–365.
- 80) Irie, H.; Watanabe, Y.; Hashimoto, K. *Chem. Lett.* **2003**, 32, 772–773.
- 81) Hwang, D. W.; Kim, H. G.; Lee, J. S.; Kim, J.; Li, W.; Oh, S. H. *J. Phys. Chem. B* **2005**, 109, 2093–2102.
- 82) Kudo, A.; Sekizawa, M. *Chem. Comm.* **2000**, 1371–1372.
- 83) Konta, R.; Ishii, T.; Kato, H.; Kudo, A. *J. Phys. Chem. B* **2004**, 108, 8992–8995.
- 84) Yoshinaga, M.; Yamamoto, K.; Sato, N.; Aoki, K.; Morikawa, T.; Muramatsu, A. *Appl. Catal. B* **2009**, 87, 239–244.
- 85) Ishihara, T.; Nishiguchi, H.; Fukamachi, K.; Takita, Y. *J. Phys. Chem. B* **1999**, 103, 1–3.
- 86) Kato, H.; Asakura, K.; Kudo, A. *J. Am. Chem. Soc.* **2003**, 125, 3082–3089.
- 87) Takata, T.; Domen, K. *J. Phys. Chem. C* **2009**, 113, 19386–19388.
- 88) Zalas, M.; Lanieceki, M. *Solar Energy Material and Solar Cells* **2005**, 89, 287–296.
- 89) Lu, G.; Li, S. *J. Photochem. Photobiol. A* **1996**, 97, 65–72.
- 90) Zong, X.; Yan, H.; Wu, G.; Ma, G.; Wen, F.; Wang, L.; Li, C. *J. Am. Chem. Soc.* **2008**, 130, 7176–7177.
- 91) Zong, X.; Wu, G.; Yan, H.; Ma, G.; Shi, J.; Wen, F.; Wang, L.; Li, C. *J. Phys. Chem. C* **2010**, 114, 1963–1968.
- 92) Zhang, W.; Wang, Y. B.; Wang, Z.; Zhong, Z. Y.; Xu, R. *Chem. Comm.* **2010**, 46, 7631–7633.
- 93) Ryu, S. Y.; Balcerski, W.; Lee, T. K.; Hoffmann, M. R. *J. Phys. Chem. C* **2007**, 111, 18195–18203.

- 94) Ryu, S. Y.; Choi, J.; Balcerski, W.; Lee, T. K.; Hoffmann, M. R. *Ind. Eng. Chem. Res.* **2007**, *46*, 7476–7488.
- 95) Silva, L. A.; Ryu, S. Y.; Choi, J.; Choi, W.; Hoffmann, M. R. *J. Phys. Chem. C* **2008**, *112*, 12069–12073.
- 96) Kambe, S.; Fujii, M.; Kawai, T.; Kawai, S.; Nakahara, F. *Chem. Phys. Lett.* **1984**, *109*, 105–109.
- 97) Sun, W.; Zhang, S.; Wang, C.; Liu, Z.; Mao, Z. *Catal. Lett.* **2007**, *119*, 148–153.
- 98) Sun, W.; Zhang, S.; Wang, C.; Liu, Z.; Mao, Z. *Catal., Lett.* **2008**, *123*, 282–288.
- 99) Wang, Y.; Zhang, Z.; Zhu, Y.; Li, Z.; Vajtai, R.; Ci, L.; Ajayan, P. M. *ACS Nano* **2008**, *2*, 1492–1496.
- 100) Hara, M.; Nunoshige, J.; Takata, T.; Kondo, J. N.; Domen, K. *Chem. Comm.* **2003**, 3000–3001.
- 101) Liu, M.; You, W.; Lei, Z.; Zhou, G.; Yang, J.; Wu, G.; Wu, G.; Ma, G.; Luan, G.; Takata, T.; Hara, M.; Domen, K.; Li, C. *Chem. Commun.* **2004**, 2192–2193.
- 102) Liu, M.; You, W.; Lei, Z.; Takata, T.; Domen, K.; Li, C. *Chin. J. Catal.*, **2006**, *27*, 556–558.
- 103) Yoshida, H. *Current Opinion in Solid State & Materials Science* **2003**, *7*, 435–442.
- 104) Zhao, D.; Rodriguez, A.; Dimitrijevic, N. M.; Rajh, T.; Koodali, R. T. *J. Phys. Chem. C* **2010**, *114*, 15728–15734.
- 105) Rustamov, M. I.; Muradov, N. Z.; Guseinova, A. D.; Bazhutin, Y. V. *Int. J. Hydrogen Energy.* **1988**, *13*, 533–538.
- 106) Bowker, M.; Davies, P. R.; Al-Mazroai, L. S. *Catal. Lett.* **2009**, *128*, 253–255.
- 107) Luo, N.; Jiang, Z.; Shi, H.; Cao, F.; Xiao, T.; Edwards, P. P. *Int. J. Hydrogen Energy* **2009**, *34*, 125–129.
- 108) Fu, N.; Lu, G. *Catal. Lett.* **2009**, *127*, 319–322.
- 109) St. John, M. R.; Furgala, A. J.; Sammells, A. F. *J. Phys. Chem.* **1983**, *87*, 801–805.
- 110) Fu, X.; Long, J.; Wang, X.; Leung, D. Y. C.; Ding, Z.; Wu, L.; Zhang, Z.; Li, Z.; Fu, X. *Int. J. Hydrogen Energy* **2008**, *33*, 6484–6491.
- 111) Li, Y.; Wang, J.; Peng, S.; Lu, G.; Li, S. *Int. J. Hydrogen Energy* **2010**, *35*, 7116–7126.
- 112) Peng, S.; Peng, Y.; Li, Y.; Lu, G.; Li, S. *Res. Chem. Intermed* **2009**, *35*, 739–749.
- 113) Fu, X.; Wang, X.; Leung, D. Y. C.; Xue, W.; Ding, Z.; Huang, H.; Fu, X. *Catal. Comm.* **2010**, *12*, 184–187.
- 114) Hu, Y. -S.; Kleiman-Shwarscstein, A.; Stucky, G. D.; Mcfarland, E. W. *Chem. Comm.* **2009**, 2652–2654.
- 115) Yuliati, L.; Yoshida, H. *Chem. Soc. Rev.* **2008**, *37*, 1593–1602.
- 116) Taylor, C. E. *Catal. Today* **2003**, *84*, 9–15.
- 117) Gongal, M. A.; Hameed, A.; Suwaiyan, A. *Appl. Catal. A* **2003**, *243*, 165–174.
- 118) Gongal, M. A.; Hameed, A.; Yamani, Z. H.; Arfaj, A. *Chem. Phys. Lett.* **2004**, *392*, 372–377.
- 119) Yoshida, H.; Kato, S.; Hirao, K.; Nishimoto, J.; Hattori, T. *Chem. Lett.* **2007**, *36*, 430–431.

Chapter 2

Photocatalytic Steam Reforming of Methane over Pt-loaded Titanium Oxide

Abstract

Photocatalytic reaction of CH₄ gas with H₂O vapor was examined over Pt/TiO₂ around room temperature (ca. 323 K) in a flow reactor. H₂ and CO₂ were the main products, and only trace amounts of C₂H₆ and CO were also observed. After an induction period, the molar ratio of H₂ to CO₂ in the outlet gas became close to 4. Thus, the main reaction is suggested as the equation CH₄ + 2H₂O(g) → 4H₂ + CO₂, which can be referred to as photocatalytic steam reforming of methane (photocatalytic SRM), where the photoenergy is converted to chemical potential of products ($\Delta G_{298K}^0 = 113 \text{ kJ mol}^{-1}$). The reaction would be promoted by photoexcited electrons and holes, which were generated by band gap photoexcitation of the TiO₂ photocatalyst. The apparent quantum yield in the range 345-385 nm with high-intensity light (60 mW cm⁻²) was 0.6%, while the one in the range 240-270 nm with low-intensity light (2 mW cm⁻²) reached 2%. Highly active Pt/TiO₂ photocatalysts consisted of anatase phase TiO₂ having large surface area and enough loading amount (more than 0.1 wt %) of metallic Pt nanosized particles, which should be loaded by the photodeposition method, preferentially in the reaction condition. During the induction period, the photoirradiated side of the catalyst in the reaction cell turned pale brown, and the reaction was much accelerated. The colored surface substances accelerating the reaction rate, whose chemical formula can be described as [CH₂O]_n, were revealed as the reaction intermediates. The reaction mechanism was also investigated.

2.1. Introduction

Since methane is a most stable chemical among hydrocarbons, the conversion of it usually requires much energy, i.e. high temperature. However, it is reported that methane can be photocatalytically activated around room temperature or at a mild condition. For example, when CH₄ was photoirradiated in the presence of suitable photocatalyst, the photocatalytic nonoxidative coupling of methane (NOCM) was promoted to produce H₂ and C₂H₆,¹⁻⁹ showing that CH₄ can be activated by a photocatalyst. Without a photocatalyst, but by using photoirradiation in the presence of H₂O, photoreaction between CH₄ and H₂O occurred in a closed reactor, in which H₂ and some organic compounds were produced.^{10, 11} Photocatalytic reaction between CH₄ and H₂O (liquid) was also investigated for conversion of CH₄ into methanol by metal-loaded WO₃ and TiO₂,¹²⁻¹⁴ in which H₂, O₂, and some organic compounds were produced. However, the photocatalytic production of H₂ and CO₂ from CH₄ and H₂O vapor (referred to as photocatalytic SRM) shown in eq. 1 has not been reported.



Recently, we found that photocatalytic SRM could be promoted around room temperature by Pt/TiO₂ and Pt/NaTaO₃:La.¹⁵ In the present study, we examined the effects of photocatalyst structure, photocatalyst preparation method, and reaction condition, and we investigated the details of the photocatalytic SRM over Pt/TiO₂ at ordinary temperature (ca. 323 K).

2.2. Experimental

2.2.1. Preparation of Photocatalysts

An anatase-type TiO₂ (JRC-TIO-8, 342 m² g⁻¹), a rutile-type TiO₂ (JRC-TIO-6, ca. 100 m² g⁻¹), and a mixture of anatase and rutile TiO₂ (JRC-TIO-4, anatase : rutile = 7:3, similar to P-25, ca. 50 m² g⁻¹) were donated by the Catalysis Society of Japan.¹⁶ The anatase-type TiO₂ was mainly used in this study. TiO₂ samples with different surface areas were prepared by calcination of JRC-TIO-8 at various temperatures (473, 573, 673, and 773 K) for 5 h in a flow of dry air. All of them were confirmed to have anatase phase by X-ray diffraction (Rigaku, RINT 1200). H₂PtCl₆·6H₂O (Kishida, >98.5%) was used as a Pt precursor. Pt was loaded on TiO₂ by an impregnation method or photodeposition methods.¹⁷ In the impregnation method, TiO₂ (3 g) was dispersed into H₂PtCl₆·6H₂O aqueous solution (20 mL) and stirred for 3 h, and left for overnight at room temperature, followed by evaporation to dryness in a water bath (308 K). The dried powder was calcined at 773 K for 5 h in a flow of dry air (referred to as Pt_T/TiO₂). A part of the Pt_T/TiO₂ sample was additionally reduced in a flow of H₂ at 773 K (referred to as Pt_{IR}/TiO₂). In the photodeposition method, catalysts were prepared under two different conditions for reduction of Pt precursor on TiO₂: One was in MeOH aqueous solution (referred to as Pt_M/TiO₂) and the other was in the reaction cell in a flow of a mixture of CH₄ gas and H₂O vapor (referred to as Pt_C/TiO₂). In the former condition, TiO₂ was dispersed into MeOH (50%) aqueous solution containing H₂PtCl₆·6H₂O in a Pyrex glass vessel with vigorous stirring, followed by photoirradiation from a 300 W xenon lamp, which emitted both UV and visible light, for 3 h with continuous stirring. The incident light intensities measured at the vessel in the ranges 230-280, 310-400, and 360-490 nm were ca. 3, 13, and 31 mW cm⁻², respectively. The suspension was then filtered off with suction, washed with distilled water, and dried at 333 K. In the latter condition, TiO₂ was dispersed into H₂PtCl₆·6H₂O aqueous solution in a Pyrex glass vessel, and stirred for 3 h without irradiation. Then, it was filtered off with suction, washed with distilled water, and dried at 333 K. The dried powder was granulated to the size of 400-600 μm and then photoirradiated in a cell made of quartz (Figure 1) in a flow photoreactor with the same 300 W xenon lamp (the light intensities measured at the cell in the ranges 230-280, 310-400, and 360-490 nm were ca.

15, 65, and 155 mW cm⁻², respectively) under a total flow rate of 30 mL min⁻¹ of a gas mixture of CH₄ (50%) and H₂O vapor (1.4%) with Ar carrier for 6 h, followed by photoirradiation in a flow of H₂O vapor (2.8%) for ca. 8 h to clean the catalyst surface. The Pt content (*x* wt %) was defined as $x = W_{\text{Pt}}(\text{g})/W_{\text{TiO}_2}(\text{g}) \times 100$, referred to as Pt(*x*)/TiO₂. The Pt content of the sample prepared by the photodeposition method was determined by ICP (inductively coupled plasma emission spectroscopy, Perkin-Elmer Optima 3300DV), and it was confirmed that most Pt was loaded quantitatively (more than 99.8%).

2.2.2. Photocatalytic Reaction Tests

Reaction tests were mainly carried out with the fixed-bed flow photoreactor. The quartz cell (Figure 1) was filled with catalysts granulated to sizes of 400-600 μm. The reaction gas was a mixture of H₂O vapor and/or CH₄ and/or Ar carrier. H₂O vapor was introduced from a saturator containing distilled water where the reaction gas passed through at room temperature or controlled temperature. Prior to the photoreaction tests, to remove organic impurities from the catalyst surface, the catalyst was irradiated by the 300 W xenon lamp in the flow of H₂O vapor (2-3%) with Ar carrier until the CO₂ concentration in the outlet gas fell below measurable limits (lower than 5 ppm). In some cases, after cleaning the catalyst surface, the catalyst was heated at 473 K in a flow of Ar gas (60 mL min⁻¹) to remove adsorbed water. The reaction gas was introduced into the reactor at a total flow rate of 20, 30, or 50 mL min⁻¹ (the variation of the flow rate from 20 to 50 mL min⁻¹ did not influence the production rate). The photocatalytic reaction was carried out around 323 K at atmospheric pressure upon irradiation from the 300 W xenon lamp. As the standard condition, the catalyst weight was 0.5 g, the photoirradiation area was 9.5 cm², and the sample was irradiated by the light of the entire wavelength region from the xenon lamp without any filters, where the light intensities measured at the cell in the ranges 230-280, 310-400, and 360-490 nm were ca. 15, 65, and 155 mW cm⁻², respectively. When a slightly different size of the quartz cell was used, the catalyst weight and the light intensity were adjusted to obtain the condition equivalent to the standard condition. In some cases, either a cutoff filter or an optical band-pass filter, which was placed between the xenon lamp and the reactor, was employed to limit the photoirradiation wavelength. The products were analyzed by an on-line gas chromatograph

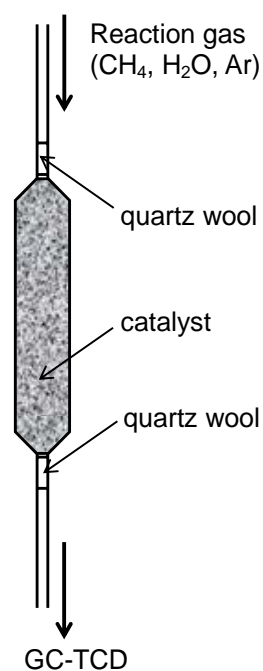


Figure 1. The photocatalytic reaction cell (typically 9.5 cm² × 1 mm) made of quartz for the flow type reactor.

with a thermal conductivity detector to detect H₂, CO₂, and CO, while C₂H₆ was analyzed by gas chromatography with a flame ionization detector. In the reaction on the catalysts having difference surface areas, we used the same catalyst weight, so the apparent area of photoirradiated catalyst in the cell was slightly different. In such a case, we made a correction on the H₂ production rate by assuming the photoirradiation area to be the same as the standard value (9.5 cm²), since the H₂ production rate was confirmed to be proportional to the apparent photoirradiation area.

In other cases, the reaction was carried out in a closed type of quartz reactor (95.4 mL) having a flat bottom (14 cm²), which was connected to a conventional vacuum system (1 × 10⁻² Pa). The catalyst (0.2 g) was spread on the flat bottom of the reactor and evacuated at 673 K for 1 h as pretreatment. After cooling to room temperature, H₂O vapor (100 μmol) and CH₄ (100 μmol) were introduced and the catalyst was photoirradiated with the 300 W xenon lamp without any filters (the light intensities measured at the flat bottom in the ranges 230-280, 310-400 and 360-490 nm were ca. 25, 108, and 258 mW cm⁻², respectively) for 3 h. The products in the gaseous phase were collected and analyzed by gas chromatography.

In order to measure the apparent quantum yield around 345-385 nm (Φ_1) on Pt_M(0.2)/TiO₂, the reaction was carried out by using an optical band-pass filter permitting only the light around 345-385 nm (Asahi spectra) under a flow of H₂O (1.5%) and CH₄ (50%) with Ar carrier in the flow reactor. The total flow rate was 50 mL min⁻¹. The light intensity measured in the range 340-380 nm was 60 mW cm⁻². The apparent quantum yield was calculated by the equation $\Phi_1 (\%) = Ne/Np \times 100$, where Ne was the number of reacted electrons under the light around 345-385 nm and Np was the number of incident photons under the light around 340-380 nm. The number of reacted electrons was determined from the H₂ production rate, assuming that two electrons produced one H₂ molecule: $2H^+ + 2e^- \rightarrow H_2$. The number of incident photons was determined from the value measured by a Si photodiode (Topcon; UVR-2 with UD-36). In another way, the apparent quantum yield on Pt_M(0.1)/TiO₂ in the range 240-270 nm (Φ_2) was calculated from the results of two runs in the photocatalytic reactions under photoirradiation of different wavelength regions: One was under the light of $\lambda > 240$ nm reflected by using a cold mirror, and the other was under the light of $\lambda > 270$ nm transmitted through a cutoff filter (Hitachi). The reaction was carried out under a mixture of H₂O (1%) and CH₄ (50%) with Ar carrier using the flow reactor. The total flow rate was 50 mL min⁻¹. The apparent quantum yield in the range 240-270 nm (Φ_2) was calculated by using the equation $\Phi_2 (\%) = \{(Ne_1 - Ne_2)/(Np_1 - Np_2)\} \times 100$, where Ne_1 and Ne_2 were the numbers of reacted electrons under the light of $\lambda > 240$ and 270 nm, respectively, and Np_1 and Np_2 were the numbers of incident photons under the light of $\lambda > 240$ and 270 nm, respectively. The number of incident photons was determined from the value measured by a Si

photodiode (Topcon; UVR-2 with UD-25) in the range 230-280 nm. The photoirradiation area was limited to 6 cm². The incident photon number in the range 240-270 nm was adjusted to be 2 mW cm⁻².

Photocatalytic reaction between D₂O (Acros, 99.8%) and CH₄ was examined on Pt_M(0.1)/TiO₂ in the flow reactor. Before the reaction, the catalyst was heated at 473 K for 1 h in a flow of Ar gas (60 mL min⁻¹) to remove adsorbed water (H₂O). The reaction was carried out at 323 K at atmospheric pressure. The total flow rate was 30 mL min⁻¹. The initial reaction gas was a mixture of CH₄ (50%) with Ar carrier for the first 90 min, and then the reaction gas was changed to a mixture of CH₄ (50%) and D₂O vapor (1.4%) with Ar carrier. The outlet gas was introduced to an on-line gas chromatograph and detected by an on-line mass spectrometer (ANELVA; AQA 100R), where H₂ ($m/z = 2$), HD ($m/z = 3$), and D₂ ($m/z = 4$) were detected. We employed the reported relative sensibility factors of H₂:HD:D₂ = 1:1.09:0.99¹⁸ for quantitative analysis. In separate experiments, the possibility of the H/D exchange reaction between CH₄ and D₂O to produce CH_xD_{4-x} ($x = 0-3$) over Pt_M(0.1)/TiO₂ was examined by using GC-MS (Shimadzu QP-5050A). The feed gases were CH₄ (50%) and D₂O vapor (1.4%) with Ar carrier at the flow rates of 15 and 30 mL min⁻¹. The possibility of the H/D exchange reaction between H₂ and D₂O to produce HDO or H₂O was also examined in a similar way in the flow of 3% for D₂O and 2.5% for H₂.

2.2.3. Characterizations of Photocatalysts

The BET specific surface area of the catalyst was calculated from the amount of N₂ adsorption at 77 K. The amount of N₂ adsorbed was determined by a thermal conductivity detector. The Pt particle size on the Pt/TiO₂ catalyst was measured by using the CO-pulse method in a flow system after the pretreatments in O₂ and then in H₂ at 473 K for 15 min each.¹⁹ The amount of residual Cl⁻ on the Pt/TiO₂ catalyst, which might be left on the catalyst through the decomposition of H₂PtCl₆ during catalyst preparation, was determined from the analysis of the filtrate at preparation by anion-exchange chromatography (Shimadzu; Shim-pack IC-A3). Transmission electron micrographs (TEM) were taken by a JEM-2010 (JEOL) to observe the Pt particles on TiO₂.

The amount of H₂O adsorption on the catalyst in the presence of CH₄ was determined by the following method. After the catalyst surface was cleaned by photoirradiation in the flow of H₂O vapor (2-3%) with Ar carrier, it was heated at 473 K under flowing Ar gas (60 mL min⁻¹) to remove adsorbed water until the H₂O concentration in the outlet gas became lower than 50 ppm. The H₂O adsorption was carried out in a flow of a gas mixture of CH₄ (50%) and H₂O (1.5%) with Ar carrier around 323 K under photoirradiation until the H₂O concentration in the outlet gas became constant. The amount of adsorbed H₂O on the catalyst was calculated from the integrated value of the amount of H₂O in the outlet gas in consideration with the amount of H₂O adsorption on the flow reactor.

In order to measure the amount of CH₄ adsorption on fresh PtM(0.2)/TiO₂ (332 m² g⁻¹), the sample was placed in the closed system (140.6 mL) and treated under evacuation (1×10^{-2} Pa) at 298 K for 90 min, followed by introduction of CH₄ (213 Pa) at room temperature without photoirradiation for 15 min. The adsorbed methane then was estimated from the decrease in the methane pressure after the adsorption process. To know the CH₄ adsorption ability after the photocatalytic SRM, the sample was irradiated in the flow reactor under a mixture of H₂O (1.4%) and CH₄ (50%) for 40 h (both sides of the quartz cell were irradiated for 20 h, respectively), and then the CH₄ adsorption amount on the used sample was measured similarly in the closed system.

Fourier transform infrared (FT-IR) spectra were recorded by using a JASCO FT-IR-300 spectrometer equipped with a cell having two CaF₂ windows for recording spectra which was connected to the vacuum system. The sample was pressed into a 0.1 g self-supporting disk. The disk in the cell was evacuated at 1×10^{-2} Pa at 673 K for 1 h. After cooling to room temperature, H₂O vapor (960 μmol) and CH₄ (960 μmol) were introduced. Then, the photocatalytic reaction was carried out for 3 h upon photoirradiation from the 300 W Xe lamp at 308 K. The IR spectra were recorded at room temperature by accumulating 200 scans at a resolution of 2 cm⁻¹. The spectra of the acetic acid and the formic acid adsorbed on TiO₂ were also recorded as references, respectively.

The Pt L_{III}-edge XANES (X-ray absorption near-edge structure) spectra of the catalysts after photocatalytic SRM and the reference samples were recorded at the BL-10B station²⁰ at KEK-PF (Photon Factory, Institute of Materials Structure Science, High Energy Accelerator Research Organization) with a Si(311) channel cut monochromator at room temperature in a transmission mode for the reference samples (Pt foil and PtO₂) and in a fluorescence mode by using the Lytle detector²¹ with a Ga filter ($\mu t = 3$) for the catalyst samples. The catalysts after the reaction were packed quickly in a polyethylene film in air, and it was confirmed that Pt was not oxidized by the air exposure. The XANES data processing was carried out by REX version 2.3 (Rigaku). Since a linear relationship was confirmed between the ratio of oxygen to platinum (O/Pt) and the intensity of the white line (an intense absorption peak at the edge),²² the normalized XANES spectrum of the sample was simulated by superposition of the XANES spectrum of Pt foil (Pt⁰) and that of PtO₂ (Pt⁴⁺) with a suitable ratio, which gave the average oxidation number of Pt on the catalyst.

2.3. Results and Discussion

2.3.1. Photocatalytic Reaction

Figure 2 shows the time course of the reaction over Pt_M(0.1)/TiO₂ upon irradiation of UV and visible light without any filters in the flow of CH₄ and H₂O. The main products were H₂ and CO₂, although trace amounts of C₂H₆ (0.014 μmol min⁻¹) and CO (ca. 0.003 μmol min⁻¹) were also detected as byproducts. The molar ratio of H₂ to CO₂ in the outlet gas (H₂/CO₂) at the steady state was close to 4, indicating that the main reaction could be described as eq. 1 mentioned above. H₂ was not produced over Pt_M(0.1)/TiO₂ in the dark, and it was not produced without catalyst under photoirradiation. These results reveal that the reaction between CH₄ and H₂O to produce H₂ and CO₂ would be promoted photocatalytically; i.e., the photocatalytic SRM shown as eq. 1 was confirmed.¹⁵ When the H₂ production rate was 0.7 μmol min⁻¹, the methane conversion was calculated to be 0.02% in the flow of 50% CH₄ and 1.4% H₂O. The reaction selectivity of the photocatalytic SRM was 85%, where the photocatalytic NOCM seemed to occur as a side reaction to produce a trace amount of C₂H₆ and H₂ as mentioned later.

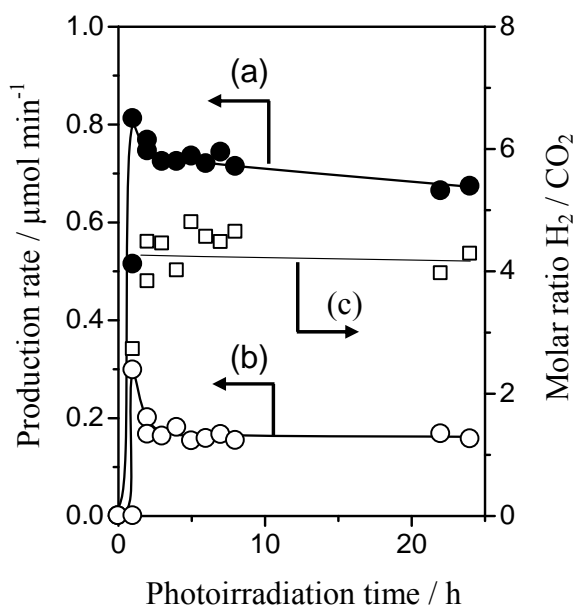


Figure 2. Time course of the production rate for (a) H₂ and (b) CO₂, and that of (c) the molar ratio of H₂ to CO₂ over Pt_M(0.1)/TiO₂ in the flow of CH₄ (50%) and H₂O (1.4%). The total flow rate was 50 ml min⁻¹.

In the time course of the production rate, an induction period was observed for the first 30 min and the amount of produced CO₂ was too small to be detected in the beginning; the production rates of H₂ and CO₂ gradually became high before they reached each constant rate. Then, both H₂ and CO₂ were produced constantly for more than 24 h, although they decreased very slowly with time. It was observed that the part of catalyst which was photoirradiated in the cell turned pale brown during the induction

period, suggesting that organic species were formed on the catalyst in the induction period. This phenomenon will be discussed later. In the case of C₂H₆ formation in the photocatalytic NOCM, no induction period was observed.

Table 1 shows the H₂ production rate at the steady state in the flow of H₂O and/or CH₄ with Ar carrier upon photoirradiation. In the flow of H₂O vapor, it was confirmed that both TiO₂ and Pt_M(0.1)/TiO₂ produced no H₂ under photoirradiation (entries 1 and 4). In the flow of CH₄ without water, although no H₂ was produced on TiO₂ (entry 2), H₂ and C₂H₆ were obtained on Pt_M(0.1)/TiO₂ photocatalyst (entry 5). This reaction would be the photocatalytic NOCM although the stoichiometric product ratio was not obtained, possibly due to the small quantities of products or consecutive reactions. This fact supports that this photocatalytic NOCM would be the side reaction for the photocatalytic SRM in the flow of CH₄ and H₂O as mentioned above. In the flow of the gas mixture of H₂O and CH₄, the H₂ production rate over Pt_M(0.1)/TiO₂ (entry 6) was about 190 times higher than that over TiO₂ (entry 3), indicating that Pt loading is important to improve the activity of TiO₂ photocatalyst for photocatalytic SRM. Thus, the turnover frequency (TF) per surface Pt atom in Pt_M(0.1)/TiO₂ could be calculated to be about 40 h⁻¹, which confirmed that this reaction proceeded photocatalytically.

Table 1 H₂ Production Rate in Various Reaction Conditions

entry	catalyst	feed gas ^a	H ₂ production rate ^b / μmol min ⁻¹
1	TiO ₂	H ₂ O	n.d.
2		CH ₄	n.d.
3		H ₂ O + CH ₄	0.004
4	Pt _M (0.1)/TiO ₂	H ₂ O	n.d.
5		CH ₄	0.063 ^c
6		H ₂ O + CH ₄	0.76 ^d

^a Feed gas composition was 50% for CH₄ and 1.6% for H₂O with Ar carrier. Total flow rate was 30 ml min⁻¹. ^b H₂ production rate was the value after 6 h upon photoirradiation when it became almost constant. ^c C₂H₆ (0.031 μmol min⁻¹) was also produced. ^d CO₂ (0.18 μmol min⁻¹), C₂H₆ (0.014 μmol min⁻¹) and CO (ca. 0.003 μmol min⁻¹) were also produced. n.d.=not detected.

Table 2 shows the wavelength dependence of the H₂ production rate at the steady state on Pt_M(0.2)/TiO₂, which was examined by using either a cutoff filter or a band-pass filter. When the irradiated light was limited to wavelength longer than 290 nm (entry 2), the production rate was reduced to be 82% of the one without the filter (entry 1). When the band-pass filter permitting only light around 345-385 nm wavelength was used, it was reduced to be 55% (entry 3). On the other hand, the reaction

was almost forbidden when using the band-pass filter permitting 385-425 nm light (entry 4). These results indicate that UV light less than ca. 385 nm was effective to promote the reaction, meaning that band gap photoexcitation of TiO₂ would promote the photocatalytic SRM. The apparent quantum yield (Φ_1) in the case of entry 3 was estimated to be 0.6% when the light intensity measured in the range 340-380 nm was 60 mW cm⁻². By another experiment, the apparent quantum yield (Φ_2) on PtM(0.1)/TiO₂ photocatalyst was estimated as 2% upon the light of low intensity of 2 mW cm⁻² in the range of 240-270 nm wavelength.¹⁵

Table 2 Effect of Irradiation Light Wavelength on Pt_M(0.2)/TiO₂

entry	Wavelength / nm	H ₂ production rate ^a / $\mu\text{mol min}^{-1}$	Relative rate (%)
1	> 200 ^b	0.62	100
2	> 290	0.51	82
3	365±20	0.34	55
4	405±20	0.05	8

^a Feed gas composition was 50% for CH₄ and 1.5% for H₂O with Ar carrier. Total flow rate was 50 ml min⁻¹. H₂ production rate was the value after 6 h upon photoirradiation for entries 1–3 and after 25 h for entry 4 when it became almost constant. ^b The light of entire wavelength was irradiated without any filters.

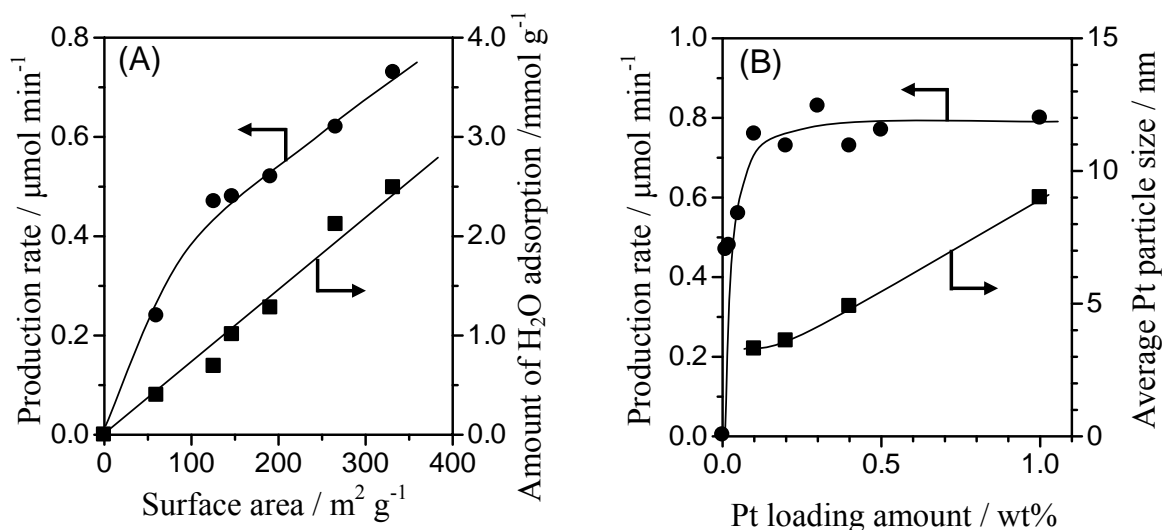


Figure 3. (A) Effect of the BET specific surface area on the H₂ production rate and the amount of H₂O adsorption in Pt_M(0.2)/TiO₂ and (B) effect of the Pt loading amount on the H₂ production rate and the average particle size of Pt in Pt_M/TiO₂. The reaction gases were CH₄ (50%) and H₂O (1.6%) and the total flow rate was 30 ml min⁻¹. H₂ production rate was the value after 6 h upon photoirradiation when it became almost constant.

2.3.2. Activities of Various Pt/TiO₂

Figure 3A shows the effect of the BET specific surface area on the H₂ production rate in the photocatalytic SRM and the amount of H₂O adsorption. The H₂ production rate increased with an increase of the BET specific surface area. The amount of H₂O adsorption also increased with increasing surface area. It is considered that, since Pt/TiO₂ photocatalysts having high surface areas could adsorb a large amount of H₂O on the surface, they could show high activities.

Table 3 shows the effect of the type of TiO₂ on this reaction. Pt_M(0.2)/TiO₂ prepared from the rutile type of TiO₂ showed no activity in the present condition (entry 1). Pt_M(0.2)/TiO₂ prepared from the TiO₂ consisting of anatase and rutile showed much lower activity than that of Pt_M(0.2)/TiO₂ prepared from the anatase type of TiO₂ having a similar specific surface area (entries 2 and 3). These results indicate that anatase type would be suitable for exhibiting high activity in this reaction, which is possibly due to the high potential level of the conduction band compared to that of rutile type.

Table 3 Activities of Pt_M(0.2)/TiO₂ Prepared from Various Types of TiO₂

entry	type of TiO ₂	specific surface area / m ² g ⁻¹	H ₂ production rate ^a / μmol min ⁻¹
1	rutile	101	n.d.
2	anatase+rutile (7:3)	53	0.09
3	anatase	60	0.24

^a Feed gas composition and the total flow rate were the same as those in Table 1. H₂ production rate was the value after 6 h upon photoirradiation when it became almost constant. n.d.=not detected.

Figure 3B shows the effect of the Pt loading amount on H₂ production rate and the average particle size of Pt on Pt_M/TiO₂. The photocatalytic activity increased with an increase of Pt amount until 0.1 wt %, indicating that a certain amount of Pt was necessary for exhibiting high activity. The Pt would promote the separation of photoexcited electrons (e⁻) and holes (h⁺) and prevent their recombination, and possibly might function as cocatalyst to activate the reactant molecules. However, the samples having more than 0.1 wt % Pt exhibited almost the same activity while the Pt particle size on TiO₂ changed between 3.3 and 9.0 nm, indicating that the activity was not concerned with such variation of the Pt particle size on TiO₂. This phenomenon is also confirmed on the other series of Pt_M/TiO₂ photocatalysts having different surface areas: there was also no correlation between the Pt particle size and the activity, and even the catalysts having almost the same Pt particle size showed different activities from each other. These facts support that the Pt particle size would not be an important factor for the activity, at least in the present condition.

We prepared Pt(0.2)/TiO₂ photocatalysts by several methods (Table 4). Pt₁(0.2)/TiO₂ prepared

by the impregnation method followed by calcination in air showed very low activity (entry 1). The surface area of TiO₂ was reduced by the calcination process and the Pt particles were oxidized judging from the brown color and the characteristic of Pt L_{III}-edge XANES. When this sample was reduced by H₂ treatment, the activity was clearly improved (entry 2). However, this improvement was not clearly observed for other Pt_I/TiO₂ samples having higher Pt loading amounts. On the other hand, Pt_M(0.2)/TiO₂ prepared by the photodeposition method in MeOH aqueous solution showed obviously higher activity (entry 3) than those of Pt_I(0.2)/TiO₂ and Pt_{IR}(0.2)/TiO₂. Even when Pt_M(0.2)/TiO₂ having a similar specific surface area was compared, the superiority of the photodeposition method was clear (entry 4). It is considered that the metallic Pt particles should be formed on the reduction sites on TiO₂ by the photodeposition method, and they could efficiently receive the excited electrons from the conduction band of TiO₂. Actually, the color of Pt_M(0.2)/TiO₂ samples was gray without any reduction treatment, and Pt-L_{III} XANES clarified that the Pt particles on them were metallic. These results indicate that the metallic Pt particles are necessary for exhibiting high activity. It should be also considered that the metallic Pt particles have a possibility to activate CH₄ molecules at moderate temperature even without photoirradiation.

Table 4 Activities of Pt(0.2)/TiO₂ Prepared by Various Methods

entry	catalyst	specific surface area / m ² g ⁻¹	H ₂ production rate ^a / μmol min ⁻¹
1	Pt _I (0.2)/TiO ₂	103	0.03
2	Pt _{IR} (0.2)/TiO ₂	113	0.22
3	Pt _M (0.2)/TiO ₂	332	0.73
4	Pt _M (0.2)/TiO ₂	126 ^b	0.47

^a Feed gas composition and the total flow rate were the same as those in Table 1. H₂ production rate was the value after 6 h irradiation when it became almost constant. ^b The anatase TiO₂ was calcined at 773 K in air before Pt loading.

In this study, we examined an in situ photodeposition method in the reaction mixture of CH₄ gas and H₂O vapor in the flow photoreactor, which gave Pt_C/TiO₂. The color of the TiO₂ adsorbing Pt precursor varied from yellow to gray during the photodeposition in the reaction mixture, indicating that the adsorbed Pt precursors changed to metal particles by photoreduction in the presence of CH₄ and H₂O as expected. Table 5 shows the effect of the photodeposition method on the H₂ production rate in the photocatalytic SRM. The Pt_C/TiO₂ catalysts showed about 1.3 times higher activity than the Pt_M/TiO₂ catalysts did (entries 1-4). To investigate the reasons for exhibiting the higher activity, some characterizations were carried out. It is confirmed that the difference in particle size of Pt would not be

the reason for the difference in the activity of the catalysts (entries 1-4). Moreover, TEM observation did not show any characteristic differences in the form and size of Pt particles. The number of residual chlorines on the catalysts would be unimportant, which was supported by the results on the sample Pt_C/TiO₂ containing a large amount of chlorines (entry 5). However, XANES analysis clarified that the average valence of Pt metal particle on Pt_C/TiO₂ was slightly higher than that of the Pt_M/TiO₂ when compared to the sample having the equivalent Pt particle size, which might be due to some differences in the circumstances of Pt particles on each sample. However, at present, it is difficult to conclude the exact reason for the high activity.

Table 5 Effect of Photodeposition Method

entry	catalyst	average particle size of Pt / nm	Cl/Pt on TiO ₂	H ₂ production rate ^a / μmol min ⁻¹
1	Pt _M (0.2)/TiO ₂	3.6	2.2	0.73
2	Pt _M (0.4)/TiO ₂	4.9	— ^b	0.73
3	Pt _C (0.2)/TiO ₂	2.4	2.6	1.01
4	Pt _C (0.4)/TiO ₂	3.2	— ^b	1.02
5	Pt _C (0.2)/TiO ₂ ^c	— ^b	6	0.85

^a Feed gas composition and the total flow rate were the same as those in Table 1. H₂ production rate was the value after 6 h irradiation when it became almost constant. ^b Not measured. ^c The all chlorines of Pt precursor (H₂PtCl₆) were supported on the catalyst by evaporation of the solution.

2.3.3. Reaction Intermediates on Catalyst Surface

Figure 4 shows the time course of the H₂ and CO₂ production rates over Pt_C(0.2)/TiO₂ photocatalyst, where the reaction gas composition was changed during the reaction. In the flow of a gas mixture of H₂O and CH₄ with Ar carrier (Figure 4A), H₂ and CO₂ were produced (curves a and b), the photoirradiated side of the catalyst turned pale brown, and the H₂/CO₂ became close to 4 (curve c). When the reaction reached the steady state, the photocatalytic SRM shown as eq. 1 would proceed constantly. Then, the feed gas was changed to only H₂O vapor with Ar carrier (Figure 4B). As a result, H₂ and CO₂ were produced for a while, and then the production rates dropped almost to zero at longer irradiation time. Interestingly, the pale brown species on the catalyst completely disappeared, suggesting that the pale brown species were not formed but consumed in the presence of H₂O. No products were observed, other than H₂ and CO₂. These results show that the pale brown species would be some organic species that could be completely decomposed to H₂ and CO₂ (the products in the photocatalytic SRM) by the reaction with H₂O (one of the reactants in the photocatalytic SRM),

indicating that these surface organic species were *the reaction intermediates*. Since the total amount of products during period B was 32 μmol for H_2 and 16 μmol for CO_2 , i.e., the ratio of H_2/CO_2 was ca. 2 (curve c), the reaction between the surface intermediates and H_2O could be described by eq 2:



where $[\text{CH}_2\text{O}]_{n,\text{ad}}$ is one of the possible expressions for the reaction intermediates as a composition formula. If the intermediates were expressed as $[\text{CH}_2\text{O}]_{n,\text{ad}}$, the formation of the reaction intermediates could be described by the following equation 3:



In reaction 3, H_2 is produced while CO_2 is not produced. At the steady state when the reaction proceeds constantly, reactions 2 and 3 should equally proceed, providing eq. 1.

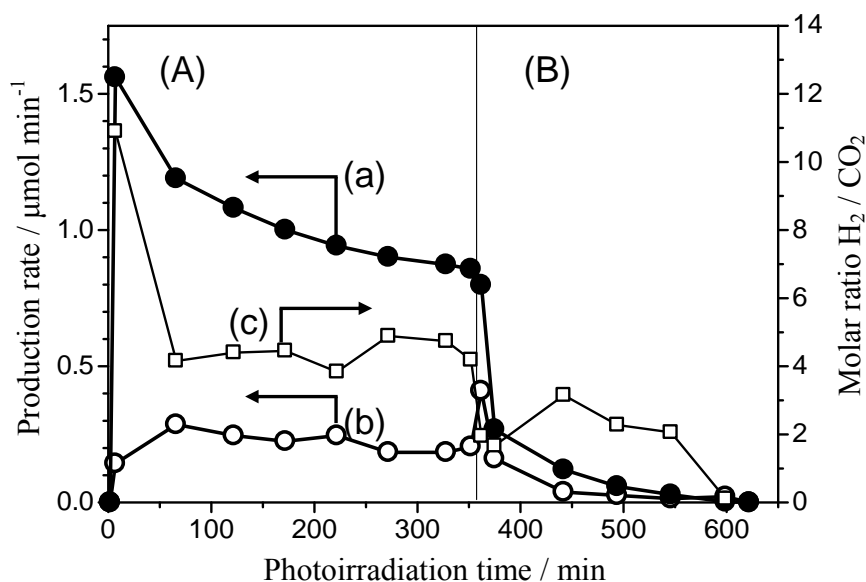


Figure 4. Time course of the production rate for (a) H_2 and (b) CO_2 , and that of (c) the H_2/CO_2 ratio over $\text{Pt}_C(0.2)/\text{TiO}_2$. The feed gases were CH_4 (50%) and H_2O (1.6%) for the period (A), and H_2O (1.6%) for the period (B). Total flow rate was 30 ml min^{-1} .

The CO_2 production rate was not high at the beginning of period A (Figure 4, curve b), which was similar to the results on $\text{Pt}_M(0.1)/\text{TiO}_2$ shown in Figure 2, where CO_2 was not detected at the first 30 min. The H_2/CO_2 ratio was higher than 4, suggesting that reaction 4 dominantly proceeded at the start of the reaction. The initial high H_2/CO_2 ratio was also reported in the case of $\text{Pt}/\text{NaTaO}_3:\text{La}$ photocatalyst.¹⁵

During the reaction, the H_2/CO_2 ratio was sometimes larger than 4 (e.g., Figures 2c and 4c),

suggesting that reaction 3 occurred slightly faster than reaction 2 did. However, the high H₂ production rate gradually decreased with time as shown in Figure 2 and Figure 4, period A. These results suggest the possibility that the organic surface species would have both the active part to form products according to reaction 2 and the inactive part that cannot produce the products. In some cases, it was observed that the pale brown surface species turned dark brown when the H₂ production rate decreased, which is probably due to the formation of the inactive organic surface species.

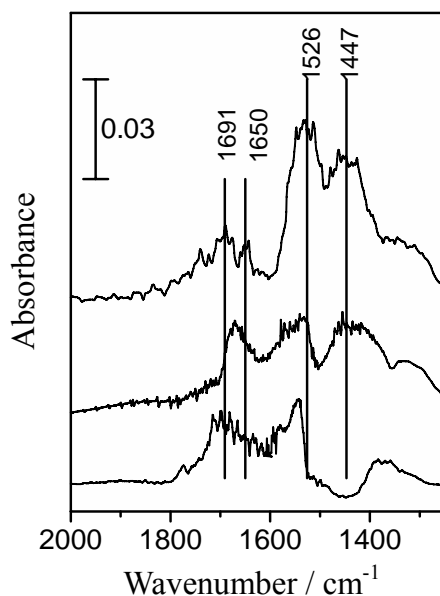


Figure 5. FT-IR spectra of (a) the surface organic products on Pt_M(0.2)/TiO₂, (b) CH₃COOH adsorbed on TiO₂ and (c) HCOOH adsorbed on TiO₂.

After the reaction intermediates were formed on Pt_M(0.2)/TiO₂ (TiO₂ was calcined at 773 K; the BET specific surface area was 126 m² g⁻¹) upon photoirradiation for 3 h in a closed reaction system, CO₂ (0.024 μmol), C₂H₆ (0.002 μmol), C₂H₄ (0.003 μmol), CH₃CHO (0.002 μmol), and CH₃-CO-CH₃ (0.004 μmol) were collected by heating of the sample at 523 K for 30 min. This showed that CO₂ and C₂H₆ as products were adsorbed on the catalyst, and others would be originated from the reaction intermediates. Figure 5 shows the FT-IR spectra of the surface organic products on Pt/TiO₂ and reference compounds on TiO₂. Spectrum a was the difference spectrum of the Pt_M(0.2)/TiO₂ disk before and after photocatalytic SRM. In the spectrum, broad absorption bands centered at 1447 and 1526 cm⁻¹ are mainly observed and two weak bands at 1650 and 1691 cm⁻¹ are also observed. The bands at 1447 and 1650 cm⁻¹, assignable to bicarbonate, carboxylate species, and carbonate species,²³ would be contributed from the adsorbed CO₂, and the band at 1650 cm⁻¹ assignable also to ν(C=C) vibration²⁴ might be also partly contributed from adsorbed C₂H₄. The broad band centered at 1447 cm⁻¹ would be

also contributed from the asymmetrical bending vibration of the methyl group ($\delta(\text{CH})$)²⁴ since it was not observed in the spectrum of HCOOH on TiO₂ but in the spectrum of CH₃COOH on TiO₂ (Figure 5b and c). The broad band center at 1526 cm⁻¹ could be assigned to antisymmetric stretching vibration of the carboxylic group, $\nu(\text{COO}^-)$, binding to an electron donor group such as the methyl group, as shown in the spectrum of CH₃COOH on TiO₂ (Figure 5b). The band at 1691 cm⁻¹ can be also assigned to $\nu(\text{C}=\text{O})$ vibration as well as adsorbed CO₂.^{23,24} These assignments suggest that the reaction intermediates would have the methyl groups and the carboxyl groups, and probably have the carbon-carbon double bonds. The attribution of these bands is almost consistent with the literature about FT-IR studies of HCOOH or CH₃COOH on TiO₂.^{25,26}

Thus, the pale brown surface species on the catalyst were indicated as the reaction intermediates, which could react with H₂O to form the products. They would be described as [CH₂O]_n, which would be composed of partially oxygenated hydrocarbons having the methyl groups, the carboxyl groups, and possibly the carbon-carbon double bonds.

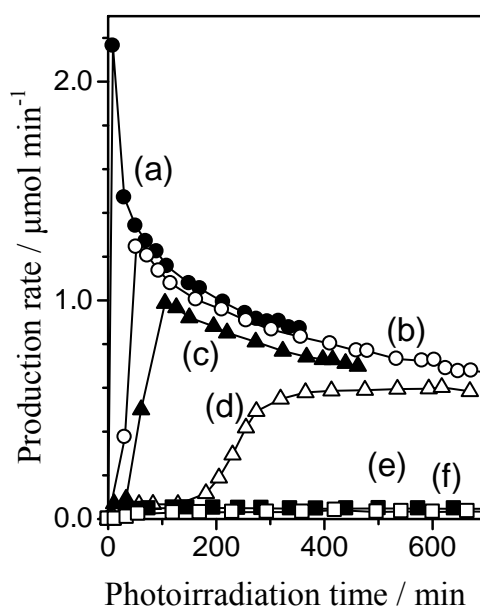


Figure 6. Time course of the H₂ production rate in various CH₄ concentrations over Pt_M(0.2)/TiO₂. The CH₄ concentration was (a) 97%, (b) 75%, (c) 50%, (d) 25%, (e, closed square) 18% and (f, open square) 10%, and H₂O concentration was 2.8%. Total flow rate was 20 ml min⁻¹.

2.3.4. Enhancement of the Reaction Rate by the Surface Intermediates

Figure 6 shows the time course of the H₂ production rate in the flow of CH₄ with various concentrations and H₂O vapor of 2.8% over Pt_M(0.2)/TiO₂. In high CH₄ concentration of more than 25%,

the catalyst showed a high H₂ production rate: the surface became pale brown and the H₂ production rates reached values similar to each other. On the other hand, when the CH₄ concentration was less than 18%, the H₂ production rate was very low and the color of the catalyst was unchanged. It was confirmed that the very slow H₂ production rate continued over 24 h at the CH₄ concentration of 18%. Figure 7 shows the effect of the CH₄ or H₂O concentration on the H₂ production rate and the H₂/CO₂ ratio, where each plot was the value taken at 6 h upon photoirradiation. In Figure 7A, a drastic increase of the H₂ production rate was observed around 25% CH₄ concentration. These results indicate that the surface intermediates would be formed under enough CH₄ concentration, and they enhanced the H₂ production rate typically more than 10 times higher than that observed in low CH₄ concentration.

The ratios of H₂/CO₂ were almost 4 in the cases of 25% and 50% CH₄, showing that the reaction reached almost the steady state (Figure 7A, b). On the other hand, in the high CH₄ concentration more than 50%, the higher H₂/CO₂ ratio more than seven was observed after 6 h upon photoirradiation; in a separate experiment, the H₂/CO₂ ratio continuously decreased but was still around 6 after 33 h upon photoirradiation in the flow of 80% CH₄. These results suggest that the surface organic species were still growing for a long period. However, the H₂ production rate gradually decreased, as shown in Figure 6, and the color of the catalyst gradually became dark brown. It is considered that excess CH₄ concentration would give excess accumulation of the inactive surface organic species. Thus, there is an optimum concentration of CH₄ to sustain the high activity with the moderate amount of the reaction intermediates, which was around 50% in the present system.

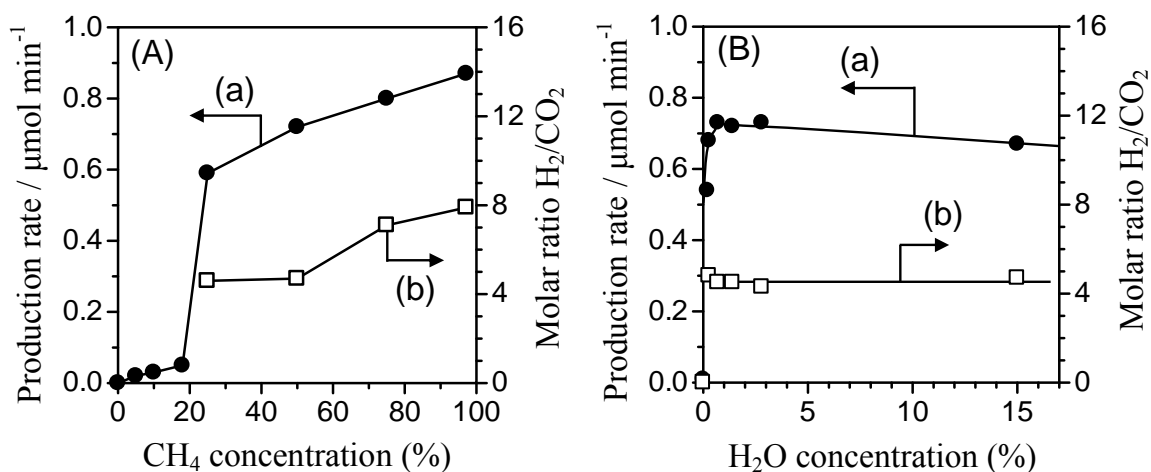


Figure 7. Effect of the (A) CH₄ and (B) H₂O concentrations on (a) the H₂ production rate and (b) the H₂/CO₂ ratio on Pt_M(0.2)/TiO₂. Fixed gas concentration was (A) H₂O 2.8% and (B) CH₄ 50%, respectively. Each plot was the value after 6 h upon photoirradiation when it became almost constant. Each total flow rate was (A) 20 ml min⁻¹ and (B) 30 ml min⁻¹.

Figure 7B shows the effect of the H₂O concentration at the CH₄ concentration of 50%. Although the H₂ production rate was low in the extremely low H₂O concentration (<0.28%), it was almost constant in the moderate H₂O concentration until saturated vapor pressure (0.28-15%). However, it was confirmed that excess H₂O that made the catalyst wet reduced the H₂ production rate, suggesting that a liquid phase of water covering the photocatalyst surface would reduce the CH₄ adsorption.

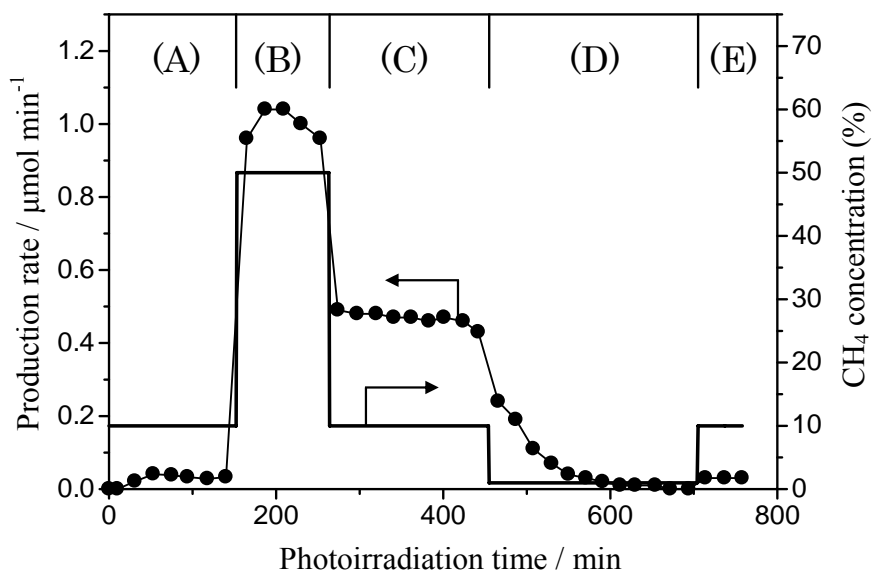


Figure 8. The variation of the H₂ production rate (left, symbols) with the feed CH₄ concentration (right, line) on Pt_M(0.2)/TiO₂. The H₂O concentration was 2.8% and the total flow rate was 30 ml min⁻¹.

Figure 8 shows the effect of the accumulation of the reaction intermediates on the H₂ production rate. In this experiment, the concentration of the feed CH₄ was transiently changed as indicated. When the CH₄ concentration was 10%, the H₂ production rate was 0.03 μmol min⁻¹ and the reaction intermediates did not accumulate on the catalyst (Figure 8A). When the CH₄ concentration was increased to 50%, the H₂ production rate was drastically accelerated to 1.0 μmol min⁻¹ and the color of the catalyst turned pale brown, indicating that the surface intermediates accumulated on the surface (Figure 8B). After that, when the concentration of CH₄ was reduced to 10% again, the H₂ production rate was varied to 0.47 μmol min⁻¹, which was not very low but obviously higher than the value in Figure 8A, and the color of the catalyst was still pale brown (Figure 8C). Thus, it is clarified that the H₂ production rate over the catalyst with a certain amount of the surface intermediates was much higher than that over the catalyst without accumulation of the surface intermediates even under the same partial pressure of CH₄. After that, switching to the extremely low CH₄ concentration (1%), the H₂ production rate gradually decreased toward very low rate (Figure 8D), where the accumulated surface intermediates

would be gradually consumed with releasing products and the color vanished. After the complete consumption of the surface intermediates, the H₂ production rate under the CH₄ concentration of 10% (Figure 8E) was the same as the initial rate in Figure 8A. These results support the above discussion.

Here, the reason why the reaction was much enhanced by the surface intermediates will be discussed. As one possibility, a certain amount of the surface intermediates accumulating on the catalyst might accelerate the adsorption of hydrophobic CH₄. To confirm this possibility, the amount of CH₄ adsorption on Pt_M(0.2)/TiO₂ (332 m² g⁻¹) before and after the photocatalytic SRM was measured, respectively. The amount of CH₄ adsorption on the fresh catalyst was 0.18 μmol g⁻¹ and that on the used catalyst was 0.24 μmol g⁻¹, suggesting that the surface intermediates improved CH₄ adsorption to accelerate the photocatalytic reaction. It has been reported that TiO₂ surface becomes amphiphilic with microstructured composition of hydrophilic and oleophilic domains by UV irradiation.²⁷ Therefore, photoirradiated TiO₂ surface of Pt/TiO₂ would have both hydrophilic domains, which could adsorb H₂O preferentially, and oleophilic domains, which could adsorb CH₄ mainly. Since both CH₄ and H₂O are necessary to form the surface intermediates shown in eq. 3, the surface intermediates might start to be formed dominantly at the border between hydrophilic and oleophilic domains. As shown in Figure 6, at the higher CH₄ concentration, a shorter induction period and a higher initial H₂ production rate were observed. In such cases, the formation of the surface intermediates shown in eq. 3 would be accelerated and the hydrophobic surface would enhance the CH₄ adsorption. In the steady state, the area of the hydrophobic surface due to the surface intermediates would become constant.

As other possibilities, the surface intermediates might trap the photoexcited holes (h⁺) to improve the charge separation between photoexcited electrons (e⁻) and holes (h⁺), or the surface intermediates might be photoexcited to enhance the reaction. As for the latter, some photocatalytic reactions have been recently reported,^{28, 29} in which photoexcitation of surface intermediates was involved in the whole photocatalytic reaction mechanism. In photoreduction of CO₂ with hydrogen or methane on MgO, adsorbed CO₂ species are reported to function as photocatalytic active sites.²⁸ In the present photocatalytic SRM, since the surface intermediates would have a similar part to the adsorbed CO₂, this might be photoexcited to enhance the photocatalytic SRM. Further studies should be carried out to clarify this possibility.

2.3.5. *Effect of Light Intensity*

Figure 9 shows the effect of the incident light intensity on the photocatalytic SRM activity over Pt_M(0.2)/TiO₂. The reaction temperature varied in the range 328-345 K under the influence of

photoirradiation, but which scarcely influenced the H₂ production rate. With increasing light intensity, the induction period shortened (Figure 9A) and the brown color of the catalyst became darker, indicating that higher light intensity would further promote the formation of the surface organic species. The reaction rate after the formation of the surface intermediates was also influenced by the light intensity. The H₂ production rate in the steady state (r) was plotted as a function of the incident light intensity (I) in Figure 9B. Similar curves were observed when using the values of the light intensity measured in the range 310-400 nm or the range 360-490 nm. As shown, the variation was not monotonic. With increasing light intensity, the increase of the H₂ production rate was accelerated first, and then the increase became small.

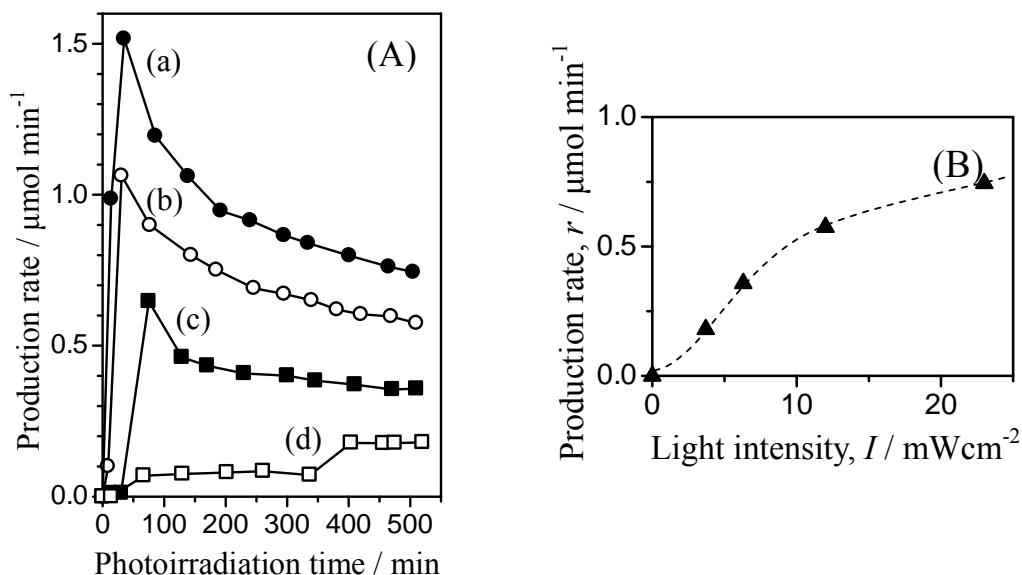


Figure 9. (A) Time course of the H₂ production rate over Pt_M(0.2)/TiO₂ upon photoirradiation with the incident light intensity of (a) 23, (b) 12, (c) 6.3 and (d) 3.7 mW cm^{-2} , respectively, and (B) a plot of the H₂ production rate around at 500 min upon photoirradiation versus the incident light intensity. The values for the light intensity were those measured in the range of 230-280 nm representatively. The reaction gases were 50% for CH₄ and 1.5% for H₂O, and total flow rate was 30 ml min^{-1} .

Upon low intensity of light, the variation was not linear and the curve could be fitted by the monomial function of degree 1.3 ($r \propto I^{1.3}$), suggesting that the whole reaction rate would be influenced by more than one photon in the photoexcitation steps, or a part of the photoabsorbed energy might be used in thermal activation for other steps. For the former case, there are some possibilities considered: for example, both CH₄ and CO₂ might be activated by photoexcited TiO₂, or besides TiO₂ the surface intermediates are additionally photoexcited to promote the reaction, or others. To clarify the details for the photoexcitation mechanisms, further studies would be necessary.

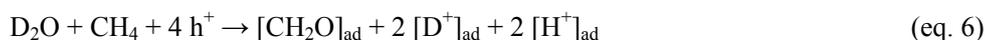
On the other hand, upon high intensity of light, the amount of photons would become enough and the excess light could not promote the photocatalytic reaction effectively, as explained generally when the light intensity reaches saturation level.

2.3.6. Reaction Mechanism

In order to understand the reaction mechanism, the photocatalytic SRM was examined in the flow of a mixture of D₂O and CH₄ with Ar carrier. Three types of hydrogen molecules, H₂, HD, and D₂, were detected, and the production rate for them at the steady state was 0.07, 0.20, and 0.35 μmol min⁻¹, respectively. The D/H value of the hydrogen products was 2.6 at the steady state. The H/D exchange reaction between CH₄ and D₂O to produce CH_xD_{4-x} (x = 0-3) scarcely occurred; only 0.4% of methane contained deuterium, supporting that the exchange reaction could not influence the D/H value mentioned above. The contribution of the H/D exchange reaction between H₂ and D₂O to produce HDO or H₂O was also negligible. Thus, the production of HD suggests that the hydrogen ions or radicals would be once produced from both CH₄ and D₂O and combined to produce hydrogen molecules. The total H₂, HD, and D₂ production rate was 0.62 μmol min⁻¹, and the contribution of the side reaction, the photocatalytic NOCM, was 0.011 μmol min⁻¹. Since the photocatalytic NOCM should produce only H₂ without deuterium, the D/H value for the photocatalytic SRM was revalued to be 2.8 at the steady state. If the reaction between D₂O and CH₄ could be shown to be like eq. 1, where two D₂O molecules and one CH₄ molecule form four hydrogen molecules, the value of D/H will be unity. A D/H value higher than unity indicates that more D₂O must be consumed, and the H atoms from CH₄ would partially react with the oxygen species to form extra H₂O molecules. If the value of D/H is 3, this reaction will be described by the following equation:



where [6D + 2H] means four hydrogen molecules containing 75% D and 25% H. The reaction intermediates would be formed by eq. 3, and they would be decomposed by eq. 2. Therefore, the following reactions are proposed in the present system, which include the formation of the additional H₂O.





Reaction 6 is the formation of the reaction intermediates with the consumption of holes, which corresponds to reaction 3. In equations 6 and 8, the reaction intermediates are described as $[\text{CH}_2\text{O}]_{\text{ad}}$, which is an initial state for $[\text{CH}_2\text{O}]_{n, \text{ad}}$. These expressions, $[\text{CH}_2\text{O}]_{\text{ad}}$ and $[\text{CH}_2\text{O}]_{n, \text{ad}}$, should not exclude the possibility of containing D atoms. If all of them contain no D atoms, additional H_2O is produced in eq 8 and the value of D/H becomes 3, while if all of them are described as $[\text{CHDO}]_{\text{ad}}$, HDO is produced and the value of D/H for molecular hydrogen becomes 1.67. Since the experimental value of D/H is 2.8 at the steady state, it is suggested that a small part of the reaction intermediates would contain D atoms. Reactions 6-8 should mainly proceed on the TiO_2 surface of Pt/TiO_2 , while reaction 9 should be promoted mainly on Pt particles where photoexcited electrons produce molecular hydrogen. The accumulation of the surface intermediates might considerably enhance the rate of reaction 6 by an increase of CH_4 adsorption. The sum of eqs 5-9 corresponds to eq 4. In the present study, the mechanism for active oxygen species could not be determined yet.

2.4. Conclusions

We summarize the present study as follows:

- (1) Photocatalytic SRM to produce hydrogen could proceed on Pt/TiO_2 upon UV irradiation around room temperature, ca. 323 K. This reaction was promoted by the electrons and holes generated by the band gap photoexcitation of TiO_2 semiconductor. The apparent quantum yield in the range of 240-270 nm light reached ca. 2% on 0.1 wt % Pt/TiO_2 photocatalyst. The photocatalytic activity was almost constant over 24 h.
- (2) High activity was obtained on Pt/TiO_2 photocatalysts having large surface areas of anatase TiO_2 and enough loading amount (larger than 0.1 wt %) of metallic Pt. The catalyst prepared by the photodeposition method showed much higher activity than that prepared by the impregnation method. The catalyst prepared by the photodeposition method under the reaction conditions in the reaction cell exhibited the highest activity among the catalysts prepared in the present study.
- (3) The reaction intermediates, possibly described as $[\text{CH}_2\text{O}]_{n, \text{ad}}$, were formed on the surface of the catalyst, and reacted with H_2O to produce H_2 and CO_2 . The formation of the surface intermediates depended on the activity of the photocatalyst, the CH_4 concentration in the reaction gas, and the incident light intensity. The moderate accumulation of the surface intermediates considerably

enhanced the reaction rate. The reaction mechanism was also proposed.

References

- 1) Kato, Y.; Yoshida, H.; Hattori, T. *Chem. Commun.* **1998**, 2389–2390.
- 2) Yoshida, H.; Matsushita, Y.; Kato, Y.; Hattori, T. *Phys. Chem. Chem. Phys.* **2002**, 4, 2459–2465.
- 3) Kato, Y.; Yoshida, H.; Satsuma, A.; Hattori, T. *Microporous Mesoporous Mater.* **2002**, 51, 223–231.
- 4) Yoshida, H.; Chaskar, M.G.; Kato, Y.; Hattori, T. *J. Photochem. Photobiol. A*, **2003**, 160, 47–53.
- 5) Yoshida, H.; Matsushita, N.; Kato, Y.; Hattori, T. *J. Phys. Chem. B* **2003**, 107, 8355–8362.
- 6) Yuliati, L.; Hattori, T.; Yoshida, H. *Phys. Chem. Chem. Phys.* **2005**, 7, 195–201.
- 7) Yuliati, L.; Hamajima, T.; Hattori, T.; Yoshida, H. *Chem. Commun.* **2005**, 4824–4826.
- 8) Yuliati, L.; Tsubota, M.; Satsuma, A.; Itoh, H.; Yoshida, H. *J. Catal.* **2006**, 238, 214–220.
- 9) Yuliati, L.; Itoh, H.; Yoshida, H. *Stud. Surf. Sci. Catal.* **2006**, 162, 961–968.
- 10) Ogura, K.; Migita, C. T.; Fujita, M. *Ind. Eng. Chem. Res.* **1988**, 27, 1387–1390.
- 11) Ogura, K.; Kataoka, M. *J. Mol. Catal.* **1988**, 43, 371–379.
- 12) Taylor, C. E.; Noceti, R. P. *Catal. Today* **2000**, 55, 259–267.
- 13) Taylor, C. E. *Catal. Today* **2003**, 84, 9–15.
- 14) Gondal, M.A.; Hameed, A.; Suwaiyan, A. *Appl. Catal. A* **2003**, 243, 165–174.
- 15) Yoshida, H.; Kato, S.; Hirao, K.; Nishimoto, J.; Hattori, T. *Chem. Lett.* **2007**, 36, 430–431.
- 16) Uchijima, T. *Catalytic Science and Technology*; Kodansha VCH: Tokyo, **1991**; Vol. 1, 393–398.
- 17) Kraeutler, B.; Bard, A. J. *J. Am. Chem. Soc.* **1978**, 100, 4317–4318.
- 18) Watanabe, K.; Miyake, H.; Matsuyama, M. *J. Vac. Sci. Technol. A* **1987**, 5, 237–241.
- 19) Hattori, T.; Matsumoto, H.; Murakami, Y. *Stud. Surf. Sci. Catal.* **1987**, 31, 815–826.
- 20) Nomura, N.; Koyama, A. *KEK Rep. B* **1989**, 89–16, 1.
- 21) Lytle, F. W.; Gregor, R. B.; Sandstorm, D. R.; Marques, E. C.; Wong, J.; Spiro, C. L.; Huffman, G. P.; Huggins, F. E. *Nucl. Instrum. Methods* **1984**, 226, 542–548.
- 22) Yoshida, H.; Nonoyama, S.; Hattori, T. *Physica Scripta*. **2005**, T115, 813–815.
- 23) Bando, K. K.; Sayama, K.; Kusama, H.; Okabe, K.; Arakawa, H. *Appl. Catal. A* **1997**, 165, 391–409.
- 24) Silverstein, R.-M.; Webster, F.-X. *Spectrometric Identification of Organic Compounds, Sixth Edition*; Wiley: New York, 1997.
- 25) Chuang, C.-C.; Wu, W.-C.; Huang, M.-C.; Huang, I.-C.; Lin, J.-L. *J. Catal.* **1999**, 185, 423–434.
- 26) Hasan, M. A.; Zaki, M. I.; Pasupulety, L. *Appl. Catal. A* **2003**, 243, 81–92.
- 27) Wang, R.; Hashimoto, K.; Fujishima, A.; Chikuni, M.; Kojima, E.; Kitamura, A.; Shimohigoshi, M.; Watanabe, T. *Nature* **1997**, 388, 431–432.
- 28) Teramura, K.; Tanaka, T.; Ishikawa, H.; Kohno, Y.; Funabiki, T. *J. Phys. Chem. B*, **2004**, 108, 346–354.
- 29) Inaki, Y.; Yoshida, H.; Hattori, T. *J. Phys. Chem. B*, **2000**, 104, 10304–10309.

Chapter 3

Photocatalytic Steam Reforming of Methane over Sodium Tantalate

Abstract

Photocatalytic steam reforming of methane was examined over modified and unmodified sodium tantalate photocatalysts around room temperature. The activity of the photocatalysts was much influenced by metal cation doped into the bulk of NaTaO₃, the crystallites size of NaTaO₃ and metal nanoparticles loaded on the surface. The highest activity was obtained over the NaTaO₃ doped with La³⁺, where moderate amount of La³⁺ should substitute for Na⁺ without distorting the crystal structure of NaTaO₃. The large crystallites size was more important factor than the high surface area for higher photocatalytic activity of NaTaO₃:La. These factors such as doping and large crystallites should increase the density and the mobility of the photoexcited carriers to improve the intrinsic photocatalytic activity. Moderate amount of Pt nanoparticles loaded on NaTaO₃:La most enhanced the activity among the examined metal particles, which would contribute for not only separation of excited electrons from holes and the successive hydrogen production but also methane activation during reaction with water or holes. The heat treatment after Pt loading, which probably formed the practical metal-semiconductor junction, was required for a high and stable photocatalytic activity. The best photocatalyst, Pt/NaTaO₃:La(2%), exhibited more than two times higher activity than Pt/TiO₂ did. The photocatalytic reaction lasted for a long time without deactivation. The effect of reaction conditions such as reaction temperature, feed gas composition and light intensity on the catalytic performance was systematically optimized and the highest H₂ production rate reached 4.5 μmol min⁻¹ (270 μmol h⁻¹), corresponding to 0.6% methane conversion and 11% water conversion, which exceeded the equilibrium conversion. The apparent quantum yield in the range of 240-270 nm for hydrogen production was estimated to be 30% when the irradiation light intensity was 2 mWcm⁻², which was higher than that of photocatalytic water splitting system employing NiO/NaTaO₃:La.

3.1. Introduction

To realize a sustainable society in the near future, the development of hydrogen production methods from renewable resources and natural energy would be important. Since water decomposition ($\text{H}_2\text{O} \rightarrow \text{H}_2 + 1/2\text{O}_2$, $\Delta G_{298\text{K}}^0 = 237 \text{ kJ mol}^{-1}$) using photoenergy with photocatalysts was a desirable method to produce hydrogen, various photocatalysts for it has been developed so far.¹ Among them NaTaO₃² and La-doped NaTaO₃ (NaTaO₃:La)³ was reported to show high photocatalytic activity for water decomposition upon UV light irradiation. Especially, NiO-loaded NaTaO₃:La³ showed the highest activity among reported photocatalysts for water decomposition in the UV light so far.¹

Use of a sacrificial reagent such as methanol⁴ and ethanol⁵ is known as one of the methods for producing hydrogen from water more effectively. Among them, methane was very attractive as a sacrificial resource for the following reasons. First, methane exists not only as abundant natural resources (e.g. natural gas and methane hydrate) but also as a main component of biogas which is one of the renewable resources. Second, it also has an advantage of high H/C values among hydrocarbons. Thus, methane has attracted much attention as one of the hydrogen sources and various methods for methane conversion have been industrially developed and studied by many researchers. For example, steam reforming of methane (SRM) by using heterogeneous catalyst such as Ni or Ru catalysts has been industrially employed for hydrogen production from methane.⁶⁻⁸ The chemical equation of SRM is shown as equation (1). To obtain the maximum amount of hydrogen effectively from methane, the reaction of produced CO with H₂O is further promoted by using both Fe-Cr and Cu-Zn catalysts shown as equation (2), i.e., water-gas shift reaction.



SRM has the positive and large Gibbs free energy (ΔG) so that high temperature typically more than 1073 K is required even in the presence of these catalysts. If utilization of solar energy instead of thermal energy becomes possible, it would be quite desirable.

It has been reported that the use of photoenergy with photocatalyst could break the thermodynamic barrier of endothermic reaction.⁹ Methane can be photocatalytically activated around room temperature or at a mild condition with¹⁰⁻¹⁹ or without²⁰⁻²⁴ the oxidant molecule such as O₂,^{10,11} H₂O,¹²⁻¹⁵ and CO₂,¹⁶⁻¹⁹ and in some cases the reaction could proceed beyond the thermodynamic barrier.⁹ When the platinum-loaded titanium oxide (Pt/TiO₂) was photoirradiated in a flowing mixture of water vapor and methane, photocatalytic steam reforming of methane (PSRM) shown as equation (3) proceeded around room temperature.^{14,15}



The chemical equation of PSRM corresponds to the sum of equation (1) and (2). This photocatalytic system has a potential to produce the environmentally-benign hydrogen by using solar energy from water and biomethane. However, the efficiency of this system is still far from the practical use. Therefore, development of an efficient photocatalyst is highly desired.

Since water activation would be one of the key steps for PSRM, the highly active photocatalysts for water decomposition such as NaTaO₃ can be regarded as possible candidates for PSRM. However, since water and methane molecules show quite different properties from each other, it was presumed that some suitable modifications should be required to apply the NaTaO₃ photocatalyst

for PSRM. Recently, we reported as a rapid communication that NaTaO₃:La(2%) modified by Pt nanoparticles provided a higher activity for PSRM than that of Pt/TiO₂.¹⁴ In the present study, we examined the details of this photocatalytic system, i.e., the effect of the structure and the modification of NaTaO₃ photocatalyst and the reaction condition on the reaction rate, and discussed the controlling factors for the performance of the NaTaO₃ photocatalysts in PSRM.

3.2. Experimental

3.2.1. Preparation of Photocatalysts

NaTaO₃ and metal-doped NaTaO₃ (NaTaO₃:M) were prepared by solid-state reaction method.^{25, 26} Starting materials employed were Na₂CO₃ (99.5%, Kishida), Ta₂O₅ (99.99%, Rare metallic), La₂O₃ (99.99%, Kishida), Nd₂O₃ (99.9%, Kishida), Gd₂O₃ (99.99%, Kishida), Y₂O₃ (99.99%, Kojunndo), Yb₂O₃ (99.9%, Wako), CaCO₃ (99.99%, Kojunndo), SrCO₃ (99.9%, Kojunndo) and BaCO₃ (99.9 %, Wako). Required starting materials were mixed by a conventional mortar. The atomic ratio was Na:Ta:M=1.05-x:1:x, where x was from 0 to 0.03. For another series of samples, they were mechanically mixed by a wet ball-milling method; where alumina balls (150 g, 1 cm of diameter), starting materials (50 g) and acetone (80 ml) were put into a plastic bottle (300 ml) and they were mixed at 120 rpm for 24 h, followed by drying in an oven (333 K) overnight. In the both cases, the mixed powder was calcined in air at 1173 K for 1 h in a platinum crucible. After cooling it to room temperature, it was ground by an alumina mortar and calcined in air at 1373 K for 10 h in a platinum crucible. The excess sodium was washed out with distilled water after calcinations. ICP-AES measurement confirmed that the expected amount of dopant (x mol%) existed in every obtained sample. The sample prepared by using the conventional mortar and the one prepared by the ball-milling method were referred to as NaTaO₃:M_C(x %) and NaTaO₃:M_{BM}(x %), respectively.

We also used other photocatalysts such as TiO₂, LiTaO₃, KTaO₃ and KTaO₃:La(2%) as references. TiO₂ (JRC-TIO-8, anatase, 338 m²g⁻¹) was supplied from the Catalyst Society of Japan. LiTaO₃ and KTaO₃ were prepared by solid-state reaction method.² Starting materials, LiCO₃ (K₂CO₃) and Ta₂O₅ were mixed by a wet ball-milling method. The molar ratio was Li(K):Ta=1.05(1.10):1. They were calcined at 1173 K for 1 h, followed by grind and further calcination at 1373 K for 10 h. The excess alkali was washed out with distilled water after calcination. KTaO₃:La(2%) was prepared by the same procedure as NaTaO₃:La(2%), where K₂CO₃ was used instead of Na₂CO₃ as the starting material. The semiconductor photocatalysts were loaded with metals (Pt, Ni, Rh, Pd, Ir, Ru, Ag and Au). The

employed precursors were as follows; $\text{H}_2\text{PtCl}_6 \cdot 6\text{H}_2\text{O}$ (Kishida, 98.5%), $\text{Pt}(\text{NO}_2)_2(\text{NH}_3)_2$ aqueous solution (Tanaka Kikinzoku, 4.533wt% as Pt), $\text{Ni}(\text{NO}_3)_2 \cdot 6\text{H}_2\text{O}$ (Wako, 98%), RhCl_3 (Kishida, 99%), PdCl_2 (Kishida, 99%), $(\text{NH}_4)_2\text{IrCl}_6$ (Kishida, 99.9%), $\text{RuCl}_3 \cdot n\text{H}_2\text{O}$ ($n=1\sim 3$) (Kishida, chemical grade), AgNO_3 (Wako, 99.8%) and HAuCl_4 (Kishida, 99%). Metals were usually loaded by an impregnation method. In some cases, Pt was loaded by a photodeposition method. In the impregnation method, the photocatalyst (5 g) was dispersed into an aqueous solution (50 ml) containing the metal precursor for 0.5 h, followed by evaporation to dryness with a rotary evaporator. The dried powder was typically calcined in air at 773 K for 6 h while Ni-loaded photocatalyst was calcined at 543 K for 1 h according to the literature.³ Some of them were additionally treated in a flow of hydrogen at 373-873 K for 0.5 h. In the photodeposition method, catalyst (1.5 g) was dispersed into methanol (1%) aqueous solution (50 ml) containing $\text{H}_2\text{PtCl}_6 \cdot 6\text{H}_2\text{O}$ as a Pt precursor in a Pyrex glass vessel with vigorous stirring, followed by photoirradiation from the top by using a 300 W xenon lamp, which entirely emitted from UV to visible light, for 15 min with continuous stirring. Then, the suspension was filtered off with suction, washed with distilled water, and dried at 333 K. The loading amount (y wt%) was changed from 0 to 1 wt%, referred to as $\text{M}(y)/\text{NaTaO}_3$ for example.

3.2.2. Photocatalytic Reaction Tests

The reaction tests were carried out with a fixed-bed flow type reactor in a similar way to the previous studies.^{14, 15} Typical procedure was described here. The catalysts were granulated to the size of 400-600 μm . The quartz cell ($60 \times 20 \times 1 \text{ mm}^3$) was filled with a mixture of the catalyst (1.0 g) and quartz granules (0.8 g). The reaction gas, a mixture of H_2O vapor and CH_4 with Ar carrier, was introduced into the reactor at the flow rate of 50 mL min^{-1} and the reaction was carried out without heating at atmospheric pressure upon photoirradiation from a 300 W xenon lamp. In a standard condition, the concentration of water vapor and methane was 1.5% ($30 \mu\text{mol min}^{-1}$) and 50% ($1020 \mu\text{mol min}^{-1}$) respectively, and the light of the entire wavelength region from the xenon lamp was irradiated without any filters, where the light intensity measured in the range of 230-280 nm and 310-400 nm were ca. 14 mW cm^{-2} and 60 mW cm^{-2} , respectively. The outlet gas was analyzed by on-line gas chromatography with a thermal conductivity detector.

The apparent quantum yield around 240-270 nm was calculated from the results of two runs in the photocatalytic reactions under photoirradiation of different wavelength regions: one was under the light of $\lambda > 240 \text{ nm}$ reflected by using a cold mirror, and the other was under the light of $\lambda > 270 \text{ nm}$ transmitted through a cutoff filter (Hitachi). The reaction was carried out under a mixture of H_2O (1.0%)

and CH₄ (50%) with Ar carrier using the flow reactor. The total flow rate was 50 mL min⁻¹. The apparent quantum yield in the range of 240-270 nm (Φ) was calculated by using the equation $\Phi (\%) = \{(N_{e1} - N_{e2}) / (N_{p1} - N_{p2})\} \times 100$, where N_{e1} and N_{e2} were the numbers of reacted electrons under the light of $\lambda > 240$ and 270 nm, respectively, and N_{p1} and N_{p2} were the numbers of incident photons under the light of $\lambda > 240$ and 270 nm, respectively. The number of reacted electrons was determined from the H₂ production rate, assuming that two electrons produced one H₂ molecule: $2\text{H}^+ + 2\text{e}^- \rightarrow \text{H}_2$. The number of incident photons was determined from the value measured by a Si photodiode in the range of 230-280 nm. The photoirradiation area was limited to 6 cm². The incident photon number in the range of 240-270 nm was adjusted to be 2 mW cm⁻².

3.2.3. Characterizations of Photocatalysts

Powder X-ray diffraction (XRD) pattern was recorded at room temperature on a Rigaku diffractometer RINT 2500 using Ni-filtered Cu K α radiation (50 kV, 100 mA). To examine the shift of X-ray diffraction line, Si powder was used as an internal standard. Diffuse reflectance (DR) UV-visible spectrum was recorded at room temperature on a JASCO V-550 equipped with an integrating sphere covered with BaSO₄. BaSO₄ was used as the reference. The Brunauer–Emmett–Teller (BET) specific surface area of the sample was calculated from the amount of N₂ adsorption, which was measured by a Yuasa Ionic Monosorb at 77 K. The Pt particle size on the Pt/NaTaO₃:La(2%) catalyst was measured by using the CO-pulse method in a flow system after the pretreatments in O₂ at 473 K and then in H₂ at desired temperature for 15 min each. TEM images were recorded by a JEOL electron microscope (JEM-2100M, 200 kV) equipped with CCD camera (Gatan, erlangshen ES500W). The Pt L_{II}-edge and L_{III}-edge XANES (X-ray Absorption Near Edge Structure) of Pt(1)/NaTaO₃:La(2%) and reference samples (Pt foil and PtO₂) were recorded at the BL-10B station²⁷ at KEK-PF (Photon Factory, Institute of Materials Structure Science, High Energy Accelerator Research Organization) with a Si (311) channel cut monochromator at room temperature in a transmission mode, although the spectra of Pt low-loading samples could not be measured due to the large absorption by Ta ions. La K-edge XAFS spectra of NaTaO₃:La samples were recorded at the NW-10A station²⁸ at KEK-PF at room temperature with a Si(311) double crystal monochromator in a transmission mode for NaTaO₃:La(1-3%) samples and in a fluorescence mode by using the Lytle-detector²⁹ (100 mm ion chamber filled with Kr) with a Ba filter ($\mu = 6$) for NaTaO₃:La(0.5-1%) samples. The pretreated samples for Pt L-edge XANES measurements were packed in each polyethylene film cell under N₂ atmosphere and the samples for La K-edge XAFS measurements were packed in air. The spectra were analyzed with a REX 2000 software (Rigaku).

Fourier transform of La K-edge EXAFS was performed in the range of ca. 5-12 Å⁻¹ after background subtraction. The inverse Fourier transform for curve fitting analysis was carried out in the range of ca. 2.5-4.2 Å, using theoretical parameters.³⁰

3.3. Results and Discussion

3.3.1. PSRM on Various Photocatalysts

Table 1 shows the formation rate of products over various photocatalysts in the flow of water vapor or in the flowing mixture of water vapor and methane upon photoirradiation. When none-loaded NaTaO₃:La_c(2%) or NaTaO₃:La_{BM}(2 %) was photoirradiated in the flow of water vapor, the hydrogen and oxygen were produced by water decomposition ($\text{H}_2\text{O} \rightarrow \text{H}_2 + 1/2\text{O}_2$) in a stoichiometric ratio as reported in the literature³ (Table 1, entries 1 and 2, the production rate of O₂ was not shown.). In the flow of water vapor and methane, oxygen was not detected at all but the hydrogen production rate became more than two times higher than the one in the flow of water vapor. Trace amount of carbon dioxide around detection limit was also observed. The reason for the increase of photocatalytic activity is considered that methane worked as a sacrifice reagent for consuming photogenerated holes or oxygen generated by water decomposition, which could reduce recombination of photoexcited electrons and holes or hydrogen consumption by oxygen ($\text{H}_2 + 1/2\text{O}_2 \rightarrow \text{H}_2\text{O}$), respectively. Instead, methane was oxidized into carbon dioxide. These facts reveal that the NaTaO₃:La photocatalyst could activate not only water but also methane to yield hydrogen although the hydrogen production rate was not high enough.

When Pt was loaded on NaTaO₃:La_c(2%), the activity for water decomposition was suppressed (Table 1, entry 3). This would be caused by the reverse reaction between hydrogen and oxygen on Pt catalyst.³¹ However, in the flowing mixture of water vapor and methane, hydrogen was largely produced on Pt/NaTaO₃:La samples (Table 1, entries 3 and 4). Production rate of carbon dioxide also increased and the molar ratio of hydrogen to carbon dioxide (H₂/CO₂) became almost four, indicating that PSRM shown in equation (3) was promoted by these photocatalysts. Although Pt co-catalyst would be not suitable for water decomposition because of promoting the reverse reaction, it could accelerate the activation of water and/or methane, and would be less active at least in this condition for the reverse reaction consuming hydrogen and/or carbon dioxide to form CO, CH₃OH, CH₄ etc.

Table 1 Result of photocatalytic reaction over various samples

Entry	Photocatalyst	S_{BET}^a / $\text{m}^2 \text{g}^{-1}$	D^b / nm	Production rate / $\mu\text{mol min}^{-1}$			
				Feed gas	H_2O	$\text{H}_2\text{O} + \text{CH}_4$	
				Product	H_2	H_2	CO_2
1	$\text{NaTaO}_3:\text{La}_C$ (2%) ^c	3.6	50		0.08	0.21	- ^d
2	$\text{NaTaO}_3:\text{La}_{BM}$ (2%) ^c	1.9	62		0.12	0.29	- ^d
3	$\text{Pt}(0.1)/\text{NaTaO}_3:\text{La}_C$ (2%) ^{c, e}	-	-		0.00	1.5	0.39
4	$\text{Pt}(0.05)/\text{NaTaO}_3:\text{La}_{BM}$ (2%) ^{c, e}	-	-			1.8	0.46
5	$\text{NiO}(0.2)/\text{NaTaO}_3:\text{La}_C$ (2%) ^c	-	-		0.16	0.18	- ^f
6	$\text{Pt}(0.1)/\text{TiO}_2$ ^{c, g}	335	-		0.00	0.76	0.18
7	NaTaO_{3BM} ^c	0.67	58			0.06	- ^f
8	KTaO_{3BM} ^c	1.5	58			0.04	- ^f
9	LiTaO_{3BM} ^c	0.48	57			0.02	- ^f
10	$\text{Pt}(0.01)/\text{KTaO}_3:\text{La}_{BM}$ (2%) ^{c, h}	5.1	58			0.28	- ^d
11	$\text{Pt}(0.03)/\text{NaTaO}_3:\text{La}_{BM}$ (2%) ^{e, i}	-	-		0.00	4.5	1.2

^a BET specific surface area. ^b Crystallite diameter calculated from x-ray diffraction line at 22.8 degree. ^c The light intensity measured in the range of 230-280 nm was 14 mW cm^{-2} . The feed gas was H_2O (1.5%) or a mixture of H_2O (1.5%) and CH_4 (50%) with Ar carrier. The total flow rate was 50 mL min^{-1} . The amount of the catalyst used for filling up the reaction cell was 0.6 g for Pt/TiO₂ and 1.0 g for others. In the latter case, the catalyst was diluted with quartz granules (0.8 g). ^d A trace amount of CO_2 was produced, which was lower than $0.08 \mu\text{mol min}^{-1}$. ^e Pt was loaded by impregnation method using $\text{Pt}(\text{NO}_2)_2(\text{NH}_3)_2$ precursor followed by calcination and H_2 reduction at 773 K. ^f CO_2 was not detected. ^g Pt/TiO₂ was prepared from TiO₂ (JRC-TIO-8) and an aqueous H_2PtCl_6 solution with 50% methanol by photodeposition method. ^h Pt was loaded by impregnation method using $\text{Pt}(\text{NO}_2)_2(\text{NH}_3)_2$ precursor followed by calcination at 773 K and H_2 reduction at 573 K. ⁱ The light intensity measured in the range of 230-280 nm was 116 mW cm^{-2} . The feed gas was H_2O (1.0%) or a mixture of H_2O (1.0%) and CH_4 (10%) with Ar carrier. The total flow rate was 50 mL min^{-1} . The catalyst (1.0 g) was diluted with quartz granules (0.8 g).

Figure 1 shows the time course of the production rate and the molar ratio of hydrogen to carbon dioxide over $\text{Pt}(0.1)/\text{NaTaO}_3:\text{La}_C$ (2%) in the flow of water vapor and methane. Initially the short induction period was observed and the molar ratio of H_2 to CO_2 was slightly higher than 4. This was perhaps due to the formation of surface reaction intermediates, as reported over Pt/TiO₂ photocatalyst during PSRM.¹⁵ After the short induction period, the H_2 production rate became constant and it sustained without deactivation for a long period, at least for 18 h. The molar ratio of H_2 to CO_2 in the outlet gas was almost constant to be four in the steady state. Although the formation of by-products such as ethane and carbon monoxide were reported in PSRM over Pt/TiO₂,¹⁵ they were not observed in the present case. This means that Pt/NaTaO₃:La can promote PSRM very selectively. The turnover frequency per surface Pt atom was estimated to be 68 h^{-1} , since Pt dispersion calculated from CO

adsorption was 0.26. This reaction did not proceed in the dark. These facts confirm that PSRM proceeded photocatalytically with very high selectivity.

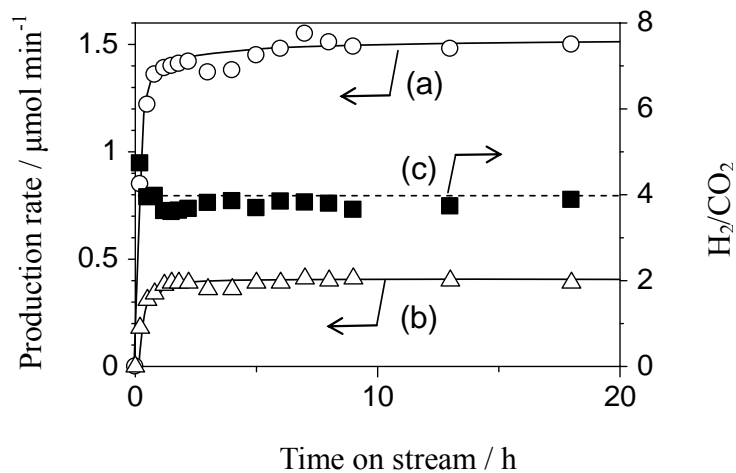


Figure 1. Time course of the production rate of (a) H₂ and (b) CO₂ on Pt(0.1)/NaTaO₃:La_c(2%), and (c) that of molar ratio of the produced H₂ to CO₂ under the standard reaction condition mentioned in the text.

NiO/NaTaO₃:La(2%), which was reported to show high activity for water decomposition,³ was also examined (Table 1, entry 5). NiO loading increased the photocatalytic activity in the flow of water vapor. However, even after the reaction gas changed to the mixture of water vapor and methane, the hydrogen production rate was almost unchanged and the production of carbon dioxide was not observed, meaning that PSRM could not occur over NiO/NaTaO₃:La_c(2%) even in the presence of water and methane. It is surprising fact that methane could not be oxidized by oxygen or active oxygen species generated during photocatalytic water splitting. Another point is that the highly active photocatalyst such as NiO/NaTaO₃:La could not activate methane molecules. Therefore, the photocatalyst with a high activity for water decomposition was not always applicable to PSRM. In other words, the photocatalyst for PSRM should be highly active for both water and methane having quite different properties from each other. It can be said that Pt co-catalyst is very important for PSRM. Thus, it is suggested that over Pt/NaTaO₃:La, methane would be activated by the Pt co-catalyst at least one time during reaction with water upon photoirradiation. Obviously, the co-catalyst such as NiO and Pt seems very important for the control of the selectivity: NiO co-catalyst would be active for water but not for methane, oxygen and hydrogen, while Pt co-catalyst would be active not only for water, oxygen and hydrogen but also for methane.

Since Pt/NaTaO₃:La showed two times higher activity than Pt/TiO₂ (Table 1, entry 6) as

reported,¹⁴ other alkali tantalate photocatalysts were also examined. The hydrogen production rate on KTaO_3 in the flow of water vapor and methane was higher than that on LiTaO_3 but lower than that on NaTaO_3 (Table 1, entries 7, 8 and 9). Since KTaO_3 has a similar crystal structure with that of NaTaO_3 , we expected that La-doping would also increase the photocatalytic activity of KTaO_3 , and thus we tried La-doping and Pt-loading for KTaO_3 photocatalyst. When we carried out the optimization of La doping amount, Pt loading method and Pt loading amount, the hydrogen production rate on $\text{Pt}(0.01)/\text{KTaO}_3:\text{La}_{BM}(2\%)$ became seven times higher than that on the bare KTaO_3 (Table 1, entry 10). However, it was much lower than that of $\text{Pt}/\text{NaTaO}_3:\text{La}$. Therefore, sodium tantalate would be the best photocatalyst among these alkali tantalates.

3.3.2. Modification of NaTaO_3 Photocatalyst

As for the preparation of $\text{NaTaO}_3:\text{La}(2\%)$ by solid state reaction method, the way to mix the starting solid materials before calcinations influenced the structure and the photocatalytic activity. The activity of $\text{NaTaO}_3:\text{La}_{BM}(2\%)$ prepared by a wet ball-milling method (Table 1, entry 2) was higher than that of the $\text{NaTaO}_3:\text{La}_c(2\%)$ prepared by using the conventional mortar (Table 1, entry 1). The activity of $\text{Pt}/\text{NaTaO}_3:\text{La}_{BM}(2\%)$ (Table 1, entry 4) was also higher than that of $\text{Pt}/\text{NaTaO}_3:\text{La}_c(2\%)$ (Table 1, entry 3), where the loading amount of Pt was optimized for each samples (see also Figure 12). $\text{NaTaO}_3:\text{La}_{BM}(2\%)$ had a larger crystallite diameter (62 nm) and a smaller BET specific surface area ($1.9 \text{ m}^2/\text{g}$) than those of $\text{NaTaO}_3:\text{La}_c(2\%)$ (50 nm, $3.6 \text{ m}^2/\text{g}$). This result indicates that the larger surface area of $\text{NaTaO}_3:\text{La}(2\%)$ does not improve the activity well. The larger crystallites size of $\text{NaTaO}_3:\text{La}$ would be a more important factor than the specific surface area for the high activity. In other words, rate determining steps of PSRM over $\text{NaTaO}_3:\text{La}$ samples in this condition may be not the surface process such as the adsorption and reaction of reactants but the bulk process such as the photogeneration and migration of electrons and holes. It is suggested that the activation of water and methane by the excited surface and Pt nanoparticles would be fast enough as compared with the supplying rate of carriers from the bulk.

Although La has been reported as the best dopant into the bulk of NaTaO_3 for water splitting,²⁵ here, we systematically examined the effect of the kinds of dopants on the bulk structure and the activity for PSRM. Five kinds of rare earth elements (La, Nd, Gd, Y, and Yb) and three kinds of alkali earth elements (Ca, Sr, and Ba) were examined as a dopant for NaTaO_3 . The shift of DR UV spectrum to shorter wavelength and the increase of BET specific surface area were observed over all of doped NaTaO_3 as reported.^{25, 26} The DR UV spectra of the representative doped samples were shown in

Figure 2, where little difference was observed among the doped samples. It is demonstrated that even small amount of doping (2 mol%) could drastically change the band structure of NaTaO₃ semiconductor. The BET specific surface areas of the sample doped with alkali earth elements (3.2-3.9 m² g⁻¹) tended to be larger than that of the sample doped with rare earth elements (1.7-2.6 m² g⁻¹). Figure 3 shows the results of the photocatalytic reaction over 2 mol%-doped samples with Pt (0.01 wt%) co-catalyst. All of doped Pt(0.01)/NaTaO₃:M_{BM}(2%) samples showed higher activity than non-doped Pt(0.01)/NaTaO_{3BM}. The highest activity was obtained over the La-doped photocatalyst, which is similar to the case for water splitting.²⁵ This result indicates that the bulk modification by doping would be commonly effective for water splitting and PSRM, suggesting that the bulk modification would contribute the intrinsic activity for these photocatalysis.

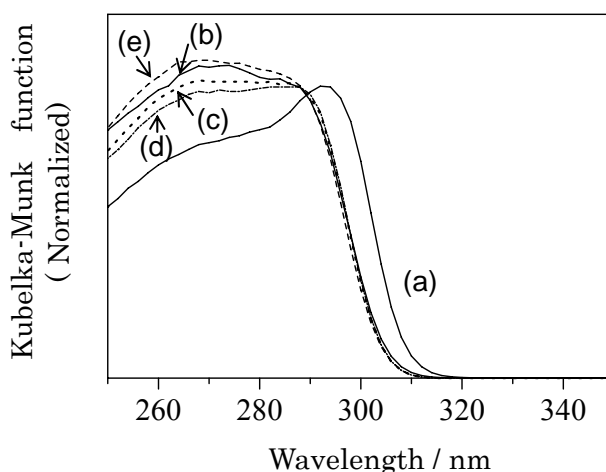


Figure 2. DR UV spectra of (a) NaTaO_{3BM}, and (b)-(e) NaTaO₃:M_{BM}(2%) samples, where M was (b) La, (c) Gd, (d) Yb and (e) Ba.

Among the dopant cation with the same valence, the metal cation having similar ionic radius to that of Na⁺ (0.139 nm), such as La³⁺ and Sr²⁺, more effectively improved the photocatalytic activity than the cations having a small or large radius such as Yb³⁺ and Ba²⁺. In the X-ray diffraction patterns of representative doped samples, only diffractions assigned to NaTaO₃ were observed for all samples (Figure 4A), indicating that there were no detectable impurity phases due to dopants. The peak intensity of doped samples was a little smaller than that of bare NaTaO₃ sample, which showed the decrease of the crystallite size. However, shift of the main diffraction line at 22.8 degree was observed for some samples (Figures 4B d-f), while no shift was observed on the dopant cation having a similar ionic radius to that of Na⁺ (Figures 4b and 4c). This fact suggests that the dopant which can fit the crystal structure without distortion is more effective to increase the photocatalytic activity of NaTaO₃. On the other hand,

the activity of the Ca-doped photocatalyst was much lower than that of the La-doped one although ionic radius of Ca was very close to that of La. Also, the Yb-doped photocatalyst showed almost the same activity as the Ca-doped one though ionic radius of Yb^{3+} was much different from that of Na^+ . These results indicate that the metal cation with higher valence would be more effective dopant to increase the photocatalytic activity. Kato et al. suggested that the increase in photocatalytic activity by La doping would result from the decrease in the particle size, the formation of nanostructure on the surface and the improved property of n-type semiconductor.³ Yamakata et al. suggested that La doping would be also effective for prolonging the lifetime of photoexcited carriers.³² Among these factors, the present result suggests that doping the metal cation with higher valence would be especially effective for increasing the n-type property of NaTaO_3 , which should be one of the improving factors for the photocatalytic activity in general.

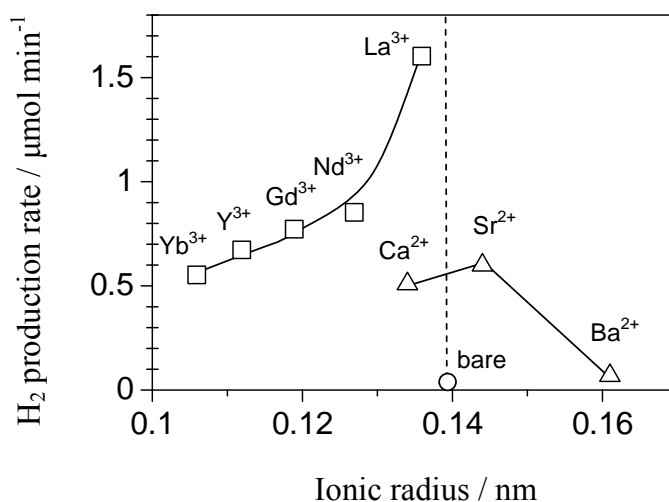


Figure 3. Dependence of the photocatalytic activity of $\text{Pt}(0.01)/\text{NaTaO}_3:\text{M}_{BM}(2\%)$ on valence and ionic radius of dopants ($\text{M}=\text{La}, \text{Nd}, \text{Gd}, \text{Y}, \text{Yb}, \text{Ca}, \text{Sr}$ and Ba). Pt was loaded by impregnation method using $\text{Pt}(\text{NO}_2)_2(\text{NH}_3)_2$ precursor followed by calcination at 773 K and H_2 reduction at 673 K. The photocatalytic reaction was carried out under the standard condition mentioned in the text.

When the doping amount of La was increased from 0 to 3 mol%, the absorption edge of UV spectra shifted to shorter wavelength (Figure 5) and the BET specific surface area increased with increasing the doping amount as reported³ (Table 2). The activity for PSRM also increased with an increase of doping amount until 2 mol%. This increase of photocatalytic activity until 2 mol% would originate from the increase of carriers. Another possibility is that it would be contributed by the upward shift of the conduction band potential, which would result in the increase of the redox potential. The increase of the surface area might also be additional reason for the increase of photocatalytic activity in this case. However, the activity of 3 mol% doped sample was lower than 1 and 2 mol% doped samples.

This was not explained by these factors. We observed that the X-ray diffraction line of $\text{NaTaO}_3:\text{La}(3\%)$ was slightly shifted to higher angle although it was not shifted until 2 mol% doping (Figure 4g). This result indicates that the crystal distortion is one of the main reasons for the decrease in the photocatalytic activity as mentioned above.

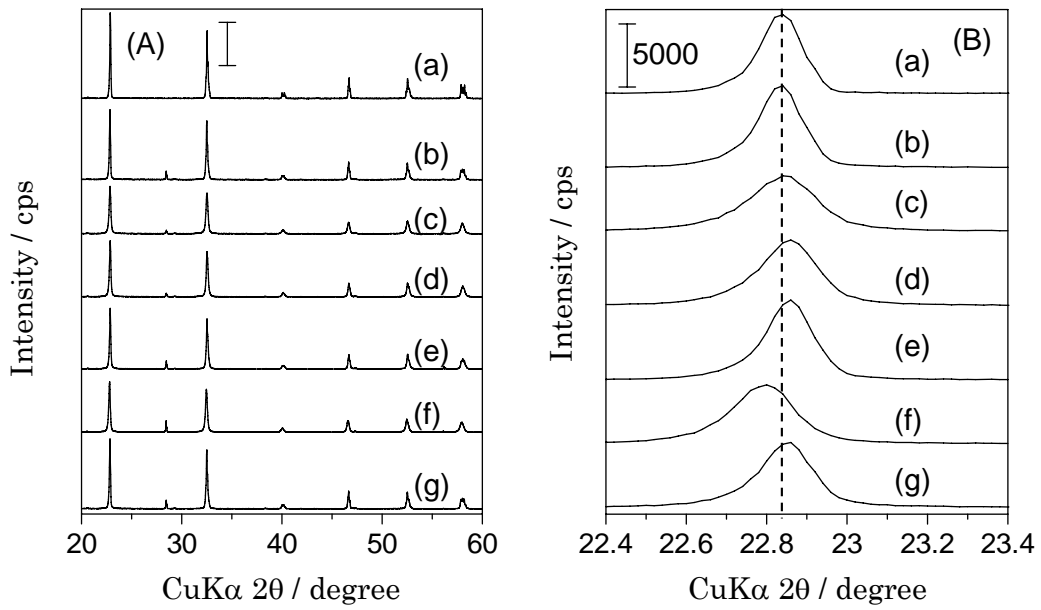


Figure 4. X-ray diffraction patterns of the samples in the range of (A) 20-60 degree and (B) 22.4-23.4 degree. Samples are (a) NaTaO_{3BM} , (b)-(f) $\text{NaTaO}_3:\text{M}_{BM}(2\%)$ and (g) $\text{NaTaO}_3:\text{La}_{BM}(3\%)$, where M was (b) La, (c) Sr, (d) Ca, (e) Nd and (f) Ba. The diffraction at 28.5 degree is of Si mixed for the angle correction.

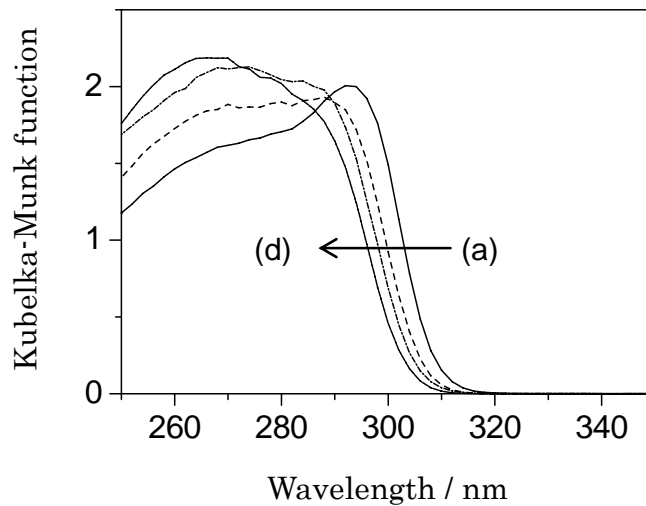


Figure 5. DR UV spectra of $\text{NaTaO}_3:\text{La}_{BM}(x\%)$ samples, where x was (a) 0%, (b) 1%, (c) 2% and (d) 3%.

Table 2 BET specific surface area, result of EXAFS analysis and the photocatalytic activity of Pt(0.01)/NaTaO₃:La(*x*)_{BM} samples

Doping amount <i>x</i> / %	S _{BET} ^a / m ² g ⁻¹	EXAFS analysis				H ₂ production rate ^d / μmol min ⁻¹
		La-Ta		La-La		
		<i>N</i> ^b	<i>R</i> ^c / Å	<i>N</i> ^b	<i>R</i> ^c / Å	
0.0	0.7	-	-	-	-	0.01
0.5	1.5	2.9	3.31	0.0	-	0.78
1.0	1.9	3.5	3.39	0.1	3.90	1.0
2.0	2.5	3.4	3.38	0.4	3.90	1.6
3.0	3.0	2.6	3.44	0.6	3.88	0.85

^a S_{BET}: BET specific surface area. ^b *N*: coordination number obtained from the curve fitting analysis of EXAFS. ^c *R*: atomic distance obtained from the curve fitting analysis of EXAFS. ^d In the photocatalytic steam reforming of methane over Pt(0.01)/NaTaO₃:La(*x*)_{BM} at the standard reaction condition. Pt was loaded by impregnation method using Pt(NO₂)₂(NH₃)₂ precursor followed by calcination at 773 K and H₂ reduction at 673 K.

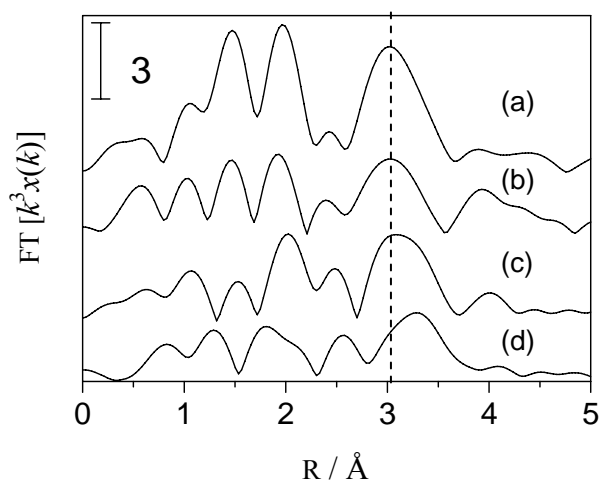


Figure 6. Fourier transformed La K-edge EXAFS spectra of NaTaO₃:La_{BM}(*x*%) samples, where *x* was (a) 0.5%, (b) 1%, (c) 2% and (d) 3%.

The details of the local structure of La in NaTaO₃ were investigated with EXAFS. Figure 6 shows the Fourier transforms of EXAFS spectra for NaTaO₃:La(0.5-3%) samples. The region for the first coordination was complicated. In NaTaO₃ crystal, twelve O²⁻ coordinated to Na⁺ were located in various distances from 2.46 to 3.09 Å calculated from ICSD (Inorganic Crystal Structure Database). Therefore, this result was reasonable if we assumed that La³⁺ would substitute for Na⁺. On the other hand, the second coordination peak was clearly observed around 3.1 Å and shifted to the longer distance with increasing the doping amount. The peak intensity gradually decreased. Thus, we carried out the inverse Fourier transform only in the second coordination region around 2.5-4.2 Å and analyzed them

by curve fitting method using McKale parameters.³⁰ Figure 7 shows the calculated curve of 3 mol% doped sample as a representative. When we assumed that the second coordination sphere was composed of La-Ta shell and La-La shell, the calculated curve fitted well the experimental curve. The curve-fitting results of NaTaO₃:La(0.5-3%) samples are shown in Table 2. It was revealed that the EXAFS for the second coordination sphere of the doped samples was mostly composed of a La-Ta shell and there was also a La-La shell as a minor component. The contribution of La-Na shell was not observed, which was probably due to the small backscattering from Na. As increasing the doping amount of La, the ratio of the La-La shell increased. The overlapping of each EXAFS would reduce the peak intensity in the region in Figure 6. The length of the La-Ta shell was almost the same as the atomic distance between Na and Ta in NaTaO₃ (3.27-3.45 Å) and the length of the La-La shell was almost the same as the atomic distance between Na and Na in NaTaO₃ (3.88 Å). These suggest that La ions predominantly substituted for the lattice Na⁺ in NaTaO₃ with a high dispersion when the doping amount of La was small. However, with further increasing the doping amount, the number of La ions substituting for the adjacent Na sites increased to form La-La pair in NaTaO₃. The former would increase the photocatalytic activity. However, the latter would decrease the activity since it would distort the crystal structure. In other words, doping trivalent cations into Na⁺ sites could increase n-type property of NaTaO₃ semiconductor to improve the photocatalytic activity, while excess doping forming La-La pair would distort the structure and disturb the smooth migration of carriers to decrease the photocatalytic activity. When trivalent La³⁺ substituted for monovalent Na⁺, some defects such as sodium vacancy would be formed beside La³⁺. This would further contribute the structural distortion, resulting the complexity and lower intensity of the EXAFS Fourier transforms at both the first and the second coordination spheres (Figure 6).

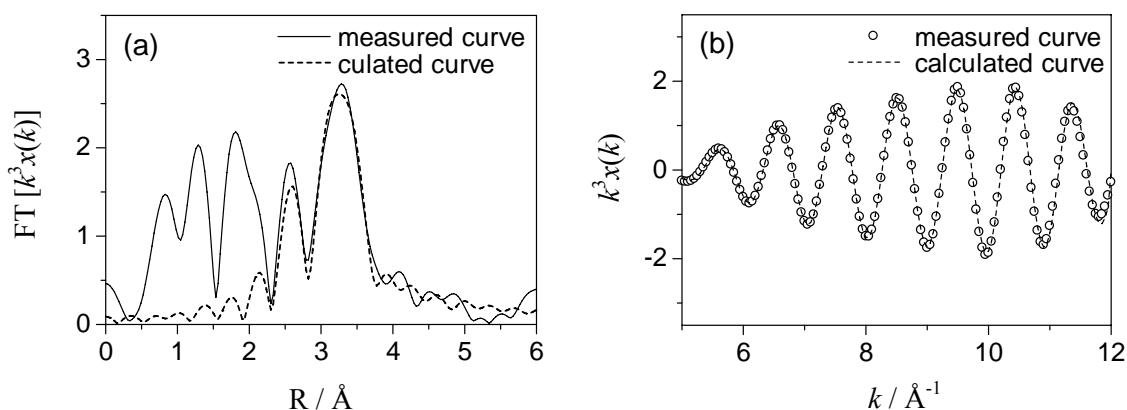


Figure 7. Curve fitting analysis of EXAFS spectra of NaTaO₃:La_{BM}(3%). (a) The Fourier transforms of EXAFS spectra and (b) the inverse Fourier transforms.

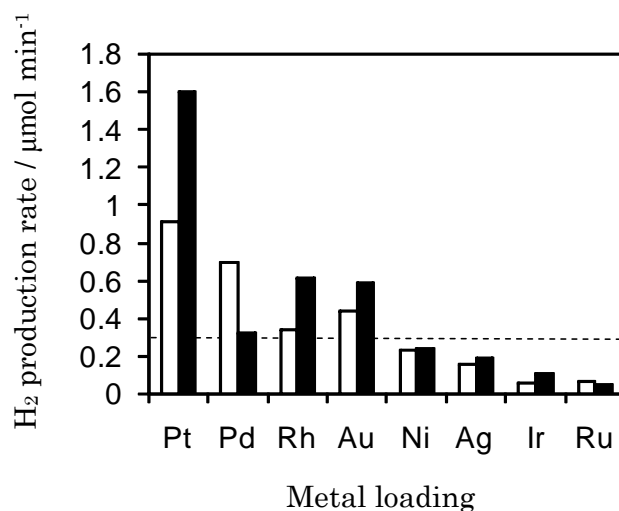


Figure 8. Hydrogen production rate over metal-loaded NaTaO₃:La_{BM}(2%). Metals were loaded by impregnation method followed by calcination in air at 773 K (white) and further H₂ reduction at 673 K (black). The loading amount was 0.01 wt%. Dotted line shows the hydrogen production rate over none-loaded NaTaO₃:La_{BM}(2%). The photocatalytic reaction was carried out under the standard condition mentioned in the text.

3.3.3. Addition of Cocatalyst on NaTaO₃:La(2 mol%)

Several kinds of metals (Ni, Ru, Rh, Pd, Ag, Ir, Pt, and Au) were examined as the surface additive of NaTaO₃:La(2%). Figure 8 shows the hydrogen production rate in the flow of water and methane over M(0.01)/NaTaO₃:La_{BM}(2%) prepared by impregnation method, followed by calcination at 773 K. The samples after further hydrogen reduction at 673 K were also compared in every photocatalyst. Precious metals such as Pt, Pd, Rh and Au increased the photocatalytic activity of NaTaO₃:La(2%). The photocatalytic activity largely varied before and after hydrogen reduction in most catalysts; the activity increased after hydrogen reduction on the Pt, Rh, and Au-loaded samples, while it decreased after hydrogen reduction on the Pd-loaded sample. This suggests that the metallic state of Pt, Rh and Au was more suitable for increasing the PSRM activity than their oxide state. However, palladium oxide would be better than palladium metal as the co-catalyst. The activity of Ni, Ag, Ir and Ru-loaded samples before and after hydrogen reduction was lower than that of bare NaTaO₃:La_{BM}(2%). Among all these samples, the Pt-loaded photocatalyst reduced in the flow of hydrogen at 673 K showed the highest activity. One possible reason for the highest activity of the Pt-loaded sample should be correlated with the largest work function of Pt among the examined metals, which would most efficiently promote the separation of photoexcited carriers from the conduction band in NaTaO₃. However, it is noted that the activity of the Pt-loaded photocatalyst was especially high, i.e., more than

two times higher activity than any other catalysts. This indicates that Pt may have some roles other than the separation of photoexcited carriers. For example, Pt may accelerate the adsorption of methane and the activation of C-H bond before reaction with water or the activated species.

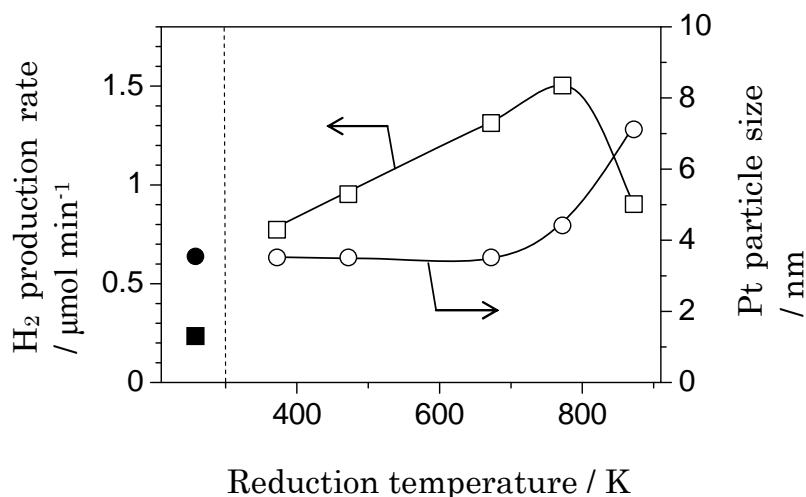


Figure 9. Effect of the hydrogen reduction temperature on the Pt particle size and the activity of Pt(0.1)/NaTaO₃:La_c(2%). Pt was loaded by impregnation method followed by calcination at 773 K before hydrogen reduction. Pt particle size was measured by CO adsorption. The closed plots show the values on the none-reduced sample. The photocatalytic reaction was carried out under the standard condition mentioned in the text.

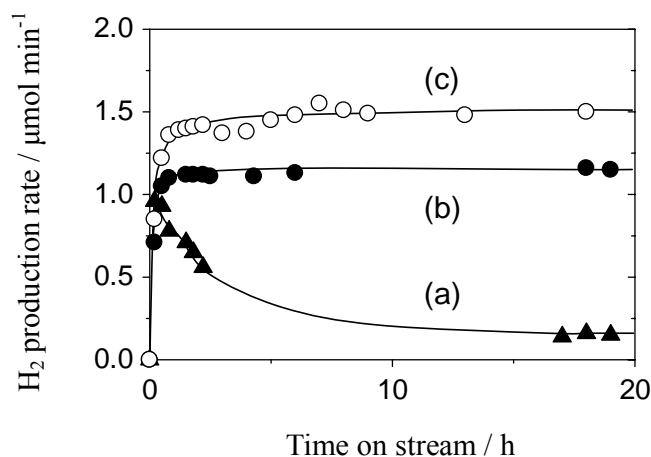


Figure 10. Time course of the H₂ production rate on Pt(0.1)/NaTaO₃:La_c(2%) samples, on which Pt was loaded (a) by photodeposition method, (b) by photodeposition method followed by calcination and reduction at 773 K, and (c) by impregnation method followed by calcination and H₂ reduction at 773 K. Pt precursor was H₂PtCl₆ for (a) and (b), and Pt(NO₂)₂(NH₃)₂ for (c), respectively. The photocatalytic reaction was carried out under the standard condition mentioned in the text.

Influence of the hydrogen reduction temperature was examined for Pt(0.1)/NaTaO₃:La_c(2%) prepared by impregnation method. The activity of all prepared samples became constant within a few

hours after the photoirradiation started in the flow of reactants and then it sustained for a long time, similar to the result shown in Figure 1. The activity first increased with an increase of the reduction temperature until 773 K, then decreased at higher reduction temperatures such as 873 K (Figure 9). The Pt particle size measured by CO adsorption before photocatalytic reaction did not largely vary with the reduction at these low temperatures less than 673 K to be 3.5 nm, and increased with increasing a reduction temperature until 7.1 nm at 873 K. On the other hand, the oxidation state of the surface Pt particles, which was confirmed by Pt L_{III}-edge XANES spectra of Pt(1)/NaTaO₃:La(2%) samples, became metallic with increasing the reduction temperature. Therefore, it was revealed that more metallic state of Pt particles was preferable for PSRM, while too large size of Pt particles might not be preferable in this system.

The influence of Pt loading method on the activity was also examined. Figure 10 shows the time course of the hydrogen production rate over Pt(0.1)/NaTaO₃:La_c(2%) samples prepared by different loading method. Pt on the sample (a) was loaded by photodeposition method. For the sample (b), Pt was loaded by photodeposition method, followed by calcination and hydrogen reduction at 773 K. For the sample (c), Pt was loaded by impregnation method, followed by calcination and hydrogen reduction at 773 K. The activity was almost the same among these photocatalysts soon after the irradiation started. However, the activity of the sample (a) drastically decreased as the irradiation time became longer. On the other hand, the activity of thermally treated samples (b) and (c) did not decrease. The same phenomena were confirmed on another set of Pt(0.1)/NaTaO₃:La_{BM}(2%) samples. These suggest that the heat treatment after Pt loading is an important factor to obtain the photocatalysts having a high and stable activity. When we compared the Pt L_{III}-edge XANES spectra of Pt(1)/NaTaO₃:La_c(2%) prepared by photodeposition without thermal treatments and that prepared by impregnation with thermal treatments, the state of Pt were similarly metallic for both samples. Thus, the difference of the stability would result from other properties than the oxidation state of the Pt particles. Then, we measured the Pt particle size of the set of Pt(0.1)/NaTaO₃:La_{BM}(2%) samples by using TEM and CO-pulse method (Figure 11 and Table 3). On the TEM images, very small Pt particles less than 5 nm were mainly observed on the photocatalyst prepared by photodeposition method (Figure 11a), where the size distribution of particles were around 2-10 nm. However, Pt particle size of the sample became larger after the photocatalytic reaction, typically 6-15 nm (Figure 11b). On the other hand, Pt particle size of the photocatalyst prepared by photodeposition method, followed by calcination and hydrogen reduction at 673 K, was a little larger than that prepared by photodeposition method without the thermal treatment, the size of which was typically 3-13 nm (Figure 11c). After the photocatalytic reaction, the Pt particle size became larger around 5-18 nm (Figure 11d), which was similar to the result of the sample

without heating treatment. These suggest that an aggregation of Pt particles was occurred over these catalysts during the photocatalytic reaction even around the room temperature. The average Pt particle sizes measured by CO adsorption listed in Table 3 also exhibited a similar tendency to the results from TEM observation. Thus, the aggregation of Pt particles is not a factor determining the activity and stability and there should be other determining factors. One of the most possible reasons would be as follows: The thermal treatment would improve the metal-semiconductor junction between Pt nanoparticles and the surface of NaTaO₃:La(2%), which would be important for both activity and stability. The positive effect of thermal treatment, i.e. the improvement of junction, would be larger than the negative effect of the aggregation of Pt particles by thermal treatment. Without the thermal treatment, the junction might become worse during the photocatalytic reaction, resulting in the decrease of activity.

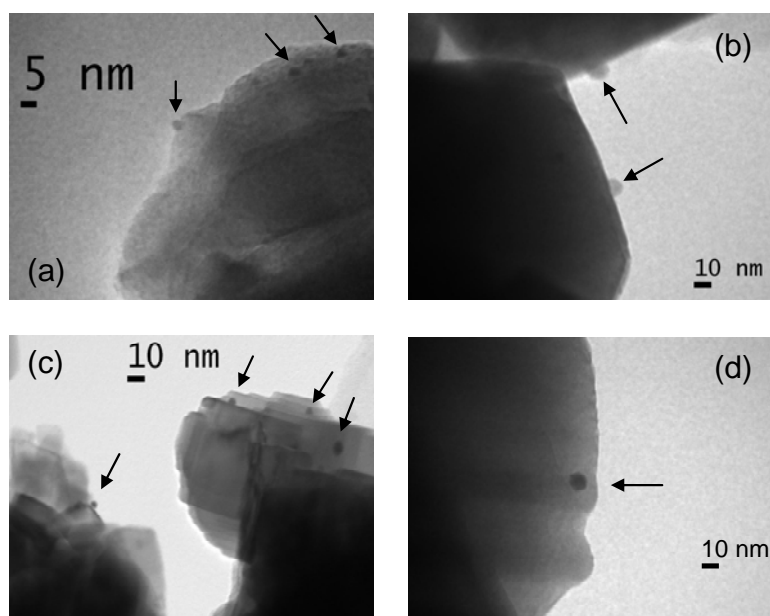


Figure 11. TEM images of Pt(0.1)/NaTaO₃:La_{BM}(2%) samples before (a and c) and after the photocatalytic reaction (b and d). On the sample (a) and (b), Pt was loaded by photodeposition method using H₂PtCl₆ precursor. On the sample (c) and (d), Pt was loaded by photodeposition method using H₂PtCl₆ followed by calcination at 773K and H₂ reduction at 673K.

With the increase of loading amount of Pt, the activity first increased then decreased in all samples. Figure 12 shows the results of two representative samples. The optimum loading amount varied for each photocatalyst sample; the optimum loading amount for NaTaO₃:La_{BM}(2%) was smaller than that for NaTaO₃:La_c(2%). Since the BET specific surface area of the former was smaller than that of the latter as listed in Table 1, it is suggested that the optimum amount would be determined by the surface area. In other words, the optimum number and size of Pt particles would depend on the specific

surface area of NaTaO₃:La catalyst. The optimum number of Pt atoms per unit surface area could be calculated as 0.8-0.9 atom nm⁻².

Table 3 Pt particle sizes on Pt(0.1)/NaTaO₃:La_{BM}(2%) samples measured by TEM and CO-pulse method

Loading method	Pt particle size /nm			
	TEM		CO-pulse method	
	Before reaction	After reaction	Before reaction	After reaction
PD ^a	2-10	6-15	6.0	7.6
PD+TT ^b	3-13	5-18	6.2	7.8

^a Pt was loaded on NaTaO₃:La_{BM}(2%) by photodeposition method using H₂PtCl₆. ^b Pt was loaded on NaTaO₃:La_{BM}(2%) by photodeposition method using H₂PtCl₆, followed by calcination at 773 K and H₂ reduction at 673 K.

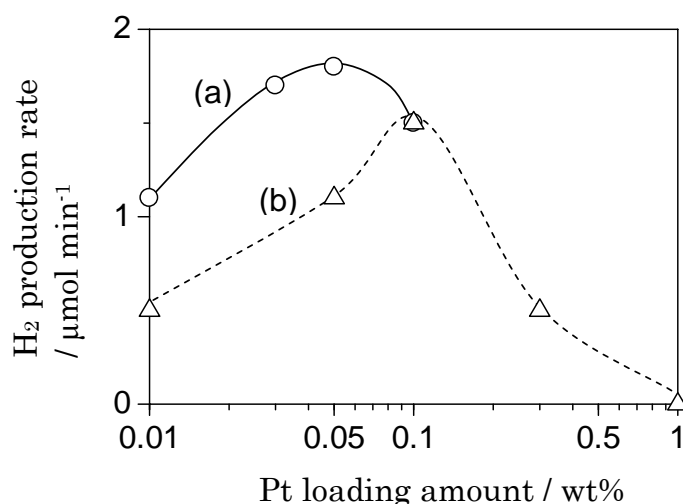


Figure 12. Effect of Pt loading amount on the photocatalytic activity of (a) Pt/NaTaO₃:La_{BM}(2%) and (b) Pt/NaTaO₃:La_C(2%). Pt was loaded by impregnation method using Pt(NO₂)₂(NH₃)₂ precursor followed by calcination and H₂ reduction at 773 K. The photocatalytic reaction was carried out under the standard condition mentioned in the text.

In conclusion of this section, the requirements for metal loading on the NaTaO₃:La photocatalyst are as follows: The additive should be metallic Pt nanoparticles, the loading amount of Pt should be optimized according to the specific surface area of the photocatalyst, and the metal-semiconductor junction should be improved by thermal treatment. Eventually, the highest activity was obtained over Pt(0.05)/NaTaO₃:La_{BM}(2%) loaded by impregnation method using Pt(NO₂)₂(NH₃)₂, followed by calcination and hydrogen reduction at 773 K, where the hydrogen production rate was 1.8 μmol min⁻¹ at the standard reaction condition (Table 1 entry 4).

3.3.4. Reaction Condition

The effect of reaction condition on the activity of Pt(0.03)/NaTaO₃:La_{BM}(2%) was examined. Figure 13 shows the effect of the reaction temperature on the hydrogen production rate in PSRM without changing other reaction conditions. Hydrogen production rate increased with the increase of reaction temperature until 348 K (Figure 13a). In this region, the Arrhenius plot for hydrogen production drew a straight line (Figure 13b) and the thermal activation energy was estimated to be ca. 14 kJ mol⁻¹. This value was much smaller than the activation energy reported for thermal SRM; 63-100 kJ mol⁻¹ for Ni-based catalyst,³³ 153±10 kJ mol⁻¹ for Ce_{0.9}Gd_{0.1}O₃ catalyst³⁴ and 122 kJ mol⁻¹ for Pt catalyst.³⁵ Therefore, the thermal energy should contribute to the mild activation steps such as migration of photoexcited carriers from the bulk to the surface, electron transfer between the surface and adsorbed substance and thermal desorption of products, and the reaction would be mainly promoted by the photoexcitation. On the other hand, the hydrogen production rate did not change with further increasing the reaction temperature above 348 K. This shows that the reaction rate at high temperature more than 348 K would not be influenced by the thermal activation steps, but determined by the photocatalytic reaction step.

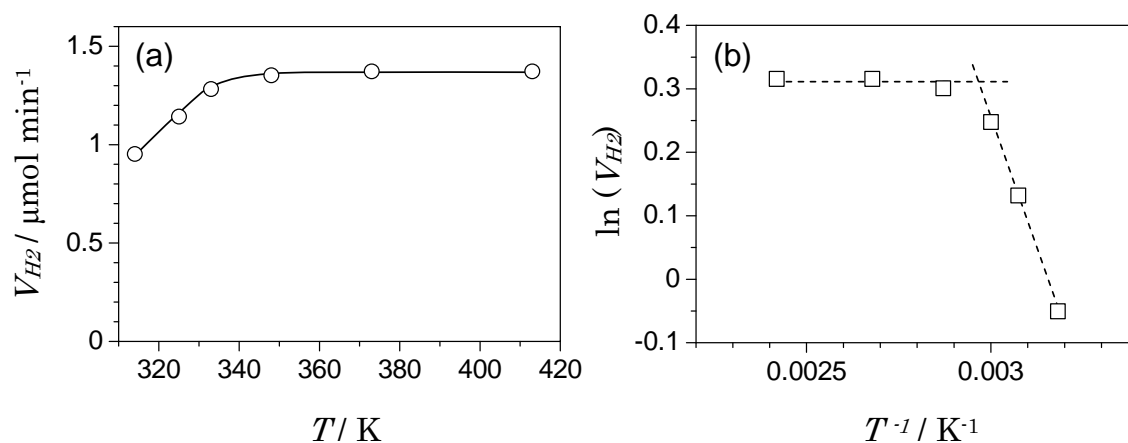


Figure 13. (a) Plot of the hydrogen production rate (V_{H_2}) vs. the reaction temperature (T) over Pt(0.03)/NaTaO₃:La_{BM}(2%) and (b) its Arrhenius plot. Pt was loaded by impregnation method using Pt(NO₂)₂(NH₃)₂ precursor followed by calcination at 773 K and H₂ reduction at 673 K. The photocatalytic reaction was carried out under the standard condition mentioned in the text.

The hydrogen production rate was largely influenced by the concentration of the reactants and the light intensity. Figure 14 shows the hydrogen production rate over Pt(0.03)/NaTaO₃:La_{BM}(2%) in the different reaction conditions. As the light intensity increased, the hydrogen production rate increased in all reaction conditions. Though the reaction temperature also increased with an increase of the light

intensity as shown in the caption of Figure 14, the influence of thermal energy in this temperature range would be small, as confirmed in Figure 13. When the concentration of methane was fixed at 20%, the optimum concentration of water vapor was very low (about 0.5%) at the low light intensity of 5 mW cm^{-2} (Figure 14A (a)). It is considered that the rate determining step in the low intensity of light would be not an adsorption of water and methane but a photoinduced reaction process of these reactants. Thus, the catalyst surface should be covered with enough reactants, especially water molecules, which were waiting for the photoexcited carriers. Therefore, the excess feed of water would disturb the adsorption of methane and accordingly reduce the photocatalytic activity. The optimum concentration of water tended to become higher with increasing the light intensity (Figure 14A (b)-(d)). It is suggested that the surface reaction rate of adsorbed molecules would increase with the increase of light intensity and higher concentration of water could become acceptable. The reaction order for water concentration in the range of 0.2-1.0% was calculated to be 0.29 in the light intensity was 14 mW cm^{-2} . It increased to be 0.53 in the intensity of 114 mW cm^{-2} . These values were much smaller than the one expected from the eq. 3. Therefore, the reaction rate was influenced by not the partial pressure of water in the gas phase but the surface concentration of adsorbed water. However, in the higher intensity of light, the reaction rate could be more controlled to some extent by the concentration of water in the gas phase.

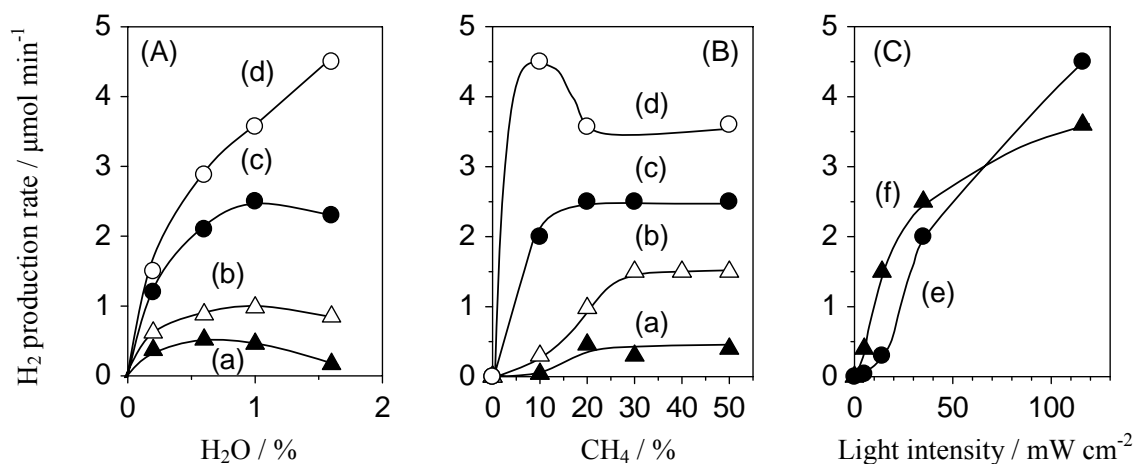


Figure 14. Effect of the feed gas composition and the light intensity on the hydrogen production rate over $\text{Pt}(0.03)/\text{NaTaO}_3:\text{La}_{BM}(2\%)$ photocatalyst. The fixed gas composition was (A) CH_4 20% and (B) H_2O 1.0% and (C) H_2O 1.0%, respectively. CH_4 concentration in (C) was (e) 10% and (f) 50%. The light intensity was (a) 5 mW cm^{-2} , (b) 14 mW cm^{-2} , (c) 35 mW cm^{-2} and (d) 116 mW cm^{-2} , which was measured representatively in the range of 230-280 nm. The temperature of photoirradiated catalyst cell was measured to be (a) 318 K, (b) 348 K, (c) 363 K and (d) 413 K. Pt was loaded by impregnation method using $\text{Pt}(\text{NO}_2)_2(\text{NH}_3)_2$ precursor followed by calcination and H_2 reduction at 773 K.

The concentration of methane complexly influenced on the photocatalytic activity (Figure 14B). In the low intensity of light, the hydrogen production rate increased at an accelerated pace with increasing the methane concentration (Figure 14B (a) and (b)). In fact, the reaction order for methane concentration was calculated to be 1.5 when the light intensity was 14 mW cm^{-2} . This value was larger than the one estimated from the eq. 1. Such acceleration was also observed for PSRM over Pt/TiO₂.¹⁵ As suggested in the previous study,¹⁵ a formation of surface organic intermediates would increase the hydrophobicity of the surface and enhance CH₄ adsorption, which would accelerate the photocatalytic reaction. In the high intensity of light, the catalyst showed high activity even if the concentration of methane was low (Figure 14B (c) and (d)). This suggests that the formation of reaction intermediates should be easier in higher intensity of light. However, too high concentration of methane rather reduced the activity, as shown in Figure 14B (d). This result suggests that the excess formation of reaction intermediates would disturb the water adsorption due to their hydrophobic property or the physical coverage of the surface.

Figure 14C shows the effect of the incident light intensity on the hydrogen production rate. When the concentration of water vapor and methane was 1.0% and 10%, respectively, the hydrogen production rate increased gradually with increasing the light intensity and then steeply increased (Figure 14C (e)). This was because the moderate accumulation of surface organic intermediates would accelerate the reaction. When the light intensity was further increased more than 35 mW cm^{-2} , the increment decreased. This was because the probability for the recombination of photoexcited electrons and holes would increase in the high intensity of light and the excess accumulation of reaction intermediates on the surface might reduce the photocatalytic reaction rate. Therefore, the apparent quantum efficiency in this reaction condition would become the highest value in the light intensity around 35 mW cm^{-2} . When the concentration of methane was as high as 50%, a similar tendency was observed (Figure 14C (f)). In this case, the most effective light intensity seems to be around 10 mW cm^{-2} and the production rate seems to be much suppressed upon higher light intensity. This would be because the excess surface organic intermediates were formed easier in the high concentration of methane. The reaction order for the light intensity in the range of $5\text{-}35 \text{ mW cm}^{-2}$ was calculated to be 2.0 in the methane concentration of 10%. Thus one may suggest that the rate determining steps, probably the formation of the surface intermediates, would be two-photon process. However, in this case, we must also consider the other effects such as the variation of surface hydrophobicity, implying that the real reaction order for the light intensity was difficult to be estimated. On the other hand, the reaction order decreased to be 0.95 when the concentration of methane was 50%, showing that excess

amount of methane would form excess intermediates on the surface and disturb the reaction as mentioned above.

We summarized the influence of reaction conditions as follows: In the optimum feed concentrations of water and methane, the surface concentrations among the adsorbed molecules and the reaction intermediates would achieve to a preferable balance and contribute the high reaction rate. As the light intensity increased, the reaction rate initially increased at an accelerated pace since the accumulation of the hydrophobic surface reaction intermediates would promote the adsorption of methane, and then increased at a moderate pace due to the excess accumulation and the high carrier concentration. The best reaction condition in the present set up was as follows; the concentrations of water vapor and methane were 1.0% and 10%, respectively, and the light intensity was to be maximum (116 mW cm^{-2}). In this condition, the hydrogen production rate was $4.5 \text{ } \mu\text{mol min}^{-1}$ (6.6 mL h^{-1}) and the conversion of methane and water reached to 0.6% and 11%, respectively (Table 1, entry 11). The methane conversion at thermal equilibrium can be calculated from thermodynamic data to be ca. 0.2% in this condition. Therefore, it is obvious that the present photocatalytic system actually exceeded the equilibrium conversion.

Table 4 Photocatalytic H₂ production rate and quantum yield in the range of 240-270 nm^a

Photocatalyst	Reaction	H ₂ production rate / $\mu\text{mol min}^{-1}$	Quantum yield / %
Pt(0.05)/NaTaO ₃ :La _{BM} (2%) ^b	H ₂ O(g)+CH ₄ ^c	0.26	30
Pt(0.1)/TiO ₂	H ₂ O(g)+CH ₄ ^c	0.02	2
NiO(0.2)/NaTaO ₃ :La _{BM} (2%)	H ₂ O(g) ^c	0.11	13
NiO(0.2)/NaTaO ₃ :La _{BM} (2%)	H ₂ O(l) ^d	0.17	20

^a The incident light intensity in the range of 240-270 nm was 2 mW cm^{-2} . The irradiation area was 6 cm^2 .

^b Pt was loaded by impregnation method using Pt(NO₂)₂(NH₃)₂ precursor followed by calcination and H₂ reduction at 773 K. ^c The feed gas was a mixture of H₂O (1.0%) and CH₄ (0 or 50%) with Ar carrier. The total flow rate was 50 mL min^{-1} . ^d The photocatalyst (0.3 g) was suspended in pure water (200 ml) with Ar bubbling (50 mL min^{-1}), which was irradiated through a quartz window on the top of the reactor.

3.3.5. Quantum yield

The incident light intensity could not be measured accurately without wavelength limitation and without limitation of irradiation area since there is a distribution of the wavelength and the light intensity. Thus, we measured the apparent quantum yield in the range of 240-270 nm at limited irradiation area. The light intensity corresponded to 2 mW cm^{-2} . The results were shown in Table 4. The quantum yield of the PSRM system employing Pt(0.05)/NaTaO₃:La_{BM}(2%) was estimated to be 30%,

which was much higher than that of Pt(0.1)/TiO₂ photocatalyst. On the other hand, the quantum yield of water splitting system employing NiO(0.2)/NaTaO₃:La_{BM}(2%), which was one of the best photocatalysts for water splitting so far,¹ was lower than that of the PSRM; 13% for water vapor splitting and 20% for liquid water splitting, respectively. Thus, the present PSRM could produce H₂ more efficiently than the water splitting systems in this condition. This would be due to suppression of the reverse reaction of water decomposition by predominantly proceeding methane oxidation, and also due to the lower ΔG than that for water splitting ($\Delta G_{298K} = 237 \text{ kJ mol}^{-1}$ and 229 kJ mol^{-1} for liquid and vapor water, respectively).

3.3.6. Proposed reaction mechanism

Finally, we propose the reaction mechanism of PSRM over Pt/NaTaO₃:La catalyst. When the Pt/NaTaO₃:La photocatalyst was photoirradiated, electron and hole pairs were produced in the conduction and valence bands, respectively, and they migrated to the surface, i.e., to the Pt nanoparticles and the surface oxygen of NaTaO₃, respectively. Moderate amount of La doping would mainly promote this process since the trivalent valence improved the n-type character of NaTaO₃. Thus, this La-doping effect would be common between water splitting and PSRM.

Next, adsorbed water and methane were activated by these carriers. Pt nanoparticles would also contribute to methane activation as co-catalyst. It is probable that Pt nanoparticles would activate methane before the reaction with water. Since the thermal activation energy of Pt/NaTaO₃:La was quite small, it is suggested that Pt would not activate methane thoroughly but contribute to the adsorption and the weak activation of C-H bonds.

Then, the reaction between activated water and methane would form the surface organic intermediates such as [CH₂O]_n, which was reported for PSRM over Pt/TiO₂,¹⁵ and it further reacted with water to produce carbon dioxide. Since the production and decomposition rate of the intermediates over Pt/NaTaO₃:La would be much faster than those of Pt/TiO₂, the accumulation of the intermediates on the surface was not apparently observed. However, the presence of the intermediates was evident from the result shown in Figure 1 and Figure 14. On the other hand, protons should be reduced by the excited electrons on the Pt nanoparticles to form molecular hydrogen.

Since the number of photoexcited carriers increased with increasing the light intensity, the high activity was obtained in the high intensity of light. On the other hand, the high quantum efficiency was obtained when the moderate amount of the organic intermediates was accumulated on the surface: In the low intensity of light or the low methane concentration (high water concentration), the production

rate of the surface organic intermediates was so low that the reaction could not proceed efficiently. Reversely, in the high intensity of light or the high methane concentration (low water concentration), excess amount of the reaction intermediates accumulated on the surface and disturbed the reaction.

NiO/NaTaO₃:La photocatalyst, which showed the high activity for water decomposition, was not suitable for PSRM because NiO could not activate methane. Although Pt/TiO₂ photocatalyst promoted PSRM, the activity was relatively low and decreased gradually because its activity for water decomposition was much lower than that for methane activation promoted by Pt co-catalyst. It is noted that the Pt/NaTaO₃:La catalyst showed the higher and more stable activity for PSRM than NaTaO₃, NiO/NaTaO₃:La and Pt/TiO₂ photocatalysts did, since this photocatalyst could activate both water and methane with preferable balance.

3.4. Conclusions

In the present study, we found that Pt-loaded NaTaO₃:La photocatalysts showed high and selective activity for PSRM around room temperature. The photocatalytic activity of NaTaO₃ was much influenced by the crystallite size, doping metal ions and the co-catalyst, except for the reaction condition such as concentration of the reactants and the light intensity. Among them, large size of NaTaO₃ crystallites and moderate amount of high valence doping metal ions substituting for Na⁺ with high dispersion should effectively improve the mobility and density of carriers. Thus, they could increase the intrinsic photocatalytic activity, which was commonly effective for both PSRM and water decomposition. On the other hand, a property of co-catalyst would mainly influence the molecular activation, especially the methane activation. Among examined co-catalyst, Pt nanoparticles with the metallic state most enhanced the PSRM activity. The thermal treatment such as calcination in air and hydrogen reduction before reaction was necessary for Pt-loaded NaTaO₃:La photocatalyst to show high and stable activity, since the treatment would probably improve the metal-semiconductor junction. The best catalyst, Pt/NaTaO₃:La(2%), showed two times higher activity than Pt/TiO₂ without deactivation for a long time and it was confirmed that the PSRM could proceed beyond the equilibrium conversion calculated from thermodynamic data. The apparent quantum yield for hydrogen production in PSRM on Pt/NaTaO₃:La was higher than that of photocatalytic water splitting system employing NiO/NaTaO₃:La. Thus, the present PSRM system would be expected as an efficient hydrogen production system.

References

- 1) Kudo, A.; Miseki, Y. *Chem. Soc. Rev.* **2009**, 38, 253–278.
- 2) Kato, H.; Kudo, A. *J. Phys. Chem. B* **2001**, 105, 4285–4292.
- 3) Kato, H.; Asakura, K.; Kudo, A. *J. Am. Chem. Soc.* **2003**, 125, 3082–3089.
- 4) Kawai, T.; Sakata, T. *J. Chem. Soc., Chem. Comm.* **1980**, 15, 694–695.
- 5) Sakata, T.; Kawai T. *Chem. Phys. Lett.* **1981**, 80, 341–344.
- 6) Rostrup-Nielsen, J. R. *Catal. Today* **1993**, 18, 305–324.
- 7) Peña, M. A.; Gómez, J. P.; Fierro, J. L. G. *Appl. Catal. A* **1996**, 144, 7–57.
- 8) Armor, J. N. *Appl. Catal. A* **1999**, 176, 159–176.
- 9) Yuliati, L.; Yoshida, H. *Chem. Soc. Rev.* **2008**, 37, 1592–1602, and references herein.
- 10) Wada, K.; Yamada, H.; Watanabe, Y.; Mitsudo, T. *J. Chem. Soc., Faraday Trans.* **1998**, 94, 1771–1778.
- 11) Ward, M. D.; Brazdil, J. F.; Mehandru, S. P.; Anderson, A. B. *J. Phys. Chem.* **1987**, 91, 6515–6521.
- 12) Taylor, C. E. *Catal. Today* **2003**, 84, 9–15.
- 13) Gondal, M. A.; Hameed, A.; Suwaiyan, A. *Appl. Catal. A* **2003**, 243, 165–174.
- 14) Yoshida, H.; Kato, S.; Hirao, K.; Nishimoto, J.; Hattori, T. *Chem. Lett.* **2007**, 36, 430–431.
- 15) Yoshida, H.; Hirao K.; Nishimoto, J.; Shimura, K.; Kato, S.; Itoh, H.; Hattori, T. *J. Phys. Chem. C* **2008**, 112, 5542–5551.
- 16) Kohno, Y.; Tanaka, T.; Funabiki, T.; Yoshida, S. *Phys. Chem. Chem. Phys.* **2000**, 2, 5302–5307.
- 17) Teramura, K.; Tanaka, T.; Ishikawa, H.; Kohno, Y.; Funabiki, T. *J. Phys. Chem. B* **2004**, 108, 346–354.
- 18) Shi, D.; Feng, Y.; Zhong, S. *Catal. Today* **2004**, 98, 505–509.
- 19) Yuliati, L.; Itoh, H.; Yoshida, H. *Chem. Phys. Lett.* **2008**, 452, 178–182.
- 20) Yoshida, H. *Catal. Surv. Asia* **2005**, 9, 1–9, and references herein.
- 21) Yuliati, L.; Tsubota, M.; Satsuma, A.; Itoh, H.; Yoshida, H. *J. Catal.* **2006**, 238, 214–220.
- 22) Yuliati, L.; Itoh, H.; Yoshida, H. *Stud. Surf. Sci. Catal.* **2006**, 162, 961–968.
- 23) Yuliati, L.; Hamajima, T.; Hattori, T.; Yoshida, H. *J. Phys. Chem. C* **2008**, 112, 7223–7232.
- 24) Yuliati, L.; Hattori, T.; Itoh, H.; Yoshida, H. *J. Catal.* **2008**, 257, 396–402.
- 25) Kato, H.; Kudo, A. *Chem. Phys. Lett.* **2000**, 331, 373–377.
- 26) Iwase, A.; Okutomi, H.; Kato, H.; Kudo, A. *Chem. Lett.* **2004**, 10, 1260–1261.
- 27) Nomura, N.; Koyama, A. *KEK Rep. B* **1989**, 89–16, 1–21.
- 28) Nomura, M.; Koike, Y.; Sato, M.; Koyama, A.; Inada, Y.; Asakura, K. *AIP Conf. Proc.* **2007**, 882, 896–898.
- 29) Lytle, F. W.; Greigor, R. B.; Sandstorm, D. R.; Marques, E. C.; Wong, J.; Spiro, C. L.; Huffman, G. P.; Huggins, F. E. *Nucl. Instrum. Methods* **1984**, 226, 542–548.

- 30) Mckale, A. G.; Veal, B. W.; Paulikas, A.P.; Chan, S. K.; Knapp, G. S. *J. Am. Chem. Soc.* **1988**, 110, 3763–3768.
- 31) Sato, S.; White, J. M. *Chem. Phys. Lett.* **1980**, 72, 83–86.
- 32) Yamakata, A.; Ishibashi, T.; Kato, H.; Kudo, A.; Onishi, H. *J. Phys. Chem B* **2003**, 51, 14383–14387.
- 33) Bobrova, I. I.; Chesnokov, V. V.; Bobrov, N. N.; Zaikovskii, V. I.; Parmon, V. N. *Kinet. Catal.* **2000**, 41, 19–24.
- 34) Ramírez-Cabrera E.; Atkinson A.; Chadwick, D. *Appl. Catal. B* **2004**, 47, 127–131.
- 35) Rioux, R. M.; Marsh, A. L.; Gaugha, J. S.; Somorjai, G. A. *Catal. Today* **2007**, 123, 265–275.

Chapter 4

Photocatalytic Steam Reforming of Methane over Gallium Oxide

4.1. Photocatalytic Activation of Water and Methane over Modified Gallium Oxide for Hydrogen Production

Abstract

Ga₂O₃ photocatalysts showed a high and stable activity for the photocatalytic steam reforming of methane (PSRM; $2 \text{ H}_2\text{O (g)} + \text{CH}_4 \rightarrow 4 \text{ H}_2 + \text{CO}_2$) around room temperature. The activity was much influenced by the cocatalyst and the crystal structure of Ga₂O₃; the highest activity was obtained over Pt-loaded beta-type Ga₂O₃ with specific surface area of 10-20 m² g⁻¹. The addition of metal cations into the bulk and/or on the surface of Ga₂O₃ was also effective to improve the photocatalytic activity; metal cations having both a smaller oxidation number than that of Ga³⁺ and a similar ionic radius to that of Ga³⁺, such as Mg²⁺ and Zn²⁺, were effective as the dopant into the bulk of β-Ga₂O₃, while cations of aluminum group such as In³⁺ and Al³⁺ were effective as the surface additives. When we compared the activity for the PSRM with those for the water decomposition (WD; $\text{H}_2\text{O} \rightarrow \text{H}_2 + 1/2 \text{ O}_2$) and the methane decomposition (MD; $\text{CH}_4 \rightarrow x/2 \text{ H}_2 + \text{CH}_{4-x}$), it was revealed that the improvement of the bulk processes would mainly influence the water activation while that of the surface processes would affect the methane activation.

4.1.1. Introduction

Hydrogen as an environmentally benign fuel should be produced from renewable resources and natural energy to realize a sustainable society. Although water decomposition (referred to as WD; $\text{H}_2\text{O} \rightarrow \text{H}_2 + 1/2 \text{ O}_2$, $\Delta G = 237 \text{ kJ mol}^{-1}$) by using solar energy and photocatalyst would be an ideal hydrogen production method,¹⁻³ it is not easy to promote this reaction effectively because of a large and positive value of Gibbs free energy change (ΔG). One possible way to accelerate the formation of hydrogen is employing a sacrificial reagent, which can consume the photogenerated holes or activated oxygen species to reduce their reverse reactions. Sacrificial reagents reported so far were some kinds of carbon-related solid materials such as active carbon,⁴ saccharides (i.e. sugar, starch and cellulose),⁵ coal and tar sand,⁶ and some kinds of compounds such as MeOH,⁷ EtOH,⁸ C₂H₄⁹ and CO.¹⁰ Since some of them such as EtOH, sugar, starch and cellulose could be recognized as renewable resources, it is also worthwhile to develop these photocatalytic systems.

Recently, we reported that hydrogen could be effectively produced from water by using methane as the sacrificial reagent.¹¹⁻¹⁴ In this photocatalytic system, a consumption of two moles of water and only one mole of methane gives four moles of hydrogen as follows:



The reaction shown in equation (1) can be also interpreted as a photocatalytic steam reforming of methane, thus referred to as PSRM.¹¹ Since methane is a main component of biogas as one of the renewable resources, the PSRM can become a desirable hydrogen production method from renewable resources and solar energy. It is expected that the PSRM would produce hydrogen more efficiently than the WD due to the low ΔG value. The PSRM also has an advantage of converting photoenergy into chemical energy.

We first discovered this reaction over the Pt/TiO₂ photocatalyst,^{11, 12} and then we once assumed that water activation would be the most important process to promote the PSRM effectively. Since many active photocatalysts for the WD in UV light region had been already reported by other researchers, such as La-doped NaTaO₃ (NaTaO₃:La),¹⁵ SrTiO₃,¹⁶ CaTiO₃,¹⁷ KTaO₃,¹⁸ and K₄Nb₆O₁₇,¹⁹ we examined these photocatalysts for the PSRM and found that NaTaO₃:La loaded with Pt cocatalyst showed a higher activity than those of Pt/TiO₂^{11, 13} and Pt/CaTiO₃.¹⁴ However, other photocatalysts showed very low activity for the PSRM even when Pt cocatalyst was loaded. These results imply that the photocatalyst for the PSRM must activate both water and methane simultaneously.

In the present study, we examined the photocatalytic activity of gallium oxide for the PSRM around room temperature (ca. 308 K). Ga₂O₃ with NiO cocatalyst was reported to show a high photocatalytic activity for the WD.^{20, 21} Ga₂O₃ photocatalyst was also reported to be active for methane activation in the photocatalytic nonoxidative coupling of methane (referred to as PCM) around room temperature²² and the photocatalytic reduction of carbon dioxide by methane at mild temperature such as 473 K.²³ Thus, it is considered that the Ga₂O₃ photocatalyst can activate both water and methane. Therefore, the Ga₂O₃ photocatalyst is expected to show a high activity for the PSRM. We here examined some kinds of Ga₂O₃ photocatalysts with or without the addition of metal ions and cocatalyst for the PSRM. We also examined to evaluate the activity for the hydrogen production from each reactant, water and methane, and discussed the controlling factors for each activation.

4.1.2. Experimental

4.1.2.1. Preparation of Photocatalysts

Ga₂O₃ samples were commercially obtained or prepared from Ga(NO₃)₃·8H₂O (Kishida, 99.0%). Two Purchased Ga₂O₃ samples from Kojundo (Lot No. 139595 and Lot No. 188962) and one from Soekawa were employed and referred to as Ga₂O₃(K₁), Ga₂O₃(K₂), and Ga₂O₃(S), respectively. BET specific surface areas of them were 4.1, 11.0 and 9.3 m² g⁻¹, respectively. Mean crystallite sizes of them were 45, 27, and 30 nm, respectively. All of them had a beta-type crystal phase and their purity were 99.99%. Other Ga₂O₃ samples with different crystal phase were prepared according to the literature.²⁴ To obtain α-Ga₂O₃, Ga(NO₃)₃·8H₂O (10 g) was dissolved in distilled water (250 ml). Then, 10 vol% ammonia water was added to the solution until no additional precipitation was observed. The suspension was filtered off with suction, washed with distilled water, and dried at 343 K overnight. The obtained powder was calcined in air at 823 K for 6 h. β-Ga₂O₃ was prepared by almost the same procedure as that of α-Ga₂O₃ but the calcination temperature was 973 K. γ-Ga₂O₃ was also prepared by almost the same procedure as that of α-Ga₂O₃ but EtOH was used as the solvent. To prepare δ-Ga₂O₃, Ga(NO₃)₃·8H₂O was calcined in the flow of air at 473 K for 12 h, then calcined at 773 K for 6 h in an oven. X-ray diffraction patterns confirmed that these Ga₂O₃ samples were successfully prepared to be in each desired crystal phase.

The several kinds of metal cations were examined as surface additives or bulk dopants for β-Ga₂O₃. The loading amount (*x*) of these cations was in the range from 0.05 to 2 mol%. The precursors of examined metal ions were as follows; Li₂CO₃ (Wako, 99.0%), Mg(NO₃)₂·6H₂O (Kishida, 99.0%), Ca(NO₃)₂·4H₂O (Kishida, 98.5%), Zn(NO₃)₂·6H₂O (Kishida, 99.0%), Sr(NO₃)₂ (Kishida, 98.0%), Al(NO₃)₃·9H₂O (Kishida, 98.0%), Sc(NO₃)₃·4H₂O (Mitsuwa, 99.9%), Y(NO₃)₃·6H₂O (Kishida, 99.9%), In(NO₃)₃·6H₂O (Kishida, 98.0%), La(NO₃)₃·6H₂O (Aldrich, 99.9%), Ce(NO₃)₃·6H₂O (Kishida, 98.0%), (NH₄)₂[TiO(C₂O₄)₂]*n*H₂O (Kishida, Chemical grade), ZrO(NO₃)₂·2H₂O (Kishida, 99.0%) and NH₄VO₃ (Kishida, 99.0%). The metal cation was added by the following procedures; the purchased β-Ga₂O₃ (2 g) was dispersed into an aqueous solution (50 ml) of the precursor and stirred for 0.5 h, followed by evaporation to dryness with a rotary evaporator. Then, the obtained powder was dried in an oven at 333 K overnight and calcined in air typically at 773 or 1273 K for 6 h. When calcined at 773 K, the metal ions were expected to be deposited as metal oxide particles or dispersed oxide species on the surface of β-Ga₂O₃, thus referred to as MO_{*y*}(*x*)/Ga₂O₃. On the other hand, when calcined at 1273 K, they were expected to form composites with β-Ga₂O₃, thus referred to as Ga₂O₃:M(*x*).

The doped and undoped Ga₂O₃ samples were loaded with metals (Pt, Rh, Au, Pd and Ni) as cocatalyst. The loading amount (*z*) of these metals was in the range from 0.01 to 0.1 wt%. The employed precursors were as follows; Pt(NO₂)₂(NH₃)₂ aqueous solution (Tanaka kikinokoku, 4.533wt% as Pt), Rh(NO₃)₃ aqueous solution (Tanaka kikinokoku, 4.282 wt% as Rh), HAuCl₄ (Kishida, 99%),

PdCl₂ (Kishida, 99%) and Ni(NO₃)₂·6H₂O (Wako, 98%). Metal cocatalysts were loaded by an impregnation method. The Ga₂O₃ sample (2 g) was dispersed into an aqueous solution (50 ml) of the metal precursor and stirred for 0.5 h, followed by evaporation to dryness with a rotary evaporator. Then, the obtained powder was dried in an oven at 333 K overnight. When we used these samples without further pretreatment before the photocatalytic reaction test, the metal precursors adsorbed on Ga₂O₃ should be reduced during the photoirradiation in the flow of water and methane (in-situ photodeposition) as reported in the previous study.¹² An oxidative pretreatment was carried out in air at 773 K for 2 h. A reductive pretreatment was carried out in the flow of hydrogen at 473 K for 0.5 h after the oxidative pretreatment. The sample with the cocatalyst was referred to as Pt(z)/Ga₂O₃ for example. MgO, ZnO, Ga₂O₃, ZnGa₂O₄ and MgGa₂O₄ were used as the reference samples for XAFS analysis. MgO (JRC-MGO-1) was supplied from the Catalyst Society of Japan and it was calcined in air at 773 K for 1 h before the measurement of XAFS. ZnO and Ga₂O₃ were commercially obtained (Kojundo, 99.99%). ZnGa₂O₄ was prepared by a solid-state reaction method. ZnO and Ga₂O₃ were physically mixed by a wet ball-milling method with acetone at room temperature (120 rpm, 24 h) and calcined in air at 1473 K for 20 h. MgGa₂O₄ was prepared by almost the same procedure as that of ZnGa₂O₄ but the calcination temperature was 1573 K. X-ray diffraction revealed that ZnGa₂O₄ and MgGa₂O₄ were obtained although very small diffractions corresponding to β-Ga₂O₃ were also detected in the MgGa₂O₄ sample.

4.1.2.2. Photocatalytic Reaction Tests

The reaction tests were carried out with a fixed-bed flow reactor in the similar way to the previous studies.¹¹⁻¹⁴ The catalysts were granulated to the size of 400-600 μm. The quartz cell (60 × 20 × 1 mm³) was filled with the mixture of the catalyst (0.8 g) and quartz granules (0.7 g). Prior to the photoreaction test, to clean the catalyst surface, the catalyst was photoirradiated by a 300 W xenon lamp in a flow of water vapor (3%) with Ar carrier. Water vapor was introduced by the carrier gas from a bubbling saturator containing distilled water at room temperature. When the reaction was carried out in the flow of methane, the reactor was further heated at 423 K for 1 h in the flow of Ar to remove the adsorbed water before the reaction. Then the reaction gas, a mixture of H₂O vapor and/or CH₄ with Ar carrier, was introduced into the quartz cell at the flow rate of 50 mL min⁻¹ and the reaction was carried out without heating at atmospheric pressure upon photoirradiation with the 300 W xenon lamp. The concentration of water vapor and methane was 1.5% (30 μmol min⁻¹) and 50% (1020 μmol min⁻¹), respectively, and the light of the entire wavelength region from the xenon lamp was irradiated without

passing any filters, where the light intensity measured in the range of 230-280 nm and 310-400 nm were ca. 14 mW cm⁻² and 60 mW cm⁻², respectively. The temperature of the reaction cell increased to ca. 308 K during the photoirradiation. The outlet gas was analyzed by on-line gas chromatography with a thermal conductivity detector. Hydrogen production rates in the flow of water and in the flowing mixture of water and methane shown in each figure and table were taken from the value of the steady state, while that in the flow of methane were the value at five hours after the reaction started.

Apparent quantum yield around 254 nm (Φ) on Pt/Ga₂O₃ was calculated from a result of the reaction experiment by using an optical band-pass filter permitting only the light around 254±20 nm (Ashahi spectra). The incident light intensity measured in the range of 254±20 nm was 7.3 mW cm⁻². The photoirradiated area was limited to 6 cm². The reaction gas was a mixture of H₂O vapor (1.5%) and CH₄ (50%) with Ar carrier. The total flow rate was 50 ml min⁻¹. The Φ was calculated by the following equation: $\Phi(\%) = N_e/N_p \times 100$, where N_e was the number of reacted electrons upon photoirradiation and N_p was the number of incident photons. The number of reacted electrons was determined from the hydrogen production rate, assuming that two electrons produced one hydrogen molecule; $2\text{H}^+ + 2\text{e}^- \rightarrow \text{H}_2$. The number of incident photons was determined from the value measured by a Si photodiode (Topcon UVR-2 with UD-25).

4.1.2.3. Characterizations of Photocatalysts

Powder X-ray diffraction (XRD) pattern was recorded at room temperature on a Rigaku diffractometer RINT 2500 using Ni-filtered Cu K α radiation (50 kV, 100 mA). Mean crystallite size of the β -Ga₂O₃ samples were estimated from the diffraction line at 35.2 degree. Diffuse reflectance (DR) UV-visible spectrum was recorded at room temperature on a JASCO V-570 equipped with an integrating sphere covered with BaSO₄. BaSO₄ was used as the reference. The Brunauer–Emmett–Teller (BET) specific surface area of the sample was calculated from the amount of N₂ adsorption at 77 K, which was measured by a Quantachrome Monosorb. Mg K-edge XANES spectra of Mg-modified Ga₂O₃ samples and reference samples (MgO, MgGa₂O₄ and β -Ga₂O₃) were measured at the BL-1A station of the UVSOR, Institute for Molecular Science, Okazaki, Japan. The spectra were recorded in a total electron yield mode at room temperature with a beryl two-crystal monochromator. The powder sample was put on the first dynode of the electron multiplier with carbon adhesive tape. Zn K-edge XAFS spectra of Zn-modified Ga₂O₃ samples and reference samples (ZnO and ZnGa₂O₄) were recorded at the NW-10A station²⁵ of KEK-PF (Photon Factory, Institute of Materials Structure Science, High Energy Accelerator Research Organization) at room temperature with a Si(311) double crystal monochromator in a

transmission mode. The samples were packed in each polyethylene film cell in air. The spectra were analyzed with a REX 2000 software (Rigaku). Fourier transform of Zn K-edge EXAFS was performed in the range of ca. 3-12 Å⁻¹ after background subtraction. The inverse Fourier transform was carried out in the range of ca. 2.5-3.5 Å. The empirical parameters for Zn-Zn and Zn-Ga shells were extracted from the second coordination peak in the spectra of ZnO and ZnGa₂O₄, respectively, and used for the curve fitting analysis. The ratio of the tetrahedrally coordinated GaO₄ species to the octahedrally coordinated GaO₆ species (T_d/O_h) was obtained from the Ga K-edge XANES analysis of the Ga₂O₃ samples, according to the previous study.²⁶

4.3. Results and Discussion

4.1.3.1. Effect of Metal Cocatalyst on Photocatalytic Activities of Ga₂O₃

Table 1 shows the hydrogen production rate over β-Ga₂O₃ photocatalysts with or without Pt co-catalyst. When β-Ga₂O₃ without metal loading was photoirradiated in the flow of water vapor (Table 1, entry 1b), a small amount of hydrogen was continuously produced by water decomposition (WD; H₂O→H₂+1/2O₂) as reported.²⁰ In the flow of methane (Table 1, entry 1c), hydrogen and ethane were produced constantly, where photocatalytically nonoxidative coupling of methane (PCM; CH₄→H₂+C₂H₆) occurred as reported.²² In the flowing mixture of water vapor and methane (Table 1, entry 1a), the hydrogen production rate was clearly higher than the sum of the values in the flow of each reactant only, i.e. water or methane. Carbon dioxide was also observed under the quantitation limit but oxygen was not observed. These imply that the PSRM (eq. 1) would occur over the β-Ga₂O₃ photocatalyst.

Table 1 Effect of Pt loading and its amount on the hydrogen production rate over the β-Ga₂O₃ photocatalysts in the flow of various reactant

Entry	Pt loading amount / wt%	Hydrogen production rate / μmol min ⁻¹		
		reactant		
		(a) H ₂ O+CH ₄	(b) H ₂ O	(c) CH ₄
1	0.00	0.15	0.02	0.01
2	0.01	0.51	0.15	0.15
3	0.02	0.58	0.08	0.14
4	0.03	0.57	0.05	0.15
5	0.05	0.55	0.02	0.16

The Ga₂O₃(S) sample was used. Pt was loaded by the impregnation method using Pt(NO₂)₂(NH₃)₂, followed by calcination at 773 K.

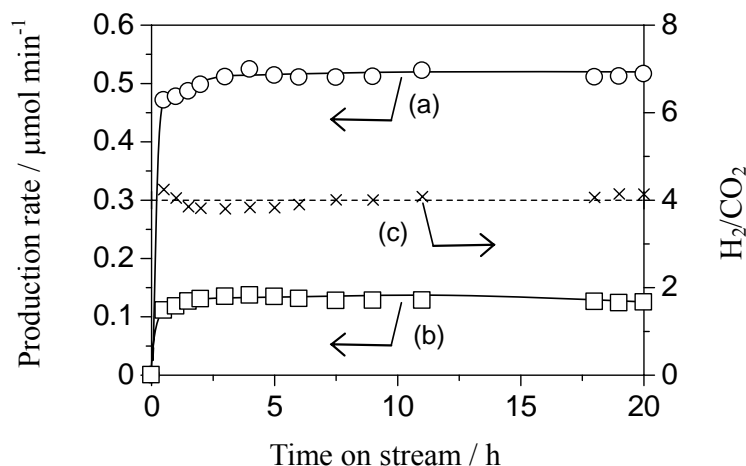


Figure 1. Time course of the production rate of (a) H₂ and (b) CO₂ on the Pt(0.01)/β-Ga₂O₃ sample, and (c) that of molar ratio of the produced H₂ to CO₂ in the flowing mixture of water vapor and methane. The Ga₂O₃(S) sample was used. Pt was loaded by the impregnation method, followed by calcination at 773 K.

Pt-loaded samples prepared by the impregnation method followed by calcination at 773 K exhibited higher hydrogen production rates in each reaction condition than the bare sample did (Table 1, entries 2-5). Figure 1 shows the time course of the production rate of hydrogen and carbon dioxide, as well as the molar ratio of hydrogen to carbon dioxide (H₂/CO₂), over the Pt(0.01)/β-Ga₂O₃ sample in the flowing mixture of water vapor and methane. The induction period was quite short as compared with Pt/TiO₂¹² and Pt/NaTaO₃:La photocatalysts.¹³ The activity was constant at least for 20 h and the molar ratio of hydrogen to carbon dioxide was constant to be four. Production of by-products such as oxygen and carbon monoxide was not observed. These facts show that all of the reacted water and methane molecules would convert into hydrogen and carbon dioxide. In other words, it could be said that hydrogen was equally produced from water and methane. If we assumed that Pt would be the active sites for the hydrogen production via reaction between proton and photoexcited electron ($2\text{H}^+ + 2\text{e}^- \rightarrow \text{H}_2$), the turnover frequency per loaded Pt atom was calculated to be 75 h⁻¹ for Pt(0.01)/β-Ga₂O₃. The reaction did not proceed in the dark or without photocatalyst. These results suggest that the PSRM would proceed photocatalytically over the Pt/β-Ga₂O₃ samples. The apparent quantum yield in the range of 254±20 nm at the light intensity of 7.3 mW cm⁻² was estimated to be 7.9%. The activity of other Pt/β-Ga₂O₃ photocatalysts was also constant for a long time, which was a similar result as shown in Figure 1. The activity of these Pt/β-Ga₂O₃ catalysts without further modification corresponded to about one third activity of Pt/NaTaO₃:La photocatalyst that was the highest activity for this reaction so far. However, since Ga₂O₃ photocatalysts showed high photocatalytic activities for both the WD and the

PCM as well as the PSRM, we can investigate the details of the photocatalyst for the PSRM through the activity tests of the Ga₂O₃ photocatalyst for each reactant.

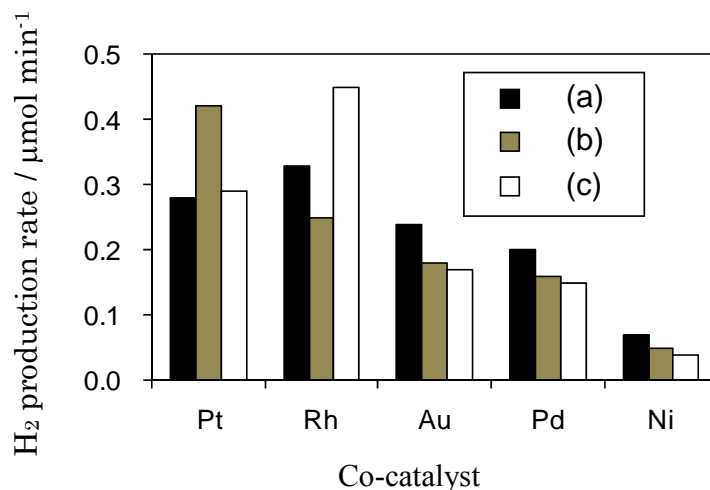


Figure 2. Effect of the loading method on the PSRM activity of the M(0.01)/ β -Ga₂O₃ samples. The metals were loaded by the impregnation method followed by (a) the in-situ photodeposition, (b) calcination at 773 K and (c) calcination at 773 K and successive hydrogen reduction at 473 K. The Ga₂O₃(S) sample was used for Rh, Au and Pd-loaded sample. In Pt and Ni-loaded sample, the Ga₂O₃(K₁) sample was used.

Other metals were also examined as the cocatalyst for the β -Ga₂O₃ photocatalyst. Figure 2 shows the hydrogen production rate in the flowing mixture of water vapor and methane over the M(0.01)/ β -Ga₂O₃ samples prepared by the different method and successive treatment. Among the Pt-loaded samples, the highest activity was obtained over the catalyst prepared by the impregnation method followed by calcination in air. Among the Rh-loaded samples, the catalyst prepared by the impregnation method followed by calcination in air and successive hydrogen reduction showed the highest activity. In the Au, Pd and Ni-loaded samples, the hydrogen production rate became the highest value when the cocatalyst was loaded by the impregnation method and the successive in-situ photodeposition. Among these photocatalysts listed here, the high activity was obtained over the Pt or Rh-loaded photocatalysts. Since these metals had a comparatively large work function, 5.7 and 5.0 eV, respectively,²⁷ the rapid separation of photoexcited electrons and holes could be expected, which would provide the high activity.

To know their activities for each reactant, i.e. water and methane, reaction tests were carried out in the flow of either water or methane. Table 2 shows the hydrogen production rate over the M(0.01)/ β -Ga₂O₃ samples prepared by the most suitable loading method. When any metal cocatalyst was loaded on the β -Ga₂O₃ sample, the hydrogen production rate increased in all kinds of reaction,

except for the Ni-loaded photocatalyst. In Table 2, the order of the activity for the PSRM in the flowing mixture of water and methane (Pt > Rh > Au > Pd > Ni) was similar with that for the WD in the flow of water (Rh > Pt > Pd > Au > Ni) and that for the MD in the flow of methane (Pt > Rh > Pd > Au > Ni). This result shows that these metal cocatalysts could similarly contribute to the activation of both water and methane.

Table 2 Effect of metal co-catalyst on the hydrogen production rate in the flow of various reactant

Photocatalyst	Hydrogen production rate / $\mu\text{mol min}^{-1}$		
	reactant		
	(a) H ₂ O+CH ₄	(b) H ₂ O	(c) CH ₄
Ga ₂ O ₃	0.15	0.02	0.01
Pt(0.01)/Ga ₂ O ₃	0.51	0.15	0.15
Rh(0.01)/Ga ₂ O ₃	0.45	0.17	0.13
Au(0.01)/Ga ₂ O ₃	0.24	0.02	0.02
Pd(0.01)/Ga ₂ O ₃	0.20	0.04	0.04
Ni(0.01)/Ga ₂ O ₃	0.07	0.01	trace

The Ga₂O₃(S) sample was used except for Ni-loaded sample. In Ni-loaded sample, the Ga₂O₃(K₁) was used. Pt was loaded by the impregnation method, followed by calcination at 773 K. Rh was loaded by the impregnation method, followed by calcination at 773 K and the hydrogen reduction at 473 K. Au, Pd and Ni were loaded by the impregnation method and reduced by the in-situ photodeposition.

4.1.3.2. Influence of the Crystal Structure of Ga₂O₃

The activity of the Ga₂O₃ photocatalysts was varied with the crystal structure. Figure 3 shows the time course of the hydrogen production rate over the Pt/Ga₂O₃ samples with different crystal phase. When the reaction was carried out in the flowing mixture of water vapor and methane, the PSRM proceeded and the molar ratio of produced H₂ to CO₂ was almost four at the steady state in all the Ga₂O₃ samples. The hydrogen production rate became constant soon over the Pt/ α -Ga₂O₃ and Pt/ β -Ga₂O₃ samples upon photoirradiation after short induction period (Figures 3a and 3b). On the other hand, the production rate on the Pt/ γ -Ga₂O₃ and Pt/ δ -Ga₂O₃ samples was low soon after the photoirradiation started (Figures 3c and 3d), but gradually increased to become each steady state. Moreover, the color of the Pt/ γ -Ga₂O₃ sample changed to pale brown after the reaction. As reported in the previous study on the Pt/TiO₂ photocatalyst,¹² surface organic intermediates were produced during the PSRM and the moderate accumulation of them could largely increase the activity. This enhancement was also observed over the Pt/NaTaO₃:La photocatalyst.¹³ Therefore, the color change over the Pt/ γ -Ga₂O₃ sample would

be concerned with the formation of the surface reaction intermediates. Since the production rate of the intermediates would be faster than the decomposition rate of them on the surface of the Pt/ γ -Ga₂O₃ sample, the large amount of the reaction intermediates would accumulate on the surface and changed the catalyst color. On the other hand, the induction period of the Pt/ δ -Ga₂O₃ sample was especially long and it continued for more than 10 h (Figure 3d). On the surface of the Pt/ δ -Ga₂O₃ sample, production rate of the intermediates would be almost equal to the decomposition rate of them. Thus, the amount of the surface intermediates very slowly increased as the photoirradiation continued and the catalyst color did not change during the reaction. The different time profile of the four Ga₂O₃ polymorphs may be influenced by the surface structure of each Ga₂O₃ sample.

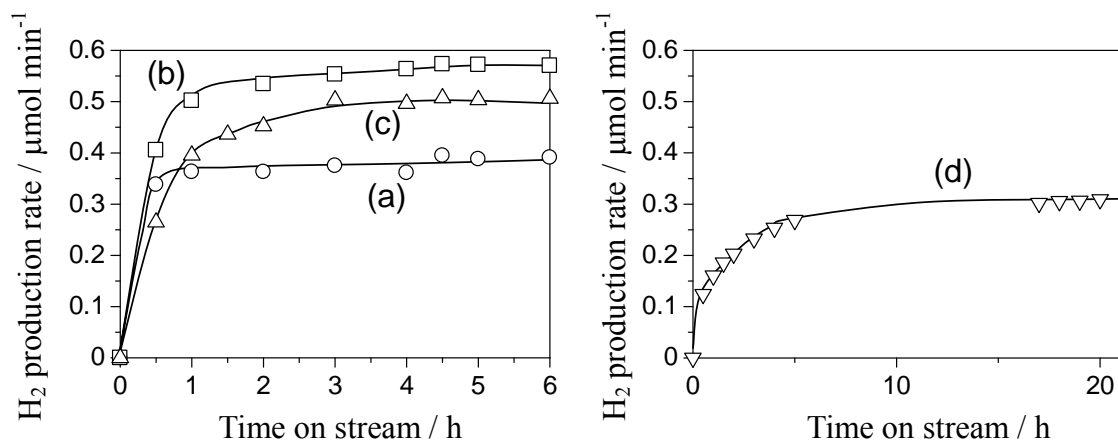


Figure 3. Time course of the hydrogen production rate in the flowing mixture of water vapor and methane over the Pt(0.05)/Ga₂O₃ samples with different crystal structures; (a) α -Ga₂O₃, (b) β -Ga₂O₃, (c) γ -Ga₂O₃ and (d) δ -Ga₂O₃. Pt was loaded by the impregnation method, followed by calcination at 773 K.

Table 3 shows the characterization results and the hydrogen production rate at the steady state over the Pt/Ga₂O₃ samples with the four Ga₂O₃ polymorphs. The loading amount of Pt was 0.05 wt% in all the Ga₂O₃ samples. The order of the production rate at the steady state in the flowing mixture of water vapor and methane was as follows; $\beta > \gamma > \alpha > \delta$. This was not coincident with the orders of the BET specific surface area ($\gamma > \delta > \alpha > \beta$), the band gap energy ($\alpha = \beta > \gamma > \delta$) or the ratio of the tetrahedrally coordinated GaO₄ species to the octahedrally coordinated GaO₆ species ($\beta > \gamma > \delta > \alpha$). Therefore, these factors would not be the determining factor for the activity in the PSRM although each of them would influence the activity for the PSRM to a greater or lesser extent. On the other hand, although the order of the activity for the PSRM in the flow of both water vapor and methane ($\beta > \gamma > \alpha > \delta$) was different from that for the WD in the flow of water vapor ($\alpha > \beta > \gamma = \delta$), it was the same as

that for the MD in the flow of methane ($\beta > \gamma > \alpha > \delta$). This suggests that the activity of these Ga₂O₃ photocatalysts for the PSRM is much influenced by the steps concerning with the methane activation, such as adsorption of methane or activation of the C-H bond on the surface. The variation of the surface structure of Ga₂O₃ originated from the crystal structure would give the various photocatalytic properties for the methane activation and the induction period.

Table 3 Effect of crystal phase on the hydrogen production rate over the Pt(0.05)/Ga₂O₃ photocatalysts in the flow of various reactant

Crystal phase ^a	SA ^b / m ² g ⁻¹	BG ^c / eV	T _d /O _h ^d	Hydrogen production rate / $\mu\text{mol min}^{-1}$		
				reactant		
				(a) H ₂ O+CH ₄	(b) H ₂ O	(c) CH ₄
α	32.6	4.7	0.20	0.39	0.03	0.10
β	18.7	4.7	0.92	0.57	0.02	0.20
γ	109.4	4.4	0.83	0.50	0.01	0.15
δ	80.8	4.3	0.76	0.31	0.01	0.05

^a The Ga₂O₃ samples were prepared from Ga(NO₃)₃·8H₂O. Pt was loaded by the impregnation method, followed by calcination at 773 K. ^b SA; BET specific surface area. ^c BG; Band gap energy. ^d T_d/O_h; Ratio of the tetrahedrally coordinated Ga species to the octahedrally coordinated Ga species, which was obtained from the Ga K-edge XAFS analysis of the Ga₂O₃ samples.

4.1.3.3. Influence of the Surface Area of β -Ga₂O₃

The effect of the specific surface area of the Pt/ β -Ga₂O₃ samples on the activity for each reaction was examined. Four kinds of the β -Ga₂O₃ samples, Ga₂O₃(K₁), Ga₂O₃(S), Ga₂O₃(K₂) and prepared β -Ga₂O₃, were employed. BET specific surface areas of these samples were 4.1, 9.3, 11.0 and 18.7 m² g⁻¹, and the crystallite size were 45, 30, 27 and 25 nm, respectively, as described in the experimental section. When the loading amount of Pt was optimized for the PSRM on each photocatalyst, the optimum amount increased with an increase of the specific surface area (Figure 4a). The hydrogen production rate in the PSRM on the samples of the optimized Pt amount first increased with the increase of the specific surface area until 10 m² g⁻¹ and then became constant with further increase (Figure 4b), which was different from the result of the Pt/TiO₂ photocatalyst that the PSRM activity increased with increasing the specific surface area of the Pt/TiO₂ photocatalyst in the entire range of 50-300 m² g⁻¹.¹² On the other hand, with the increase of the specific surface area the hydrogen production rate in the WD decreased (Figure 4c) and the one in the MD increased (Figure 4d).

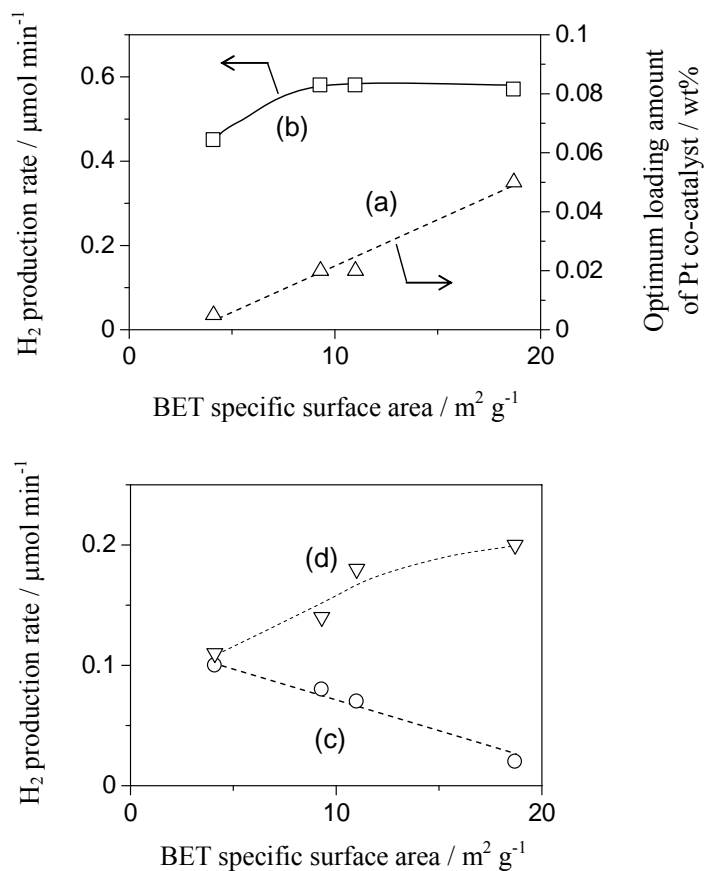


Figure 4. Effect of the BET specific surface area of the β - Ga_2O_3 samples on (a) the optimum loading amount of Pt in the PSRM, and on the hydrogen production rate (b) in the flow of both water vapor and methane (the PSRM), (c) in the flow of water vapor (the WD) and (d) in the flow of methane (the MD). The β - Ga_2O_3 samples were commercially obtained or prepared from $\text{Ga}(\text{NO}_3)_3 \cdot 8\text{H}_2\text{O}$. Pt was loaded by the impregnation method, followed by calcination at 773 K.

Here, to discuss the reaction process we assume that the whole reaction process could be roughly divided into two processes; one was the photo-generation of electrons and holes in the bulk of Ga_2O_3 , followed by the migration of them to the surface, i.e., *the bulk process*, and the other was the reaction between these carriers and the reactants on the surface, i.e., *the surface process*. In the present case, with the increase of the specific surface area, the crystallite size of the photocatalyst was confirmed to decrease. Since the activity for the WD decreased with the decrease of the crystallite size of the photocatalyst, it was considered that the reaction rate for the water activation would be mainly determined by the bulk process. The decrease of the crystallite size would cause the increase of defect structures such as the grain boundary and promote the recombination of photoexcited carriers. On the other hand, two possible reasons are suggested for increasing the activity for the MD with the increase of BET specific surface area. One is that the adsorption and reaction sites of each reactant would

increase with the increase of the surface. The other is that migration length of photogenerated carriers to the surface would decrease, which may be effective for the smooth migration of photoproduced carriers. However, from the result of the WD (Figure 4c), the latter possibility could not be considered. Therefore, it is reasonable that the activity for the MD would be determined by the surface process. In the case of the PSRM, since the activation of both water and methane would be necessary, there would be the optimum value of the specific surface area. In the present case, it would be around 10-20 m² g⁻¹ (Figure 4b).

4.1.3.4. Doping Effect of Metal Ion

The addition of metal ions was examined to increase the activity of the Pt/ β -Ga₂O₃ photocatalysts. Doping metal ions into the bulk of β -Ga₂O₃ was carried out by the impregnation method, followed by calcination at 1273 K (Ga₂O₃:M), where the doping amount was 2 mol%. Then, Pt cocatalyst (0.01 wt%) was loaded on the doped sample. Figure 5 shows their activities for the PSRM, which were plotted against the ionic radius of the metal ions. The activity for the PSRM increased when Mg²⁺, Zn²⁺ or Li⁺ was added. These metal ions had a similar ionic radius with that of Ga³⁺ (0.62 Å). Among the metal ions having a similar ionic radius from Al³⁺ to Li⁺ (0.54-0.76 Å), the addition of Al³⁺, Ti⁴⁺, Zr⁴⁺ or Sc³⁺ decreased the photocatalytic activity, while that of Mg²⁺, Zn²⁺ or Li⁺ increased the activity. This result indicates that the metal ion having a smaller oxidation number than that of Ga³⁺ would be effective in increasing the activity for the PSRM. When the effect of doping amount was also examined in the range of 0.1-2 mol% for the Mg-doped catalyst, the highest activity was obtained over the 1 mol% doped catalyst (Figure 5, closed symbol), which showed 1.4 times higher activity than that of the undoped Pt/ β -Ga₂O₃ (bare sample). Therefore, it is concluded that the activity for the PSRM can be increased by doping suitable amount of metal ions having a smaller oxidation number than that of Ga³⁺ and a similar ionic radius to that of Ga³⁺. The radius of the metal ions introduced in the bulk would influence the crystal structure of β -Ga₂O₃. Metal ions having a similar ionic radius with that of Ga³⁺ are expected not to distort the crystal structure when they substitute for Ga³⁺ and not to give a negative effect for the activity. On the other hand, the oxidation number of the dopant cation would influence the electron density in the crystal, which might increase the photocatalytic activity. Influence of the oxidation number of the dopant on photocatalysis has been investigated by many researchers. In the WD using Pt/TiO₂²⁸ and NiO/NaTaO₃,^{29, 30} metal ions with a larger oxidation number than that of the substituted element were effective as the dopant. In the WD using NiO/KTaO₃,¹⁸ RuO₂/GaN,³¹ and Rh-Cr/SrTiO₃,³² metal ions with a smaller oxidation number than that of the substituted element were effective. In the WD using Ni/ β -Ga₂O₃,²¹ only Zn-doped catalyst showed extremely high activity and

the oxidation number of dopant cation was not correlated with the activity. And, in the present study, in the PSRM using Pt/Ga₂O₃, metal ions with a smaller oxidation number were effective as the dopant. These facts suggest that the optimum oxidation number of the dopant would be determined by not only the kind of the semiconductor but also the kinds of the cocatalyst and the reaction.

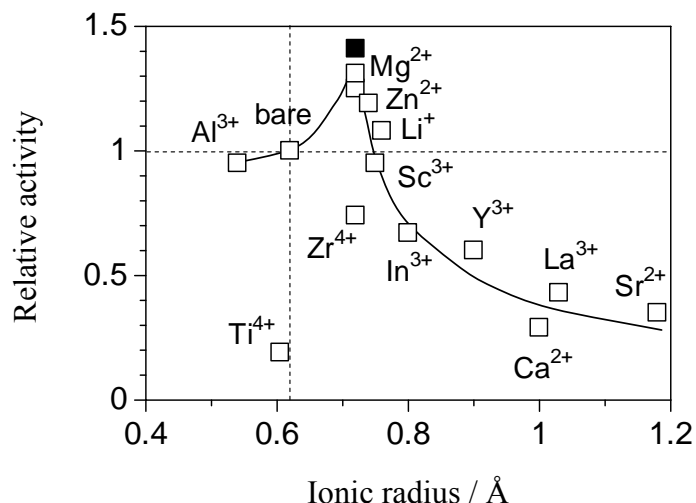


Figure 5. Relative activity of the Pt(0.01)/β-Ga₂O₃:M(2) and Pt(0.01)/β-Ga₂O₃:Mg(1) samples to the Pt(0.01)/β-Ga₂O₃ sample for the PSRM plotted vs. ionic radius of each doping metal ion (M). Filled square shows the value of the Pt(0.01)/β-Ga₂O₃:Mg(1) sample. The Ga₂O₃(S) and Ga₂O₃(K₁) samples were used. Pt was loaded by the impregnation method, followed by calcination at 773 K.

When the several kinds of the doped samples were characterized by DR UV-vis, XRD and N₂ adsorption, no clear differences were observed between the doped and undoped β-Ga₂O₃ samples, which was probably due to the low doping amount. However, clear differences were observed by XAFS analysis. The state of Mg²⁺ and Zn²⁺, both of which enhanced the activity of β-Ga₂O₃ for the PSRM, were investigated with XAFS. Figure 6 shows the X-ray absorption spectra of the Mg-loaded β-Ga₂O₃ samples and the reference samples. The MgO sample showed a Mg K-edge XANES and the β-Ga₂O₃ sample showed a Ga L₁-edge XANES (Figures 6a and 6f), since Mg K-edge and Ga L₁-edge are at 1303 and 1301 eV, respectively. Mg K-edge XANES spectrum of the MgO sample showed some peaks at 1304, 1310 and 1322 eV and Ga L₁-edge XANES of the Ga₂O₃ sample was a broad spectrum around 1306 eV. In the spectrum of the MgGa₂O₄ sample (Figure 6e), the absorptions of both Mg K-edge and Ga L₁-edge should be overlapped. The spectra of the Mg²⁺-loaded Ga₂O₃ samples calcined at various temperatures were much different from each other (Figures 6b-6d). For the sample calcined at 773 K (Figure 6b), the spectrum was similar to that of the MgO sample (Figure 6a). When the sample was calcined at 1073 and 1273 K (Figures 6c and 6d), the spectra were the same as that of the MgGa₂O₄ spinel (Figure 6e). It is suggested that the Mg ions would form a MgGa₂O₄ spinel-like local structure by

substituting for the Ga ions at the tetrahedral site when calcined at 1073 K and higher temperatures. The same tendency was also observed over Zn K-edge XANES spectra of the Zn-loaded β -Ga₂O₃ samples, as shown in Figure 7. The spectrum of the sample calcined at 773 K (Figure 7b) was almost the same as that of the ZnO sample (Figure 7a). When the calcination temperature increased to 1073 K and higher temperatures (Figures 7c-7e), the spectrum became almost the same as that of the ZnGa₂O₄ spinel (Figure 7f). These results suggest that the metal ions would exist in the metal oxide particles on the surface of the Ga₂O₃ when the calcination temperature was 773 K, while the sample calcined at 1073 K and higher temperatures, it would have a local structure like the spinel as the result of solid-solid reaction with the Ga₂O₃. As is the case of the Mg ions mentioned above, the Zn ions would also substitute for the tetrahedrally coordinated Ga site in the bulk of β -Ga₂O₃.

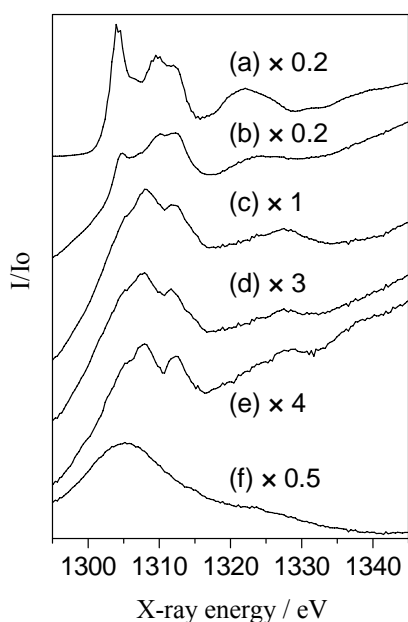


Figure 6. X-ray absorption spectra of (a) MgO, (b)-(d) the Mg(2 mol%)-loaded β -Ga₂O₃ samples, (e) MgGa₂O₄ and (f) β -Ga₂O₃. The calcination temperature was (b) 773 K, (c) 1073 K and (d) 1273 K.

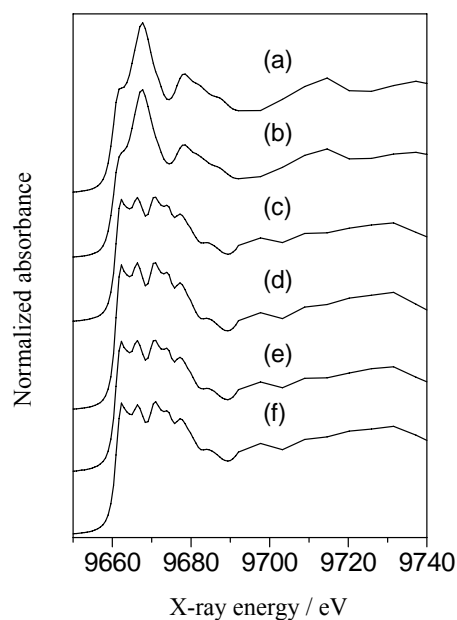


Figure 7. Zn K-edge XANES spectra of (a) ZnO, (b)-(e) the Zn(2 mol%)-loaded β -Ga₂O₃ samples and (f) ZnGa₂O₄. The calcination temperature was (b) 773 K, (c) 1073 K, (d) 1273 K and (e) 1473 K.

The local structure of the Zn ions added to the β -Ga₂O₃ was further examined with EXAFS in detail. Figure 8 shows the Fourier transforms of Zn K-edge EXAFS spectra for the Zn-loaded β -Ga₂O₃ samples and the reference samples. The analysis of the first coordination peak around 1.2-1.9 Å, which would correspond to the Zn-O shell, would be difficult to clarify the details for substitution, since the atomic distance between Zn and O in the ZnO (1.98 Å) and ZnGa₂O₄ (1.98 Å) samples and that between Ga and O in the β -Ga₂O₃ sample (1.8-2.0 Å) were very close to each other. On the other hand, the

second coordination sphere around 2.5-3.5 Å, which would correspond to the Zn-metal shell, provided clear evidences through the curve fitting analysis with the empirical parameters extracted from the second coordination peak for the Zn-Zn and Zn-Ga shells in the spectra of the ZnO and ZnGa₂O₄ samples, respectively, as shown in Table 4. The second coordination peak for the Zn-loaded β-Ga₂O₃ calcined at 773 K was only composed of the Zn-Zn shell and the length was almost the same as that of the Zn-Zn shell in the ZnO sample (3.22 Å). On the other hand, for the sample calcined at 1073 K and higher temperatures, it was only composed of the Zn-Ga shell and the length was the same as that of the Zn-Ga shell in the ZnGa₂O₄ sample (3.46 Å). It is concluded that the Zn ions would be existed on the surface as metal oxide without mixing with the Ga₂O₃ when calcined at 773 K, and when calcined at 1073 K and higher temperatures, they would react with the Ga₂O₃ to form the spinel ZnGa₂O₄ partially or substitute Ga ion in the β-Ga₂O₃ having a spinel-like local structure. The small amounts of composites in semiconductor photocatalysts might show a positive effect for the activity. For example, in the famous TiO₂ sample, P-25 (Degussa) is composed of anatase TiO₂ (major, band gap: 3.2 eV) and rutile TiO₂ (minor, band gap: 3.0 eV), and it was proposed that the existence of small amounts of rutile TiO₂ would promote the separation of photoexcited carriers and increase the photocatalytic activity.^{33,34} The same phenomenon might be seen in the present case, since the band gap of ZnGa₂O₄ (4.3 eV)³⁵ and MgGa₂O₄ (4.55 eV)³⁶ was a little smaller than that of β-Ga₂O₃ (4.7 eV). The influence of the dopant on the electron density would be still another possibility as mentioned above.

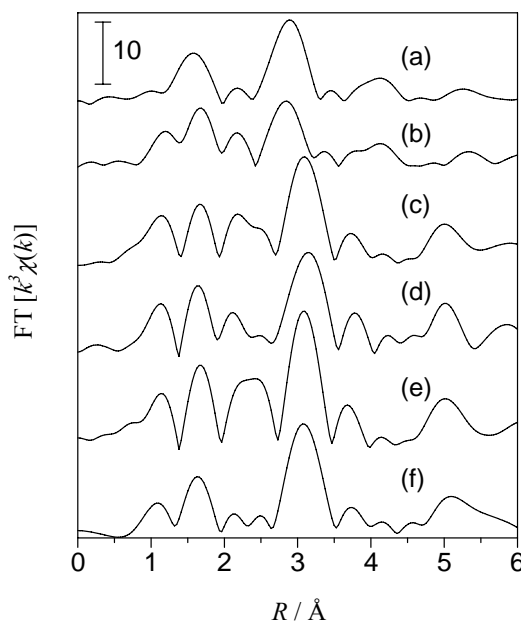


Figure 8. Zn K-edge XANES spectra of (a) ZnO, (b)-(e) the Zn(2 mol%)-loaded β-Ga₂O₃ samples and (f) ZnGa₂O₄. The calcination temperature was (b) 773 K, (c) 1073 K, (d) 1273 K and (e) 1473 K.

Table 4 Fitting analysis for the second coordination peak of Zn K-edge EXAFS spectra

Sample	Calcination temperature / K	Zn-Zn		Zn-Ga		Debye-waller factor ($\Delta\sigma$)
		N^a	$R^b / \text{\AA}$	N^a	$R^b / \text{\AA}$	
ZnO ^c	-	12.0	3.22	-	-	0.060
ZnGa ₂ O ₄ ^d	-	-	-	12.0	3.46	0.060
Zn-loaded Ga ₂ O ₃ ^e	773	7.7	3.20	0.0	-	0.050
Zn-loaded Ga ₂ O ₃ ^e	1073	0.0	-	10.8	3.47	0.055
Zn-loaded Ga ₂ O ₃ ^e	1273	0.0	-	13.6	3.48	0.067
Zn-loaded Ga ₂ O ₃ ^e	1473	0.0	-	11.3	3.47	0.047

^a Coordination number. ^b Atomic distance. ^c The empirical parameter for the Zn-Zn shell was extracted from the second coordination peak in the spectrum of the ZnO sample. ^d The empirical parameter for the Zn-Ga shell was extracted from the second coordination peak in the spectrum of the ZnGa₂O₄ sample. ^e The Ga₂O₃(K₁) sample was used. Loading amount of Zn was 2 mol%. Zn ion was loaded by the impregnation method, followed by calcination at various temperatures for 6 h.

Table 5 Effect of the reaction gas on the hydrogen production rate over the Pt(0.01)/ β -Ga₂O₃:M photocatalysts in the flow of various reactant

Metal ion	H ₂ production rate / $\mu\text{mol min}^{-1}$		
	reactant		
	(a) H ₂ O+ CH ₄	(b) H ₂ O	(c) CH ₄
Mg 1mo%	0.72	0.30	0.13
Al 1mol%	0.63	0.17	0.14
bare	0.51	0.15	0.15
In 2mol%	0.33	0.04	0.05
Sr 2 mol%	0.18	0.11	0.02

The Ga₂O₃(S) sample was used. Pt was loaded by the impregnation method, followed by calcination at 773 K.

The activities for the WD and the MD were examined for some of the Pt(0.01)/ β -Ga₂O₃:M samples in the flow of each reactant. Results are shown in Table 5. The hydrogen production rate in the WD increased in the sample doped with Mg²⁺ (1 mol%) or Al³⁺ (1 mol%) but it decreased in the sample doped with In³⁺ (2 mol%) or Sr²⁺ (2 mol%), which was the same tendency as the activity for the PSRM. On the other hand, the hydrogen production rate in the MD did not increase in all samples. These results show that metal ions doped into the bulk of the β -Ga₂O₃ would contribute to the improvement of water activation.

4.1.3.5. Loading Effect of Metal Ion

Loading metal oxide particles on the surface of the β -Ga₂O₃ was carried out by the impregnation method, followed by calcination at 773 K. In this case, the optimum loading amount for the improvement of the photocatalytic activity was found typically to be around 0.1 mol%. The activities of the Pt(0.01)/ β -Ga₂O₃ samples loaded with 0.1 mol% of metal ions, Pt(0.01 wt%)/MO_x(0.1)/Ga₂O₃, are shown in Figure 9. It is difficult to find clear correlation between the activity and the ionic radius or the oxidation number of metal ions, which was different from the result shown in Figure 5. In other words, the activity of the catalyst calcined at 773 K showed a different tendency from that of the catalyst calcined at 1273 K. This seems reasonable because the state of metal ions would be different between these two series of samples. The addition of Al³⁺, Zr⁴⁺, Mg²⁺, Zn²⁺ or In³⁺ increased the photocatalytic activity. These ions would exist as metal oxide particles on the β -Ga₂O₃ surface as analogically suggested from the XAFS analyses on the Mg²⁺ and Zn²⁺-loaded samples. The highest activity was obtained over In₂O₃ loaded catalyst, Pt(0.01)/In₂O₃(0.1)/ β -Ga₂O₃, which showed 1.3 times higher activity than the Pt(0.01)/ β -Ga₂O₃ sample without the addition of metal ions. It could be said that a high activity was obtained when the homologous element of Ga such as In³⁺ and Al³⁺ was added. Although the reason for this result has not been clarified, one possibility is that homologous elements of Ga may be easily dispersed on the surface of the β -Ga₂O₃ and form a kind of the active sites to increase the activity. On the other hand, the addition of metal ions that may be easily reduced in the presence of methane upon photoirradiation, such as V⁵⁺, Ti⁴⁺ and Ce⁴⁺, largely decreased the photocatalytic activity. Therefore, it was suggested that metal ions without changing their oxidation number would be effective as the surface additives.

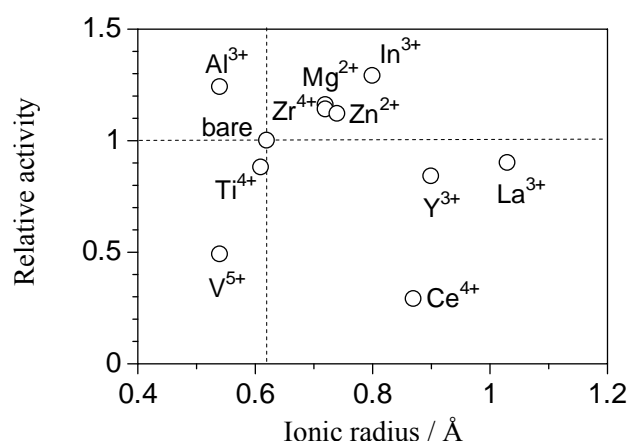


Figure 9. Relative activity of the Pt(0.01)/MO_x(0.1)/ β -Ga₂O₃ samples to the Pt(0.01)/ β -Ga₂O₃ sample for the PSRM plotted vs. ionic radius of each doping metal ion (M). The Ga₂O₃(S) sample was used. Pt was loaded by the impregnation method, followed by calcination at 773 K.

The activities for the WD and the MD were examined for some of the Pt(0.01)/MO_x/β-Ga₂O₃ samples in the flow of each reactant. Results are shown in Table 6. The activity for the WD did not increase in all samples. However, the order of the activity for the MD was the same as that of the activity for the PSRM. These suggest that the metal ions existed on the surface of the β-Ga₂O₃ would contribute to the enhancement of the methane activation. Results of Tables 5 and 6 support our hypotheses mentioned above that the bulk property of the photocatalyst would mainly influence the water activation while the surface property of the photocatalyst would mainly influence the methane activation.

Table 6 Effect of the reaction gas on the hydrogen production rate over the Pt(0.01)/MO_x(0.1)/β-Ga₂O₃ photocatalysts in the flow of various reactant

Metal ion	H ₂ production rate / μmol min ⁻¹		
	reactant		
	(a) H ₂ O+ CH ₄	(b) H ₂ O	(c) CH ₄
In	0.66	0.12	0.17
Al	0.63	0.14	0.16
bare	0.51	0.15	0.15
Y	0.43	0.15	0.14
V	0.25	0.12	0.02

The Ga₂O₃(S) sample was used. Pt was loaded by the impregnation method, followed by calcination at 773 K.

Since the different effects were obtained by the addition of metal ions on the surface and the doping of them into the bulk of β-Ga₂O₃, both modifications were examined at the same time. Mg ion (1 mol%) was added on β-Ga₂O₃, followed by calcination at 1273 K to obtain the doped β-Ga₂O₃:Mg(1) sample. Then, In ion (0.05 mol%) was mounted on the Mg-doped sample, followed by calcination at 773 K to obtain the In₂O₃(0.05)/β-Ga₂O₃:Mg(1) sample. Finally, Pt was deposited on the sample. The photocatalytic activity of this sample was compared with the Pt(0.01)/β-Ga₂O₃, Pt(0.01)/β-Ga₂O₃:Mg(1) and Pt(0.01)/In₂O₃(0.05)/β-Ga₂O₃ samples, as shown in Table 7. As mentioned above, the Pt/β-Ga₂O₃:Mg sample showed 1.3 times higher activity than the Pt/β-Ga₂O₃ sample did (Table 7, entry 2). The activity of the Pt/In₂O₃/β-Ga₂O₃ sample was also 1.2 times higher than that of the Pt/β-Ga₂O₃ sample (Table 7, entry 3). It was found that the activity of the Pt/In₂O₃/β-Ga₂O₃:Mg sample was 1.6 times higher than that of the Pt/β-Ga₂O₃ sample (Table 7, entry 4). The activity of this doubly modified Pt/β-Ga₂O₃ catalyst was also in good agreement with the expected activity based on the assumption that

both Mg^{2+} doping and In_2O_3 loading would enhance the activity independently at the same time ($1.2 \times 1.3 = 1.6$). These results suggest that the each modification would improve the bulk property and the surface property, respectively, and each of which would enhance the activation of water and methane, respectively.

Table 7 Effect of the Mg doping and the In_2O_3 addition on the hydrogen production rate in the PSRM over the $\text{Pt}(0.01)/\beta\text{-Ga}_2\text{O}_3$ photocatalyst

Entry	Photocatalyst	H_2 production rate / $\mu\text{mol min}^{-1}$
1	$\text{Pt}/\beta\text{-Ga}_2\text{O}_3$	0.41
2	$\text{Pt}/\beta\text{-Ga}_2\text{O}_3:\text{Mg}(1)$	0.55
3	$\text{Pt}/\text{In}_2\text{O}_3(0.05)/\beta\text{-Ga}_2\text{O}_3$	0.48
4	$\text{Pt}/\text{In}_2\text{O}_3(0.05)/\beta\text{-Ga}_2\text{O}_3:\text{Mg}(1)$	0.65

The $\text{Ga}_2\text{O}_3(\text{K}_1)$ sample was used. Pt was loaded by the impregnation method, followed by calcination at 773 K.

4.1.4. Conclusions

Photocatalytic steam reforming of methane proceeded over Ga_2O_3 around room temperature (ca. 308 K). The activity was largely influenced by the crystal structure and surface area of the Ga_2O_3 samples as well as cocatalyst. In the present study, the Pt-loaded $\beta\text{-Ga}_2\text{O}_3$ photocatalyst with specific surface area of $10\text{-}20 \text{ m}^2 \text{ g}^{-1}$ was effective for the PSRM without deactivation for a long time.

The $\beta\text{-Ga}_2\text{O}_3$ sample with a large surface area was effective for the methane activation, while the one with a small surface area was effective for the water activation. In other words, the rate for methane activation would be mainly determined by the surface process such as surface reaction or adsorption/desorption, while that for the water activation would be influenced by the bulk process such as migration of carriers or their recombination probability. The metal cocatalyst influenced the activation of both water and methane, because metal cocatalyst would not only promote the separation of electrons and holes to reduce their recombination but also work as the reaction site on the surface.

The activity of the $\text{Pt}/\beta\text{-Ga}_2\text{O}_3$ sample was further enhanced by the addition of metal ions into the bulk and on the surface. As the dopant into the bulk of $\beta\text{-Ga}_2\text{O}_3$, the metal ions with smaller oxidation number having similar ionic radius with that of Ga^{3+} , such as Mg^{2+} and Zn^{2+} , were effective. On the other hand, the homologous elements of Ga^{3+} , such as In^{3+} and Al^{3+} , were most effective as the surface additives. These two kinds of modification could independently improve the activation of water and methane, respectively, at the same time. These factor confirmed that the bulk property of Ga_2O_3

would mainly influence the water activation, while the surface property affected the methane activation, respectively.

References

- 1) Maeda, K.; Domen, K. *J. Phys. Chem. C* **2007**, 111, 7851–7861.
- 2) Kudo, A.; Miseki, Y. *Chem. Soc. Rev.* **2009**, 38, 253–278.
- 3) Inoue, Y. *Energy Environ. Sci.* **2009**, 2, 364–386.
- 4) Sakata, T.; Kawai, T. *Nature* **1979**, 282, 283–284.
- 5) Kawai, T.; Sakata, T. *Nature* **1980**, 286, 474–476.
- 6) Hashimoto, K.; Kawai, T.; Sakata, T. *J. Phys. Chem.* **1984**, 88, 4083–4088.
- 7) Kawai, T.; Sakata, T. *J. Chem. Soc., Chem. Comm.* **1980**, 15, 694–695.
- 8) Sakata, T.; Kawai, T. *Chem. Phys. Lett.* **1981**, 80, 341–344.
- 9) Sato, S.; White, J.M. *Chem. Phys. Lett.* **1980**, 70, 131–134.
- 10) Sato, S.; White, J.M. *J. Am. Chem. Soc.* **1980**, 102, 7206–7210.
- 11) Yoshida, H.; Kato, S.; Hirao, K.; Nishimoto, J.; Hattori, T. *Chem. Lett.* **2007**, 36, 430–431.
- 12) Yoshida, H.; Hirao, K.; Nishimoto, J.; Shimura, K.; Kato, S.; Itoh, H.; Hattori, T. *J. Phys. Chem. C* **2008**, 112, 5542–5551.
- 13) Shimura, K.; Kato, S.; Yoshida, T.; Itoh, H.; Hattori, T.; Yoshida, H. *J. Phys. Chem. C* **2010**, 114, 3493–3503.
- 14) Shimura, K.; Yoshida, H. *Energy Environ. Sci.* **2010**, 3, 615–617.
- 15) Kato, H.; Asakura, K.; Kudo, A. *J. Am. Chem. Soc.* **2003**, 125, 3082–3089.
- 16) Domen, K.; Naito, S.; Soma, M.; Ohnishi, T.; Tamaru, K. *J. Chem. Soc., Chem. Commun.* **1980**, 12, 543–544.
- 17) Mizoguchi, H.; Ueda, K.; Orita, M.; Moon, S-C.; Kajihara, K.; Hirano, M.; Hosono, H. *Mater. Res. Bull.* **2002**, 37, 2401–2406.
- 18) Ishihara, T.; Nishiguchi, H.; Fukamachi, K.; Takita, Y.; *J. Phys. Chem. B* **1999**, 103, 1–3.
- 19) Kudo, A.; Sayama, K.; Tanaka, A.; Asakura, K.; Domen, K.; Muruya, K.; Onishi, T. *J. Catal.* **1989**, 94, 89–94.
- 20) Yanagida, T.; Sakata, Y.; Imamura, H. *Chem. Lett.* **2004**, 33, 726–727.
- 21) Sakata, Y.; Matsuda, Y.; Yanagida, T.; Hirata, K.; Imamura, H.; Teramura, K. *Catal. Lett.* **2008**, 125, 22–26.
- 22) Yuliati, L.; Hattori, T.; Itoh, H.; Yoshida, H. *J. Catal.* **2008**, 257, 396–402.
- 23) Yuliati, L.; Itoh, H.; Yoshida, H. *Chem. Phys. Lett.* **2008**, 452, 178–182.
- 24) Zheng, B.; Hua, W.; Yue, Y.; Gao, Z. *J. Catal.* **2005**, 232, 143–151.
- 25) Nomura, M.; Koike, Y.; Sato, M.; Koyama, A.; Inada, Y.; Asakura, K. *AIP Conf. Proc.* **2007**, 882, 896.
- 26) Nishi, K.; Shimizu, K.; Takamatsu, M.; Yoshida, H.; Satsuma, A.; Tanaka, T.; Yoshida, S.; Hattori, T. *J.*

- Phys. Chem. B* **1998**, 102, 10190–10195.
- 27) Michaelson, H. B. *J. Appl. Phys.* **1977**, 48, 4729–4733.
- 28) Karakitsou, K.E.; Verykios X. E. *J. Phys. Chem.* **1993**, 97, 1184–1189.
- 29) Kato, H.; Kudo, A. *Chem. Phys. Lett.* **2000**, 331, 373–377.
- 30) Iwase, A.; Okutomi, H.; Kato, H.; Kudo, A. *Chem. Lett.* **2004**, 10, 1260–1261.
- 31) Arai, N.; Saito, N.; Nishiyama, H; Inoue, Y.; Domen, K.; Sato, K. *Chem. Lett.* **2006**, 35, 796–797.
- 32) Takata, T.; Domen K. *J. Phys. Chem. C* **2009**, 113, 19386–19388.
- 33) Ohno, T.; Sarukawa, K.; Tokieda K.; Matsumura. M. *J. Catal.* **2001**, 203, 82–86.
- 34) Hurum, D. C.; Agrios, A. G; Gray K. A.; Rajh, T.; Thurnauer, C. *J. Phys. Chem. B* **2003**, 107, 4545–4549.
- 35) Ikarashi, K.; Sato, J.; Kobayashi, H.; Saito, N.; Nishiyama, H.; Inoue Y. *J. Phys. Chem. B* **2002**, 106, 9048–9053.
- 36) Moriga, T.; Sakamoto, T.; Sato, Y.; Khalid, A. H.; Suenari, R.; Nakabayashi, I. *J. Solid State Chem.* **1999**, 142, 206–213.

4.2. Thermal Acceleration of Electron Migration in Gallium Oxide Photocatalysts

Abstract

In the photocatalytic steam reforming of methane ($\text{CH}_4 + 2\text{H}_2\text{O} \rightarrow 4\text{H}_2 + \text{CO}_2$) over gallium oxide ($\beta\text{-Ga}_2\text{O}_3$), hydrogen production rate increased with an increase of the reaction temperature before reaching ca. 343 K, and then it became constant. Arrhenius plot for the production rate in the lower temperature range showed a straight line and the thermal activation energy was typically less than ca. 10 kJ mol^{-1} . The thermal activation energy was varied with the irradiation light intensity, the crystallite size of Ga_2O_3 and the loading of metal cocatalyst. Lower thermal activation energy was given by higher intensity of the irradiation light, larger crystallite size of Ga_2O_3 particles and larger particle size of cocatalyst, while higher one was given by the surface defects and/or the alloyed cocatalyst. These facts suggest that the thermal energy would promote the migration of photoexcited carriers both in the bulk of Ga_2O_3 and at the metal-semiconductor junction between the metal cocatalyst and Ga_2O_3 .

4.2.1. Introduction

Photocatalytic reaction using solar energy attracts much attention as one of the methods for solving the environmental and energy problems. For the development of highly efficient photocatalytic system, it is very important to understand the reaction mechanism of photocatalysis. Usually the reaction rate for the photocatalytic reaction is expected to be independent on the reaction temperature because the photoexcited electrons and holes would work as the active species for the reaction ideally without any additional activation energy. However, thermal acceleration of the photocatalytic reaction rate has been reported by many researchers so far. For example, there are many reports in the field of oxidative degradation of organic compounds such as formic acid,¹ 2-propanol,² phenol,³ methyl orange,⁴ and acetone⁵ over TiO_2 photocatalyst. It was also reported for the dehydrogenation of various alcohols over a Pt/TiO_2 photocatalyst,⁶ the hydrogen production from aqueous methanol solution over a Rh/TiO_2 photocatalyst⁷ and the water splitting over $\text{Pt-RuO}_2/\text{TiO}_2$ photocatalyst.⁸ The thermal acceleration was also observed over photocatalysts other than TiO_2 , such as Pt/SrTiO_3 photocatalyst⁹ for hydrogen production from aqueous methanol solution and $\text{Rh}_{2-y}\text{Cr}_y\text{O}_3$ -loaded $(\text{Ga}_{1-x}\text{Zn}_x)(\text{N}_{1-x}\text{O}_x)$ ¹⁰ and $\text{Rh}_{2-y}\text{Cr}_y\text{O}_3$ -loaded $\text{Ga}_2\text{O}_3:\text{Zn}$ photocatalysts¹¹ for water splitting. We also found that the reaction rate over $\beta\text{-Ga}_2\text{O}_3$ for photocatalytic reduction of carbon dioxide by methane was promoted by the assist of thermal

energy.¹² Thermal activation energies of these photocatalytic reactions were typically small values less than 30 kJ mol⁻¹. This suggests that the thermal energy would contribute to the mild activation steps such as desorption of products, or migration of photoexcited electrons and holes. However, there are few reports to clarify the mechanism of thermal activation in these photocatalytic reactions.

Recently, our research group found that some kinds of Pt-loaded semiconductors such as TiO₂,^{13, 14} NaTaO₃:La,^{13, 15} Ga₂O₃¹⁶ and CaTiO₃,^{17, 18} promoted photocatalytic steam reforming of methane (PSRM; CH₄ + 2H₂O → 4H₂ + CO₂) around room temperature. This reaction is attractive since it has a potential to convert solar energy into chemical potential of the storable hydrogen by using methane which is a renewable resource. We found that the reaction rate in the PSRM also increased with an increase of the reaction temperature.¹⁵ In the present study, we examined the contribution of the thermal energy on the activity of β-Ga₂O₃ for the PSRM in detail, and successfully found that the thermal energy contributed to the acceleration of the electron migration both in the bulk of Ga₂O₃ and at the metal-semiconductor junction on the metal-loaded Ga₂O₃ photocatalyst.

4.2.2. Experimental

4.2.2.1. Preparation of Photocatalysts

β-Ga₂O₃ samples were commercially obtained (Kojundo, 99.99%, 11.7 m² g⁻¹) or prepared by homogeneous precipitation method.¹⁹ They are referred to as Ga₂O₃(K) and Ga₂O₃(HP), respectively. In the homogeneous precipitation method, Ga(NO₃)₃·xH₂O (4.0 g, Kojundo, 99.999%) and urea (6.0 g, Kishida, 99.0%) were dissolved in distilled water (400 ml), followed by heating at 357 K until pH of the solution reached to 6 (it took about 4 h), where white precipitate was gradually obtained as hydrolysis of the urea proceeded. The suspension was filtered off with suction, washed with distilled water, and dried at 353 K in an oven. Then, the obtained powders were calcined in air at 923–1423 K for 6 h. The prepared Ga₂O₃ samples were referred to as Ga₂O₃(HP, *x*), where *x* shows the calcination temperature.

Ga₂O₃ samples were loaded with metal cocatalysts (Pt, Rh, Pd and Ru). The loading amount (*y*) of these metals was in the range from 0 to 0.1 wt%. The employed precursors were as follows; Pt(NO₂)₂(NH₃)₂ aqueous solution (Tanaka kikinzo, 4.533wt% as Pt), H₂PtCl₆·6H₂O (Wako, 99.9%), RhCl₃·3H₂O (Kishida, 99%), PdCl₂ (Kishida, 99%) and (NH₄)₃RuCl₆ (Mitsuwa, chemical grade). Metal cocatalysts were loaded by an impregnation method. The Ga₂O₃ powder (2.0 g) was dispersed into an

aqueous solution (50 ml) of the metal precursor and stirred for 0.5 h, followed by evaporation to dryness with a rotary evaporator. Then, the obtained powder was dried in an oven at 323 K overnight. When we used these samples without further pretreatment before the photocatalytic reaction test, the metal precursors adsorbed on Ga₂O₃ should be reduced upon photoirradiation in a flow of water vapor and methane (in-situ photodeposition) as reported in the previous study.¹⁴ In other cases, an oxidative pretreatment was carried out in air at 773 K for 2 h, or a reductive pretreatment was carried out in a flow of hydrogen (10 ml min⁻¹) at 373–673 K for 0.5 h. The sample with the cocatalyst was referred to as Pt(y)/Ga₂O₃ for example.

4.2.2.2. *Photocatalytic Reaction Tests*

The reaction tests were carried out with a fixed-bed flow reactor.^{13–18} The catalysts were granulated to the size of 400–600 μm. The quartz cell (60 × 20 × 1 mm³) was filled with the mixture of the catalysts (0.8 g) and quartz granules (0.7 g). The reaction gas, a mixture of water vapor and methane, was introduced into the reactor at the flow rate of 40 mL min⁻¹ and the reaction was carried out upon photoirradiation with a 300 W xenon lamp. In a standard condition, the concentration of water vapor and methane was 1.5% and 50%, respectively, and the light of the entire wavelength region from the xenon lamp was irradiated without passing any filters, where the light intensity measured in the range of 254±10 and 365±15 nm were ca. 14 and 60 mW cm⁻², respectively. The reaction temperature was typically changed in the range of ca. 308–353 K. The outlet gas was analyzed by on-line gas chromatography with a thermal conductivity detector.

4.2.2.3. *Characterizations of Photocatalysts*

Powder X-ray diffraction (XRD) pattern was recorded at room temperature on a Rigaku diffractometer RINT 2500 using Ni-filtered Cu Kα radiation (50 kV, 100 mA). The mean crystallite size was calculated with the Scherrer equation. Diffuse reflectance (DR) UV-visible spectrum was recorded at room temperature on a JASCO V-570 equipped with an integrating sphere covered with BaSO₄. BaSO₄ was used as the reference. The Brunauer–Emmett–Teller (BET) specific surface area of the sample was calculated from the amount of N₂ adsorption at 77 K, which was measured by a Quantachrome Monosorb. The Pt particle size on the Pt/Ga₂O₃ catalysts prepared by in-situ photodeposition was measured by using the CO-pulse method in a flow system after the pretreatment in H₂ at 423 K for 0.5 h. SEM images were recorded by a JSM-6330F. Rh K-edge

XAFS (X-ray Absorption Near Edge Structure) spectra were recorded at the NW-10A station²⁰ of KEK-PF (Photon Factory, Institute of Materials Structure Science, High Energy Accelerator Research Organization) at room temperature with a Si(311) double crystal monochromator in a transmission mode. The samples were packed in each polyethylene film cell in N₂ atmosphere. The spectra were analyzed with a REX 2000 software (Rigaku). Fourier transform of Rh K-edge EXAFS was performed in the range of ca. 3–12 Å⁻¹. The inverse Fourier transform was carried out in the range of ca. 1.6–3.2 Å and the curve fitting analysis was performed by using theoretical parameters.²¹

4.2.3. Results and Discussion

4.2.3.1. Thermal Activation Energy

In the present study, it was confirmed that hydrogen and carbon dioxide were produced constantly at a stoichiometric ratio (4:1) on all the samples. Figure 1A shows the time course of the hydrogen production rate at stepwise increasing temperature over the Pt(0.07)/β-Ga₂O₃(K) photocatalyst as a representative. The hydrogen production rate over Pt/β-Ga₂O₃ became constant soon after the photoirradiation started (Figure 1Aa), as reported in the previous study.¹⁶ The temperature of the reaction cell was 318 K at that time. When we increased the reaction temperature to 323 K without changing the other conditions, the hydrogen production rate slightly increased and became constant soon (Figure 1Ab). With increasing the reaction temperature stepwise, the production rate increased until 334 K (Figure 1A a–d). However, hydrogen production rate did not change with further increasing the reaction temperature to 344 K (Figure 1A d–f). We also confirmed that the each production rate was a reproducible value for each reaction temperature and it was not influenced by the thermal history of the sample. Figure 1B shows the corresponding Arrhenius plot. In the lower temperature range between 318 and 334 K, the Arrhenius plot showed a straight line and the thermal activation energy (E_a) was calculated to be 5.4 kJ mol⁻¹. Tendency of the production rate vs. the reaction temperature was common to all the β-Ga₂O₃ samples examined. The values of the thermal activation energy depended on the structure of β-Ga₂O₃ and loading of metal cocatalyst, as described later. The E_a values were typically lower than ca. 10 kJ mol⁻¹, although only some samples showed higher values such as 20 kJ mol⁻¹ and some showed 0 kJ mol⁻¹. These values were similar to the results of other photocatalytic reactions reported,^{1–12} and obviously much lower than the reported values for the thermal steam reforming of methane using heterogeneous catalysts (for example, 63–153 kJ mol⁻¹).^{22–24} Therefore, it was suggested

that the thermal energy for the PSRM would contribute to the mild activation steps only. This means that the main activation was done by the photoenergy. On the other hand, it was also clarified that the steps concerning the thermal energy would not influence the whole reaction rate at higher reaction temperatures in this photocatalytic reaction.

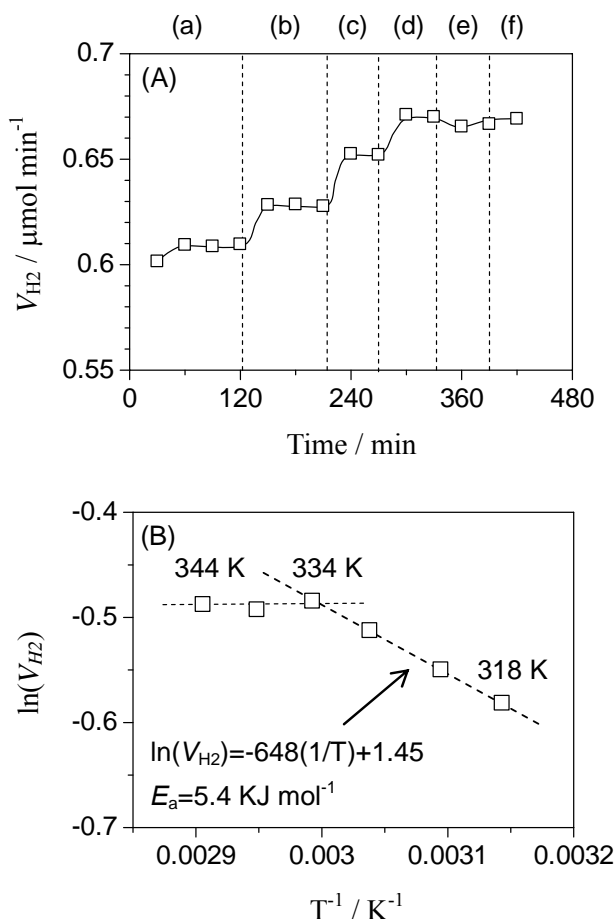


Figure 1. (A) Time course of the hydrogen production rate (V_{H_2}) in the PSRM over Pt(0.07 wt%)/Ga₂O₃(K) at stepwise-increasing temperature and (B) the corresponding Arrhenius plot. The reaction temperature was (a) 318, (b) 323, (c) 329, (d) 334, (e) 339 and (f) 344 K, respectively. Pt was loaded by the impregnation method using Pt(NO₂)₂(NH₃)₂, followed by calcination at 773 K.

4.2.3.2 Influence of the Light Intensity on the Thermal Activation Energy.

The photocatalytic reaction rate and the thermal activation energy in the lower reaction temperature range (<334 K) were recorded over a Pt(0.1)/Ga₂O₃(K) photocatalyst in various intensity of the irradiation light. The hydrogen production rate at the reaction temperature of 318 K linearly increased with the increase of the light intensity (Figure 2a). This shows that the rate determining photoexcitation step of the PSRM over the Pt/ β -Ga₂O₃ photocatalyst would be one-photon process. On the other hand, the thermal activation energy in each photoirradiation

condition was found to decrease with increasing the light intensity (Figure 2b).

In general, the whole mechanism of the photocatalytic reaction can be divided into several steps as follows; (i) photoexcitation of the semiconductor, (ii) migration of photoexcited carriers from bulk to surface, (iii) electron transfer from the conduction band of the semiconductor to metal cocatalyst, (iv) adsorption of reactants, (v) surface reaction of photoexcited carriers and reactants, and (vi) desorption of products. Among them, steps (i), (iv), (v) and (vi) would not influence on the variation of the thermal activation energy with the incident light intensity; Since the reaction temperature was too small to excite band excitation, thermal energy should not influence step (I). If the irradiation light intensity increased, the rates for steps (iv), (v) and (vi) would vary. However, the activation energy for these processes should not be varied with the incident light intensity. Thus, the result of Figure 2b shows that the thermal energy would contribute to the steps concerning the number of carriers, such as the migration and transfer of the photoexcited carriers.

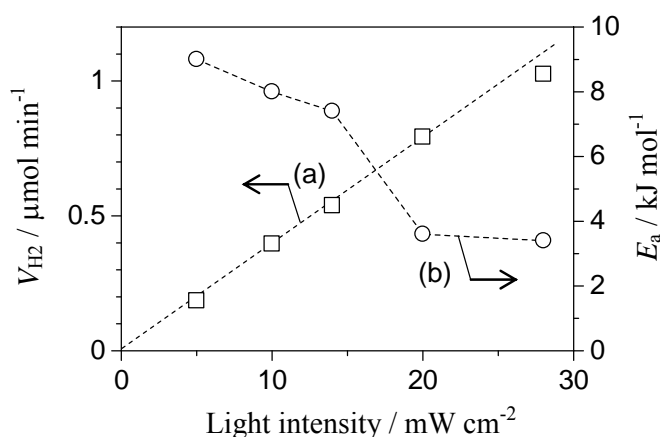


Figure 2. Influence of the irradiation light intensity on (a) the hydrogen production rate at the reaction temperature of 318 K (V_{H_2}), and (b) the thermal activation energy (E_a) in the PSRM over Pt(0.1 wt%)/ $\text{Ga}_2\text{O}_3(\text{K})$. Pt was loaded by the impregnation method using $\text{Pt}(\text{NO}_2)_2(\text{NH}_3)_2$, followed by calcination at 773 K.

Here, we tentatively propose two possibilities for further discussion. One is that the thermal energy would contribute to the excitation of electrons captured in some kinds of trap sites under the conduction band as illustrated in Figure 3a. Several kinds of trap sites would exist in Ga_2O_3 photocatalyst, and larger thermal energy would be required to excite the electrons captured in the deeper trap sites. In the low intensity of light, the number of the photoexcited carriers should be low and the majority of excited electrons should be captured in these trap sites. Only when sufficiently large thermal energy was added to the system, the electrons captured in the various trap sites, including the deep ones, became to contribute to the enhancement of the reaction rate. Thus, the thermal activation energy would be large under the low light intensity. On the other hand, when

the number of photoexcited electrons is large in the high intensity of light, all the trap sites were filled with a part of the excited electrons, and untrapped electrons would remain enough in the conduction band. In this case, the electrons captured in the deep trap sites would be minor and would not much influence the production rate even if they were excited by the thermal energy. Thus, E_a would be low in the high intensity of the light. The same explanation is applicable to the hole in the valance band. Hussein et al.⁶ and Karakitsou et al.⁸ also proposed that thermal energy would contribute to the migration of carriers in the bulk of semiconductor photocatalyst.

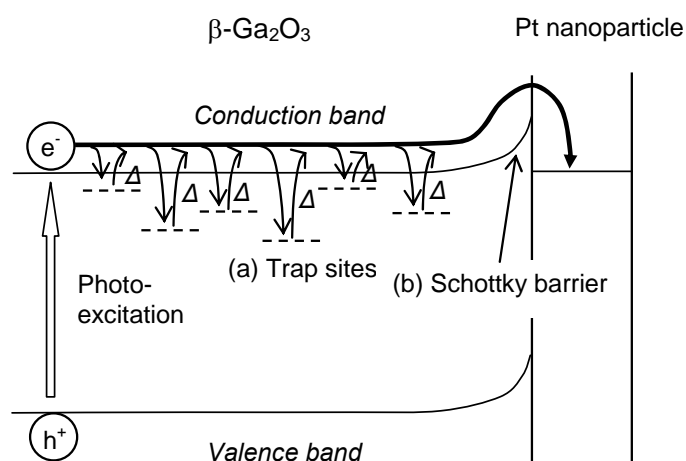


Figure 3. Proposed thermal activation mechanism of electron migration in the photocatalytic reaction.

Another possibility is that the thermal energy would contribute to the transfer of photoexcited electrons from the conduction band of the Ga_2O_3 semiconductor to Pt cocatalyst as illustrated in Figure 3b. It is generally accepted that Schottky barrier was generated when n-type semiconductor is connected with metal having a large work function such as Pt. Therefore, the thermal energy could contribute to overcome this barrier. Since the number of the photoexcited electrons in the conduction band increased with increasing the light intensity, the occupied level might increase and the relative height of the barrier would be reduced. Thus, E_a would decrease with an increase of the light intensity.

These two hypotheses will be discussed further below.

4.2.3.3. Influence of the Structure of $\beta\text{-Ga}_2\text{O}_3$

Several $\beta\text{-Ga}_2\text{O}_3$ samples having various sizes of crystallites and various specific surface areas were prepared by the homogeneous precipitation method, followed by calcination at various

temperatures.¹⁹ From their XRD patterns, the sample calcined at 923 K and higher temperatures had β -type crystal structure. From SEM images (Figure 4), rod-like particles with homogeneous shape and size (1-2 μm) were observed. The size and shape of the particles were not drastically changed with increasing the calcination temperature, except for the sample calcined at 1473 K. DR UV-vis spectra of the $\text{Ga}_2\text{O}_3(\text{HP})$ samples were not varied with the calcination temperature. However, as shown in Figure 5a, the crystallite size of these samples determined from XRD increased gradually from 25 to 35 nm with increasing the calcination temperature from 923 to 1273 K, and then it steeply increased to 72 nm with further increasing the calcination temperature. BET specific surface areas of these samples were almost constant around $17 \text{ m}^2\text{g}^{-1}$ at the calcination temperatures from 923 to 1273 K, and then they drastically decreased to $3 \text{ m}^2\text{g}^{-1}$ with further increasing the calcination temperature to 1473 K (Figure 5b).

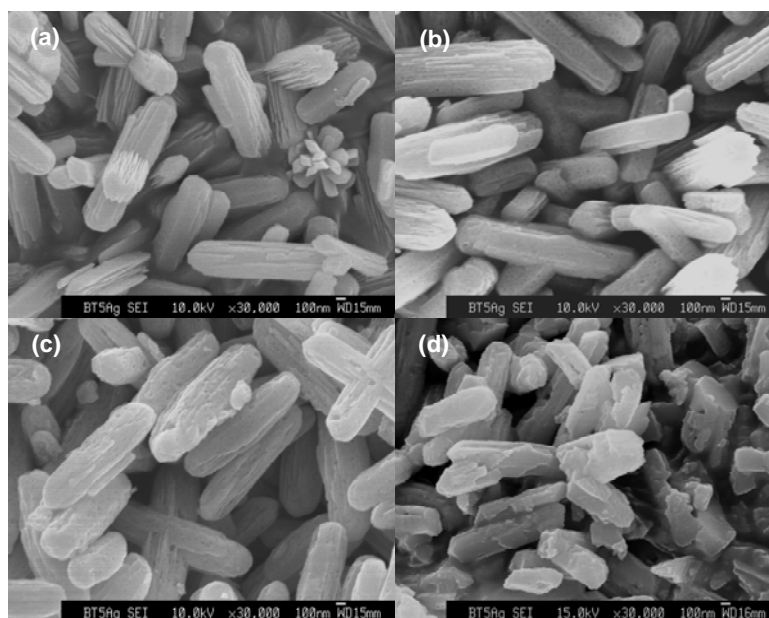


Figure 4. SEM images of the $\text{Ga}_2\text{O}_3(\text{HP})$ samples calcined at (a) 873 (b) 1073 (c) 1273 and (d) 1473 K.

The photocatalytic activity of these samples without loading Pt cocatalyst was plotted in Figure 5c. The hydrogen production rate in the PSRM on the samples calcined at 923–1073 K did not much increase with the increase of the calcination temperature and the highest activity was obtained over the $\text{Ga}_2\text{O}_3(\text{HP}, 1273)$ sample. Then, it drastically decreased with further increasing the calcination temperature. This result suggests that the β - Ga_2O_3 sample having both a large surface area and a large crystallite size would be most effective for the PSRM. On the other hand, the thermal activation energy of the $\text{Ga}_2\text{O}_3(\text{HP}, 923)$ sample was ca. 10 kJ mol^{-1} . It clearly

decreased with increasing the calcination temperature and it reached to zero for the Ga_2O_3 samples calcined at 1273–1473 K (Figure 5d). For the Ga_2O_3 samples calcined at 923–1273 K, the specific surface areas were similar around $15\text{--}18\text{ m}^2\text{g}^{-1}$, but defects structure in the crystal and/or grain boundary should decrease with an increase of the calcination temperature judging from the gradual increase of the average crystallite size. Therefore, the decrease of the trap sites for photoexcited carriers would result in the increase of the hydrogen production rate and the decrease of the thermal activation energy. This supports the first hypothesis that the thermal energy would help the electron out of the trap sites to migrate smoothly in the conduction band of Ga_2O_3 .

On the other hand, for the Ga_2O_3 calcined at higher temperatures (1273–1473 K), their thermal activation energies were constantly zero, which would be originated from the large size of the crystallites with low amounts of defects. However, the drastic decrease of the specific surface area of the photocatalyst would decrease the reaction rate on these samples.

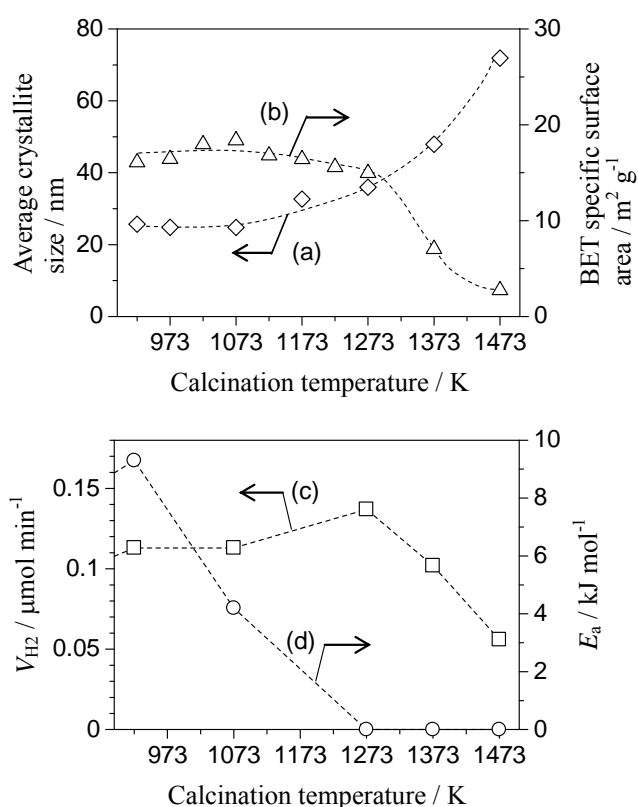


Figure 5. (a) The mean crystallite size, (b) the BET specific surface area, (c) the hydrogen production rate at the reaction temperature of 318 K (V_{H_2}), and (d) the thermal activation energy (E_a) in the PSRM over the $\beta\text{-Ga}_2\text{O}_3(\text{HP})$ samples calcined at various temperatures, on which Pt was not deposited.

4.2.3.4. Influence of the Metal Cocatalyst

Effect of Pt loading on the thermal activation energy was examined. Pt was loaded on the Ga₂O₃(HP, 1473) sample by an impregnation and successive in-situ photodeposition method. As shown in Figure 5d, the thermal activation energy of this Ga₂O₃ sample was zero. When 0.01 wt% of Pt was loaded on it, hydrogen production rate largely increased from 0.06 to 0.23 μmol min⁻¹ and the thermal activation energy also increased to ca. 10 kJ mol⁻¹ (Figure 6). This clearly supports the second hypothesis that the thermal energy would be also required for the transfer of photoexcited electrons from the conduction band of Ga₂O₃ to Pt cocatalyst. In other words, the thermal energy would be necessary to overcome Schottky barrier. When the loading amount of Pt increased, the hydrogen production rate slowly increased (Figure 6a) but the thermal activation energy gradually decreased (Figure 6b). For the sample loaded with 0.1 wt% of Pt, thermal activation energy was zero. This shows that the electron transfer from Ga₂O₃ to Pt cocatalyst in a high loading sample would become easier than that in the low loading sample.

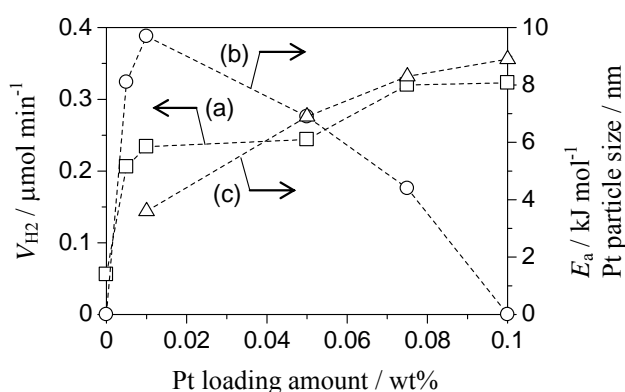


Figure 6. (a) The hydrogen production rate at the reaction temperature of 318 K (V_{H_2}), (b) the thermal activation energy (E_a) in the PSRM over the Ga₂O₃(HP, 1473) sample and the Pt/Ga₂O₃(HP, 1473) samples of various Pt-loading amount, and (c) the particle size of Pt on the Pt/Ga₂O₃(HP, 1473) samples. Pt was loaded by the impregnation method using H₂PtCl₆, followed by in-situ photodeposition.

The Pt particle size measured by CO pulse method monotonically increased with increasing the Pt-loading amount (Figure 6c). It was also reported that work function of metal nano-particles decreased with increasing the particle size.^{25, 26} This means that the work function of the Pt nano-particles in a high loading sample would be smaller than that in a low loading sample. We estimated the work function of Pt nano-particles by using the equation proposed in ref. 25, assuming that hemispherical Pt nano-particles were loaded on β -Ga₂O₃. The decrease of the work function of Pt cocatalyst was ca. 0.09 eV (8.6 kJ mol⁻¹) when the Pt-loading amount increased from 0.01 to 0.1 wt%. This value was close to the variation of the thermal activation energy shown in Figure 6b (9.7 kJ mol⁻¹).

Since the height of the Schottky barrier depends on the potential difference between the Fermi level of Pt and that of Ga₂O₃, the Schottky barrier should become smaller with increasing the particle size of Pt. In other words, it would decrease with increasing the loading amount of Pt. Thus, the thermal activation energy of Pt/Ga₂O₃ decreased with increasing the loading amount of Pt. It was suggested that influence of the Schottky barrier on the electron migration would become negligible on the sample with 0.1 wt% of Pt in the present case.

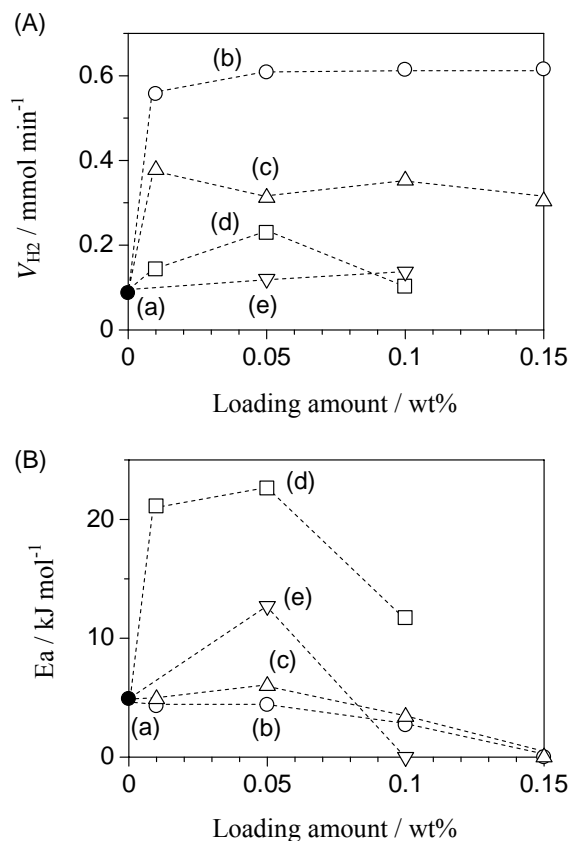


Figure 7. (A) The hydrogen production rate at the reaction temperature of 318 K (V_{H_2}) and (B) the thermal activation energy (E_a) in the PSRM over Ga₂O₃(K) and metal-loaded Ga₂O₃(K) samples; (a) Ga₂O₃(K), and Ga₂O₃(K) loaded with (b) Pt, (c) Rh, (d) Pd and (e) Ru. Cocatalyst was loaded by the impregnation method, followed by in-situ photodeposition.

We prepared Ga₂O₃ samples loaded with various metals (Pt, Rh, Pd and Ru) as the cocatalyst and examined their photocatalytic activity and thermal activation energy for the PSRM (Figure 7). Ga₂O₃(K) was used as the photocatalyst and metal cocatalysts were loaded by the impregnation method and successive in-situ photodeposition. The hydrogen production rate of the metal-loaded samples was higher than that of the bare sample (Figure 7A). The loading amount did not much influence the hydrogen production rate except for the Pd-loaded sample. On the other hand, the thermal activation energy was largely varied with the loading amount of cocatalyst. In many cases, the thermal activation energy first increased and then decreased with increasing the

loading amount (Figure 7B). The thermal activation energies of Pt- and Rh- loaded samples were zero when the loading amount was 0.15 wt%, and that of Ru-loading sample was zero when it was 0.1 wt%. These phenomena consisted with the results shown in Figure 6. Therefore, it was suggested that the particle size of cocatalyst would largely influence the thermal activation energy of the Ga_2O_3 photocatalyst for the PSRM. Note that the thermal activation energy observed for the bare $\text{Ga}_2\text{O}_3(\text{K})$ sample was suppressed by loading enough amount of Pt, Rh and Ru. It is generally believed that loading metal cocatalyst would largely accelerate the migration of photoexcited electrons in the bulk. Thus, over the metal-loaded samples thermal activation energy for the excitation of electrons captured in the trap sites may not be observed, but that to overcome the the Schottky barrier between semiconductor and metal cocatalyst may be observed.

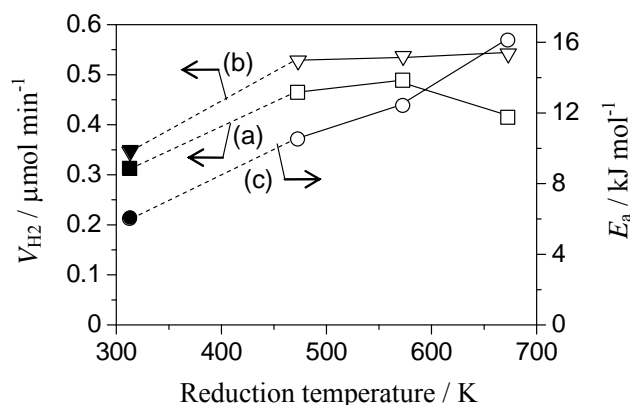


Figure 8. The hydrogen production rate (V_{H_2}) at reaction temperatures of (a) 318 K and (b) 333 K, and (c) the thermal activation energy (E_a) over $\text{Rh}(0.05 \text{ wt}\%)/\beta\text{-Ga}_2\text{O}_3(\text{K})$ reduced at various temperatures. The closed plots show the values on the sample prepared by the impregnation and successive in-situ photodeposition.

Among these samples, we further examined the influence of hydrogen reduction pretreatment for the $\text{Rh}(0.05)/\text{Ga}_2\text{O}_3(\text{K})$ sample (Figure 8). The hydrogen production rate at the reaction temperature of 318 K was improved by the reduction pretreatment and the highest activity was obtained over the sample reduced at 573 K as the pretreatment (Figure 8a). However, it decreased with the reduction treatment at 673 K. On the other hand, the hydrogen production rate at the reaction temperature of 333 K was enhanced by the reduction at 473 K and then became constant in the samples reduced at 473 K and higher temperatures (Figure 8b). One may think that the reduction at higher temperature would give larger particles of Rh due to the aggregation and reduce the activation energy according to the results shown in Figures 6 and 7. However, thermal activation energy was 6.0 kJ mol^{-1} in the nonreduced sample and it increased to 16.1 kJ mol^{-1} with increasing the reduction temperature to 673 K (Figure 8c).

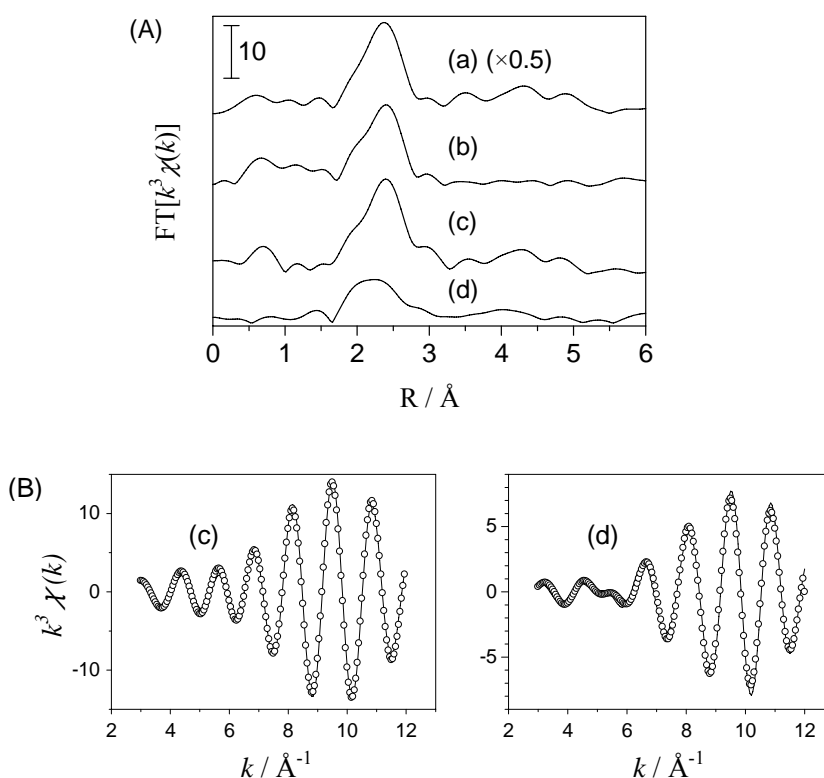


Figure 9. (A) The Fourier transforms of Rh K-edge EXAFS spectra of (a) Rh foil and (b)–(d) Rh(1 wt%)/ β -Ga₂O₃(K) samples reduced at various temperatures and (B) the results of the curve fitting analysis on the inverse Fourier transforms, where the solid lines show the observed spectra and the circles show the calculated ones. Reduction temperature was (b) 373, (c) 573 and (d) 673 K.

Thus, the state of Rh cocatalyst on these samples was examined with XAFS. Rh K-edge XANES spectra of Rh(1)/Ga₂O₃ samples reduced at various temperatures were very similar with that of Rh foil (not shown). No clear differences were observed among the spectra of the photocatalyst samples. However, clear differences were observed on their EXAFS spectra. Fourier transforms of the EXAFS spectra of the Rh/Ga₂O₃ samples reduced at 373 and 573 K were very similar with that of Rh foil (Figure 9A a–c). However, the spectrum of the Rh/Ga₂O₃ sample reduced at 673 K was much different from those of other samples at the range of 1.6–3.2 Å (Figure 9Ad). We calculated the inverse Fourier transforms of this part (Figure 9B) and found the clear difference in the k -range of 4–6 Å⁻¹. And then, we performed the curve fitting analysis on these inverse Fourier transforms and attained the clear fitting shown in Figure 9B, the open circles. Table 1 presents the fitting parameters. The first coordination peak (around 2.4 Å) of the samples reduced at 373 and 573 K was composed of a Rh-Rh shell and the atomic distance was the same as that of Rh foil, showing that the Rh cocatalyst was loaded as Rh metal nano-particles (Table 1). Fitting analysis showed that the first coordination peak of the sample reduced at 673 K was composed of a

Rh-Rh shell and a Rh-Ga shell. Therefore, in the present case, Rh cocatalyst would form Ga-Rh alloy on the sample reduced at 673 K. It was reported that Pt and Pd loaded on Ga₂O₃ also formed alloy such as Ga₃Pt₅ and Ga₂Pd₅ when they were reduced in hydrogen atmosphere at 573-773 K.²⁷ ²⁸ At the same time, the present result shows that the surface of Ga₂O₃ would be reduced. Thus, two possible reasons were proposed for the increase of the thermal activation energy: One is the formation of defects on the surface of Ga₂O₃, and the other would be the change of metal-semiconductor junction due to the formation of alloy. These changes would disturb the smooth migration of photoexcited carriers and increase the activation energy. On the other hand, the hydrogen production rate at the high reaction temperature was constant among the reduced samples (Figure 8b). It seems that the thermal energy at the reaction temperature of 333 K could compensate for the negative effects of the formation of the Ga-Rh alloy or the surface defects.

Table 1 Result of EXAFS curve fitting analysis for Rh foil and Rh(1 wt%)/Ga₂O₃(K) samples

Sample	Reduction temperature / K	Rh-Rh		Rh-Ga	
		N^a	$R^b / \text{Å}$	N^a	$R^b / \text{Å}$
Rh foil	–	9.0	2.70	–	–
Rh/Ga ₂ O ₃	373	4.9	2.70	–	–
Rh/Ga ₂ O ₃	573	4.2	2.70	–	–
Rh/Ga ₂ O ₃	673	1.5	2.69	1.5	2.59

^a Coordination number. ^b Atomic distance.

4.2.4. Conclusion

We examined the influence of the thermal energy on the photocatalytic activity of Ga₂O₃ for the PSRM, and found that the production rate increased with the increase of the reaction temperature until less than ca. 343 K and the thermal activation energy was typically a small value less than 10 kJ mol⁻¹. The thermal energy would contribute to the migration of photoexcited carriers both in the bulk of Ga₂O₃ and at the metal-semiconductor junction between Ga₂O₃ and metal cocatalyst.

The incident light intensity, the crystallite size of Ga₂O₃ and the particle size of cocatalyst were the important factors determining the thermal activation energy. In the low intensity of the incident light, or in the photocatalysts consisting of small crystallites, which have low crystallinity with many trap sites, large thermal activation energy was required to help the smooth migration of photoexcited

carriers. In the samples loaded with small metal nano-particles, the additional thermal energy largely enhanced the photocatalytic activity since it would help the electrons to transfer from the conduction band to the metal cocatalysts beyond the high Schottky barrier. These facts can be applied to improve the efficiency of other photocatalytic reactions. We found that an estimation of the thermal activation energy in the photocatalysis would be useful to evaluate the states of both the defects and the electron migration in the semiconductor photocatalysts.

References.

- 1) Bideau, M.; Claudel, B.; Otterbien, M. *J. Photochem. Photobiol. A* **1980**, 14, 291–302.
- 2) Harvey, P. R.; Rudham, R., Ward, S *J. Chem. Soc. Faraday Trans.* **1983**, 179, 1381–1390.
- 3) Okamoto, K.; Yamamoto, Y.; Tanaka, H.; Tanaka, M.; Itaya, A. *Bull. Chem. Soc. Jpn.* **1985**, 58, 2023–2028.
- 4) Chen, L. C.; Chou, T. C. *Ind. Eng. Chem. Res.* **1993**, 32, 1520–1527.
- 5) Vorontsov, A. V.; Stoyanova, I. V.; Kozlov, D. V.; Simagina, V. I.; Savinov, E. N. *J. Catal.* **2000**, 189, 360–369.
- 6) Hussein F. H. and Rudham R. *J. Chem. Soc. Faraday Trans.* **1987**, 83, 1631–1639.
- 7) Naito, S. *Can. J. Chem.* **1986**, 64, 1795–1799.
- 8) Karakitsou, K.; Verykios X. E. *J. Catal.* **1995**, 152, 360–367.
- 9) Puangpetch, T.; Sreethawong, T.; Yoshikawa, S.; Chavadej, S. *J. Mol. Catal. A: Chem.* **2009**, 312, 97–106.
- 10) Hisatomi, T.; Maeda, K.; Takanebe, K.; Kubota, J.; Domen, K. *J. Phys. Chem. C* **2009**, 113, 21458–21466.
- 11) Hisatomi, T.; Miyazaki, K.; Takanebe, K.; Maeda, K.; Kubota, J.; Sakata, Y.; Domen, K. *Chem. Phys. Lett.* **2010**, 486, 144–146.
- 12) Yuliati, L.; Itoh, H.; Yoshida, H. *Chem. Phys. Lett.* **2008**, 452, 178–182.
- 13) Yoshida, H.; Kato, S.; Hirao, K.; Nishimoto, J.; Hattori, T. *Chem. Lett.* **2007**, 36, 430–431.
- 14) Yoshida, H.; Hirao, K.; Nishimoto, J.; Shimura, K.; Kato, S.; Itoh, H.; Hattori, T. *J. Phys. Chem. C* **2008**, 112, 5542–5551.
- 15) Shimura, K.; Kato, S.; Yoshida, T.; Itoh, H.; Hattori, T.; Yoshida, H. *J. Phys. Chem. C* **2010**, 114, 3493–3503.
- 16) Shimura, K.; Yoshida, T.; Yoshida, H. *J. Phys. Chem. C* **2010**, 114, 11466–11474.
- 17) Shimura, K.; Yoshida, H. *Energy Environ. Sci.* **2010**, 3, 615–617.

- 18) Shimura, K.; Miyanaga, H; Yoshida, H. *Stud. Surf. Sci. Catal.* **2010**, 175, 85–92.
- 19) Yoshida, H.; Maeda, K. *Stud. Surf. Sci. Catal.* **2010**, 175, 351–354.
- 20) Nomura, M.; Koike, Y.; Sato, M.; Koyama, A.; Inada, Y.; Asakura, K. *AIP Conf. Proc.* **2007**, 882, 896.
- 21) Mckale, A. G.; Veal, B. W.; Paulikas, A.P.; Chan, S. K.; Knapp, G. S. *J. Am. Chem. Soc.* **1988**, 110, 3763–3768.
- 22) Bobrova, I. I.; Chesnokov, V. V.; Bobrov, N. N.; Zaikovskii, V. I.; Parmon, V. N. *Kinet. Catal.* **2000**, 41, 19–24.
- 23) Ramírez-Cabrera, E.; Atkinson, A.; Chadwick, D. *Appl. Catal. B* **2004**, 47, 127–131.
- 24) Rioux, R.M.; Marsh, A.L.; Gaugha, J.S.; Somorjai, G.A. *Catal. Today* **2007**, 123, 265–275.
- 25) Wood, D. M. *Phys. Rev. Lett.* **1981**, 46 749.
- 26) Perdew, J. P. *Rhys. Rev. B* **1988**, 37, 6175–6180.
- 27) Iwase, N.; Mayanagi T.; Ogawa, N.; Sakata, K.; Takezawa, N. *Catal. Lett.* **1998**, 54, 119–123.
- 28) Penner, S.; Lorenz, H.; Jochum, W.; Stoger-Pollach, M.; Wang, D.; Rameshan, C.; Klotzer, B. *Appl. Catal. A*, **2009**, 358, 193–202.

4.3. Doping Effect on Photocatalytic Activity of Gallium Oxide for Hydrogen Production from Water and Methane

Abstract

Some series of Ga₂O₃ samples doped with metal ions (Zn²⁺, Y³⁺ and Zr⁴⁺) were systematically prepared by the homogeneous precipitation method (HP) and the impregnation method (IMP), and the local structure of the dopants and the activity of the doped Ga₂O₃ for photocatalytic steam reforming of methane (CH₄ + 2H₂O → 4H₂ + CO₂) were studied. Zn-doping increased the photocatalytic activity of Ga₂O₃, while doping of Y or Zr ions did not change or decreased the activity. XAFS study revealed that the doped Zn ions substituted for Ga³⁺ in Ga₂O₃ sample prepared by the HP method, while they existed as ZnGa₂O₄ in the sample prepared by the IMP method. From the measurement of thermal activation energy of the photocatalysis, it was revealed that the former Zn species would improve the bulk electric property of Ga₂O₃ with less crystal distortion, while the latter species would work as the surface active phase to enhance the photocatalytic activity.

4.3.1. Introduction

Development of the hydrogen production method from renewable resources and natural energy would be important to realize a sustainable society. Hydrogen production from biomass or its derivatives is one of the most desired ways. Our research group found that some kinds of Pt-loaded semiconductors such as Pt/TiO₂ and Pt/Ga₂O₃ promoted photocatalytic steam reforming of methane (PSRM; CH₄ + 2H₂O → 4H₂ + CO₂) around room temperature and at atmosphere pressure.¹⁻⁶ Although the PSRM is an attractive reaction to convert solar energy into chemical potential of the storable hydrogen by using renewable resources, water and methane, the efficiency of this photocatalytic system is still low. Thus, the development of the efficient photocatalysts is required now.

Doping of foreign elements is one of the effective ways to increase the photocatalytic activity and has been examined on many systems by various reserchers. For example, doping metal ions was effective for the improvement of the activity of various photocatalysts such as TiO₂,⁷ KTaO₃,⁸ NaTaO₃,^{9, 10} GaN,¹¹ CeO₂,¹² SrTiO₃¹³ and TaON¹⁴ for water splitting. The increase of the photocatalytic activity has been usually explained as the improvement of the bulk electric property as follows: Doping can reduce the recombination sites (e.g. metal ion species such as Ce³⁺ in CeO₂ and Ti³⁺ in SrTiO₃) for the migration of the photoexcited carriers.¹²⁻¹⁴ Or, dopant ions would form

the donor or acceptor level in the forbidden band to enhance the concentration and the mobility of carriers.^{7, 8, 10}

Gallium oxide (Ga_2O_3) is one of the attractive photocatalyst materials because it has been known to show high photocatalytic activities for various reactions such as water decomposition,¹⁵ conversion of methane,^{4, 16} reduction of carbon dioxide,^{17, 18} and decomposition of organic compounds.¹⁹ Zn-doped Ga_2O_3 was also reported to show a high photocatalytic activity for water splitting.²⁰ These facts motivated us to examine the effect of doping on the Ga_2O_3 photocatalyst. However, there were few reports to show the effect of the doping method on the local structure of the dopant, and the effect of the local structure on the photocatalytic behavior in detail.

In the previous study, we prepared $\beta\text{-Ga}_2\text{O}_3$ samples doped with various ions by the impregnation method and examined their activity for the PSRM.⁴ The suitable ionic radius and the oxidation number of the dopant for the photocatalytic activity were revealed. The high activity was obtained when the dopant had a similar ionic radius with that of Ga^{3+} and a smaller oxidation number than that of Ga^{3+} .

In the present study, metal-doped Ga_2O_3 samples were systematically prepared by a homogeneous precipitation method and the impregnation method. Three metal ions with the different ionic radius and the oxidation number, Zn^{2+} , Y^{3+} and Zr^{4+} , were employed as the dopant. Although the ionic radii of Zn^{2+} (0.74 Å) and Zr^{4+} (0.72 Å) are close to that of Ga^{3+} (0.62 Å), their oxidation numbers are different from that of Ga ion. The oxidation number of Y ion is the same as Ga ion but the ionic radius (0.90 Å) is much larger than that of Ga^{3+} . We carefully discussed the effect of the local structures of the dopant on the photocatalytic activity for the PSRM.

4.3.2. Experimental

4.3.2.1. Preparation of Photocatalysts

$\beta\text{-Ga}_2\text{O}_3$ samples were prepared by the homogeneous precipitation method (HP)^{21, 22} and the impregnation method (IMP).⁴ The starting materials employed were $\text{Ga}(\text{NO}_3)_3 \cdot x\text{H}_2\text{O}$ (Kojundo, 99.999%, a molecular weight of 256), $\text{Zn}(\text{NO}_3)_2 \cdot 6\text{H}_2\text{O}$ (Kishida, 99.0%), $\text{Y}(\text{NO}_3)_3 \cdot 6\text{H}_2\text{O}$ (Kishida, 99.9%), $\text{ZrO}(\text{NO}_3)_2 \cdot 2\text{H}_2\text{O}$ (Kishida, 99.0%) and urea (Kishida, 99.0%). In the HP method, $\text{Ga}(\text{NO}_3)_3 \cdot x\text{H}_2\text{O}$ (4 g), precursor of the dopant and urea (6 g) were dissolved in distilled water (400 ml). Doping amount was changed from 0 to 3 mol%. This solution was heated at 363 K using hot water bath, where white precipitate was gradually obtained as hydrolysis of the urea proceeded.

After neutralization of the solution (it took about 4 h), it was cooled to room temperature. The suspension was filtered off with suction, washed with distilled water, and dried at 323 K in an oven. Then, the obtained powders were calcined in air at 1273 K for 6 h.

In the IMP method, the purchased β -Ga₂O₃ (Kojundo, 99.99%, 4.1 m²g⁻¹, 2 g) was dispersed into an aqueous solution (50 ml) of the precursor and stirred for 0.5 h, followed by evaporation to dryness with a rotary evaporator. Doping amount was changed from 0 to 2 mol%. Then, the obtained powder was dried in an oven at 323 K overnight and calcined in air at 1273 K for 6 h. The prepared Ga₂O₃ samples was referred to as Ga₂O₃:M(*a*, *x*), where M, *a* and *x* show the kind of metal ion, the preparation method (HP or IMP) and the doping amount (mol%), respectively.

Three purchased β -Ga₂O₃ samples and one β -Ga₂O₃ sample prepared by the precipitation method were used as the reference samples for the photocatalytic reaction. Two Purchased Ga₂O₃ samples from Kojundo (Lot No. 139595 and Lot No. 188962) and one from Soekawa were employed and referred to as Ga₂O₃(K₁), Ga₂O₃(K₂), and Ga₂O₃(S), respectively. In the precipitation method, Ga(NO₃)₃·8H₂O (Kishida, 99.0%, 10 g) was dissolved in distilled water (250 ml). Then, 10 vol% ammonia water was added to the solution until no additional precipitation was observed. The suspension was filtered off with suction, washed with distilled water, and dried at 343 K overnight. The obtained powder was calcined in air at 973 K for 6 h. The sample prepared by the precipitation method was referred to as Ga₂O₃(P).

Ga₂O₃ samples were loaded with Pt cocatalyst. The loading amount was 0.01 or 0.05 wt%. The employed precursors were H₂PtCl₆·6H₂O (Wako, 99.9%) and Pt(NO₂)₂(NH₃)₂ aqueous solution (Tanaka kikinzo, 4.533wt% as Pt). Pt cocatalyst was loaded by an impregnation method. The doped or undoped Ga₂O₃ powder (2 g) was dispersed into an aqueous solution (50 ml) of Pt precursor and stirred for 0.5 h, followed by evaporation to dryness with a rotary evaporator. Then, the obtained powder was dried in an oven at 323 K overnight. When we used this sample without further pretreatment before the reaction, the Pt precursor adsorbed on Ga₂O₃ should be reduced during the photoirradiation in the flow of water and methane (in-situ photodeposition) as reported in the previous study.² Otherwise, an oxidative pretreatment was carried out in air at 773 K for 2 h.

ZnO, ZnGa₂O₄, Y₂O₃, Y₃Ga₅O₁₂ and ZrO₂ were used as the reference samples for the XAFS analysis. ZnO (Kojundo, 99.99%), Y₂O₃ (Kojundo, 99.99%) and ZrO₂ (Soekawa, 99.99%) were commercially obtained. ZnGa₂O₄ was prepared by a solid-state reaction method. ZnO and Ga₂O₃ were physically mixed by a wet ball-milling method with acetone at room temperature (120 rpm, 24 h) and calcined in air at 1473 K for 20 h. Y₃Ga₅O₁₂ was prepared from Y(NO₃)₃·6H₂O,

$\text{Ga}(\text{NO}_3)_3 \cdot x\text{H}_2\text{O}$ and urea by the homogeneous precipitation method, followed by calcination in air at 1573 K for 10 h. X-ray diffraction revealed that ZnGa_2O_4 and $\text{Y}_3\text{Ga}_5\text{O}_{12}$ were obtained without impurity phases.

4.3.2.2. Photocatalytic Reaction Tests

The reaction tests were carried out with a fixed-bed flow reactor.^{1-6, 22} The catalysts were granulated to the size of 400–600 μm . The quartz cell ($60 \times 20 \times 1 \text{ mm}^3$) was filled with the mixture of the catalysts (0.8 g) and quartz granules (0.6 g). The reaction gas, a mixture of water vapor and methane, was introduced into the reactor at the flow rate of 40 mL min^{-1} and the reaction was carried out upon photoirradiation with a 300 W xenon lamp. In a standard condition, the concentration of water vapor and methane was 1.5% and 50%, respectively, and the light of the entire wavelength region from the xenon lamp was irradiated without passing any filters, where the light intensity measured in the range of 254 ± 10 and $365 \pm 15 \text{ nm}$ were ca. 14 and 60 mW cm^{-2} , respectively. The reaction temperature was typically controlled in the range of 308–353 K. The outlet gas was analyzed by on-line gas chromatography with a thermal conductivity detector.

4.3.2.3. Characterizations of Photocatalysts

Powder X-ray diffraction (XRD) pattern was recorded at room temperature on a Rigaku diffractometer MiniFlexII/AP using Ni-filtered $\text{Cu K}\alpha$ radiation (30 kV, 15 mA). Mean crystallite size of each sample was estimated from the diffraction line at 35.2 degree with the Scherrer equation. Diffuse reflectance (DR) UV-visible spectrum was recorded at room temperature on a JASCO V-570 equipped with an integrating sphere covered with BaSO_4 . BaSO_4 was used as the reference. The Brunauer–Emmett–Teller (BET) specific surface area of the sample was calculated from the amount of N_2 adsorption at 77 K, which was measured by a Quantachrome Monosorb. SEM images were recorded by a S-5200 (Hitachi). XAFS spectra were recorded at the NW-10A station²³ of KEK-PF (Photon Factory, Institute of Materials Structure Science, High Energy Accelerator Research Organization) at room temperature with a Si(311) double crystal monochromator in a transmission mode for $\text{Ga}_2\text{O}_3\text{:M}(1-3)$ and the reference samples, and in a fluorescence mode by using the Lytle-detector²⁴ (100 mm ion chamber filled with Kr) with a suitable filter for $\text{Ga}_2\text{O}_3\text{:M}(0.5-1)$ samples. The samples were packed in each polyethylene film cell in air atmosphere. The spectra were analyzed with a REX 2000 software (Rigaku). Fourier transform of EXAFS spectra was performed in the range of ca. 3–12 \AA^{-1} .

The inverse Fourier transform of EXAFS spectra was carried out for the first coordination peak in the range of ca. 1.2–2.4 Å and the curve fitting analysis was performed by using theoretical parameters.²⁵

4.3.3. Results and Discussion

4.3.3.1. Characterization of Metal-doped Ga_2O_3

Figure 1 shows the X-ray diffraction patterns of $\text{Ga}_2\text{O}_3\text{:M(HP)}$ samples. XRD patterns of the undoped $\text{Ga}_2\text{O}_3\text{(HP)}$ sample was assigned to beta-type Ga_2O_3 (Figure 1a). When small amount of metal ions was doped, their diffraction patterns were almost the same as that of the undoped one. However, additional phases were observed with increasing the doping amount. Among the Zn-doped samples, the formation of ZnGa_2O_4 was confirmed on the 3%-doped sample (Figure 1Ae). Among the Y-doped samples, the formation of $\text{Y}_3\text{Ga}_5\text{O}_{12}$ was observed on the 3%-doped sample (Figure 1Be). Among the Zr-doped samples, diffraction lines of ZrO_2 was observed when more than 1% of Zr ions were added (Figure 1C c and d). These results show that at least parts of added metal ions would exist as an additional phase without substituting for Ga ion in $\beta\text{-Ga}_2\text{O}_3$ when the doping amount was large.

Figure 2 shows the mean crystallite size and the BET specific surface areas of the $\text{Ga}_2\text{O}_3\text{:Zn(HP)}$ samples representatively. When the doping amount of Zn ion increased from 0 to 3%, crystallite size and specific surface area of the samples were constant around 27 nm and 16

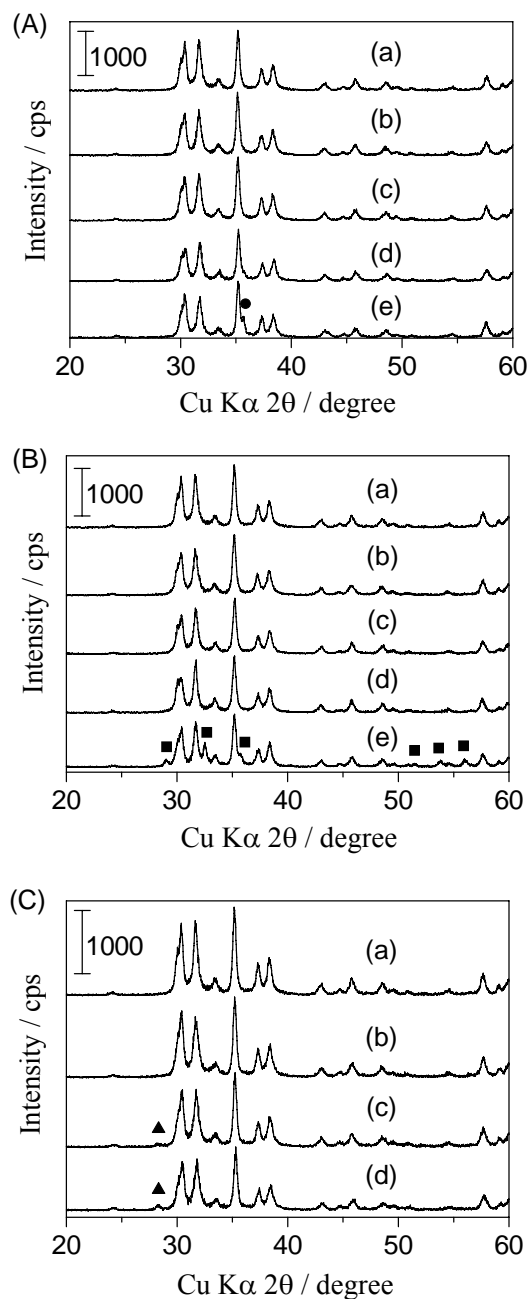


Figure 1. XRD patterns of $\text{Ga}_2\text{O}_3\text{:M(HP)}$ samples, where M was (A) Zn, (B) Y and (C) Zr. Doping amount was (a) 0, (b) 0.5, (c) 1, (d) 2 and (e) 3%. Black circle, square and triangle show the diffraction line of ZnGa_2O_4 , $\text{Y}_3\text{Ga}_5\text{O}_{12}$ and ZrO_2 , respectively.

m^2g^{-1} , respectively. Also in the case of $\text{Ga}_2\text{O}_3:\text{Y}(\text{HP})$ and $\text{Ga}_2\text{O}_3:\text{Zr}(\text{HP})$ samples, these values were almost the same as those of the undoped one.

The size and shape of the particles were observed with SEM measurement. Figure 3 shows these for the undoped and 3%-doped $\text{Ga}_2\text{O}_3(\text{HP})$ samples as representatives. The rod-like particles about $1\ \mu\text{m}$ were observed for the undoped sample (Figure 3a). For the $\text{Ga}_2\text{O}_3:\text{Zn}$ samples, not only the rod-like particles but also small particles with irregular shapes were observed, especially for the samples with a large doping amount (Figure 3b) This result shows that doping the large amount of Zn ions would disturb the crystal growth of $\beta\text{-Ga}_2\text{O}_3$. However, the morphology of the particles were not changed, when Zr or Y ions were doped (Figure 3 c and d).

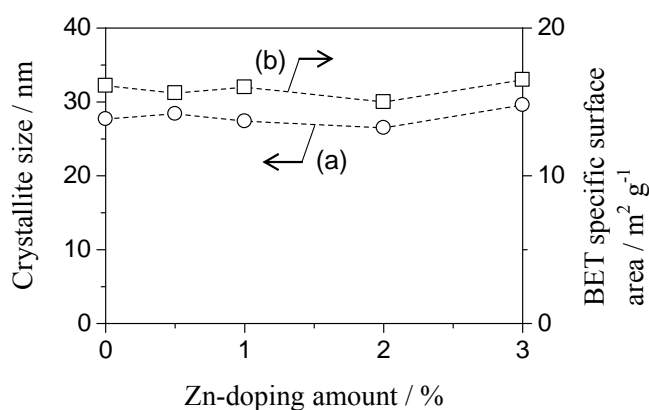


Figure 2. (a) The mean crystallite size and (b) the BET specific surface area of $\text{Ga}_2\text{O}_3:\text{Zn}(\text{HP})$ samples.

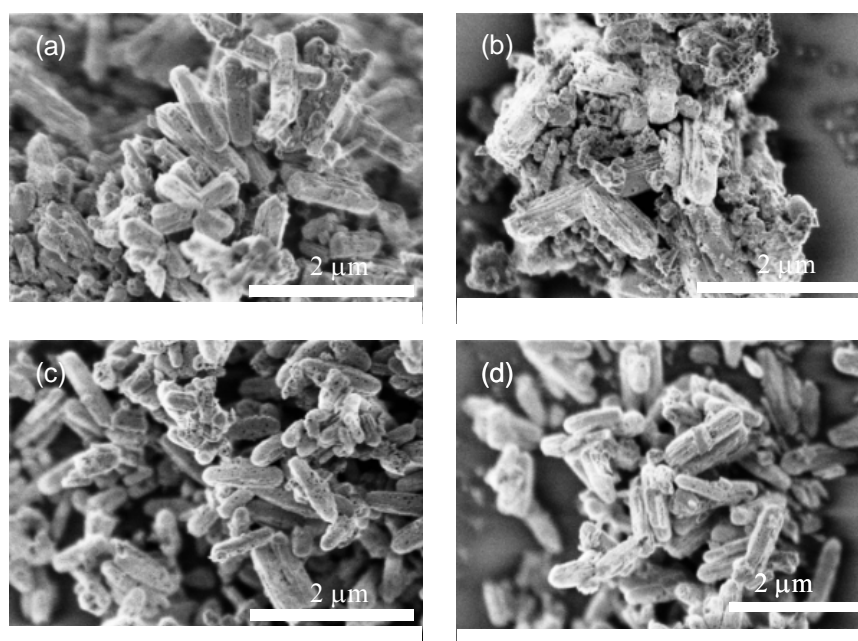


Figure 3. SEM images of (a) bare Ga_2O_3 and (b)-(d) $\text{Ga}_2\text{O}_3:\text{M}(3)$ samples prepared by the HP method, where M was (b) Zn, (c) Y and (d) Zr.

Figure 4 shows the UV-vis spectra of the Ga₂O₃:Zn(HP) samples. When the doping amount of Zn ion increased from 0 to 3%, the spectra were hardly varied with the doping amount. Similarly for the Ga₂O₃:Y(HP) and Ga₂O₃:Zr(HP) samples, their spectra were almost the same as that of undoped β-Ga₂O₃.

Ga₂O₃:M(IMP, 1) samples were also characterized by XRD, UV-vis and N₂-adsorption. No clear differences were observed between the doped and undoped β-Ga₂O₃ samples probably due to the small amount of doping.

As a conclusion of this section, doping of metal ions did not much influence the crystallite size, the specific surface area, bandgap of β-Ga₂O₃. However, change in the morphology of β-Ga₂O₃ and coexistence of additional phase were observed when the doping amount was large.

4.3.3.2. Photocatalytic Activity for the PSRM

The photocatalytic activities of doped and undoped Ga₂O₃ samples with Pt cocatalyst for the PSRM were examined. It was confirmed that hydrogen and carbon dioxide were produced constantly at the stoichiometric ratio (4:1) on all the samples.

Table 1 Photocatalytic activity of various β-Ga₂O₃ samples

Photocatalyst	$S^a / \text{m}^2 \text{g}^{-1}$	D^b / nm	Pt ^c / wt%	$V_{\text{H}_2}^d / \mu\text{mol min}^{-1}$
Ga ₂ O ₃ (HP)	16.1	27	0.05	0.98
Ga ₂ O ₃ (K ₁)	4.1	45	0.005	0.45
Ga ₂ O ₃ (S)	9.3	30	0.02	0.58
Ga ₂ O ₃ (K ₂)	11.0	27	0.02	0.58
Ga ₂ O ₃ (P)	18.7	25	0.05	0.57

^a BET specific surface area. ^b Mean crystallite size. ^c Pt-loading amount. ^d The hydrogen production rate for the PSRM.

The hydrogen production rate of undoped β-Ga₂O₃ sample prepared by the HP method was compared with those of the other β-Ga₂O₃ samples (Table 1). The activity of the Ga₂O₃(HP) sample was much higher than those of the purchased samples. The high activity of the Ga₂O₃(HP) sample would be

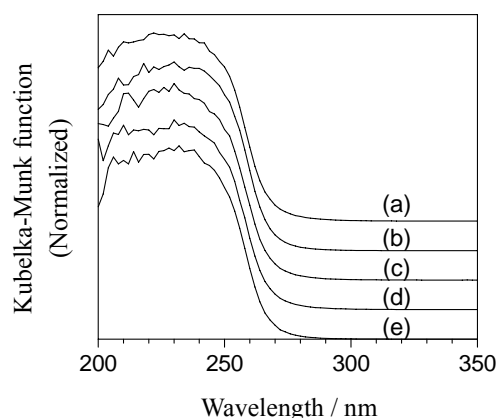


Figure 4. DR UV-vis spectra of Ga₂O₃:Zn(HP) samples. Doping amount was (a) 0, (b) 0.5, (c) 1, (d) 2 and (e) 3%.

originated from its larger specific surface area as compared with those of the purchased ones. The activity of Ga₂O₃(HP) sample was also higher than that of β-Ga₂O₃ sample prepared by the simple precipitation method using aqueous ammonia, although the specific surface area of the former was smaller than that of the latter. SEM images showed that Ga₂O₃ sample prepared by the precipitation method was composed of approximately-spherical particles. Thus, it is suggested that the specific rod-like shape of the Ga₂O₃(HP) sample would also influence the high photocatalytic activity.

Effect of doping on the photocatalytic activity was examined (Figures 5 and 6). For the Ga₂O₃:Zn(HP) samples, the hydrogen production rate first increased slightly and then decreased with increasing the doping amount (Figure 5Aa). For the Ga₂O₃:Y(HP) samples, the photocatalytic activity decreased with increasing the doping amount (Figure 5Ba). For the Ga₂O₃:Zr(HP) samples, the activity was constant and was not varied with the doping amount (Figure 5Ca). These results were not necessarily consistent with the results for the metal-doped Ga₂O₃ samples prepared by the IMP method (Figure 6). The photocatalytic activities of the Ga₂O₃:Zn(IMP) samples were also higher than that of the undoped Ga₂O₃. However, the enhancements of

the activity by Zn-doping were larger for the Ga₂O₃:Zn(IMP) samples (1.25 times) than that for the Ga₂O₃:Zn(HP, 0.5) sample (1.09 times). The less improvement in the Ga₂O₃:Zn(HP) sample would be originated from the high activity of the undoped Ga₂O₃(HP) sample (Table 1). The high doping amounts such as 1 and 2 mol% were still effective for the Ga₂O₃:Zn(IMP) sample, which was also different from

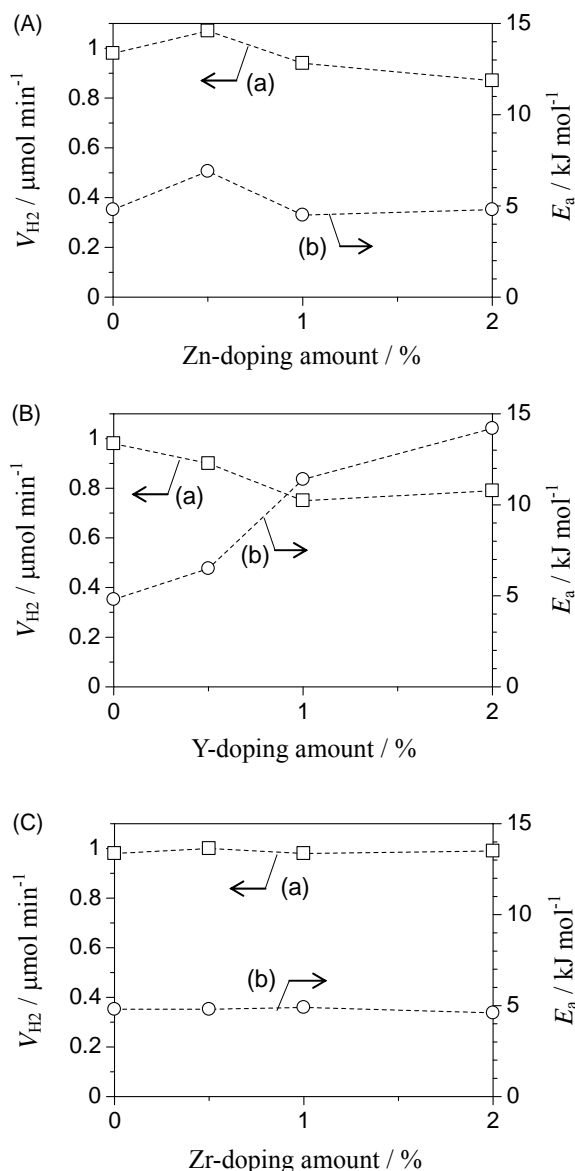


Figure 5. (a) The hydrogen production rate at 335 K (V_{H_2}) and (b) the thermal activation energy (E_a) in the PSRM over the Pt(0.05)/Ga₂O₃:M(HP) samples, where M was (A) Zn, (B) Y and (C) Zr. Pt was loaded by the impregnation method using H₂PtCl₆, followed by in-situ photodeposition.

that for the Ga₂O₃:Zn(HP) sample. Y-doping similarly decreased the photocatalytic activities for both series of samples prepared by the HP and IMP methods. The activities of the Ga₂O₃:Zr(IMP) samples were smaller than that of the undoped Ga₂O₃, although Zr-doping did not influence the activity for the Ga₂O₃:Zr(HP) samples.

Thermal activation energy of the Ga₂O₃:M(HP) samples were examined. Figure 7 shows the Arrhenius plot for the hydrogen production rate over the Pt(0.05)/Ga₂O₃:Zn(HP, 0.5) and Pt(0.05)/Ga₂O₃:Y(HP, 1) samples as representatives. When the reaction temperature increased without changing other reaction conditions, the hydrogen production rate first increased and then became constant as similar with the case for undoped Ga₂O₃ samples.²¹ In the lower temperature range, the Arrhenius plot showed a straight line and thermal activation energies were 6.9 kJ mol⁻¹ for the Pt(0.05)/Ga₂O₃:Zn(HP, 0.5) and 11.4 kJ mol⁻¹ for the Pt(0.05)/Ga₂O₃:Y(HP, 1) sample. These values were similar with the thermal activation energy of the undoped Ga₂O₃ samples.

Thermal activation energies of Ga₂O₃:M(HP) samples were plotted in Figure 5b. Thermal activation energy of the Ga₂O₃:Zn (HP, 0.5) was slightly higher than that of the undoped Ga₂O₃(HP). However, activation energies of the Ga₂O₃:Zn(HP, 1) and Ga₂O₃:Zn(HP, 2) samples were almost the same as that of the undoped sample (Figure 5Ab). For the Ga₂O₃:Y(HP) samples, thermal activation energy monotonically increased with an increase of the doping amount (Figure 5Bb). For the Ga₂O₃:Zr(HP) samples, the activation

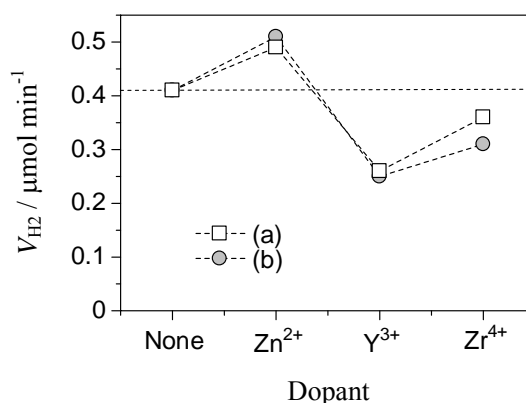


Figure 6. The hydrogen production rate (V_{H_2}) in the PSRM over Pt(0.01)/Ga₂O₃:M(IMP) samples. Doping amount was (a) 1 and (b) 2%. Pt was loaded by the impregnation method using Pt(NO₂)₂(NH₃)₂, followed by calcination at 773 K.

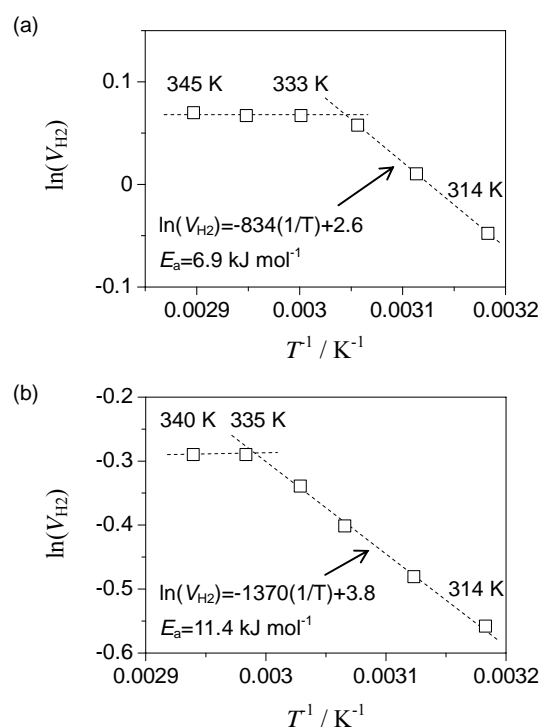


Figure 7. Arrhenius plot for the hydrogen production rate (V_{H_2}) in the PSRM over the (a) Pt(0.05)/Ga₂O₃:Zn(HP, 1) and (b) Pt(0.05)/Ga₂O₃:Y(HP, 1). Pt was loaded by the impregnation method using H₂PtCl₆, followed by in-situ photodeposition.

energy was not varied with the doping amount and the same as that of the undoped Ga₂O₃(HP) sample (Figure 5Cb).

As a conclusion of this section, the photocatalytic activity was varied with not only the kinds and the amount of the dopant but also the doping method.

4.3.3.3. Local Structure of Zn Ions in Ga₂O₃:Zn Samples

To clarify how the dopant existed on the Ga₂O₃, we analyzed the local structure of the dopant with XAFS. Figure 8A shows the Zn K-edge XANES spectra of the Zn-doped Ga₂O₃ samples and the reference samples. The spectra of the Ga₂O₃:Zn(HP) samples were largely varied with its doping amount. The spectrum of the Ga₂O₃:Zn(HP, 0.5) sample (Figure 8Ab) was different from those of the ZnO (Figure 8Aa) and ZnGa₂O₄ (Figure 8Ah) samples. As the doping amount increased, the spectra of Ga₂O₃:Zn(HP) samples were gradually changed and the spectra of 2%- and 3%-doped samples were almost the same as that of the ZnGa₂O₄. Thus, it is suggested that Zn ions having a similar local structure with that of the ZnGa₂O₄ would increase with increasing the doping amount. On the other hand, the spectra of the Ga₂O₃:Zn(IMP) samples (Figure 8A f and g) were not varied with the doping amount and were almost the same as that of the ZnGa₂O₄. This shows that the local structure of Zn ions in all the Ga₂O₃:Zn(IMP) samples was similar with that of the ZnGa₂O₄.

The local structure of Zn ions in the Ga₂O₃:Zn samples was also elucidated with EXAFS. Figure 8B shows the Fourier transforms of the Zn K-edge EXAFS spectra of the Zn-doped Ga₂O₃ samples and the reference samples. Although the first coordination peaks of the ZnO (Figure 8Ba) and ZnGa₂O₄ (Figure 8Bh) samples

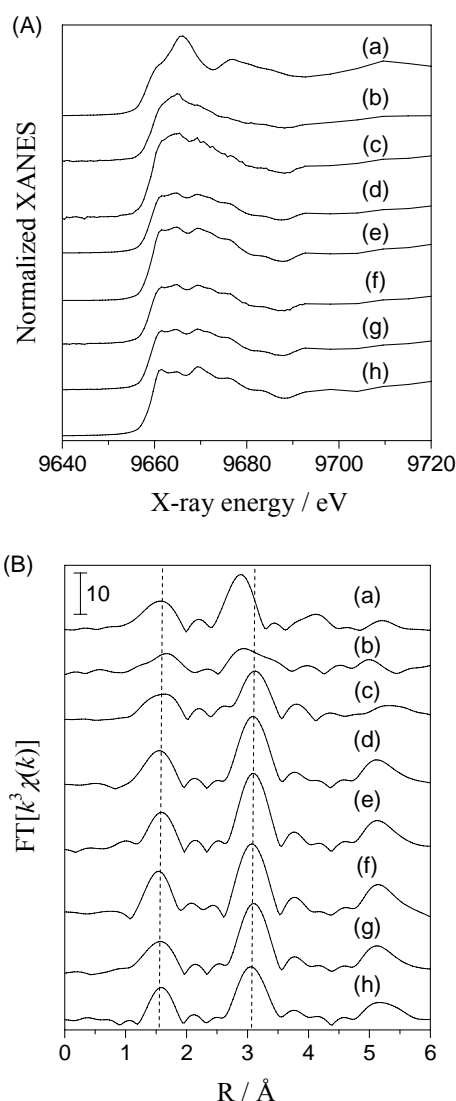


Figure 8. (A) Zn K-edge XANES spectra and (B) the Fourier transforms of Zn K-edge EXAFS spectra of (a) ZnO, (b)-(e) Ga₂O₃:Zn(HP), (f)-(g) Ga₂O₃:Zn(IMP) and (h) ZnGa₂O₄. Doping amount was (b) 0.5, (c) 1, (d) 2, (e) 3, (f) 0.5 and (g) 1%.

were observed at almost the same distance, the second coordination peak of the ZnGa_2O_4 shifted to the longer distance than that of the ZnO . The spectrum of the $\text{Ga}_2\text{O}_3:\text{Zn}(\text{HP}, 0.5)$ (Figure 8Bb) was different from those of the ZnO and ZnGa_2O_4 samples. The spectra varied with increasing the doping amount. The spectra of the $\text{Ga}_2\text{O}_3:\text{Zn}(\text{HP}, 2)$ and $\text{Ga}_2\text{O}_3:\text{Zn}(\text{HP}, 3)$ samples were almost the same as that of the ZnGa_2O_4 sample. The spectra of the $\text{Ga}_2\text{O}_3:\text{Zn}(\text{IMP})$ samples (Figure 8B f and g) were also almost the same as that of the ZnGa_2O_4 sample.

Table 2 Result of EXAFS curve-fitting analysis for ZnO , $\text{Ga}_2\text{O}_3:\text{Zn}$ and ZnGa_2O_4 samples

Sample	Zn-O	
	N^a	$R^b / \text{\AA}$
ZnO	3.9 (4.0) ^c	1.98 (1.98) ^c
$\text{Ga}_2\text{O}_3:\text{Zn}(\text{HP}, 0.5)$	N_t : 1.2 N_o : 2.5	1.91 2.09
$\text{Ga}_2\text{O}_3:\text{Zn}(\text{HP}, 1)$	4.2	2.01
$\text{Ga}_2\text{O}_3:\text{Zn}(\text{HP}, 2)$	3.9	1.97
$\text{Ga}_2\text{O}_3:\text{Zn}(\text{HP}, 3)$	3.9	1.98
$\text{Ga}_2\text{O}_3:\text{Zn}(\text{IMP}, 0.5)$	4.0	1.97
$\text{Ga}_2\text{O}_3:\text{Zn}(\text{IMP}, 1)$	4.0	1.97
ZnGa_2O_4	3.8 (4.0) ^c	1.98 (1.98) ^c

^a Coordination number. N_t shows that for the tetrahedral Zn species and N_o shows that for the octahedral Zn species. ^b Atomic distance. ^c The value in parentheses shows the one reported in the crystal data base.

Curve fitting analysis was carried out for the first coordination peak around 1.6 Å by using theoretical parameters for a Zn-O shell and the results were listed in Table 2. Coordination number and atomic distance of Zn-O in the ZnO and ZnGa_2O_4 samples coincided with the reported values in the crystal data base (ICSD #26170 for ZnO and ICSD #81105 for ZnGa_2O_4). The first coordination peak of the $\text{Ga}_2\text{O}_3:\text{Zn}(\text{HP}, 3)$ sample was composed of one Zn-O shell, and the coordination number and atomic distance were almost the same as that of ZnGa_2O_4 . Combining with the results of XRD and XANES, Zn species in the $\text{Ga}_2\text{O}_3:\text{Zn}(\text{HP}, 3)$ sample should exist as ZnGa_2O_4 . When the doping amount of Zn decreased, the coordination number and the atomic distance were almost constant until 1%, showing that the major Zn species in these samples would

exist as ZnGa_2O_4 . However, they largely changed in the 0.5%-doped sample. The first coordination peak for the $\text{Ga}_2\text{O}_3:\text{Zn}(\text{HP}, 0.5)$ sample was composed of two Zn-O shells: a Zn-O shell with a shorter distance might correspond to Zn ions substituting for tetrahedrally coordinated Ga species in $\beta\text{-Ga}_2\text{O}_3$ and that with a longer distance might be the one substituting for the octahedrally coordinated Ga species in $\beta\text{-Ga}_2\text{O}_3$. The atomic distances of two Zn-O shells in the $\text{Ga}_2\text{O}_3:\text{Zn}(\text{HP}, 0.5)$ sample (1.91 and 2.09 Å) were larger than those between Ga and O in $\beta\text{-Ga}_2\text{O}_3$ (ca. 1.83 and 2.01 Å). This should be because the ionic radius of Zn^{2+} (0.74 Å) was larger than that of Ga^{3+} (0.62 Å). Thus, the two Zn-O shells would correspond to the tetrahedral and octahedral species, respectively. On the other hand, the coordination number and atomic distance of the $\text{Ga}_2\text{O}_3:\text{Zn}(\text{IMP})$ samples were almost the same as those of the ZnGa_2O_4 sample, showing that the Zn species in the $\text{Ga}_2\text{O}_3:\text{Zn}(\text{IMP})$ samples would exist as ZnGa_2O_4 .

Results of the XAFS analysis show that the Zn ions would substitute for both the tetrahedrally and octahedrally coordinated Ga species in the $\beta\text{-Ga}_2\text{O}_3$ when the small amount of Zn ions were doped by the HP method. However, ZnGa_2O_4 would form when the large amount of Zn was doped by the HP method and the sample was prepared by the IMP method.

3.3.3.4. Local Structure of Y Ions in $\text{Ga}_2\text{O}_3:\text{Y}$ Samples

The local structure of Y ion in the $\text{Ga}_2\text{O}_3:\text{Y}$ sample was examined with XAFS. Figure 9A shows Y K-edge XANES spectra of the Y_2O_3 , $\text{Y}_3\text{Ga}_5\text{O}_{12}$ and $\text{Ga}_2\text{O}_3:\text{Y}$ samples. The spectra of the $\text{Ga}_2\text{O}_3:\text{Y}$ samples (Figure 9A b-g) were similar with those of the Y_2O_3 and $\text{Y}_3\text{Ga}_5\text{O}_{12}$ sample (Figure 9A a and h). Clear differences were not observed. However, the Fourier transforms of EXAFS spectra of the $\text{Ga}_2\text{O}_3:\text{Y}$ samples were largely varied with the doping amount and the doping method. When the doping amount was not more than 2%, the spectra of the $\text{Ga}_2\text{O}_3:\text{Y}(\text{HP})$ samples (Figure 9B b-d) were different from those of the Y_2O_3 and $\text{Y}_3\text{Ga}_5\text{O}_{12}$ samples (Figure 9B a and h). However, the spectrum of the 3%-doped sample (Figure 9Be) was similar with that of the $\text{Y}_3\text{Ga}_5\text{O}_{12}$ sample. On the other hand, the spectra of the $\text{Ga}_2\text{O}_3:\text{Y}(\text{IMP})$ samples (Figure 9B f and g) were different from those of the $\text{Y}_3\text{Ga}_5\text{O}_{12}$ and $\text{Ga}_2\text{O}_3:\text{Y}(\text{HP})$ samples but was comparatively similar with that of the Y_2O_3 sample.

The curve fitting analysis was carried out for the first coordination peak around 1.8 Å and the results were listed in Table 3. The first coordination peaks of the $\text{Ga}_2\text{O}_3:\text{Y}(\text{IMP})$ samples were composed of one Y-O shell and the atomic distance was close to that of Y_2O_3 . The coordination numbers were smaller than that of Y_2O_3 . Thus, it is suggested that the Y ions on the $\text{Ga}_2\text{O}_3:\text{Y}(\text{IMP})$

samples would exist as Y_2O_3 with small particle sizes. From the crystal date base (ICSD #14343), one Y ion in $Y_3Ga_5O_{12}$ was surrounded by four oxygen ions at 2.34 Å in distance and four oxygen ions at 2.43 Å in distance (totally eight oxygen). Since the distances of two Y-O shells were relatively close to each other, the first coordination peak for the $Y_3Ga_5O_{12}$ was fitted by one Y-O shell at 2.38 Å in distance. The first coordination peak for the $Ga_2O_3:Y(HP, 3)$ sample was also composed of one Y-O shell and the coordination number and atomic distance were almost the same as $Y_3Ga_5O_{12}$. Combining with the results of XRD and XANES, the Y species on the $Ga_2O_3:Y(HP, 3)$ sample should exist as $Y_3Ga_5O_{12}$. The first coordination peaks for the $Ga_2O_3:Y(HP, 0.5-2)$ samples were composed of two Y-O shells: a Y-O shell with a shorter distance might correspond to the Y ions substituting for the tetrahedrally coordinated Ga species in $\beta-Ga_2O_3$, while that with a longer distance might be the one substituting for the octahedrally coordinated Ga species in $\beta-Ga_2O_3$. The distances of the Y-O shells in the $Ga_2O_3:Y(HP, 0.5-2)$ samples (2.21-2.23 and 2.38-2.41 Å) were much larger than those of Ga-O in $\beta-Ga_2O_3$ (ca. 1.83 and 2.01 Å) and Zn-O in $Ga_2O_3:Zn(HP, 0.5)$ (1.92 and 2.09 Å). This should be because the ionic radius of Y^{3+} (0.90 Å) was much larger than those of Ga^{3+} (0.62 Å) and Zn^{2+} (0.74 Å). It was suggested that large crystal distortion would be locally induced by Y-doping.

As a conclusion of this section, the Y ions would substitute for both the tetrahedrally and octahedrally coordinated Ga species in $\beta-Ga_2O_3$ and largely distort the local structure of $\beta-Ga_2O_3$, when the small amount of Y ions was doped by the HP method. However, the major Y ions would exist as $Y_3Ga_5O_{12}$, when the doping amount was larger than 3%. In the samples prepared by the IMP method, the major Y ions would not substitute for Ga ions in Ga_2O_3 but exist as small Y_2O_3

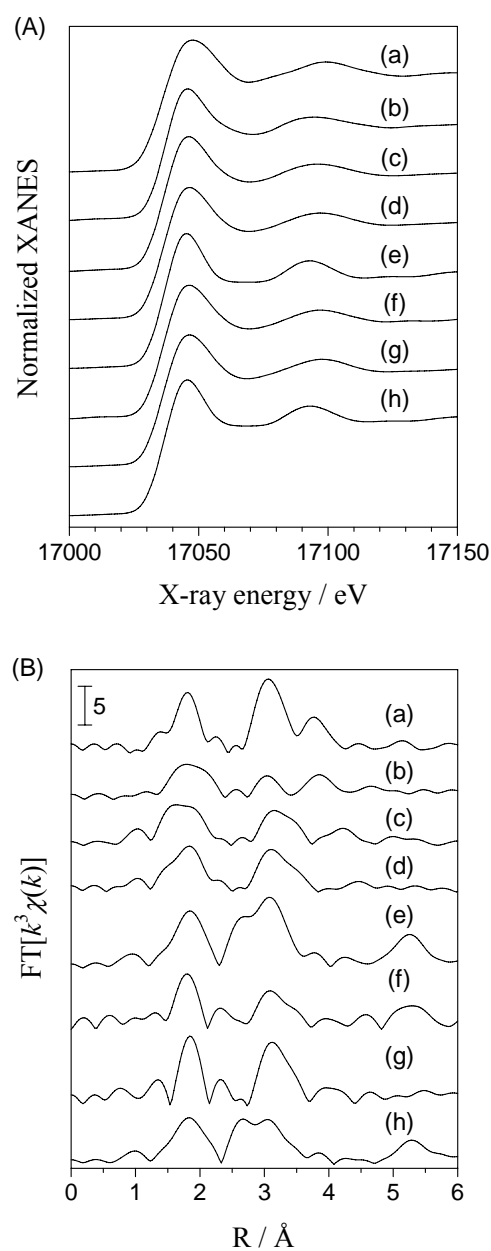


Figure 9. (A) Y K-edge XANES spectra and (B) the Fourier transforms of Y K-edge EXAFS spectra of (a) Y_2O_3 , (b)-(e) $Ga_2O_3:Y(HP)$, (f)-(g) $Ga_2O_3:Y(IMP)$ and (h) $Y_3Ga_5O_{12}$. Doping amount of Y was (b) 0.5, (c) 1, (d) 2, (e) 3, (f) 0.5 and (g) 1%.

particles on the β -Ga₂O₃.

Table 3 Result of EXAFS curve-fitting analysis for Y₂O₃, Ga₂O₃:Y and Y₃Ga₅O₁₂ samples

Sample	Y-O	
	N^a	$R^b / \text{\AA}$
Y ₂ O ₃	6.0	2.29
	(6.0) ^c	(2.288) ^c
Ga ₂ O ₃ :Y(HP, 0.5)	N_t : 1.4	2.23
	N_o : 3.6	2.41
Ga ₂ O ₃ :Y(HP, 1)	N_t : 1.5	2.21
	N_o : 3.4	2.38
Ga ₂ O ₃ :Y(HP, 2)	N_t : 1.6	2.22
	N_o : 3.4	2.38
Ga ₂ O ₃ :Y(HP, 3)	6.8	2.38
Ga ₂ O ₃ :Y(IMP, 0.5)	3.6	2.29
Ga ₂ O ₃ :Y(IMP, 1)	3.4	2.31
Y ₃ Ga ₅ O ₁₂	6.6	2.38
	(4.0) ^c	(2.338) ^c
	(4.0) ^c	(2.428) ^c

^a Coordination number. N_t shows that for the tetrahedral Y species and N_o shows that for the octahedral Y species. ^b Atomic distance. ^c The value in parentheses shows the one reported in the crystal data base.

4.3.3.5. Local Structure of Zr Ions in Ga₂O₃:Zr Samples

The local structure of the Zr ions in the Ga₂O₃:Zr samples were also examined with XAFS. Figure 10A shows the Zr K-edge XANES spectra of the ZrO₂ and Ga₂O₃:Zr samples. The spectra of the Ga₂O₃:Zr(HP) samples (Figure 10A b-d) were not varied with the doping amount and very similar with that of the bulk ZrO₂ sample (Figure 10Aa). On the other hand, the spectra of the Ga₂O₃:Zr samples prepared by the IMP method (Figure 10A e and f) were different from that of the ZrO₂ sample.

From the Fourier transforms of EXAFS spectra, the first coordination peak (around 1.6 Å) of the Ga₂O₃:Zr(HP) samples (Figure 10B b-d) was also similar with that of the ZrO₂ sample (Figure 9Ba). Fitting analysis showed that the first coordination peak for the Ga₂O₃:Zr(HP) samples was composed of one Zr-O shell, and the coordination number and the atomic distance were almost the same as those of the ZrO₂ sample (Table 4). Combining with the results of XRD and XANES,

the Zr ions on the Ga₂O₃:Zr(HP) sample would exist as small ZrO₂ particles. Intensity of the second coordination peak of the Ga₂O₃:Zr(HP) samples (around 3.0 Å) increased with increasing the Zr-doping amount (Figure 10B b-d). This shows that the particle size of ZrO₂ would increase with an increase of the doping amount.

The Fourier transforms of EXAFS spectra of the Ga₂O₃:Zr(IMP) samples (Figure 9B e and f) were different from those of the ZrO₂ and Ga₂O₃:Zr(HP) samples. The fitting analysis for the first coordination peak showed that the distance of Zr-O in the Ga₂O₃:Zr(IMP) sample was different from that of Zr-O in the ZrO₂ sample. The second coordination peak for the Ga₂O₃:Zr(IMP) samples shifted to the longer distance than those of the ZrO₂ and Ga₂O₃:Zr(HP) samples. Since one Ga³⁺ ion in β-Ga₂O₃ was surrounded by 11 Ga³⁺ at various distances from 3.04 to 3.61 Å (ICSD #34243), the fitting analysis for the second coordination peak was difficult. However, we roughly carried out the curve fitting analysis for the second coordination peak of the Ga₂O₃:Zr(IMP) samples, assuming that the second coordination peak of them was composed of one Zr-Ga shell. The atomic distance and the coordination number of the Zr-Ga shell were ca. 3.5 Å and 8. Thus, we could not distinguish whether Zr ions in the Ga₂O₃:Zr(IMP) sample would substitute for Ga ions in β-Ga₂O₃ or form composite oxide with Ga₂O₃.

XAFS study showed that Zr ions in the Ga₂O₃:Zr(HP) samples would exist as small ZrO₂ particles, while those in the Ga₂O₃:Zr(IMP) samples would substitute for Ga ions in β-Ga₂O₃ or form composite oxide with Ga₂O₃.

4.3.3.6. Relationship between the Local Structure of the Dopant and the Photocatalytic Activity

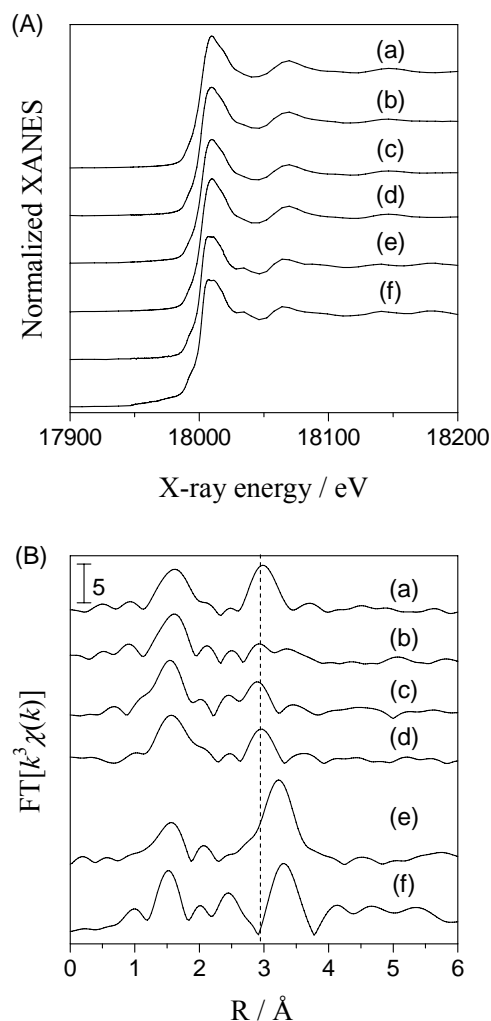


Figure 10. (A) Zr K-edge XANES spectra and (B) the Fourier transforms of Zr K-edge EXAFS spectra of (a) ZrO₂, (b)-(d) Ga₂O₃:Zr(HP) and (e)-(f) Ga₂O₃:Zr(IMP). Doping amount of Zr was (b) 0.5, (c) 1, (d) 2, (e) 0.5 and (f) 1%.

Influence of the doping on the photocatalytic activity was discussed. Basically, the photocatalytic activity tends to be influenced by the structure of the semiconductor such as the crystallite size, the specific surface area, bandgap and the morphology. In the present study, except for high-doping Ga₂O₃:Zn(HP) samples, doping metal ions, however, did not much influence these structural factors of Ga₂O₃. Thus, it is suggested that the activity of these doped catalysts would be mainly influenced by the state of the dopant. On the other hand, the destruction of the rod-like shape of the particles and the decrease of the photocatalytic activity were observed for the high-doping Ga₂O₃:Zn(HP) samples. Thus, the change of morphology would be one of the main reasons for the decrease of the photocatalytic activity of these samples.

Table 4 Result of EXAFS curve-fitting analysis for ZrO₂ and Ga₂O₃:Zr samples

Sample	Zr-O	
	<i>N</i> ^a	<i>R</i> ^b / Å
ZrO ₂	5.1 (7.0) ^c	2.13 (2.051–2.285) ^c
Ga ₂ O ₃ :Zr(HP, 0.5)	5.0	2.12
Ga ₂ O ₃ :Zr(HP, 1)	4.9	2.11
Ga ₂ O ₃ :Zr(HP, 2)	5.2	2.13
Ga ₂ O ₃ :Zr(IMP, 0.5)	2.7	2.08
Ga ₂ O ₃ :Zr(IMP, 1)	2.5	2.05

^a Coordination number. ^b Atomic distance. ^c The value in parentheses shows the one reported in the crystal data base.

Prepared metal-doped Ga₂O₃ samples were divided in two groups. One is that the added metal ions would substitute for Ga ions in β-Ga₂O₃. The other is that the metal ions would exist as metal oxide particles on the Ga₂O₃. Low-doping Ga₂O₃:Zn(HP) and Ga₂O₃:Y(HP) samples belong the former group, and Ga₂O₃:Zn(IMP), Ga₂O₃:Y(IMP) and Ga₂O₃:Zr(HP) samples belong the latter group. We could not distinguish whether Zr ions in Ga₂O₃:Zr(IMP) would substitute for Ga ions in Ga₂O₃ or make composite oxide with Ga₂O₃.

Among the former samples, the photocatalytic activity of the low-doping Ga₂O₃:Zn(HP) was higher than that of the undoped Ga₂O₃, while the activities of the Ga₂O₃:Y(HP) samples were lower than that of the undoped sample. This shows that doping metal ions with smaller oxidation number than that of Ga³⁺ would increase the activity. The doping metal ions with a small oxidation number would introduce the oxygen vacancy, which would trap the electrons in the semiconductor to reduce the

recombination sites of photoexcited electrons (perhaps Ga^+ in the case of $\beta\text{-Ga}_2\text{O}_3$), as proposed by various researchers (Figure 11b).^{8, 12-14} Since the migration of both the photoexcited electrons and holes must be equally promoted for the photocatalytic reaction, the optimum doping amount should exist as shown in Figure 11b. However, with further increasing the doping amount of Zn, the migration of photoexcited electrons would be further promoted, while that of holes would be suppressed due to the excess formation of the oxygen vacancies (Figure 11c). On the other hand, the substitution of Y^{3+} for Ga^{3+} decreased the activity, although Y ion having the same oxidation number as that of Ga^{3+} would not influence the electric property of Ga_2O_3 . Fitting analysis of EXAFS showed that Y doping would largely distort the local structure of Ga_2O_3 . Thus, this large crystal distortion would disturb the smooth migration of the photoexcited carriers to decrease the photocatalytic activity.

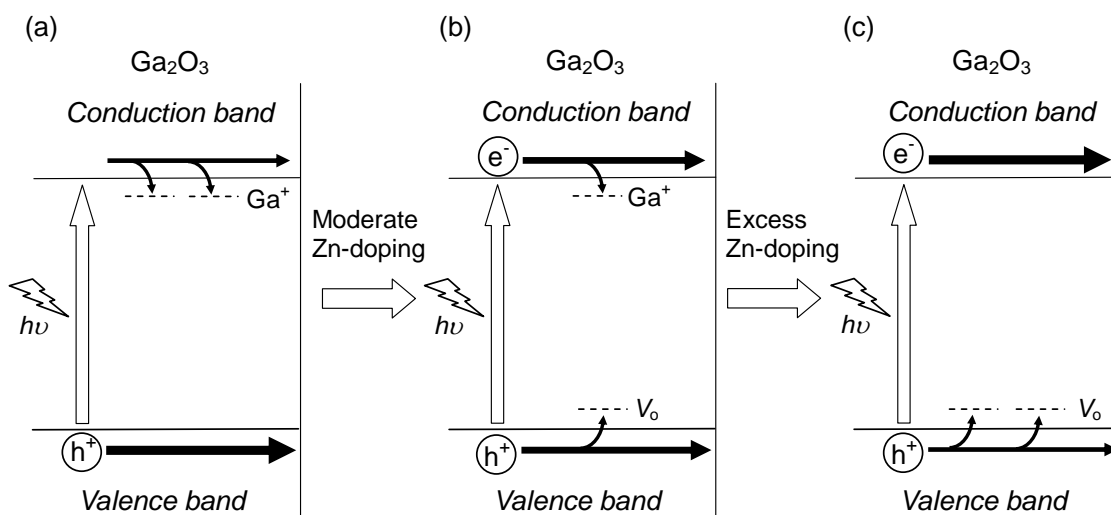


Figure 11. Effect of doping Zn ions on the migration of photoexcited carriers. V_o shows the oxygen vacancy: (a) photoexcited electrons in conduction band cannot smoothly migrate without doping, (b) both electrons and holes can equally migrate in the presence of optimum amount of dopant, and (c) holes in valence band cannot smoothly migrate with excess amount of dopant.

Among the latter groups, the photocatalytic activity of the $\text{Ga}_2\text{O}_3:\text{Zn(IMP)}$ samples was higher than that of the undoped Ga_2O_3 . This shows that loading of ZnGa_2O_4 on the surface of Ga_2O_3 would increase the photocatalytic activity. The reason why loading small amount of ZnGa_2O_4 on Ga_2O_3 increased the activity was not clear. Thus, it is speculated that the ZnGa_2O_4 might work as the adsorption sites of reactants or the cocatalyst on the ZnGa_2O_4 might promote the separation of photoexcited carriers. The activity of $\text{Ga}_2\text{O}_3:\text{Y(IMP)}$ was lower than that of the undoped sample. This shows that an existence of Y_2O_3 would decrease the activity. As reported in the previous study, even loading 0.1 wt% of Y_2O_3 on the surface of $\beta\text{-Ga}_2\text{O}_3$ decreased the activity, since Y_2O_3 may block the

active site for the reaction.⁴ Ga₂O₃:Zr(HP) showed the same activity as the undoped Ga₂O₃ did. It is identified that precipitation of Ga³⁺ should start at pH=3 in the aqueous solution, while that of Zr⁴⁺ should start at pH=2. This means that ZrO₂ particles existing in the Ga₂O₃:Zr(HP) sample would be surrounded by Ga₂O₃. Thus, it may not influence the photocatalytic activity.

To examine the effect of doping for the migration of photoexcited carriers, we measured the thermal activation energy of the Ga₂O₃:M(HP) samples. In the previous study,²¹ we examined the effect of thermal energy on the activity of Ga₂O₃ photocatalysts for the PSRM and clearly showed that the thermal energy contributed to the migration of photoexcited carriers in the bulk of Ga₂O₃ and at the metal semiconductor junction on the metal-loaded Ga₂O₃. Therefore, in the present study it was proposed that doping metal ions would influence the thermal activation energy of the photocatalyst. Thermal activation energies of the Ga₂O₃:Zn(HP, 0.5) and Ga₂O₃:Y(HP,0.5-2) samples were larger than that of the undoped Ga₂O₃, while those of the Ga₂O₃:Zn(HP, 1-2) and Ga₂O₃:Zr(HP, 0.5-2) samples were almost the same as that of the undoped Ga₂O₃. This result is reasonable because the metal ions on the former group would substitute for Ga ions in Ga₂O₃, while the metal ions on the latter samples would exist as metal oxide particles on the Ga₂O₃. For the Ga₂O₃:Zn(HP, 0.5) sample, the substitution of Zn ions would introduce the oxygen vacancy to increase the thermal activation energy. In the Ga₂O₃:Y(HP, 0.5-2) samples, since added Y ions largely distorted the local structure of Ga₂O₃, larger thermal energy would be required for the smooth migration of carriers as the activation energy.

4.3.4. Conclusions

Ga₂O₃ samples doped with metal ions (Zn²⁺, Y³⁺ and Zr⁴⁺) were prepared by the homogeneous precipitation (HP) method and the impregnation (IMP) method. Although doping metal ions did not much influence the crystallite size, the specific surface area, the bandgap and morphology of the particles except for the high-doping Ga₂O₃:Zn(HP) samples, the local structure of the dopant was varied with both the doping method and doping amount as well as the kind of the dopant. In the low-doping Ga₂O₃:Zn(HP) and Ga₂O₃:Y(HP) samples, metal ions substituted for Ga³⁺ in Ga₂O₃ and distorted the local structure of Ga₂O₃ more or less. On the other hand, in the high-doping Ga₂O₃:Zn(HP), Ga₂O₃:Zn(IMP), Ga₂O₃:Y(IMP) and Ga₂O₃:Zr(HP) samples, metal ions existed as small metal oxide particles such as ZnGa₂O₄, Y₂O₃ and ZrO₂. In the Ga₂O₃:Zr(IMP) sample, it was not clear whether Zr ions would substitute for Ga ions in Ga₂O₃ or form composite oxide with Ga₂O₃.

The photocatalytic activity of the prepared Ga₂O₃ samples for the photocatalytic steam reforming of methane was examined. The substitution of Zn²⁺ for Ga³⁺ increased the photocatalytic

activity, while that of Y^{3+} and Zr^{4+} for Ga^{3+} decreased it, showing that metal ions having a lower valence than that of Ga^{3+} and a similar ionic radius with that of Ga^{3+} would be effective as dopant. This was because the bulk electric property of Ga_2O_3 would be improved with less distortion of the crystal structure. The formation of the $ZnGa_2O_4$ phase on Ga_2O_3 was also effective for the increase of the photocatalytic activity.

References.

- 1) Yoshida, H.; Kato, S.; Hirao, K.; Nishimoto, J.; Hattori, T. *Chem. Lett.* **2007**, 36, 430–431.
- 2) Yoshida, H.; Hirao, K.; Nishimoto, J.; Shimura, K.; Kato, S.; Itoh, H.; Hattori, T. *J. Phys. Chem. C* **2008**, 112, 5542–5551.
- 3) Shimura, K.; Kato, S.; Yoshida, T.; Itoh, H.; Hattori, T.; Yoshida, H. *J. Phys. Chem. C* **2010**, 114, 3493–3503.
- 4) Shimura, K.; Yoshida, T.; Yoshida, H. *J. Phys. Chem. C* **2010**, 114, 11466–11474.
- 5) Shimura, K.; Yoshida, H. *Energy Environ. Sci.* **2010**, 3, 615–617.
- 6) Shimura, K.; Miyanaga, H.; Yoshida, H. *Stud. Surf. Sci. Catal.* **2010**, 175, 85–92.
- 7) Karakitsou, K.E.; Verykios X. E. *J. Phys. Chem.* **1993**, 97, 1184–1189.
- 8) Ishihara, T.; Nishiguchi, H.; Fukamachi, K.; Takita, Y.; *J. Phys. Chem. B* **1999**, 103, 1–3.
- 9) Kato, H.; Asakura, K.; Kudo, A. *J. Am. Chem. Soc.* **2003**, 125, 3082–3089.
- 10) Iwase, A.; Okutomi, H.; Kato, H.; Kudo, A. *Chem. Lett.* **2004**, 10, 1260–1261.
- 11) Arai, N.; Saito, N.; Nishiyama, H.; Domen, K.; Kobayashi, H.; Sato, K.; Inoue Y. *Catal. Today* **2007**, 129, 407–413.
- 12) Kadowaki, H.; Saito, N.; Nishiyama, H.; Inoue, Y. *Chem. Lett.* **2007**, 36, 440–441.
- 13) Takata, T.; Domen K. *J. Phys. Chem. C* **2009**, 113, 19386–19388.
- 14) Maeda, K.; Terashima, H.; Kase, K.; Higashi, M.; Tabata, M.; Domen, K. *Bull. Chem. Soc. Jpn* **2008**, 81, 927–937.
- 15) Yanagida, T.; Sakata, Y.; Imamura, H. *Chem. Lett.* **2004**, 33, 726–727.
- 16) Yuliati, L.; Hattori, T.; Itoh, H.; Yoshida, H. *J. Catal.* **2008**, 257, 396–402.
- 17) Yuliati, L.; Itoh, H.; Yoshida, H. *Chem. Phys. Lett.* **2008**, 452, 178–182.
- 18) Tsuneoka, H.; Teramura, K.; Shishido, T.; Tanaka, T.; *J. Phys. Chem. C* **2010**, 114, 8892–8898.
- 19) Hou, Y. D.; Wu, L.; Wang, X. C.; Ding, Z. X.; Li, Z. H.; Fu, X. Z. *J. Catal.* **2007**, 250, 12–18.
- 20) Sakata, Y.; Matsuda Y.; Yanagida T.; Hirata, K.; Imamura, H.; Teramura, K. *Catal. Lett.* **2008**, 125, 22–26.

- 21) Yoshida, H.; Maeda, K. *Stud. Surf. Sci. Catal.* **2010**, 175, 351–354.
- 22) Shimura, K.; Maeda, K.; Yoshida, H. *J. Phys. Chem. C*, in revision.
- 23) Nomura, M.; Koike, Y.; Sato, M.; Koyama, A.; Inada, Y.; Asakura, K. *AIP Conf. Proc.* **2007**, 882, 896.
- 24) Lytle, F. W.; Gregor, R. B.; Sandstorm, D. R.; Marques, E. C.; Wong, J.; Spiro, C. L.; Huffman, G. P.; Huggins, F. E. *Nucl. Instrum. Methods* **1984**, 226, 542–548.
- 25) Mckale, A. G.; Veal, B. W.; Paulikas, A.P.; Chan, S. K.; Knapp, G. S. *J. Am. Chem. Soc.* **1988**, 110, 3763–3768.

Chapter 5

Photocatalytic Hydrogen Production from Water Vapor and Methane over Pt/CaTiO₃

5.1. Hydrogen Production from Water and Methane over Pt-loaded Calcium Titanate Photocatalyst

Abstract

Pt/CaTiO₃ photocatalysts exhibited a higher production rate of hydrogen in the flowing mixture of water vapour and methane than that in the flow of water vapour only, since both the photocatalytic steam reforming of methane and the photocatalytic water decomposition simultaneously proceeded.

5.1.1. Introduction

Hydrogen has attracted much attention as one of the key components for solving the environmental and energy problems. Water decomposition (referred to as WD; $\text{H}_2\text{O} \rightarrow \text{H}_2 + 1/2\text{O}_2$) using photoenergy and photocatalyst is a very desirable system because it can produce hydrogen from renewable resources and solar energy. Many kinds of photocatalysts for the WD have been developed by many researchers.¹ However, practically available photocatalysts have not been found yet. This is probably because the WD would be a fundamentally challenging reaction with a large and positive value of Gibbs free energy change and the reverse reaction between hydrogen and oxygen to form water ($\text{H}_2 + 1/2\text{O}_2 \rightarrow \text{H}_2\text{O}$) can be easily promoted.

It is known that a sacrificial reagent such as methanol,² ethanol,³ saccharides,⁴ and CO⁵ can accelerate the hydrogen production by consuming photogenerated holes or photocatalytically produced oxygen species. In these kinds of reactions, only renewable resources can act as the sacrificial reagents to produce the truly environmentally-benign hydrogen. Our research group also found that some kinds of photocatalysts with Pt cocatalyst such as Pt/NaTaO₃:La and Pt/TiO₂ could effectively produce hydrogen from water by using methane as the sacrificial reagent, which can be referred to as the photocatalytic steam reforming of methane (PSRM; $2\text{H}_2\text{O} + \text{CH}_4 \rightarrow 4\text{H}_2 + \text{CO}_2$).⁶⁻⁸ In the reaction over these reported photocatalysts, the production of oxygen had not been observed and almost stoichiometric ratio of hydrogen and carbon dioxide ($\text{H}_2/\text{CO}_2=4$) were produced. If we use methane from biogas as one of the renewable resources, the PSRM can be also recognized as one of the hydrogen production methods from renewable resources and natural energy.

In the present research, we employed Pt/CaTiO₃ photocatalysts, which had been already reported to show the activity for the WD,⁹ and examined their photocatalytic activity for hydrogen

production in the flow of water and methane. We newly found that hydrogen could be produced through both the PSRM and the WD simultaneously in the coexistence of water vapour and methane.

5.1.2. Experimental

A CaTiO₃ sample was prepared by a solid-state reaction method. Starting materials, CaCO₃ (Kojundo, 99.99%) and rutile TiO₂ (Kojundo, 99.9%), were physically mixed by a wet ball-milling method using acetone. Obtained powder was put on an alumina boat and calcined in air at 1273 K for 10 h. The prepared CaTiO₃ sample was characterized by XRD, SEM, UV-vis spectra and N₂ adsorption. We confirmed that it had a crystal structure of CaTiO₃ perovskite and the average crystallite size was 31 nm. In SEM images, aggregated particles sized from 0.5 to 1 μm were observed. Band gap estimated from the UV-vis spectrum was ca. 3.5 eV. BET specific surface area was 1.7 m² g⁻¹. Pt cocatalyst was loaded on the CaTiO₃ sample by a photodeposition method. The CaTiO₃ sample (2.5 g) was dispersed in methanol (10 vol %) aqueous solution containing H₂PtCl₆, followed by photoirradiation for 1 h using a 300 W xenon lamp. Loading amount was in the range of 0.005-0.05 wt%.

The reaction tests were carried out with a fixed-bed flow type reactor.⁶⁻⁸ The catalysts were granulated to the size of 400-600 μm. The quartz cell (60 × 20 × 1 mm³) was filled with the mixture of catalyst (1.0 g) and quartz granules (0.4 g). The reaction gas, water vapour or a mixture of water vapour and methane, with argon carrier was introduced into the reactor at the flow rate of 40 mL min⁻¹ and the reaction was carried out upon photoirradiation with the 300 W xenon lamp. The concentration of water vapour and methane was 1.5% and 50%, respectively, and the light of the entire wavelength region from the xenon lamp was irradiated without passing any optical filters, where the light intensity measured in the range of 230-280 nm and 310-400 nm were ca. 14 and 60 mW cm⁻², respectively. The outlet gas was analysed by on-line gas chromatography with a thermal conductivity detector. No products were observed when the CaTiO₃ without Pt cocatalyst was photoirradiated in the flow of water vapour and in the mixture of water and methane (Table 1, entry 1).

5.1.3. Results and Discussion

Production of hydrogen and oxygen with the stoichiometric ratio (2:1) was observed over Pt(0.04 wt%)/CaTiO₃ photoirradiated in the flow of water (Fig. 1A), as reported in the literature.⁹ When the flow of methane was additionally introduced into the reactor, the hydrogen production rate became almost four times higher than that in the flow of water vapour and the production of carbon dioxide and

oxygen was also observed (Fig. 1B). The hydrogen production rate over Pt(0.04 wt%)/CaTiO₃ almost corresponded to the value calculated from the production rate of oxygen and carbon dioxide when they were assumed to be produced through the WD and the PSRM, respectively. This shows that these two reactions simultaneously occurred over photoirradiated Pt/CaTiO₃ in the mixture of water and methane. This phenomenon was found for the first time and quite different from the result of the previous studies.⁶⁻⁸ Over the reported photocatalysts such as Pt/NaTaO₃:La, the production of oxygen was never observed and only the PSRM proceeded in a very high selectivity in the mixture of water vapour and methane. In addition, it was interesting that the oxygen production rate increased after the introduction of methane (Fig. 1B). In other words, methane could accelerate the WD.

The activity of the Pt/CaTiO₃ photocatalyst largely varied with the loading amount of the Pt cocatalyst. Table 1 shows the hydrogen production rate in the flow of water or in the flowing mixture of water and methane. In the former condition, almost the stoichiometric ratio of hydrogen and oxygen were produced over every catalyst. In the latter condition, hydrogen, oxygen and carbon dioxide were produced. The products distribution indicated that only the two reactions, the WD and the PSRM, proceeded over every photocatalyst. Thus, the hydrogen production rate through the WD and the PSRM could be separately calculated from the production rate of oxygen and carbon dioxide, respectively, as listed in Table 1. In the flow of water, the hydrogen production rate increased with increasing the Pt loading amount until 0.01 wt% and then decreased as shown in Table 1. It is well known that Pt cocatalyst promotes the separation of the photoexcited carriers to increase the photocatalytic activity, while it also catalytically promotes the reverse reaction of the WD to decrease the apparent hydrogen production rate.¹⁰

When the reaction was carried out in the flow of water and methane over the Pt/CaTiO₃ sample of low Pt loading (Pt ≤ 0.01 wt%) (Table 1, entries 2 and 3), the PSRM proceeded but hydrogen production rate through the WD was lower than that in the flow of water. This was usual because the active oxygen species photoformed from water might be used for methane oxidation in the presence of methane, and the both the PSRM and the WD must competitively share the photoexcited carriers and

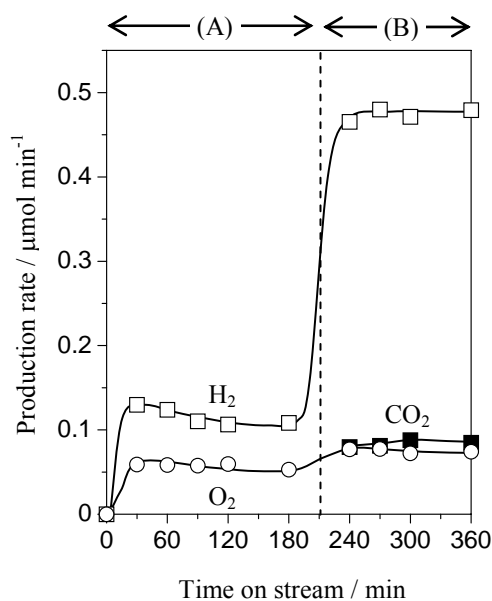


Figure 1. Time course of the production rate over Pt(0.04 wt%)/CaTiO₃ photocatalyst in the flow of (A) H₂O vapour (1.5%) and (B) a mixture of water vapour (1.5%) and methane (50%).

surface active sites. However, the total hydrogen production rate also became smaller than that in the flow of water, implying that the PSRM would not proceed effectively in the low Pt-loading samples.

Table 1 Hydrogen production rate over various Pt/CaTiO₃ photocatalysts

Entry	Pt ^a / wt%	H ₂ production rate / $\mu\text{mol min}^{-1}$					
		Reactant(s): Reaction(s):	H ₂ O ^b		H ₂ O+CH ₄ ^c		
			WD	WD	PSRM	Total	R ^d / %
1 ^e	0		n.d.	n.d.	n.d.	0.00	-
2 ^e	0.005		0.21	0.09	0.08	0.17	47
3 ^e	0.01		0.34	0.12	0.15	0.27	56
4 ^e	0.03		0.22	0.24	0.34	0.58	59
5 ^e	0.04		0.11	0.15	0.33	0.48	69
6 ^e	0.05		0.01	0.08	0.33	0.41	80
7 ^f	0.04		0.02	0.07	0.38	0.45	84
8 ^f	0.05		n.d.	0.05	0.40	0.45	89

^a Loading amount of Pt. ^b Reactant was H₂O (1.5%). ^c Reactants were H₂O (1.5%) and CH₄ (50%). ^d Ratio of the PSRM to the total rate in the flow of water and methane. ^e Reaction temperature was 313 K. ^f Reaction temperature was 323 K. n.d.=not detected

However, on the samples loaded with 0.03 wt% of Pt and more (Table 1, entries 4, 5 and 6), the PSRM predominately proceeded and the total production rate of hydrogen in the flow of water and methane became higher than that in the flow of water. The contribution of the PSRM to the total hydrogen production rate (R) also increased with an increase of the Pt-loading amount. These results show that a large amount of Pt would promote the methane activation. Furthermore, even the hydrogen production rate through the WD in the flow of water and methane was higher than that in the flow of water. Thus, it is suggested that the activated methane species or the reaction intermediates in the PSRM would accelerate the water activation or suppress the reverse reaction of the WD (Fig. 2). Although the reason has not clarified yet, some possibilities are tentatively proposed as follows: the surface species photoformed from methane and water may change the surface hydrophilic/hydrophobic properties to provide a suitable amount of water layers for promoting the WD and suppressing the reverse reaction, or they may modify the surface property of Pt particles to suppress the reverse reaction. Further investigation is necessary to clarify this point.

When the reaction temperature increased from 313 to 323 K, the activity for the WD largely decreased (Table 1, entries 7 and 8), but that for the PSRM increased. The decrease in the activity for the WD would support the presence of the reverse reaction catalysed by Pt cocatalyst.¹⁰ The increase of

the PSRM activity at higher temperatures was also observed on the Pt/NaTaO₃:La photocatalyst.⁸ The reasons are now investigated in detail.

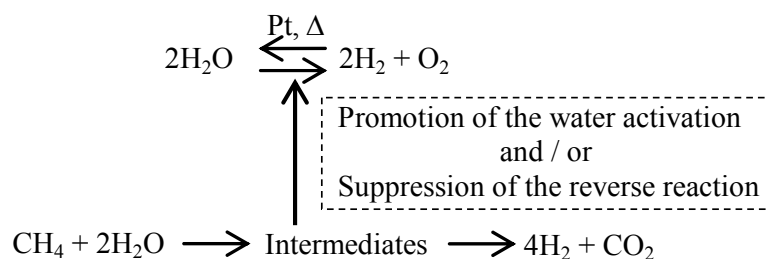


Figure 2. Proposed reaction scheme for acceleration of the water decomposition over Pt/CaTiO₃ photocatalyst in the flow of water and methane upon photoirradiation.

5.1.4. Conclusions

In the flow of water and methane, hydrogen was photocatalytically produced through both the WD and the PSRM over Pt/CaTiO₃. As a result, a higher hydrogen production rate was attained. Hydrogen production rate through the WD was enhanced in the presence of methane over Pt/CaTiO₃ of high Pt loading. It is suggested that the activated methane species or the reaction intermediates would accelerate the WD or suppress the reverse reaction.

References

- 1) Kudo, A.; Miseki, Y. *Chem. Soc. Rev.* **2009**, 38, 253–278.
- 2) Kawai, T.; Sakata, T. *J. Chem. Soc., Chem. Comm.* **1980**, 15, 694–695.
- 3) Sakata, T.; Kawai, T. *Chem. Phys. Lett.* **1981**, 80, 341–344.
- 4) Kawai, T.; Sakata, T. *Nature* **1980**, 286, 474–476.
- 5) Sato, S.; White, J.M. *J. Am. Chem. Soc.* **1980**, 102, 7206–7210.
- 6) Yoshida, H.; Kato, S.; Hirao, K.; Nishimoto, J.; Hattori, T. *Chem. Lett.* **2007**, 36, 430–431.
- 7) Yoshida, H.; Hirao, K.; Nishimoto, J.; Shimura, K.; Kato, S.; Itoh, H.; Hattori, T. *J. Phys. Chem. C* **2008**, 112, 5542–5551.
- 8) Shimura, K.; Kato, S.; Yoshida, T.; Itoh, H.; Hattori, T.; Yoshida, H. *J. Phys. Chem. C* **2010**, 114, 3493–3503.
- 9) Mizoguchi, H.; Ueda, K.; Orita, M.; Moon, S-C.; Kajihara, K.; Hirano M.; Hosono, H. *Mater. Res. Bull.* **2002**, 37, 2401–2406.
- 10) Sato, S.; White, J. M. *Chem. Phys. Lett.* **1980**, 72, 83–86.

5.2. Preparation of Calcium Titanate Photocatalysts for Hydrogen Production

Abstract

Various CaTiO₃ samples having different particle sizes, shapes, crystal defects and impurity phases were prepared by three methods, i.e., co-precipitation, homogeneous precipitation and solid-state reaction methods. The CaTiO₃ samples were loaded with Pt cocatalyst (0.1 wt%) and examined for both the photocatalytic water decomposition (WD) and the photocatalytic steam reforming of methane (PSRM). The highest activities for the WD and the PSRM were obtained over the samples prepared by the solid-state reaction method from rutile and anatase TiO₂, respectively. The controlling factors in their activity were discussed.

5.2.1. Introduction

The development of a hydrogen production method from renewable resources and natural energy would be important to realize a sustainable society. Since the photocatalytic water decomposition (referred to as WD; $\text{H}_2\text{O} \rightarrow \text{H}_2 + 1/2\text{O}_2$, =237 kJ/mol) would be one of the most desirable systems, various photocatalysts for it has been developed so far.¹ On the other hand, the photocatalytic hydrogen production from water and biomass such as ethanol,² saccharides³ and methane⁴ is also valuable. In these systems, hydrogen could be obtained more efficiently than the WD due to low ΔG values, and the carbon dioxide formed from them would not influence the global warming in the carbon neutral concept. We found that some kinds of Ptloaded semiconductors could efficiently produce hydrogen from water vapor and methane ($\text{CH}_4 + 2\text{H}_2\text{O} \rightarrow 4\text{H}_2 + \text{CO}_2$, =113 kJ/mol),⁴⁻⁷ which can be also interpreted as photocatalytic steam reforming of methane, thus referred to as PSRM.

CaTiO₃ has been known to show the photocatalytic activities. Pt-loaded CaTiO₃ has been reported to show photocatalytic activities for both the WD⁸ and the PSRM⁷ upon UV light irradiation. Generally, the important factors of the semiconductor photocatalyst in these reactions are considered to be some structural ones such as the crystallite size, the specific surface area and the band structure. In the present study, we prepared various CaTiO₃ samples by some methods and examined their photocatalytic activities for both the WD and the PSRM. And, we discussed the important factors of CaTiO₃ structure in the photocatalytic activities for the WD and the PSRM.

5.2.2. Experimental

5.2.2.1 Preparation of Photocatalysts

CaTiO₃ samples were prepared by three methods, i.e., co-precipitation method (CP), homogeneous precipitation method (HP) and solid-state reaction method (S).

In the co-precipitation method, CaCl₂·2H₂O (Wako, 99.9%, 5.4 g) and TiCl₄ HCl solution (Wako, 16–17% as Ti, 11.0 g) were dissolved in distilled water (100 ml). The solution was slowly added to an aqueous solution (300 ml) of (NH₄)₂C₂O₄·H₂O (Kishida, 99.5%, 10.4 g), where white precipitation was soon obtained. After neutralization of the solution by an aqueous NH₃ (Wako, 10%) the white precipitation was recovered by centrifugal separation and washed with distilled water several times. The obtained powder was dried at 353 K, followed by calcination in air at various temperatures (973–1273 K) for 10 h. The product yield was ca. 60 %.

In the homogeneous precipitation method, (COOH)₂·2H₂O (9.3 g), CaCl₂·2H₂O (5.4 g), and TiCl₄ HCl solution (11.0 g) were added to distilled water (300 ml), followed by heating up to 363 K. After an addition of (NH₂)₂CO (Kishida, 99.0%, 33.1 g) to the solution, it was kept at 363 K until pH of the solution reached to 7 (it took about 5.5 h), where white precipitate was gradually obtained as hydrolysis of the urea proceeded. The precipitates were recovered by centrifugal separation and washed with distilled water. The obtained powder was dried at 353 K, followed by calcination in air at various temperatures (973–1273 K) for 10 h. The product yield was ca. 60 %.

In the solid-state reaction method, the starting materials were physically mixed by a wet ball-milling method. As the starting TiO₂ material, employed were a purchased TiO₂ (Kojundo, 99.9%, rutile, 2.1 m²/g), JRC-TiO-6 (Catalysis Society of Japan, rutile, 100 m²/g), JRC-TiO-7 (ibid, anatase, 270 m²/g) and JRC-TiO-7 pre-calcined in air at 673 K for 5 h (anatase, 130 m²/g), which referred to as R₂, R₁₀₀, A₂₇₀ and A₁₃₀, respectively. CaCO₃ (Kojundo, 99.99%, 22.1 g), TiO₂ (17.6 g), alumina balls (150 g, 1 cm in diameter) and acetone (80 ml) were put into a plastic bottle (300 ml) and mixed well at room temperature (120 rpm, 24 h), followed by drying in an oven (343 K) overnight. The mixed powder was calcined in air at various temperatures (1073–1473 K) for 10 h. The prepared CaTiO₃ samples were referred to as CaTiO₃(method, TiO₂ source (if necessary), calcination temperature) such as CaTiO₃(CP, 973) and CaTiO₃(S, R₂, 1073).

Pt cocatalyst was loaded by a photodeposition method, as the similar way to the previous study.⁷ Loading amount was 0.1 wt%. The CaTiO₃ sample (2.0 g) was dispersed in a methanol aqueous solution (10 vol%, 400 ml) containing H₂PtCl₆ (Wako, 99.9%), followed by photoirradiation for 1 h

using a 300 W xenon lamp.

5.2.2.2. *Photocatalytic Reaction Test*

The reaction tests were carried out with a fixed-bed flow type reactor.⁴⁻⁷ The catalysts were granulated to the size of 400–600 μm . The quartz cell ($60 \times 20 \times 1 \text{ mm}^3$) was filled with a mixture of the catalyst (0.8 g) and quartz granules (0–0.7 g). The reaction gas, water vapor (1.5%) or a mixture of water vapor (1.5%) and methane (50%), with argon was fed to the reactor at the flow rate of 40 ml/min and the reaction was carried out upon photoirradiation with the 300 W xenon lamp. The light intensity measured in the range of 230–280 and 310–400 nm were 42 and 84 mW/cm^2 , respectively. The temperature of the reaction cell was ca. 323 K. The outlet gas was analyzed by on-line gas chromatography with a thermal conductivity detector.

5.2.2.3. *Characterization of Photocatalysts*

Powder X-ray diffraction (XRD) patterns were recorded on a MiniFlex II/AP (Rigaku) using Ni-filtered Cu $K\alpha$ radiation by using Si powder as an internal standard. Mean crystallite size of each sample was estimated from the diffraction line at 33.2 degree. Diffuse reflectance (DR) UV-vis spectra were recorded on a V-670 (JASCO) equipped with an integrating sphere. The Brunauer-Emmett-Teller (BET) specific surface area was calculated from the amount of N_2 adsorption at 77 K, which was measured on a Monosorb (Quantachrome). SEM images were recorded by S-5200 (Hitachi).

5.2.3. Results and Discussion

5.2.3.1. *Characterization of CaTiO_3 Samples Prepared by the CP and HP Methods*

Figure 1 shows the SEM images of the representative CaTiO_3 samples prepared by the CP and HP methods. For $\text{CaTiO}_3(\text{CP}, 1073)$, various sized particles (ca. 50–500 nm) were observed (Figure 1a). When the calcination temperature increased to 1273 K, the size increased to ca. 0.1–5 μm and the shape was still irregular (Figure 1b). For $\text{CaTiO}_3(\text{HP}, 1073)$, very small particles (ca. 50–200 nm) were observed and the size and shape of the particles were rather uniform in comparison with the $\text{CaTiO}_3(\text{CP})$ samples (Figure 1c). When the calcination temperature increased to 1273 K, the size slightly increased to ca. 200–500 nm (Figure 1d).

The different morphology of these two series of CaTiO_3 samples would be originated from the

generation mechanism of the precursors. In the preparation of the CaTiO₃(CP) samples, the white precipitation, i.e., CaTiO(C₂O₄)₂·H₂O, was produced as soon as the aqueous solution containing Ca²⁺ and Ti⁴⁺ ions was added to the aqueous solution of C₂O₄²⁻. However, it took a few second to finish pouring out the solution. When the formation of the metal complex and the successive crystallization are faster than the diffusion of the metal cations into the solution of ligand, the precipitation would occur heterogeneously in the solution, and then the size and the shape of the particles would become inhomogeneous. On the other hand, for the CaTiO₃(HP) samples, as the urea hydrolyzed, C₂O₄²⁻ ion was gradually produced in the solution and reacted with Ca²⁺ and Ti⁴⁺ ions to form CaTiO(C₂O₄)₂·H₂O. Since C₂O₄²⁻ ion was homogeneously produced in the solution, the size and the shape of the particles in the precursor and the calcined sample would be uniform.

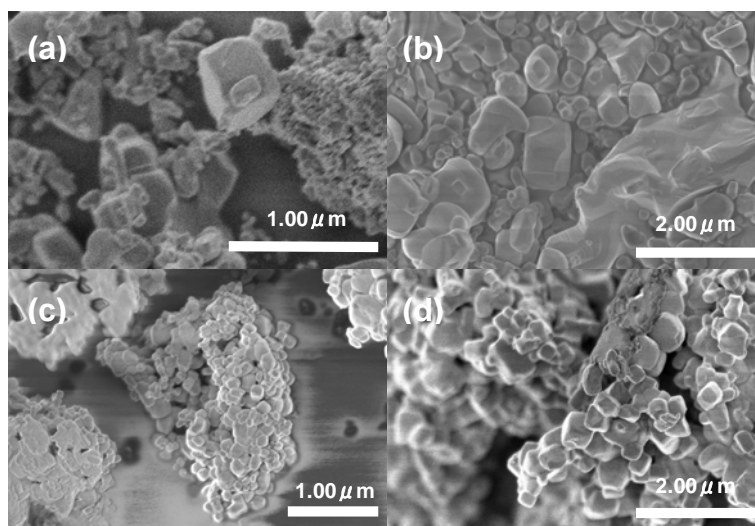


Figure 1. SEM images of (a) CaTiO₃(CP 1073), (b) CaTiO₃(CP, 1273), (c) CaTiO₃(HP, 1073) and (d) CaTiO₃(HP, 1273).

Figure 2 shows the XRD patterns of the representative CaTiO₃ samples. In the CaTiO₃(CP) samples, a single phase of CaTiO₃ was obtained by calcination at 1073 K and higher temperatures (Figure 2b). In the CaTiO₃(HP) samples, CaTiO₃ could be prepared at 1073 K and higher calcination temperatures, but impurities such as Ca(OH)₂ also existed there (Figure 2d). In the HP method, the hydrolysis of urea forms both NH₃ and CO₂. Produced CO₂ dissolved in water to form CO₃²⁻ ion, which precipitated Ca²⁺ ion as CaCO₃ (see Figure 2c). This would change the ratio of Ca²⁺ to Ti⁴⁺ in the calcined sample and provide the excess Ca specie as Ca(OH)₂ in air.

Figure 3 shows the DR UV-vis spectra of the CaTiO₃(CP) and CaTiO₃(HP) samples calcined at 1073 and 1273 K. The absorption edge of the CaTiO₃(HP) samples was slightly at the shorter

wavelength than that of $\text{CaTiO}_3(\text{CP})$ samples calcined at each temperature, and the edges shifted to longer wavelength when calcined at higher temperatures for each sample. The shift would be concerned with the variation of the crystallite size. The band gap estimated from the adsorption edge of the spectra was 3.5–3.6 eV. The color of the $\text{CaTiO}_3(\text{CP})$ sample calcined at 973 K was white, while that of the sample calcined at 1073 K was light pink and it became dark with increasing the calcination temperature. In the $\text{CaTiO}_3(\text{HP})$ samples, even the sample calcined at 973 K looked pink and the color became dark with increasing the calcination temperature. These result consisted with the absorption at visible light region in the UV-vis spectra (Figure 3 b-d). The maximum of the band was around 500 nm for the samples of dark pink. The formation of crystal defects such as Ti^{3+} sites and oxygen vacancies would be the reason for the coloration. The deeper colors of the $\text{CaTiO}_3(\text{HP})$ samples than those of the $\text{CaTiO}_3(\text{CP})$ samples would show the existence of larger amount of the crystal defects. In addition, when $\text{Ti}(\text{SO}_4)_2$ was used instead of TiCl_4 in the CP method, the color of the sample became much deeper. From these results, it is suggested that unreacted additives such as urea and the counter anions of the starting materials such as Cl^- would adsorb on the surface of the precursor and cause the formation of defects during the calcination.

Figure 4 shows the crystallite size and the BET specific surface area of the $\text{CaTiO}_3(\text{CP})$ and $\text{CaTiO}_3(\text{HP})$

samples. As the calcination temperature increased, the crystallite size tended to increase though the $\text{CaTiO}_3(\text{HP})$ samples calcined at 1173 and 1273 K were exceptional (Figure 4a). However, the surface area was not inversely proportional to the crystallite size, which would be due to the presence of polycrystal particles including very small crystallites and amorphous parts. The specific surface areas of $\text{CaTiO}_3(\text{CP}, 973)$ and $\text{CaTiO}_3(\text{HP}, 973)$ samples were 18 and 24 m^2/g , respectively, and they drastically decreased to less than 10 m^2/g with increasing the calcination temperature (Figure 4b). The crystallite size and the specific surface area of the samples calcined at the same temperature were almost the same

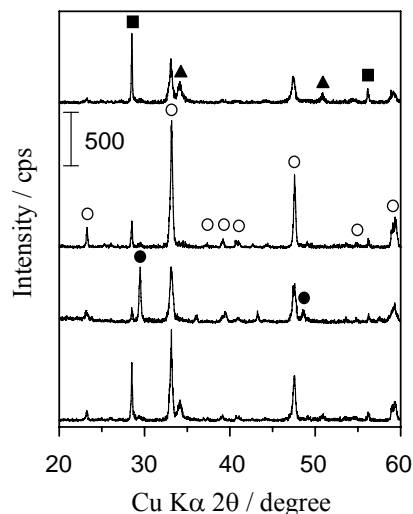


Figure 2. XRD patterns of (a) $\text{CaTiO}_3(\text{CP}, 973)$, (b) $\text{CaTiO}_3(\text{CP}, 1073)$, (c) $\text{CaTiO}_3(\text{HP}, 973)$ and (d) $\text{CaTiO}_3(\text{HP}, 1073)$. \circ : CaTiO_3 , \blacktriangle : $\text{Ca}(\text{OH})_2$, \bullet : unknown and \blacksquare : Si for the angle correction.

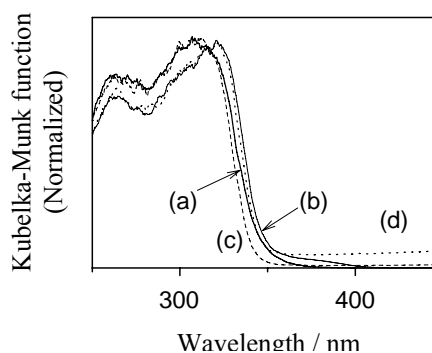


Figure 3. DR UV-vis spectra of (a) $\text{CaTiO}_3(\text{CP}, 1073)$, (b) $\text{CaTiO}_3(\text{CP}, 1273)$, (c) $\text{CaTiO}_3(\text{HP}, 1073)$ and (d) $\text{CaTiO}_3(\text{HP}, 1273)$.

values, which implied that they would be mainly influenced by not the preparation method but the calcination temperature.

As a conclusion of this section, the CP method provided the single phase of CaTiO_3 having irregular morphology, and the HP method gave the small CaTiO_3 particles of a uniform shape although the crystal defects and the impurity phase of $\text{Ca}(\text{OH})_2$ existed.

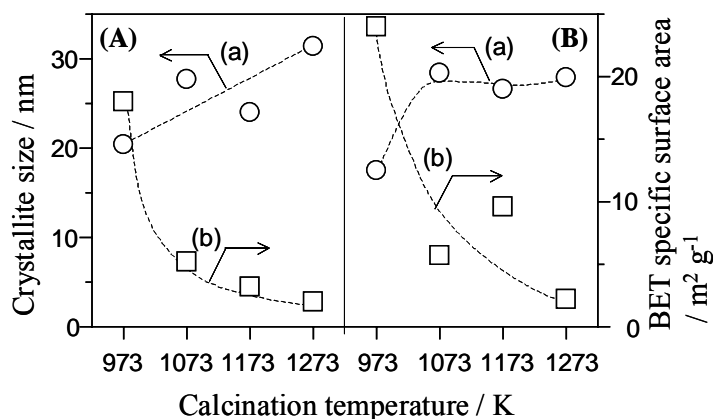


Figure 4. (a) Crystallite size and (b) specific surface area of the CaTiO_3 samples calcined at various temperatures prepared by (A) the CP method and (B) the HP method.

5.2.3.2. Characterization of CaTiO_3 Samples Prepared by the S Method

Influence of the calcination temperature was examined for the $\text{CaTiO}_3(\text{S}, \text{R}_2)$ samples. In their SEM images, aggregated particles were observed. Figure 5a shows the representative one. The particle size (ca. 1 μm) did not depend on the calcination temperature and was almost the same as that of R_2 used as the starting TiO_2 material. In their XRD patterns, large diffraction lines assignable to unreacted TiO_2 (rutile) and $\text{Ca}(\text{OH})_2$ were observed when the sample was calcined at 1073 K (Figure 6a) and they were hardly observed for the sample calcined at 1273 K and higher temperatures (Figure 6b). For $\text{CaTiO}_3(\text{S}, \text{R}_2, 1073)$, a large absorption band assigned to TiO_2 (rutile) was observed (Figure 7a), while it quite decreased but still remained in $\text{CaTiO}_3(\text{S}, \text{R}_2, 1273)$ (Figure 7b). These Results shows that higher temperature than 1273 K was required to obtain a pure CaTiO_3 by the S method from this rutile TiO_2 sample. The colors of the samples calcined at 1173 K and lower temperatures were white, while that of $\text{CaTiO}_3(\text{S}, \text{R}_2, 1273)$ was light pink. In other words, these $\text{CaTiO}_3(\text{S})$ samples had a smaller amount of crystal defects than $\text{CaTiO}_3(\text{CP})$ and $\text{CaTiO}_3(\text{HP})$ sample did, although high temperatures were required to obtain a single phase.

Other three kinds of TiO_2 powders, R_{100} , A_{130} and A_{270} , were also examined as the starting

materials for the preparation of CaTiO_3 samples by the S method, followed by calcination at 1273 K. When TiO_2 powders of higher surface area were used, the particle size of CaTiO_3 samples became smaller as shown in SEM images (Figure 5 b–5d). From XRD, the formation of CaTiO_3 was confirmed and no impurity phases were observed (not shown). From UV-vis spectra, the small absorption in the range of 350–400 nm disappeared in the three $\text{CaTiO}_3(\text{S}, 1273)$ samples (Figures. 7c and 7d). These results show that no impurities existed in the three $\text{CaTiO}_3(\text{S}, 1273)$ samples prepared from TiO_2 particles of high surface area.

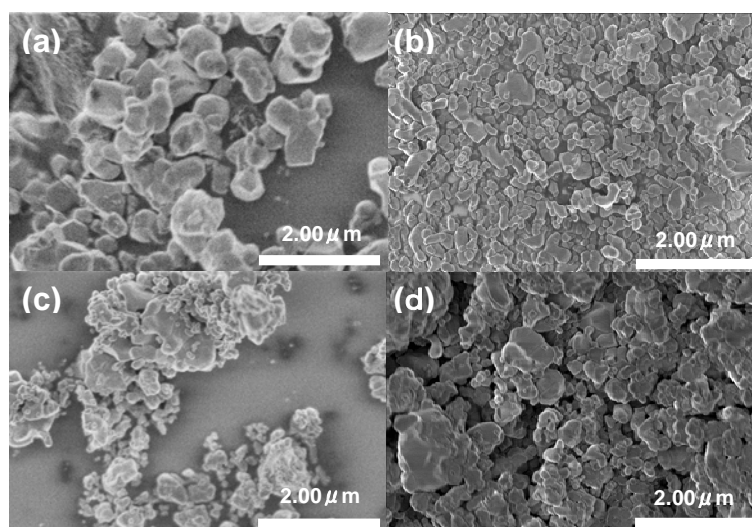


Figure 5. SEM images of representative $\text{CaTiO}_3(\text{S}, 1273)$ samples. Starting TiO_2 material is (a) R_2 , (b) R_{100} , (c) A_{130} and (d) A_{270} .

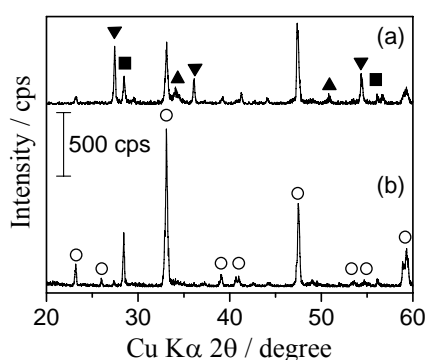


Figure 6. XRD patterns of (a) $\text{CaTiO}_3(\text{S}, \text{R}_2, 1073)$, and (b) $\text{CaTiO}_3(\text{S}, \text{R}_2, 1273)$. ○: CaTiO_3 , ▲: $\text{Ca}(\text{OH})_2$, ▼: $\text{TiO}_2(\text{Rutile})$ and ■: Si for the angle correction.

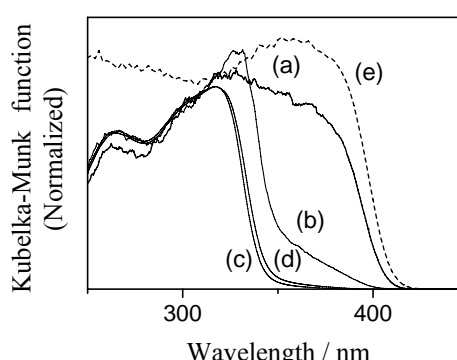


Figure 7. DR UV-vis spectra of $\text{CaTiO}_3(\text{S}, \text{R}_2, 1073)$, (b) $\text{CaTiO}_3(\text{S}, \text{R}_2, 1273)$, (c) $\text{CaTiO}_3(\text{S}, \text{R}_{100}, 1273)$, (d) $\text{CaTiO}_3(\text{S}, \text{A}_{130}, 1273)$ and (e) TiO_2 (rutile). $\text{CaTiO}_3(\text{S}, \text{A}_{270}, 1273)$ showed the same spectrum as (d).

The colors of the four $\text{CaTiO}_3(\text{S}, 1273)$ samples including including $\text{CaTiO}_3(\text{S}, \text{R}_2, 1273)$ were pale pink, showing that amount of crystal defects would be similarly small. The crystallite size did not depend on the kind of TiO_2 (Figure 8Ba), while the specific surface areas of three $\text{CaTiO}_3(\text{S}, 1273)$ samples prepared from TiO_2 particles of high surface area were larger than that of $\text{CaTiO}_3(\text{S}, \text{R}_2, 1273)$ (Figure 8Bb). The specific surface areas of the two CaTiO_3 samples prepared from anatase were smaller than that of $\text{CaTiO}_3(\text{S}, \text{R}100, 1273)$, suggesting that the specific surface area of A_{130} and A_{270} would be reduced by sintering to be less than $100 \text{ m}^2/\text{g}$ before the solid-solid reaction started.

As a conclusion of this section, it was found that the CaTiO_3 samples of high surface area without impurities could be obtained by using TiO_2 of high specific surface area as the starting materials.

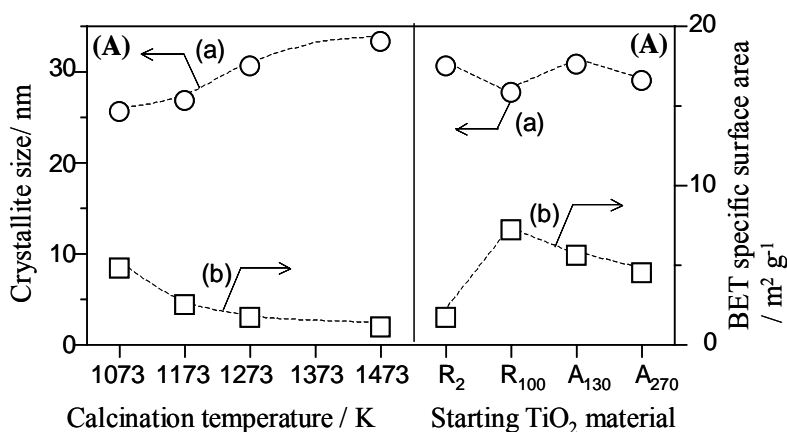


Figure 8. (a) Crystallite size and (b) BET specific surface area of (A) $\text{CaTiO}_3(\text{S}, \text{R}_2)$ samples calcined at various temperatures and (B) $\text{CaTiO}_3(\text{S}, 1273)$ prepared from various TiO_2 raw materials.

5.2.3.3. Photocatalytic Activities of the Prepared CaTiO_3 Samples

Figure 9 shows the hydrogen production rate in the WD and the PSRM over $\text{Pt}(0.1 \text{ wt}\%)/\text{CaTiO}_3$ samples. On almost all the samples, the hydrogen production rate in the PSRM was much higher than that in the WD. Another experiments showed that the loading amount of 0.1 wt% employed here was suitable for the PSRM but excess for the WD since Pt could promote the reverse reaction of the WD ($\text{H}_2 + 1/2\text{O}_2 \rightarrow \text{H}_2\text{O}$).⁹ The hydrogen production rate in the WD on the $\text{Pt}/\text{CaTiO}_3(\text{CP})$ and $\text{Pt}/\text{CaTiO}_3(\text{S})$ samples tended to increase with decreasing the calcination temperature (Figures. 9Aa and 9Ca). In other words, it increased with increasing the specific surface area of the catalyst or decreasing the defects. Thus, one possibility is that the number of the surface Pt nano-particles per unit area decreased with the increase of the surface area and the reverse reaction between the oxygen produced on

the CaTiO_3 surface and the hydrogen produced over Pt might decrease. However, the activities of the $\text{Pt}/\text{CaTiO}_3(\text{CP}, 973)$ and $\text{Pt}/\text{CaTiO}_3(\text{HP}, 973)$ samples were low, although the specific surface areas of them were high. This shows that a large crystallite size would be also important to promote the WD. The highest activity for the WD was obtained over $\text{Pt}/\text{CaTiO}_3(\text{S}, \text{R}_2, 1073)$ having a high surface area and a relatively large crystallite size. Among the four $\text{Pt}/\text{CaTiO}_3(\text{S}, 1273)$ samples prepared from various TiO_2 samples, $\text{Pt}/\text{CaTiO}_3(\text{S}, \text{R}_{100}, 1273)$ with the largest surface area showed the highest activity for the WD (Figure 9Da).

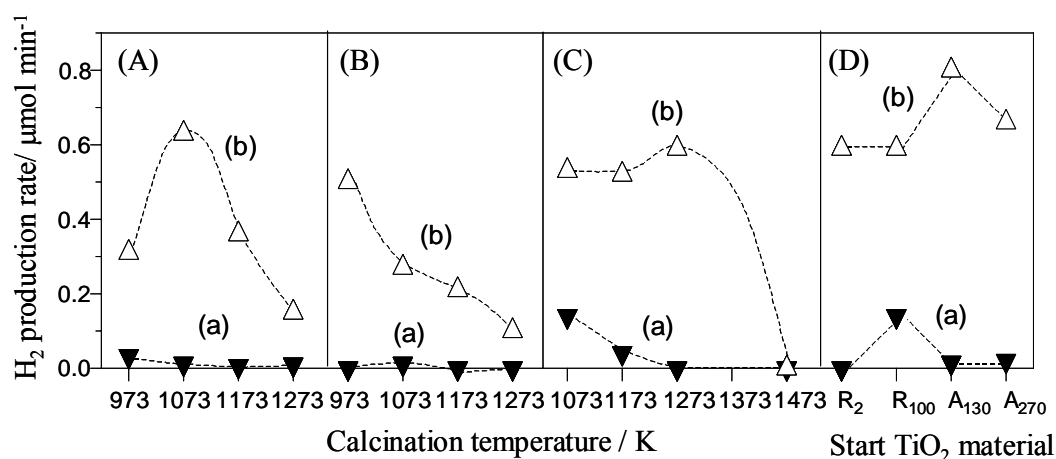


Figure 9. Hydrogen production rate on the $\text{Pt}(0.1 \text{ wt}\%)/\text{CaTiO}_3$ samples in (a) the WD and (b) the PSRM; (A) the $\text{Pt}/\text{CaTiO}_3(\text{CP})$ samples, (B) the $\text{Pt}/\text{CaTiO}_3(\text{HP})$ samples, (C) the $\text{Pt}/\text{CaTiO}_3(\text{S}, \text{R}_2)$ samples and (D) the $\text{Pt}/\text{CaTiO}_3(\text{S}, 1273)$ samples prepared from various TiO_2 raw materials.

In the $\text{CaTiO}_3(\text{CP})$ and $\text{CaTiO}_3(\text{S}, \text{R}_2)$ samples, the activity for the PSRM first increased with increasing the calcination temperature (Figures. 9Ab and 9Cb), and the highest activity was obtained over $\text{CaTiO}_3(\text{CP}, 1073)$ and $\text{CaTiO}_3(\text{S}, \text{R}_2, 1273)$ samples, respectively. The increase of the activity would be related to the increase of the crystallite size (Figures. 4 and 8), which would promote the smooth migration of photogenerated carriers in the conduction and valence bands to the surface. However, the activity decreased with further increasing the calcination temperature though the crystallite size increased. The colors of $\text{CaTiO}_3(\text{CP}, 1073)$ and $\text{CaTiO}_3(\text{S}, \text{R}_2, 1273)$ samples were pale pink, while those of the samples calcined at higher temperatures were grayish pink. Therefore, these defects would decrease the activity. On the other hand, in the $\text{CaTiO}_3(\text{HP})$ samples, the activity monotonously decreased with increasing the calcination temperature (Figure 9Bb). As mentioned, in these samples, the colors were pink even when calcined at 973 K and became dark with increasing the calcination temperature. Thus, the negative effect of the defects formation would become superior to the positive effect of the crystallite growth, resulting the decrease of the activity. These facts in Figure. 9

A–C show that the CaTiO₃ samples with large crystallite sizes and few crystal defects would be effective for promoting the PSRM.

Among the four CaTiO₃(S, 1273) samples (Figure. 9D), the CaTiO₃ samples prepared from anatase showed higher activity than the CaTiO₃ samples prepared from rutile. The highest activity was obtained over CaTiO₃(S, A₁₃₀, 1273). Though the colors of the CaTiO₃(S, A₁₃₀, 1273) and CaTiO₃(S, A₂₇₀, 1273) samples were similar to each other, the specific surface area and the crystallite size of the former were a little larger than those of the latter as shown in Figure 8. These factors would improve the PSRM activity.

5.2.4. Conclusions

We prepared CaTiO₃ samples by three methods, i.e., co-precipitation (CP), homogeneous precipitation (HP) and solid-state reaction (S) methods, and examined their photocatalytic activities for the water decomposition (WD) and the steam reforming of methane (PSRM). By the CP method, large CaTiO₃ particles without impurity phases could be obtained at 1073 K and higher temperatures though the particle size and shape were inhomogeneous. By the HP method, small CaTiO₃ particles with the regular shape could be obtained although the crystal defects formed even at low temperatures like 973 K and impurities such as Ca(OH)₂ coexisted. By the S method, the crystallites with few defects could be produced, though high temperatures such as 1273 K or higher were required to obtain pure CaTiO₃. When rutile TiO₂ of large surface area was used as the starting material for the S method, CaTiO₃ of high specific surface area was obtained. CaTiO₃(S, R₂, 1073) and CaTiO₃(S, R₁₀₀, 1273) showed the highest activity for the WD and CaTiO₃(S, A₁₃₀, 1273) was the best for the PSRM. For the WD, the high surface area was more important than the large crystallite size, while, for the PSRM, the large crystallite size was more important. The CaTiO₃ samples with few defects showed high activities for both reactions.

References

- 1) Kudo, A.; Miseki, Y. *Chem. Soc. Rev.* **2009**, 38, 253–278.
- 2) Sakata, T.; Kawai, T. *Chem. Phys. Lett.* **1981**, 80, 341–344.
- 3) Kawai, T.; Sakata, T. *Nature* **1980**, 286, 474–476.
- 4) Yoshida, H.; Kato, S.; Hirao, K.; Nishimoto, J.; Hattori, T. *Chem. Lett.* **2007**, 36, 430–431.
- 5) Yoshida, H.; Hirao, K.; Nishimoto, J.; Shimura, K.; Kato, S.; Itoh, H.; Hattori, T. *J. Phys. Chem. C* **2008**, 112, 5542–5551.

- 6) Shimura, K.; Kato, S.; Yoshida, T.; Itoh, H.; Hattori, T.; Yoshida, H. *J. Phys. Chem. C* **2010**, 114, 3493–3503.
- 7) Shimura, H.; Yoshida, H. *Energy Environ. Sci.* **2010**, 3, 615–617.
- 8) Mizoguchi, H.; Ueda, K.; Orita, M.; Moon, S-C.; Kajihara, K.; Hirano M.; Hosono, H. *Mater. Res. Bull.* **2002**, 37, 2401–2406.
- 9) Sato, S.; White, J. M. *Chem. Phys. Lett.* **1980**, 72, 83–86.

Chapter 6

Photocatalytic Steam Reforming of Methane over Potassium Titanate

Abstract

Photocatalytic steam reforming of methane (PSRM) was examined over metal-loaded $\text{K}_2\text{Ti}_6\text{O}_{13}$. Although Pt-loading increased the photocatalytic activity of $\text{K}_2\text{Ti}_6\text{O}_{13}$ for the PSRM, the progress of side reaction and the deactivation of photocatalyst were observed. On the other hand, Rh-loaded $\text{K}_2\text{Ti}_6\text{O}_{13}$ showed two times higher activity than Pt-loaded one did and selectively promoted the PSRM without deactivation for a long time. Over the highly active Rh/ $\text{K}_2\text{Ti}_6\text{O}_{13}$ photocatalyst, Rh cocatalyst existed as the mixture of small metallic Rh and large Rh oxide particles. The former would accelerate hydrogen formation and promote the electron migration in the conduction band, while the latter would promote the oxidative reaction and enhance the migration of holes in the valence band, respectively.

6.1. Introduction

Development of the hydrogen production method from renewable resources and natural energy is important to realize a sustainable society. Hydrogen production from biomass or its derivatives is one of the promising ways. Our research group found that some kinds of Pt-loaded semiconductors such as Pt/ TiO_2 and Pt/ Ga_2O_3 promoted photocatalytic steam reforming of methane (PSRM; $\text{CH}_4 + 2\text{H}_2\text{O} \rightarrow 4\text{H}_2 + \text{CO}_2$) around room temperature.¹⁻⁶ The PSRM is an attractive reaction to convert solar energy into the chemical potential of the storable hydrogen by consuming only renewable resources, methane and water. The efficiency of this photocatalytic system is, however, still low and development of an efficient photocatalyst is required now.

Loading cocatalysts is one of the effective ways to improve the photocatalytic activity, and various cocatalysts have been developed by many researchers. For example, NiO_x ,⁷⁻⁹ RuO_2 ¹⁰ and Rh-Cr^{11, 12} cocatalysts were effective to increase the activity of various photocatalysts for the water decomposition. PdS,¹³ MoS_2 ,¹⁴ and NiS¹⁵ increased the photocatalytic activity of CdS photocatalyst for the hydrogen production from water. Ru^{16, 17} was effective for the improvement of the oxynitride photocatalysts for the hydrogen production from aqueous alcohol solution. Pt¹⁸ and Pd¹⁹ were reported to enhance the activity of WO_3 photocatalyst for the degradation of organic compounds. Of course, Pt-loaded TiO_2 was very famous for showing high photocatalytic activities for various reactions.²⁰ Since the effective cocatalyst was varied with kinds of the semiconductor and photocatalytic reaction, the optimization of cocatalyst would be necessary for each system and reaction condition.

In the present study, influence of the cocatalysts for the PSRM was examined by using potassium titanate ($\text{K}_2\text{Ti}_6\text{O}_{13}$) photocatalyst. $\text{K}_2\text{Ti}_6\text{O}_{13}$ loaded with RuO_2 cocatalyst had been reported to show photocatalytic activity for the water splitting.²¹ $\text{K}_2\text{Ti}_6\text{O}_{13}$ loaded with Pt cocatalyst was also reported to show the photocatalytic activity for the decomposition of water including Na_2CO_3 .²² Since the water activation would be one of the important steps in the PSRM, it was considered that $\text{K}_2\text{Ti}_6\text{O}_{13}$ has a possibility to show an activity for the PSRM. In the present study, we newly found that Rh-loaded $\text{K}_2\text{Ti}_6\text{O}_{13}$ showed a high photocatalytic activity for the PSRM and the hydrogen production rate over this sample was higher than that over Pt-loaded $\text{K}_2\text{Ti}_6\text{O}_{13}$. We carefully examined the influence of the loading method on both the structure of Rh cocatalyst and the PSRM activity of the loaded photocatalyst. Important factors for Rh-loaded $\text{K}_2\text{Ti}_6\text{O}_{13}$ photocatalyst to exhibit a high activity were proposed here.

6.2. Experimental

6.2.1. Preparation of Photocatalysts

$\text{K}_2\text{Ti}_6\text{O}_{13}$ was prepared by the solid-state reaction method. Starting materials employed were K_2CO_3 (Kishida, 99.5%) and rutile- TiO_2 (Kojundo, 99.9%). They were mechanically mixed in a stoichiometric ratio by a wet ball-milling method, where alumina balls (150 g, 1 cm in diameter), starting materials (ca. 20 g) and acetone (80 ml) were put into a plastic bottle (300 ml) and they were mixed at 120 rpm for 24 h, followed by drying in an oven (333 K) overnight. The mixed powder was calcined in air at 1273 K for 10 h in a platinum crucible. After cooling it to room temperature, it was ground by an alumina mortar and washed with distilled water.

$\text{Na}_2\text{Ti}_6\text{O}_{13}$, TiO_2 and $\beta\text{-Ga}_2\text{O}_3$ were used as the reference samples. $\text{Na}_2\text{Ti}_6\text{O}_{13}$ was prepared by the same procedure as $\text{K}_2\text{Ti}_6\text{O}_{13}$, where Na_2CO_3 (Kishida, 99.5%) was used instead of K_2CO_3 as the starting material. TiO_2 (JRC-TIO-8, anatase, $338 \text{ m}^2\text{g}^{-1}$) was supplied from the Catalyst Society of Japan and calcined in air at 673 K for 6 h as the pretreatment. $\beta\text{-Ga}_2\text{O}_3$ was commercially obtained (Kojundo, 99.99%).

The semiconductor photocatalysts were loaded with metal cocatalysts (Rh, Pt, Ru, Pd and Au). The loading amount (x) of these metals was in the range from 0.01 to 1 wt%. The employed precursors were as follows; $\text{RhCl}_3 \cdot 3\text{H}_2\text{O}$ (Kishida, 99%), $\text{H}_2\text{PtCl}_6 \cdot 6\text{H}_2\text{O}$ (Wako, 99.9%), $(\text{NH}_4)_3\text{RuCl}_6$ (Mitsuwa, chemical grade), PdCl_2 (Kishida, 99%) and HAuCl_4 (Kishida, 99%). Cocatalysts were loaded by an impregnation method or a photodeposition method. In the impregnation method, the photocatalyst

powder (2.0 g) was dispersed into an aqueous solution (50 ml) of the metal precursor and stirred for 0.5 h, followed by evaporation to dryness with a rotary evaporator. Then, the dried powder was calcined in air at 773 K for 2 h, and/or reduced in a flow of hydrogen (10 ml min^{-1}) at 473 K for 0.5 h as the pretreatment. In the photodeposition method, catalyst (2.5 g) was dispersed into aqueous methanol (10%) solution (400 ml) containing precursor of metal cocatalyst in a Pyrex glass vessel with vigorous stirring, followed by photoirradiation from the top by using a 300 W xenon lamp, which entirely emitted from UV to visible light, for 2 h with continuous stirring. Then, the suspension was filtered off with suction, washed with distilled water, and dried at 323 K. The sample with the cocatalyst was referred to as Rh(x)/K₂Ti₆O₁₃ for example.

6.2.2. Photocatalytic Reaction Tests

The reaction tests were carried out with a fixed-bed flow reactor.¹⁻⁶ The catalysts were granulated to the size of 400–600 μm . The quartz cell ($60 \times 20 \times 1 \text{ mm}^3$) was filled with the mixture of the catalysts (0.8 g) and quartz granules (0–0.6 g). The reaction gas, a mixture of water vapor and methane, was introduced into the reactor at the flow rate of 40 mL min^{-1} and the reaction was carried out upon photoirradiation with a 300 W xenon lamp. In a standard condition, the concentration of water vapor and methane was 1.5% and 50%, respectively, and the light of the entire wavelength region from the xenon lamp was irradiated without passing any filters, where the light intensity measured in the range of 254 ± 10 and $365 \pm 15 \text{ nm}$ were ca. 14 and 60 mW cm^{-2} , respectively. The temperature of the reaction cell increased to ca. 323 K during photoirradiation. The outlet gas was analyzed by on-line gas chromatography with a thermal conductivity detector. Hydrogen production rates shown in each figure and table were taken from the value at 6 h after the reaction started.

6.2.3. Characterizations of Photocatalysts

Powder X-ray diffraction (XRD) pattern was recorded at room temperature on a Rigaku diffractometer MiniFlexII/AP using Ni-filtered Cu K α radiation (30 kV, 15 mA). The mean crystallite size of the sample was estimated from the diffraction line at 30.3 degree with the Scherrer equation. Diffuse reflectance (DR) UV-visible spectrum was recorded at room temperature on a JASCO V-570 equipped with an integrating sphere covered with BaSO₄, where BaSO₄ was used as the reference. The Brunauer–Emmett–Teller (BET) specific surface area of the sample was calculated from the amount of N₂ adsorption at 77 K, which was measured by a Quantachrome Monosorb. SEM images were recorded

by a S-5200 (Hitachi). TEM images were recorded by a JEOL electron microscope (JEM-2100M, 200 kV) equipped with CCD camera (Gatan, erlangshen ES500W). Rh K-edge XAFS (X-ray Absorption Fine Structure) were recorded at the NW-10A²³ station of KEK-PF (Photon Factory, Institute of Materials Structure Science, High Energy Accelerator Research Organization, Japan) at room temperature with a Si(311) double crystal monochromator in a transmission mode for Rh foil, and in a fluorescence mode by using the Lytle-detector²⁴ (100 mm ion chamber filled with Kr) with a Ru filter ($\mu t=6$) for the Rh-loaded samples. The spectra were analyzed with a REX 2000 software (Rigaku). Fourier transform of Rh K-edge EXAFS was performed in the range of ca. 3–12 Å⁻¹. The inverse Fourier transform was carried out in the range of ca. 0.9–3.2 Å and the curve fitting analysis was performed by using theoretical parameters.²⁵

6.3. Results and Discussion

6.3.1. Effect of Cocatalyst

The prepared K₂Ti₆O₁₃ sample was characterized by XRD, UV-vis, N₂ adsorption and SEM. From the XRD patterns, the formation of K₂Ti₆O₁₃ with a rectangular tunnel structure (ICSD #25712) was confirmed and no impurity phases were observed (Figure 1A). The mean crystallite size of the sample was 22 nm. From the UV-vis spectrum, absorption assigned to TiO₂ (rutile) was not observed (Figure 1B). The bandgap estimated from the absorption edge was ca. 3.4 eV. BET specific surface area of the sample was 2.3 m² g⁻¹. From the SEM image, aggregated particles sized from 0.1 to 2 μm were observed (Figure 1C).

At first, we loaded Pt cocatalyst on it by the photodeposition method and examined the photocatalytic activity for the PSRM. Figure 2 shows the time course of the production rates and the molar ratio of hydrogen and carbon dioxide over the Pt(0.085)/K₂Ti₆O₁₃ as the representative. Production of both hydrogen and carbon dioxide was observed and the

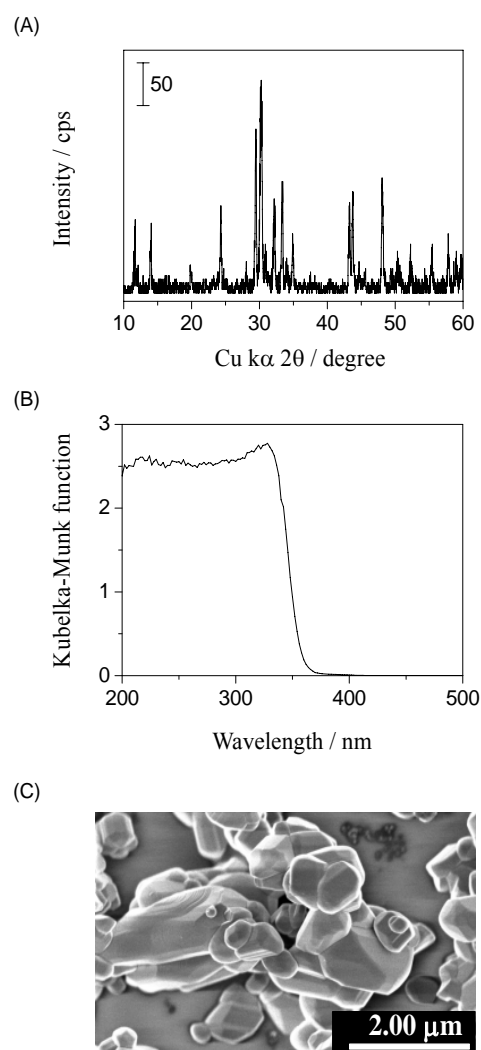


Figure 1. (A) XRD pattern, (B) UV-vis spectrum and (c) SEM image of K₂Ti₆O₁₃.

initial production rate was high. However, the production rates of them gradually decreased as the photocatalytic reaction continued. A small amount of carbon monoxide was produced constantly as a minor by-product. The molar ratio of hydrogen and carbon dioxide was almost four soon after the photocatalytic reaction started but became slightly higher than 4 after the reaction progressed. These facts show that over Pt/K₂Ti₆O₁₃ photocatalysts, part of methane would not be completely oxidized into carbon dioxide and the produced by-product might gradually accumulate on the catalyst surface to decrease the activity of Pt/K₂Ti₆O₁₃ photocatalyst. The decrease of the activity and the formation of CO were also observed over Pt/TiO₂.² As the photocatalytic reaction continued, the activity of Pt/NaTaO₃:La prepared by the photodeposition method largely decreased and the structural change of Pt cocatalyst was observed during the reaction.³ This may be the another possible reason for the decrease of the activity of Pt/K₂Ti₆O₁₃ photocatalysts.

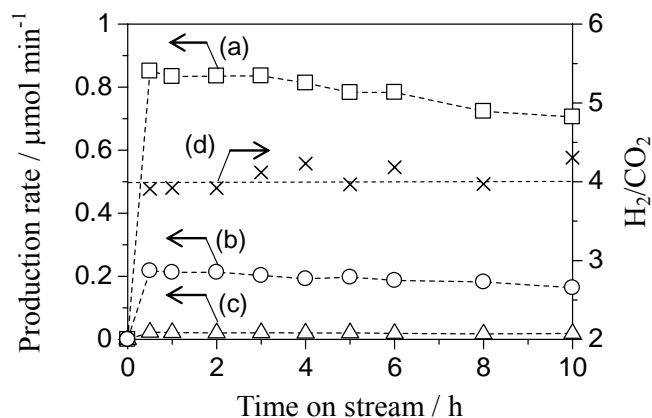


Figure 2. Time course of the production rate of (a) H₂, (b) CO₂ and (c) CO on Pt(0.085)/K₂Ti₆O₁₃ sample, and (d) that of molar ratio of the produced H₂ and CO₂ (H₂/CO₂) in the flowing mixture of water vapor and methane. Pt cocatalyst was loaded by the photodeposition method.

On the other hand, as shown in Figure 3, Rh/K₂Ti₆O₁₃ showed a higher and more stable activity for the PSRM than Pt/K₂Ti₆O₁₃ did. Induction period for the production rate was observed. This would be due to the accumulation of the reaction intermediates as reported in the previous studies.²⁻⁴ Another possibility is that Rh cocatalyst may be partially more reduced upon the photoirradiation in the flow of water vapour and methane. After the induction period, the production rate was constant and the molar ratio of hydrogen to carbon dioxide (H₂/CO₂) was almost four. Formation of by-products such as CO was not observed. These show that the PSRM would selectively proceed on Rh/K₂Ti₆O₁₃ photocatalysts.

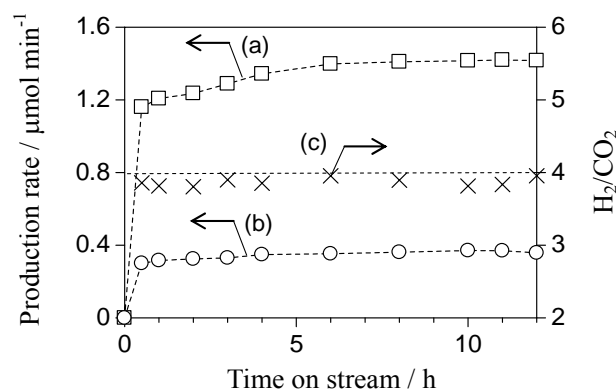


Figure 3. Time course of the production rate of (a) H_2 and (b) CO_2 on $\text{Rh}(0.04)/\text{K}_2\text{Ti}_6\text{O}_{13}$ sample, and (c) that of molar ratio of the produced H_2 and CO_2 (H_2/CO_2) in the flowing mixture of water vapor and methane. Rh cocatalyst was loaded by the photodeposition method.

Figure 4 shows the hydrogen production rate (at 6 h after the reaction started) in the flow of water vapour and methane over metal(0.03 wt%)-loaded $\text{K}_2\text{Ti}_6\text{O}_{13}$ samples prepared by a photodeposition method or an impregnation followed by calcination at 773 K. The hydrogen production rates over the Ru-, Pd- and Au-loaded samples were almost the same as that over the bare $\text{K}_2\text{Ti}_6\text{O}_{13}$. On the other hand, loading Rh or Pt largely increased the activity. The activity of the sample prepared by the photodeposition method (Figure 4a) was higher than that of the sample prepared by the impregnation and successive calcination (Figure 4b). The especially high activity was obtained over the $\text{Rh}/\text{K}_2\text{Ti}_6\text{O}_{13}$ prepared by the photodeposition method. The loading method of cocatalyst much influenced on the activity of the $\text{Rh}/\text{K}_2\text{Ti}_6\text{O}_{13}$ photocatalysts, which will be discussed later.

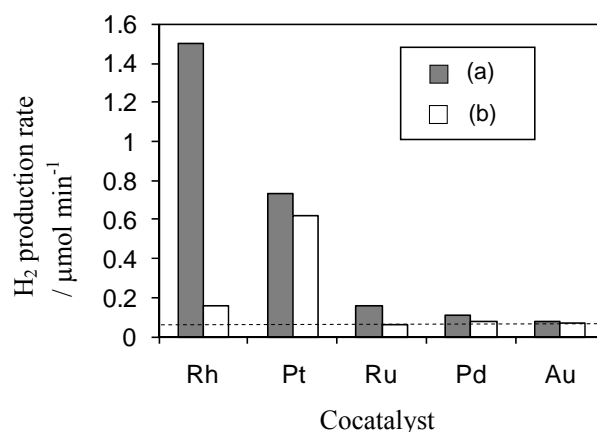


Figure 4. The hydrogen production rate over metal(0.03)-loaded $\text{K}_2\text{Ti}_6\text{O}_{13}$ samples in the flowing mixture of water vapor and methane. Metal cocatalysts were loaded by (a) the photodeposition method and (b) the impregnation method followed by calcination at 773 K. Dotted line shows the hydrogen production rate over the bare $\text{K}_2\text{Ti}_6\text{O}_{13}$ sample.

Influence of Rh- and Pt-loading amount on the activity was examined. The activity of Rh-loaded sample first increased and then decreased with increasing the loading amount. The highest activity was obtained over the 0.03 wt%-loaded sample (Figure 5a). On the other hand, the activity of Pt-loaded samples first increased with increasing the loading amount and became constant when the loading amount was larger than 0.025 wt% (Figure 5b). At the optimum loading amount, the Rh-loaded sample showed two times higher activity than the Pt-loaded one did. The hydrogen production rate over Rh/K₂Ti₆O₁₃ was higher than those over Pt/TiO₂,² Pt/Ga₂O₃⁴ and Pt/CaTiO₃⁵ photocatalysts, and almost the same as that over Pt/NaTaO₃:La³ under the same reaction condition.

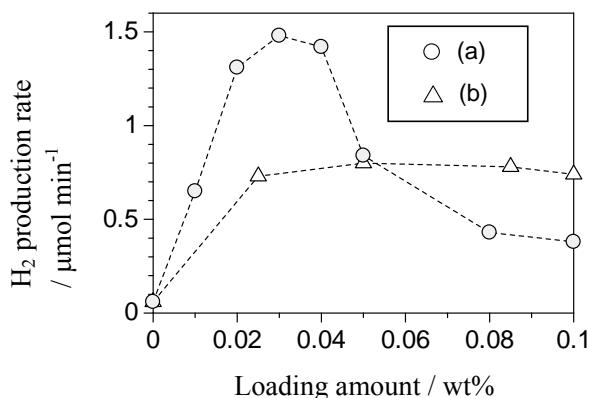


Figure 5. Influence of the loading amount of (a) Rh and (b) Pt on the hydrogen production rate in the flowing mixture of water vapor and methane. Rh and Pt were loaded on K₂Ti₆O₁₃ by the photodeposition method.

The photocatalytic reaction of hydrogen and carbon dioxide was examined over the bare and 0.03 or 0.1 wt% metal (Rh, Pt, Ru, Pd and Au)-loaded K₂Ti₆O₁₃ samples to confirm the contribution of each cocatalyst to the reverse reaction of the PSRM, where the reaction mixture (H₂ 5% and CO₂ 12.5% with Ar carrier) was flowed at 40 ml min⁻¹. Formation of CO and CH₄ was not observed for the bare and all the metal-loaded K₂Ti₆O₁₃ samples in the present condition. It was reported that Rh/TiO₂²⁶ and Ga₂O₃²⁷ showed a high photocatalytic activity for the reduction of carbon dioxide by hydrogen but NaTaO₃²⁸ was less active for it. On the other hand, for the PSRM, TiO₂ and Ga₂O₃ photocatalysts showed lower activity than NaTaO₃:La and K₂Ti₆O₁₃ did. Therefore, a high photocatalytic activity of the present K₂Ti₆O₁₃ samples as well as the reported NaTaO₃:La photocatalysts for the PSRM may be due to the less activity for the reverse reaction.

As shown in Figures 4 and 5, the activity of the Rh/K₂Ti₆O₁₃ photocatalysts was largely

influenced by the loading method and amount of Rh cocatalyst. This shows that the particle size and oxidation state of Rh would largely influence the photocatalytic activity. On the other hand, the activity of Pt-loaded sample did not severely vary with the Pt-loading method and its amount, showing that the particle size and oxidation state of Pt would not much influence the function of Pt cocatalyst.

6.3.2. Influence of Rh-loading Method

The photocatalytic activity of the Rh/K₂Ti₆O₁₃ samples prepared by different methods were further examined. Three Rh(0.03 wt%)-loaded K₂Ti₆O₁₃ samples were prepared by the impregnation and successive different thermal pretreatments; reduction at 473 K, calcination at 773 K before reduction at 473 K, and calcination at 773 K. Another one sample was prepared by the photodeposition method. Among these four samples, the catalyst prepared by the photodeposition method (Figure 6d) showed the higher activity than those prepared by the impregnation method (Figure 6 a–c) did. Among the samples prepared by the impregnation method, the sample reduced in H₂ (Figure 6a) showed the highest activity. The sample reduced after calcination (Figure 6b) showed a higher activity than that only calcined in air (Figure 6c) did.

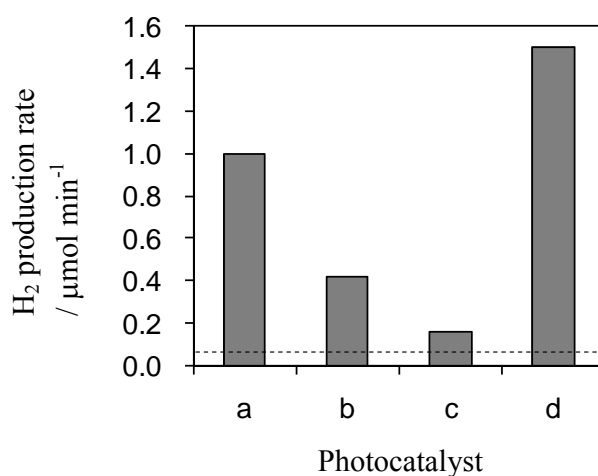


Figure 6. The hydrogen production rate in the PSRM over Rh(0.03)/K₂Ti₆O₁₃ samples. Rh cocatalyst was loaded by (a)-(c) the impregnation method and successive thermal pretreatments and (d) the photodeposition method. As the pretreatment, sample (a) was reduced in a flow of H₂ at 473 K, sample (b) was calcined in air at 773 K and reduced in a flow of H₂ at 473 K, and sample (c) was calcined in air at 773 K. Dotted line shows the hydrogen production rate over the bare K₂Ti₆O₁₃ sample.

The local structure of Rh cocatalysts on the Rh(0.1 wt%)/K₂Ti₆O₁₃ prepared by the four methods was examined with XAFS. Figure 7A shows the Rh K-edge XANES spectra of Rh foil and

Rh(0.1)/K₂Ti₆O₁₃ samples and Figure 7B shows their derivative spectra. The absorption edge in the spectrum of Rh/K₂Ti₆O₁₃ sample prepared by the impregnation and hydrogen reduction (referred to as sample *a*, Figure 7Ba) was almost the same energy (23210 eV) as that in the spectrum of Rh foil (Figure 7Be). In the sample prepared by the impregnation, calcination and hydrogen reduction (referred to as sample *b*, Figure 7Bb), the edge was slightly shifted to higher energy but close to that of Rh foil. On the other hand, the large edge shifts to higher energy were observed for the spectra of Rh/K₂Ti₆O₁₃ samples prepared by the impregnation and calcination (referred to as sample *c*, Figure 7Bc), and by the photodeposition (referred to as sample *d*, Figure 7Bd). These show that the oxidation state of Rh cocatalyst on the former two samples (*a* and *b*) would be close to that of Rh metal, while the state of Rh on the latter two samples (*c* and *d*) would be oxidized.

Figure 7C shows the Rh K-edge EXAFS spectra of the Rh foil and the Rh(0.1)/K₂Ti₆O₁₃ samples. In the sample *a*, a very small peak was observed at 1.5 Å, which corresponded to Rh-O (Figure 7Ca). The curve-fitting analysis showed that the atomic distance between Rh and O was ca. 2.06 Å. This value was close to the Rh-O distance in Rh₂O₃ (2.03–2.05 Å) but was different from that in RhO₂ (1.93–2.02 Å). The second coordination peak corresponding to Rh-Rh was largely observed at 2.4 Å. The fitting analysis showed that the atomic distance was 2.70 Å. This value was almost the same as that of Rh-Rh in Rh metal (2.69 Å). The

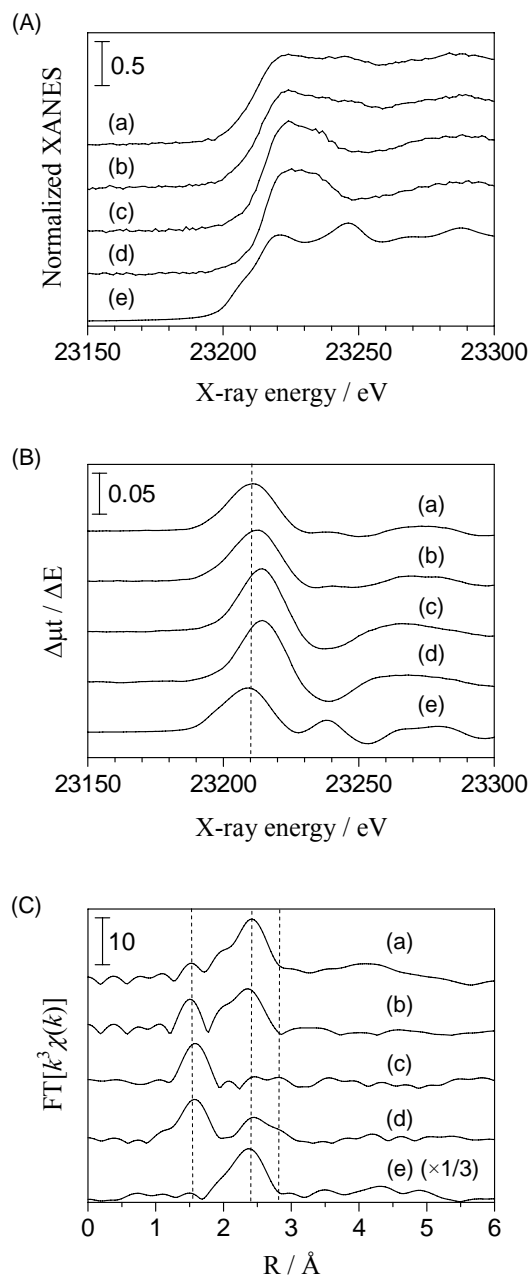


Figure 7. (A) Rh K-edge XANES, (B) derivative spectra of the Rh K-edge XANES and (C) the Fourier transforms of Rh K-edge EXAFS spectra for (a)-(d) Rh(0.1)/K₂Ti₆O₁₃ samples and (e) Rh foil. Rh cocatalyst was loaded by (a)-(c) the impregnation method and successive thermal pretreatments and (d) the photodeposition method. As the pretreatment, sample (a) was reduced in a flow of H₂ at 473 K, sample (b) was calcined in air at 773 K and reduced in a flow of H₂ at 473 K, and sample (c) was calcined in air at 773 K.

intensity of this peak was quite small as compared with Rh foil. These results indicate that most of Rh species on the sample *a* would exist as small Rh metal particles. For the sample *b*, two peaks assigned to Rh-O in Rh oxide and Rh-Rh in Rh metal were observed, showing that small Rh metal and comparatively small Rh oxide particles would coexist on the sample *b* (Figure 7Cb). For the sample *c*, the large peak for Rh-O in Rh oxide was observed but the peak assigned to Rh-Rh in Rh metal was hardly observed (Figure 7Cb). A small peak was also observed at 2.8 Å. Fitting analysis showed that this peak at 2.8 Å corresponded to Rh-Rh in Rh oxide. It is suggested that Rh species on the sample *c* would exist as relatively large Rh oxide particles. From the spectrum of the sample *d*, three peaks assigned to Rh-O in Rh oxide (1.6 Å), Rh-Rh in Rh metal (2.4 Å) and Rh-Rh in Rh oxide (2.8 Å) were observed (Figure 6Cd). The peak for Rh-Rh in Rh metal was clearly observed not for the sample *c* but for the sample *d*, showing that amount of Rh metal on the sample *d* would be larger than that on the sample *c*. Thus, it was suggested that Rh species on the sample *d* would be composed of small Rh metal and large Rh oxide particles.

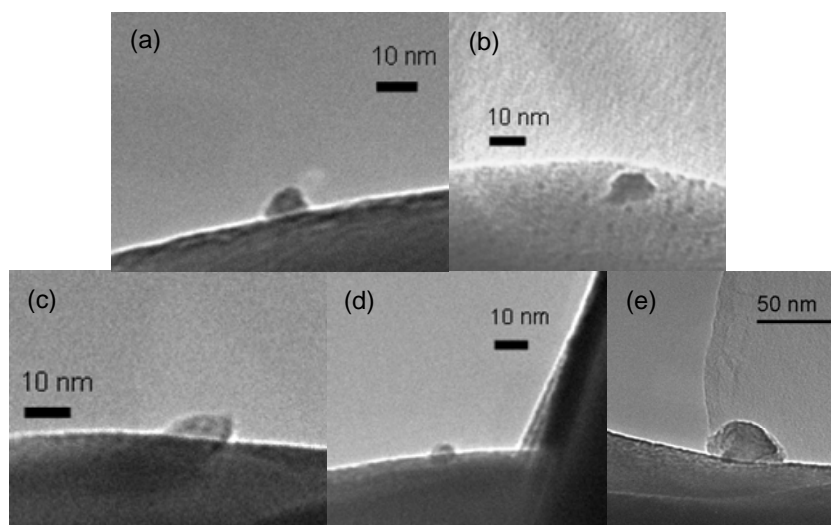


Figure 8. TEM images of Rh(0.1)/K₂Ti₆O₁₃ samples. Rh cocatalyst was loaded by (a)-(c) the impregnation method and successive thermal pretreatments and (d)-(e) the photodeposition method. As the pretreatment, sample (a) was reduced in a flow of H₂ at 473 K, sample (b) was calcined in air at 773 K and reduced in a flow of H₂ at 473 K, and sample (c) was calcined in air at 773 K.

Rh cocatalysts in these Rh/K₂Ti₆O₁₃ samples were observed with TEM. From the samples prepared by the impregnation method, small particles less than 10 nm were observed (Figure 8 a-c). Many spherical particles were observed for the samples *a* and *b*, while relatively asymmetric large particles were observed for the sample *c*. On the other hand, not only the small spherical particles less than 10 nm but also asymmetric particles as large as 50 nm were observed in the sample

prepared by the photodeposition method (Figure 8 d and e). Considering the result of EXAFS, the smaller particles would be Rh metal, while the larger ones would be Rh oxide.

As shown in Figure 6, the sample *a* showed the highest activity among the sample prepared by the impregnation method. Most of Rh species on the sample *a* would be loaded as metallic Rh (Figure 9a). On the other hand, Rh species on the samples *b* and *c* contained Rh oxide more or less. In the sample *b*, the reductive treatment was carried out after the oxidative one. Thus, the outside of Rh cocatalyst would be reduced, while the inside would be oxidized (Figure 9b). Rh species on the sample *c* should be entirely oxidized (Figure 9c). Rh metal particles on the sample *a* would function as a good cocatalyst for hydrogen production, which may promote the migration of photoexcited electrons in the conduction band to show a high activity. In the sample *b*, Rh oxide core would decrease the activity which may disturb the smooth migration of electrons. However, the activity of the sample *d* was higher than that of the sample *a*, although Rh species on the sample *d* would be a mixture of small metallic Rh and large Rh oxide particles (Figure 9d). Therefore, it is suggested that large Rh oxide particles on sample *d* would have different roles from those of Rh metal and contribute to the increase of the entire photocatalytic activity. Although Rh species on the sample *c* were existed as Rh oxide, increment of the activity by Rh-loading was small. This shows that the coexistence of Rh metal and Rh oxide would be important for the high photocatalytic activity.

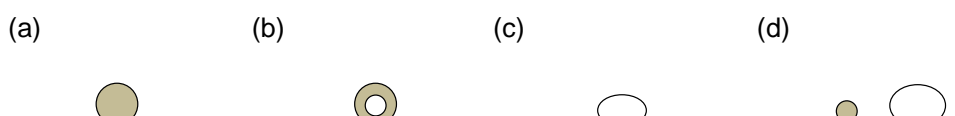


Figure 9. Proposed structure of Rh cocatalyst loaded on $K_2Ti_6O_{13}$. Rh cocatalyst was loaded by (a)-(c) the impregnation method and successive thermal pretreatments and (d) the photodeposition method. As the pretreatment, sample (a) was reduced in a flow of H_2 at 473 K, sample (b) was calcined in air at 773 K and reduced in a flow of H_2 at 473 K, and sample (c) was calcined in air at 773 K. Gray particle shows the Rh metal and white one shows the Rh oxide.

In general, it is accepted that precious metals such as Pt and Rh should capture the photoexcited electron and work as the reduction sites in the photocatalytic reaction. On the other hand, the metal oxides such as RuO_2 ²⁹⁻³¹ and IrO_2 ³²⁻³⁴ would work as the oxidation sites. Although there were few reports to use Rh oxide cocatalyst for photocatalytic reactions, Harriman et al., reported that Rh_2O_3 worked as a catalyst for O_2 evolution under photoelectrochemical condition with a photosensitizer and a sacrificial reagent.³⁵ Hrussanova et al. found that a RhO_x electrode in

acid solution exhibited a high activity for the electrochemical oxygen evolution.³⁶ Thus, Rh oxide can be expected to function as the oxidation sites for the photocatalytic reactions.

Rh₂O₃ is a *p*-type semiconductor, and the bandgap and the electron affinity are 1.4 and 3.6 eV, respectively (Figure 10Aa).³⁷ K₂Ti₆O₁₃ is a *n*-type semiconductor and the bandgap was 3.4 eV. It was reported that for metal oxide without partly-filled *d*-levels, the potential of the valence band edge was generally around ca. 3.0 V (vs. NHE).³⁸ Thus, the band structure of K₂Ti₆O₁₃ was estimated as shown in Figure 10Ab. Work function of Rh metal was reported to 5.0 eV (Figure 10Ac).³⁹ The junction between Rh and K₂Ti₆O₁₃ would form Schottky barrier and that between Rh₂O₃ with *p*-type property and K₂Ti₆O₁₃ with *n*-type property would form band bending as shown in Figure 10B.

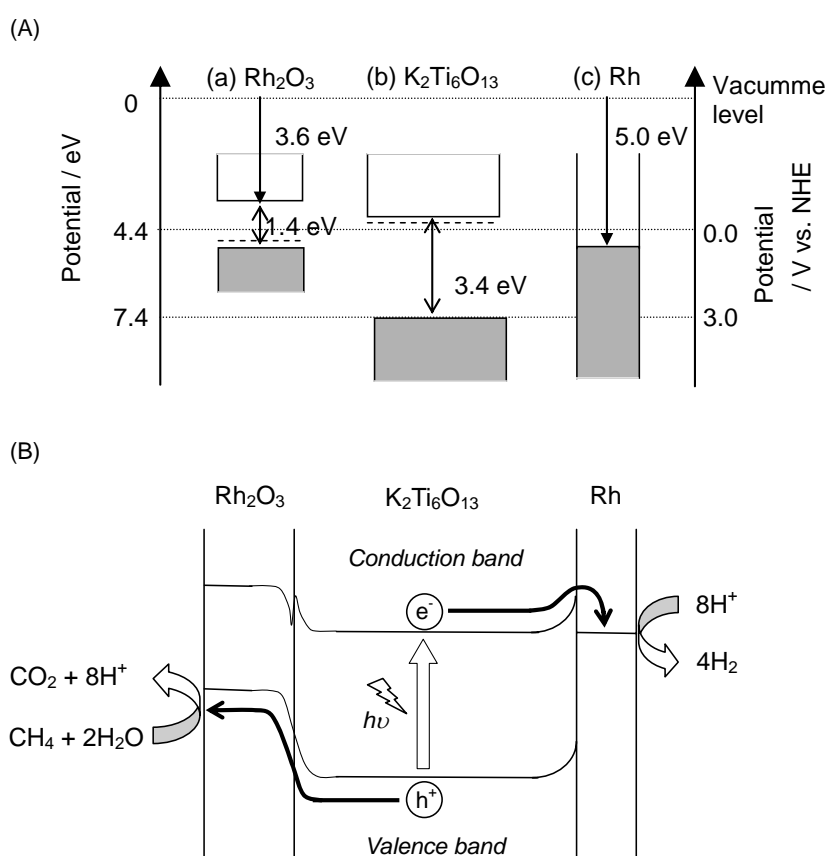


Figure 10. (A) Band structure of (a) Rh₂O₃, (b) K₂Ti₆O₁₃ and (c) Rh metal, and (B) proposed reaction mechanism in the PSRM over the Rh/K₂Ti₆O₁₃ prepared by the photodeposition method.

Thus, the reaction mechanism over Rh/K₂Ti₆O₁₃ prepared by the photodeposition method was proposed as follows; Small Rh metal particles would enhance the hydrogen production and promote the migration of electrons, while large Rh oxide particles would accelerate the CO₂ production and promote the migration of holes. In other words, loading of two cocatalysts for both the oxidation and reduction

would improve the whole photocatalytic activity. There are some reports showing that loading of two different cocatalysts for the oxidative and reductive reactions increased the photocatalytic activity; for example Pt+PdS/CdS,¹³ Pt+RuO₂/ZnGe₂O₄,⁴⁰ Rh-Cr+Mn₃O₄/GaN-ZnO,⁴¹ and Rh+Ag₂S/Sm₂Ti₂S₂O₅.⁴² However, it should be noted that in the present case, the simple photodeposition of Rh on K₂Ti₆O₁₃ could generate both the Rh metal for the reduction and the Rh oxide for the oxidation to increase the entire photocatalytic activity.

6.3.3. Comparison with Other Semiconductor Photocatalysts

Influence of Pt- and Rh-loading on the activity of other photocatalysts for the PSRM was examined (Figure 11). Pt and Rh were loaded by the photodeposition method and the loading amount was optimized for each sample as shown in the caption of Figure 11. For the β -Ga₂O₃ and TiO₂ photocatalysts, Pt-loaded sample showed a higher activity than Rh-loaded one did (Figure 11 a and d). On the other hand, for the K₂Ti₆O₁₃ and Na₂Ti₆O₁₃ photocatalysts, Rh-loaded sample showed a higher activity than Pt-loaded one did (Figure 11 b and c).

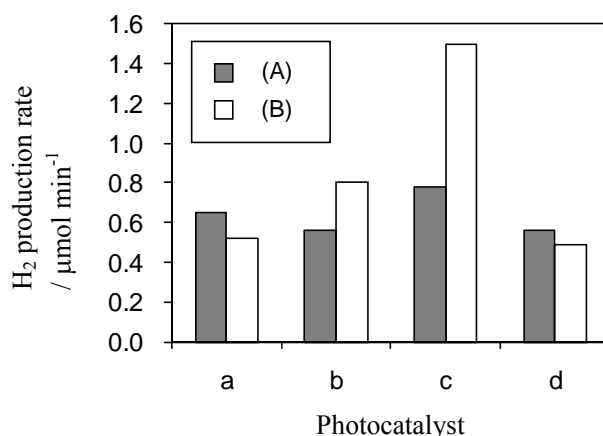


Figure 11. The hydrogen production rate over various photocatalysts loaded with (A) Pt and (B) Rh cocatalysts for the PSRM. Photocatalysts used for the reaction were (a) β -Ga₂O₃, (b) Na₂Ti₆O₁₃, (c) K₂Ti₆O₁₃ and (d) TiO₂. Cocatalysts were loaded by the photodeposition method. Loading amount of cocatalysts was optimized for each photocatalyst sample: (A) (a) 0.05 wt%, (b) 0.05 wt%, (c) 0.05 wt% and (d) 0.1 wt%; (B) (a) 0.05 wt%, (b) 0.05 wt%, (c) 0.03 wt% and (d) 0.3 wt%.

The local structure of Rh cocatalysts on four Rh(0.1 wt%)-loaded photocatalysts prepared by the photodeposition method was examined. Figure 12A shows Rh K-edge XANES spectra of Rh foil and the photocatalysts and Figure 12B shows their derivative spectra. The absorption edge in the spectra of all Rh-loaded samples shifted to higher energy than that in the spectra of Rh foil did (Figure 12 B). This shows that all Rh-loaded photocatalysts would contain Rh oxide species to

some extent. The edge shift in the spectrum of Rh/K₂Ti₆O₁₃ was as large as that in the spectra of Rh/Ga₂O₃ and Rh/Na₂Ti₆O₁₃, but was larger than that in the spectrum of Rh/TiO₂. This shows that the amount of Rh oxide in Rh/K₂Ti₆O₁₃ was larger than that in Rh/TiO₂.

The state of Rh cocatalyst was also examined with EXAFS. The Fourier transforms of Rh K-edge EXAFS spectra of Rh foil and Rh-loaded samples were shown in Figure 12C. The peaks at 1.5, 2.4 and 2.8 Å would correspond to Rh-O in Rh oxide, Rh-Rh in Rh metal and Rh-Rh in Rh oxide, respectively. Rh species on Rh/K₂Ti₆O₁₃ were the mixture of moderately small Rh metal particles and moderately large Rh oxide particles, as shown in Figure 9d. On the spectrum of Rh/Ga₂O₃, very large two peaks assigned to Rh-O and Rh-Rh in Rh oxide were observed (Figure 12Ca). This shows that Rh species on Ga₂O₃ would exist as very large Rh oxide. On the spectra of Rh/K₂Ti₆O₁₃, three peaks assigned to Rh-O in Rh oxide, Rh-Rh in Rh metal and Rh-Rh in Rh oxide were observed (Figure 12Cb). Rh-Rh in Rh metal for Rh/Na₂Ti₆O₁₃ was smaller than that for Rh/K₂Ti₆O₁₃. Rh-Rh in Rh oxide for Rh/Na₂Ti₆O₁₃ was smaller than that for Rh/K₂Ti₆O₁₃. It is suggested that Rh on Na₂Ti₆O₁₃ would exist as very small Rh metal and relatively large Rh oxide. On the spectrum of Rh/TiO₂, small peak assignable to Rh-O in Rh oxide and large peak assignable to Rh-Rh in Rh metal were observed (Figure 12Cd). It is suggested that most of the Rh species on TiO₂ would exist as small Rh metal particles. The

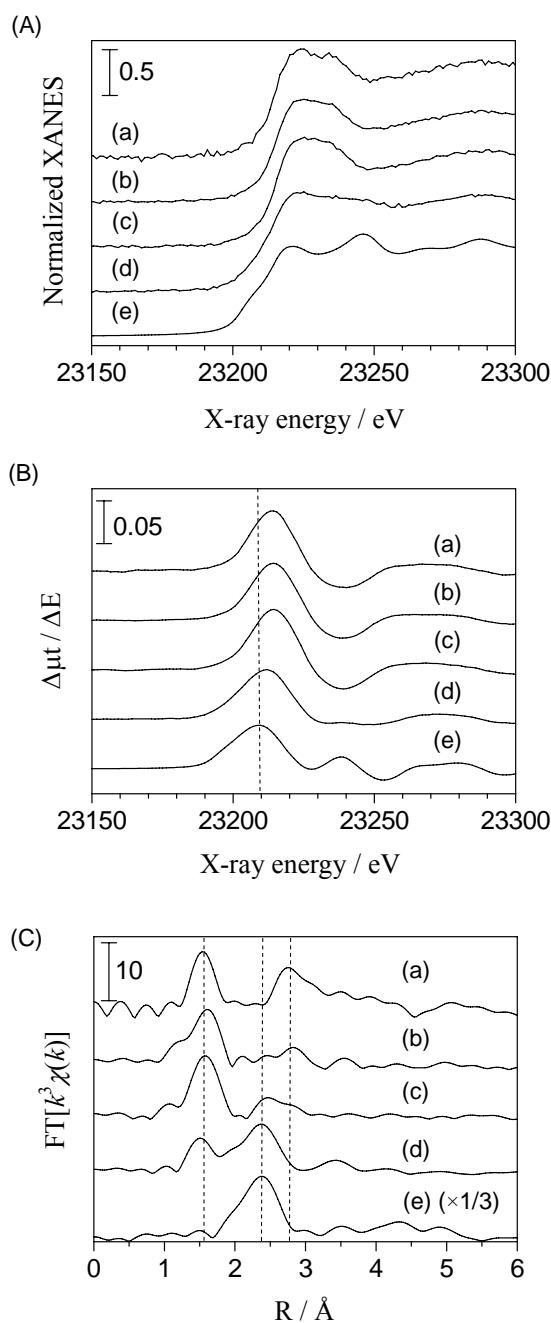


Figure 12. (A) Rh K-edge XANES, (B) derivative spectra of the Rh K-edge XANES and (C) the Fourier transforms of Rh K-edge EXAFS spectra of (a)-(d) the Rh(0.1 wt%)-loaded semiconductors and (e) Rh foil. The semiconductors used were (a) Rh/Ga₂O₃, (b) Rh/Na₂Ti₆O₁₃, (c) Rh/K₂Ti₆O₁₃ and (d) Rh/TiO₂. Rh cocatalyst was loaded by the photodeposition method.

results of XAFS analysis also show that the coexistence of small Rh metal and large Rh oxide particles would increase the photocatalytic activity.

Table 1 BET specific surface area, band gap, and the particle sizes of Rh metal and Rh oxide loaded on each photocatalyst sample

Photocatalyst	SA ^a / m ² g ⁻¹	BG ^b / eV	Mean particle size ^c	
			Rh metal	Rh oxide
β -Ga ₂ O ₃	11.7	4.6	– ^d	Very large
Na ₂ Ti ₆ O ₁₃	1.5	3.5	Very small	Large
K ₂ Ti ₆ O ₁₃	2.2	3.4	Moderately small	Moderately large
TiO ₂	140	3.2	Small	– ^e

^a BET specific surface area. ^b Bandgap. ^c Particle sizes of Rh metal and Rh oxide were estimated from the peak intensity at 2.4 and 2.8 Å in Figure 11C, respectively. ^d Rh metal would not exist. ^e Rh oxide would not exist.

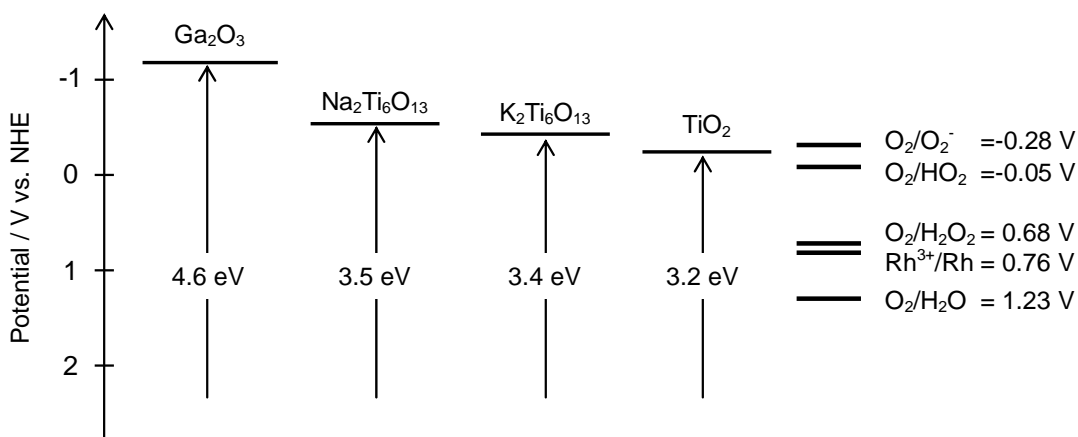


Figure 13. Proposed potential of the conduction band edge of the semiconductors and the reduction potential of oxygen and Rh ion.

Bandgap, BET specific surface area and mean particle size of Rh metal and Rh oxide estimated from the EXAFS spectra are summarized in Table 1. The bandgaps of β -Ga₂O₃, Na₂Ti₆O₁₃, K₂Ti₆O₁₃ and anatase-TiO₂ were 4.6, 3.5, 3.4 and 3.2 eV, respectively. The larger size of Rh metal particles, the smaller bandgap of the semiconductors, while the larger size of Rh oxide particle, the larger bandgap of the semiconductors. From these facts, the mechanism of Rh photodeposition is tentatively proposed as follows; In the present study, the photodeposition of Rh was carried out in an aqueous methanol solution in the atmosphere. Thus, photoexcited electrons would be consumed for not only the reduction of Rh ions but also the reduction of oxygen. In other

words, the reduction of Rh ions ($\text{Rh}^{3+} + 3\text{e}^- \rightarrow \text{Rh}$, 0.76 V vs NHE) would compete with those of oxygen. As the bandgap of metal oxide increased, potential of the conduction band edge would shift cathodically (Figure 13) and the reduction of oxygen would be promoted. This means that the activated oxygen species formed would increase, which may oxidize the Rh ions to form Rh oxide particles. On the other hand, this mechanism would not be applied to the case of Pt photodeposition. The coexistence of oxygen would not much influence the loading of Pt cocatalyst, since Pt would be easily reduced ($\text{Pt}^{2+} + 2\text{e}^- \rightarrow \text{Pt}$, 1.19 V vs NHE) and not easily oxidized.

6.4. Conclusion

The photocatalytic steam reforming of methane (PSRM) was examined over metal-loaded $\text{K}_2\text{Ti}_6\text{O}_{13}$ photocatalysts. Among the examined metal-loaded photocatalysts, Rh-loaded $\text{K}_2\text{Ti}_6\text{O}_{13}$ prepared by the photodeposition method showed the highest activity and proceeded the PSRM selectively without deactivation for a long time. On the other hand, loading Pt cocatalyst on $\text{K}_2\text{Ti}_6\text{O}_{13}$ promoted the PSRM with formation of by-product and caused deactivation, although Pt cocatalyst has been usually effective for the reported photocatalysts for the PSRM.¹⁻⁶

XAFS analysis showed that over the highly active Rh/ $\text{K}_2\text{Ti}_6\text{O}_{13}$ photocatalyst, Rh cocatalyst would be loaded as the mixture of moderately small Rh metal particles and moderately large Rh oxide particles. The former would accelerate the hydrogen production and promote the electron migration in the conduction band, while the latter would promote the oxidation of water and methane to carbon dioxide, and enhance the migration of holes in the valence band.

Rh-loading by the photodeposition method tends to form metallic Rh particles on the photocatalysts with small bandgap, on the other hand, to form Rh oxide particles on the photocatalysts with large bandgap. In $\text{Na}_2\text{Ti}_6\text{O}_{13}$ and $\text{K}_2\text{Ti}_6\text{O}_{13}$ photocatalysts with medium band gap, the formed Rh species were a mixture of moderately small Rh metal and moderately large Rh oxide. Rh loading was effective for $\text{Na}_2\text{Ti}_6\text{O}_{13}$ and $\text{K}_2\text{Ti}_6\text{O}_{13}$, but not for Ga_2O_3 and TiO_2 in the PSRM, confirming that coexistence of Rh metal and large Rh oxide would be effective for the improvement of photocatalytic activity.

References.

- 1) Yoshida, H.; Kato, S.; Hirao, K.; Nishimoto, J.; Hattori, T. *Chem. Lett.* **2007**, 36, 430–431.
- 2) Yoshida, H.; Hirao, K.; Nishimoto, J.; Shimura, K.; Kato, S.; Itoh, H.; Hattori, T. *J. Phys. Chem. C*

- 2008, 112, 5542–5551.
- 3) Shimura, K.; Kato, S.; Yoshida, T.; Itoh, H.; Hattori, T.; Yoshida, H. *J. Phys. Chem. C* **2010**, 114, 3493–3503.
 - 4) Shimura, K.; Yoshida, T.; Yoshida, H. *J. Phys. Chem. C* **2010**, 114, 11466–11474.
 - 5) Shimura, K.; Yoshida, H. *Energy Environ. Sci.* **2010**, 3, 615–617.
 - 6) Shimura, K.; Miyanaga, H.; Yoshida, H. *Stud. Surf. Sci. Catal.* **2010**, 175, 85–92.
 - 7) Domen, K.; Kudo, A.; Onishi, T.; Kosugi, N.; Kuroda, H. *J. Phys. Chem.* **1986**, 90, 292–295.
 - 8) Kudo, A.; Tanaka, A.; Domen, K.; Maruya, K.; Aika, K.; Ohishi, T. *J. Catal.* **1988**, 111, 67–76.
 - 9) Kato, H.; Asakura, K.; Kudo, A. *J. Am. Chem. Soc.* **2003**, 125, 3082–3089.
 - 10) Inoue, Y. *Energy Environ. Sci.* **2009**, 2, 364–386.
 - 11) Maeda, K.; Teramura, K.; Lu, D. L.; Takata, T.; Saito, N.; Inoue, Y.; Domen, K. *Nature* **2006**, 440, 295.
 - 12) Maeda, K.; Teramura, K.; Saito, N.; Inoue, Y.; Domen, K. *J. Catal.* **2006**, 243, 303–308.
 - 13) Yan, H. J.; Yang, J. H.; Ma, G. J.; Wu, G. P.; Zong, X.; Lei, Z. B.; Shi, J. Y.; Li, C. *J. Catal.* **2009**, 266, 165–168.
 - 14) Zong, X.; Wu, G. P.; Yan, H. J.; Ma, G. J.; Shi, J. Y.; Wen, F. Y.; Wang, L.; Li, C. *J. Phys. Chem. C* **2010**, 114, 1963–1968.
 - 15) Zhang, W.; Wang, Y. B.; Wang, Z.; Zhong, Z. Y.; Xu, R.; *Chem. Comm.* **2010**, 46, 7631–7633.
 - 16) Hara, M.; Nunoshige, J.; Takata, T.; Kondo, J. N.; Domen, K. *Chem. Comm.* **2003**, 3000–3001.
 - 17) Liu, M. Y.; You, W. S.; Lei, Z. B.; Zhou, G. H.; Yang, J. J.; Wu, G. P.; Ma, G. J.; Luan, G. Y.; Takata, T.; Hara, M.; Domen, K.; Li, C. *Chem. Comm.* **2004**, 2192–2193.
 - 18) Abe, R.; Takami, H.; Murakami, N.; Ohtani, B. *J. Am. Chem. Soc.* **2008**, 130, 7780–7781.
 - 19) Arai, T.; Horiguchi, M.; Yanagida, M.; Gunji, T.; Sugihara, H.; Sayama, K. *Chem. Comm.* **2008**, 5565–5567.
 - 20) Mills, A.; LeHunte, S. *J. Photochem. Photobiol. A* **1997**, 108, 1–35.
 - 21) Inoue, Y.; Kubokawa, T.; Sato, K. *J. Phys. Chem.* **1991**, 95, 4059–4063.
 - 22) Sayama, K.; Arakawa, H. *J. Photochem. Photobiol. A: Chem.* **1994**, 77, 243–247.
 - 23) Nomura, M.; Koike, Y.; Sato, M.; Koyama, A.; Inada, Y.; Asakura, K. *AIP Conf. Proc.* **2007**, 882, 896.
 - 24) Lytle, F. W.; Greigor, R. B.; Sandstorm, D. R.; Marques, E. C.; Wong, J.; Spiro, C. L.; Huffman, G. P.; Huggins, F. E. *Nucl. Instrum. Methods* **1984**, 226, 542–548.
 - 25) Mckale, A. G.; Veal, B. W.; Paulikas, A.P.; Chan, S. K.; Knapp, G. S. *J. Am. Chem. Soc.* **1988**, 110, 3763–3768.

- 26) Kohno, Y.; Hayashi, H.; Takenaka, S.; Tanaka, T.; Funabiki, T.; Yoshida, S. *J. Photochem. Photobiol. A* **1999**, 126, 117–123.
- 27) Teramura, K.; Tsuneoka, H.; Shishido, T.; Tanaka, T. *Chem. Phys. Lett.* **2008**, 467, 191–194.
- 28) Teramura, K.; Okuoka, S.; Tsuneoka, H.; Shishido, T.; Tanaka, T. *Appl. Catal. B* **2010**, 96, 565–568.
- 29) Kalyanasundaram, K.; Gratzel, M. *Angew. Chem., Int. Edit. Engl.* **1979**, 18, 701–702.
- 30) Kawai, T.; Sakata, T. *Chem. Phys. Lett.* **1980**, 72, 87–89.
- 31) Duonghong, D.; Borgarello, E.; Gratzel, M.; *J. Am. Chem. Soc.* **1981**, 103, 4685–4690.
- 32) Hara, M.; Waraksa, C. C.; Lean, J. T.; Lewis, B. A.; Mallouk, T. E. *J. Phys. Chem. A* **2000**, 104, 5275–5280.
- 33) Kasahara, A.; Nukumizu, K.; Hitoki, G.; Takata, T.; Kondo, J. N.; Hara, M.; Kobayashi, H.; Domen, K. *J. Phys. Chem. A* **2002**, 106, 6750–6753.
- 34) Iwase, A.; Kato, H.; Kudo, A. *Chem. Lett.* **2005**, 34, 946–947.
- 35) Harriman, A.; Pickering, I.J.; Thomas, J. M.; Christensen, P. A. *J. Chem. Soc. Faraday Trans.* **1988**, 84, 2795–2806.
- 36) Hrussanova, A.; Guerrini E.; Trasatti, S. *J. Electroanal. Chem.* 2005, **564**, 151–157.
- 37) Koffyberg, F. P. *J. Phys. Chem. Solids* **1992**, 53, 1285–1288.
- 38) Scaife, D. E. *Solar Energy* **1980**, 25, 41–54.
- 39) Michaelson, H. B. *J. Appl. Phys.* **1977**, 48, 4729–4733.
- 40) Ma, B.; Wen, F.; Jiang, H.; Yang, J.; Ying, P.; Li, C. *Catal. Lett.* 2010, **134**, 78–86.
- 41) Maeda, K.; Xiong, A.; Yoshinaga, T.; Ikeda, T.; Sakamoto, N.; Hisatomi, T.; Takashima, M.; Lu, D.; Kanehara, M.; Setoyama, T.; Teranishi, T.; Domen K. *Angew. Chem. Int. Ed.* **2010**, 49, 4096–4099.
- 42) Zhang, F.; Maeda, K.; Takata, T.; Domen K. *Chem. Comm.* **2010**, 46, 7313–7315.

Chapter 7

Summary

7.1. Summary of each chapter

The main results for each chapter are summarized as follows:

Chapter 1: General Introduction

In this chapter, the photocatalytic hydrogen production from water and biomass derivatives was compared with the other hydrogen production methods from biomass. Although various attempts had been done to achieve the efficient hydrogen evolution, such as development of various semiconductors and cocatalyst, modification of photocatalyst, the morphology control of photocatalyst, the optimization of reaction condition, the efficiency for the photocatalytic hydrogen production from water and biomass derivatives was still low. However, it should be noted that this photocatalytic system is very attractive since this system can convert the solar energy into chemical potential of the storable hydrogen by consuming only renewable resources.

Chapter 2: Photocatalytic Steam Reforming of Methane over Pt-loaded Titanium Oxide

In the chapter 2, the photocatalytic steam reforming of methane was examined over Pt/TiO₂ photocatalysts. The highly active photocatalyst was anatase-type TiO₂ with a large surface area, which was loaded with metallic Pt nanoparticles by the in-situ photodeposition method. The reaction intermediates, possibly described as [CH₂O]_n, were formed on the surface of the catalyst, and reacted with water to produce H₂ and CO₂. The accumulation of the reaction intermediates depended on the activity of the photocatalyst and reaction conditions. Moderate accumulation of surface intermediates could accelerate the reaction rate.

Chapter 3: Photocatalytic steam reforming of methane over sodium tantalate

In this chapter, the photocatalytic steam reforming of methane was examined over sodium tantalite. The photocatalytic activity of NaTaO₃ was largely influenced by the doping metal ions and loading the cocatalyst. The highest activity was obtained over the NaTaO₃ doped with La³⁺, where a moderate amount of La³⁺ substituted for Na⁺ without distorting the crystal structure and would improve the density and the mobility of carriers to improve the activity. Among the examined metal cocatalyst, Pt nanoparticles most enhanced the activity. The heat treatment after the addition of Pt, which would improve the metal-semiconductor junction, was required for a high and stable activity. The apparent

quantum yield for the photocatalytic steam reforming of methane employing Pt/NaTaO₃:La was higher than that of the photocatalytic water splitting employing NiO/NaTaO₃, which had been the best photocatalyst for the water decomposition so far. Thus, it was confirmed that this photocatalytic system would be an efficient hydrogen production system.

Chapter 4: Photocatalytic Steam Reforming of Methane over Gallium Oxide

In the chapter 4.1, the structural factors influencing the photocatalytic activity of gallium oxide was examined. The Pt-loaded β -Ga₂O₃ photocatalyst with specific surface area of 10-20 m² g⁻¹ was effective for photocatalytic steam reforming of methane without deactivation for a long time. The activity of the Pt/ β -Ga₂O₃ sample was further enhanced by the addition of metal ions into the bulk and on the surface. And, these two kinds of modification could independently improve the activity at the same time. From the comparison of the activity for photocatalytic steam reforming of methane with those for the water decomposition ($\text{H}_2\text{O} \rightarrow \text{H}_2 + 1/2 \text{O}_2$) and the methane decomposition ($\text{CH}_4 \rightarrow x/2 \text{H}_2 + \text{CH}_{4-x}$), it was revealed that the improvement of the bulk processes would mainly influence the water activation while that of the surface processes would affect the methane activation.

In the chapter 4.2, the author examined the influence of the external thermal energy on the photocatalytic activity of Ga₂O₃ for photocatalytic steam reforming of methane. The production rate increased with an increase of the reaction temperature before reaching ca. 343 K, and then it became constant. Arrhenius plot for the production rate in the lower temperature range showed a straight line and the thermal activation energy was typically less than ca. 10 kJ mol⁻¹. The thermal activation energy was varied with the irradiation light intensity, the crystallite size of Ga₂O₃ and the loading of metal cocatalyst. It was suggested that the thermal energy would promote the migration of the photoexcited carriers both in the bulk of Ga₂O₃ and at the metal-semiconductor junction between the metal cocatalyst and Ga₂O₃.

In the chapter 4.3, some series of Ga₂O₃ samples doped with metal ions (Zn²⁺, Y³⁺ and Zr⁴⁺) were systematically prepared by the homogeneous precipitation method (HP) and the impregnation method (IMP), and the local structure of the dopants and the activity of the doped Ga₂O₃ for photocatalytic steam reforming of methane were studied. Zn-doping increased the photocatalytic activity of Ga₂O₃, while doping of Y or Zr ions did not change or decreased the activity. XAFS study revealed that the doped Zn ions substituted for Ga³⁺ in Ga₂O₃ sample prepared by the HP method, while they existed as ZnGa₂O₄ in the sample prepared by the IMP method. From the measurement of thermal activation energy of the photocatalysis, it was revealed that the former Zn species would improve the

bulk electric property of Ga_2O_3 with the less crystal distortion, while the latter species would work as the surface active phase to enhance the photocatalytic activity.

Chapter 5: Photocatalytic Hydrogen Production from Water Vapor and Methane over Pt/CaTiO₃

In the chapter 5.1, the increase of the hydrogen production rate from water on Pt/CaTiO₃ was accelerated by the introduction of methane. Even in the presence of methane, both photocatalytic steam reforming of methane and water decomposition proceeded over Pt/CaTiO₃. With increasing the loading amount of Pt, the hydrogen production rate in the photocatalytic steam reforming of methane increased. Furthermore, the hydrogen production rate through the water decomposition in the flow of water vapour and methane was higher than that in the flow of water. It is suggested that the activated methane species or the reaction intermediates would accelerate the water decomposition or suppress its reverse reaction.

In the chapter 5.2, various CaTiO₃ samples having different particle sizes, shapes, crystal defects and impurity phases were prepared by three methods, i.e., co-precipitation, homogeneous precipitation and solid-state reaction methods. The CaTiO₃ samples were loaded with Pt cocatalyst and examined for both the photocatalytic water decomposition and the photocatalytic steam reforming of methane. The highest activities for water decomposition and photocatalytic steam reforming of methane were obtained over the samples prepared by the solid-state reaction method from rutile and anatase TiO₂, respectively. CaTiO₃ with a large crystallite size and few crystal defects was effective for photocatalytic steam reforming of methane, while the state of Pt cocatalyst largely influenced the activity for water decomposition.

Chapter 6: Photocatalytic Steam Reforming of Methane over Potassium Titanate

In this chapter, the photocatalytic steam reforming of methane was examined over metal-loaded K₂Ti₆O₁₃. Although Pt-loading increased the photocatalytic activity of K₂Ti₆O₁₃ for this reaction, the progress of side reaction and the deactivation of photocatalyst were observed. On the other hand, Rh-loaded K₂Ti₆O₁₃ showed two times higher activity than Pt-loaded one did and selectively promoted the photocatalytic steam reforming of methane without deactivation for a long time. Over the highly active Rh/K₂Ti₆O₁₃ photocatalyst, Rh cocatalyst existed as the mixture of small metallic Rh and large Rh oxide particles. The former would accelerate hydrogen formation and promote the electron migration in the conduction band, while the latter would promote the oxidative reaction and enhance the migration of holes in the valence band, respectively.

7.2 General Conclusions

Based on the summary of each chapter mentioned above, catalyst design for the photocatalytic steam reforming of methane could be drawn as the following:

1. The moderate accumulation of reaction intermediates would promote the adsorption of methane to enhance the production rate over Pt/TiO₂. Thus, the control of the surface hydrophobic or hydrophilic property for optimizing the adsorbed amount of reactants and surface intermediates should be very important to enhance the activity.
2. Preparation of photocatalysts with a large surface area and few crystal defects is important to increase the photocatalytic activity, since on these photocatalysts both the bulk processes such as the migration of photoexcited carriers and the surface processes such as the adsorption of reactants could be well enhanced.
3. Activation of both water and methane would be important to increase the activity for photocatalytic steam reforming of methane. Doping metal ions in the bulk and loading them on the surface are effective way to promote the activation of both water and methane.
4. Improving the junction between the metal cocatalyst and the semiconductor is important to show a high and stable activity. Co-loading of two cocatalysts for the oxidation and reduction is useful way to increase the photocatalytic activity.
5. Thermal energy would promote the migration of photoexcited carriers more or less when the photocatalyst had a low crystallinity of the semiconductor, a high schottky barrier or an imperfect metal-semiconductor junction.

7.3 Perspective and Outlook

In this thesis, the author examined the development of the catalyst for the photocatalytic steam reforming of methane around room temperature and succeeded in increasing the photoatalytic activity largely. Furthermore, the author could obtain much useful knowledge for the preparation of the effective photocatalyst. In the best photocatalyst, the hydrogen production rate reached 4.5 $\mu\text{mol min}^{-1}$ (270 μmol

h^{-1}), corresponding to 0.6% methane conversion and 11% water conversion, which exceeded the equilibrium conversion calculated from thermodynamic data. The apparent quantum yield for the hydrogen production was 30% in the range of 240-270 nm. However, this photocatalytic system is still far from the practical use.

Many things must be achieved for a practical application. Development of more active photocatalysts driven in visible light is the most important problems to utilize the solar energy, since the light intensity of the visible region is most large in the sunlight. On the other hand, improvement of the photo-reactor would be also required to achieve an efficient hydrogen production. We hope that this photocatalytic system will contribute as one of the hydrogen production methods in the near future.

List of Publications

Original papers corresponding to this thesis

Chapter 2

1. Hydrogen Production from Methane and Water on Platinum Loaded Titanium Oxide Photocatalysts
H. Yoshida, K. Hirao, J. Nishimoto, K. Shimura, S. Kato, H. Itoh and T. Hattori
J. Phys. Chem. C 2008, **112**, 5542–5551.

Chapter 3

2. Photocatalytic Steam Reforming of Methane over Sodium Tantalate
K. Shimura, S. Kato, T. Yoshida, H. Itoh, T. Hattori and H. Yoshida
J. Phys. Chem. C 2010, **114**, 3493–3503.

Chapter 4

3. Photocatalytic Activation of Water and Methane over Modified Gallium Oxide for Hydrogen Production
K. Shimura, T. Yoshida and H. Yoshida,
J. Phys. Chem. C 2010, **114**, 11466–11474.
4. Thermal Acceleration of Electron Migration in Gallium Oxide Photocatalysts
K. Shimura, K. Maeda and H. Yoshida
J. Phys. Chem. C, in revision.
5. Doping Effect on Photocatalytic Activity of Gallium Oxide for Hydrogen Production from Water and Methane
K. Shimura and H. Yoshida
to be submitted.

Chapter 5

6. Hydrogen Production from Water and Methane over Pt-loaded Calcium Titanate Photocatalyst
K. Shimura and H. Yoshida
Energy Environ. Sci. **3**, 2010, 615–617.

7. Preparation of Calcium Titanate Photocatalysts for Hydrogen Production

K. Shimura, H. Miyanaga and H. Yoshida

Stud. Surf. Sci. Catal. **175**, 2010, 85–92.

Chapter 6

8. Cooperative Rhodium Metal and Rhodium Oxide Cocatalysts for Photocatalytic Steam Reforming of Methane over Potassium Titanate

K. Shimura, H. Kawai, T. Yoshida and H. Yoshida

to be submitted.